

INFORMATYKA AUTOMATYKA POMIARY



www.e-IAPGOS.pl

W GOSPODARCE I OCHRONIE ŚRODOWISKA

ISSN 2083-0157

Kwartalnik Naukowo-Techniczny



fot. Andrzej Kotyra

Lublin – host city of the International
Interdisciplinary PhD Workshop 2020

4/2019

październik – grudzień

Wydanie pod redakcją naukową
prof. dr hab. inż. Waldemara Wójcika

INFORMATYKA AUTOMATYKA POMIARY

W GOSPODARCE I OCHRONIE ŚRODOWISKA
Informatics Control Measurement in Economy and Environment Protection

p-ISSN 2083-0157, e-ISSN 2391-6761, www.e-iagpos.pl

INTERNATIONAL PROGRAMME COMMITTEE – RADA PROGRAMOWO-NAUKOWA

Chairman

Przewodniczący

Waldemar WÓJCIK

Lublin University of Technology,
Lublin, Poland

Deputy of Chairman

Zastępca przewodniczącego

Jan SIKORA

Research and Development
Center Netrix S.A.,
Lublin, Poland

Members

Członkowie

Kazimierz ADAMIAK

University of Western Ontario,
Ontario, Canada

Darya ALONTSEVA

D.Serikbaev East Kazakhstan
State Technical University,
Ust-Kamenogorsk, Kazakhstan

Shin-ichi AOQUI

Sojo University,
Kumamoto, Japan

Javier BALLESTER

Universidad de Zaragoza,
Saragossa, Spain

Yurii BOBALO

Lviv Polytechnic National
University, Lviv, Ukraine

Oleksy BORYSENKO

Department of Electronics
and Computer Technics,
Sumy, Ukraine

Hartmut BRAUER

Technische Universität Ilmenau,
Ilmenau, Germany

Kathleen CURRAN

School of Medicine
& Medical Science,
Dublin, Ireland

Milan DADO

University of Žilina,
Žilina, Slovakia

Jarmila DEDKOVA

Brno University of Technology,
Brno, Czech Republic

Andrzej DEMENKO

Poznan University of Technology,
Poznań, Poland

Pavel FIALA

Brno University of Technology,
Brno, Czech Republic

Vladimir FIRAGO

Belarusian State University,
Minsk, Belarus

Ryszard GOLEMAN

Lublin University of Technology,
Lublin, Poland

Jan GÓRSKI

AGH University of Science
and Technology,
Cracow, Poland

Stanisław GRATKOWSKI

West Pomeranian University
of Technology Szczecin,
Szczecin, Poland

Antoni GRZANKA

Warsaw University of Technology,
Warsaw, Poland

Jeni HEINO

Helsinki University of Technology,
Helsinki, Finland

Oleksandra HOTRA

Lublin University of Technology,
Lublin, Poland

Zenon HOTRA

Lviv Polytechnic National
University, Lviv, Ukraine

Wojciech JARZYNA

Lublin University of Technology,
Lublin, Poland

Mukhtar JUNISBEKOV

M.Kh. Dulaty Taraz
State University,
Taraz, Kazakhstan

Piotr KACEJKO

Lublin University of Technology,
Lublin, Poland

Krzysztof KLUSZCZYŃSKI

Silesian University of Technology,
Gliwice, Poland

Yurii KRAK

Taras Shevchenko National
University of Kyiv,
Kiev, Ukraine

Piotr KSIĄŻEK

Medical University of Lublin,
Lublin, Poland

Piotr LESIAK

University of Economics
and Innovation in Lublin
Lublin, Poland

Volodymyr LYTVYENENKO

Kherson National
Technical University,
Kherson, Ukraine

Artur MEDVID

Riga Technical University,
Riga, Latvia

Paweł MERGO

Maria Curie-Skłodowska
University, Lublin, Poland

Andrzej NAFALSKI

University of South Australia,
Adelaide, Australia

Il Han PARK

Sungkyunkwan University,
Suwon, Korea

Lucjan PAWŁOWSKI

Lublin University of Technology,
Lublin, Poland

Sergey PAVLOV

Vinnytsia National
Technical University,
Vinnytsia, Ukraine

Denis PREMEL

CEA Saclay,
Gif-sur-Yvette, France

Jason RILEY

The Eunice Kennedy Shriver
National Institute of Child Health
and Human Development,
Bethesda, USA

Ryszard ROSKOSZ

Gdańsk University of Technology,
Gdańsk, Poland

Tomasz RYMARCZYK

Research and Development
Center Netrix S.A.,
Lublin, Poland

Dominik SANKOWSKI

Lodz University of Technology,
Lodz, Poland

Stanislav SLOSARCIK

Technical University of Kosice,
Kosice, Slovakia

Jan SROKA

Warsaw University of Technology,
Warsaw, Poland

Bohdan STADNYK

Lviv Polytechnic
National University,
Lviv, Ukraine

Henryka Danuta

STRYCZEWSKA

Lublin University of Technology,
Lublin, Poland

Batyrbek SULEMENOV

Kazakh National Research
Technical University
after K.I.Satpayev,
Almaty, Kazakhstan

Mirosław ŚWIERCZ

Białystok University
of Technology,
Białystok, Poland

Stanisław TARASIEWICZ

Université Laval,
Quebec, Canada

Murielle TORREGROSSA

University of Strasbourg,
Strasbourg, France

Sławomir TUMAŃSKI

Warsaw University of Technology,
Warsaw, Poland

Andrzej

WAC-WŁODARCZYK

Lublin University of Technology,
Lublin, Poland

Zygmunt WARSZA

Industrial Research Institute
for Automation and Measurements,
Warsaw, Poland

Sotoshi YAMADA

Kanazawa University,
Kanazawa, Japan

Xiaoyi YANG

Beihang University,
Beijing, China

Mykola YERMOSHENKO

International Academy
of Information Sciences,
Kiev, Ukraine

Athanasios

ZACHAROPOULOS

University College London,
London, United Kingdom

Ivan ZHARSKI

Belarusian National
Technical University,
Minsk, Belarus

Cao ZHIHONG

Institute of Soil Science Chinese
Academy of Sciences,
Nanjing, China

Paweł ŻUKOWSKI

Lublin University of Technology,
Lublin, Poland

EDITORIAL BOARD – KOMITET REDAKCYJNY

Editor-in-Chief
 Redaktor naczelny

Paweł KOMADA
 Lublin University
 of Technology,
 Lublin, Poland
 p.komada@pollub.pl

Topical Editors
 Redaktorzy działowi

Electrical Engineering
Elektrotechnika

Jan SIKORA
 Research
 and Development
 Center Netrix S.A.,
 Lublin, Poland
 sik59@wp.pl

Computer Science
Informatyka

Dominik SANKOWSKI
 Lodz University
 of Technology,
 Lodz, Poland
 dsan@kis.p.lodz.pl

Electronics
Elektronika

Paweł FIALA
 Brno University
 of Technology,
 Brno, Czech Republic
 fialap@feec.vutbr.cz

Automatic
Automatyka

Waldemar WÓJCIK
 Lublin University
 of Technology,
 Lublin, Poland
 waldemar.wojcik@pollub.pl

Mechtronics
Mechatronika

Krzysztof KLUSZCZYŃSKI
 Silesian University
 of Technology,
 Gliwice, Poland
 krzysztof.kluszczyński@polsl.pl

EDITOR STAFF – ZESPÓŁ REDAKCYJNY

Deputy Editors
 Zastępcy redaktora

Jan SIKORA
 Research
 and Development
 Center Netrix S.A.,
 Lublin, Poland
 sik59@wp.pl

Dominik SANKOWSKI
 Lodz University
 of Technology,
 Lodz, Poland
 dsan@kis.p.lodz.pl

Paweł FIALA
 Brno University
 of Technology,
 Brno, Czech Republic
 fialap@feec.vutbr.cz

Andrzej SMOLARZ
 Lublin University
 of Technology,
 Lublin, Poland
 a.smolarz@pollub.pl

Technical Editor
 Redaktor techniczny

Tomasz ŁAWICKI
 Lublin University
 of Technology,
 Lublin, Poland
 t.lawicki@pollub.pl

Statistical Editor
 Redaktor statystyczny

Barbara KOWAL
 Lublin University
 of Technology,
 Lublin, Poland
 b.kowal@pollub.pl

Linguistic correction – Korekta językowa: **Andrew Zachary WARCHOŁ**

EDITORIAL OFFICE – REDAKCJA

Redakcja czasopisma
Informatyka, Automatyka, Pomiary w Gospodarce i Ochronie Środowiska
 Katedra Elektroniki i Technik Informatycznych
 Politechnika Lubelska
 ul. Nadbystrzycka 38A
 20-618 Lublin
 tel. +48 81 53 84 309
 fax: +48 81 53 84 312
 www.e-iapgos.pl, ph.pollub.pl/index.php/iapgos
 iapgos@pollub.pl

PUBLISHER – WYDAWCA

Politechnika Lubelska
 ul. Nadbystrzycka 38D
 20-618 Lublin
 tel. +48 81 53 84 100
 www.pollub.pl, ph.pollub.pl

PRINTING HOUSE – DRUKARNIA

Agencja Reklamowa TOP
 87-800 Włocławek
 ul. Toruńska 148
 tel. +48 54 423 20 40
 nakład: 100 egzemplarzy

OTHER INFORMATION – INNE INFORMACJE

Czasopismo jest indeksowane w bazach:

BazTech:	baztech.icm.edu.pl
IC Journals Master List:	www.journals.indocopernicus.com
Google Scholar	scholar.google.pl
POL-index	pbn.nauka.gov.pl

Czasopismo *Informatyka, Automatyka, Pomiary w Gospodarce i Ochronie Środowiska* zostało objęte finansowaniem przez Ministerstwo Nauki i Szkolnictwa Wyższego w ramach programu *Wsparcie dla czasopism naukowych* w latach 2019-2020.

Czasopismo znajduje się w wykazie czasopism naukowych opublikowanym w Komunikacie Ministra Nauki i Szkolnictwa Wyższego z dnia 31 lipca 2019 r., pozycja 27864 – z przypisaną liczbą punktów przyznawanych za publikację równą 20.

Zasady publikowania artykułów, przygotowania tekstów, zasady etyczne, procedura recenzowania, wykazy recenzentów oraz pełne teksty artykułów dostępne są na stronie internetowej czasopisma:

www.e-iapgos.pl

W celu zwiększenia oddziaływania czasopisma w środowisku naukowym redakcja zaleca:

- w artykułach publikowanych w IAPGOS cytować artykuły z renomowanych czasopism międzynarodowych (szczególnie indeksowanych w bazach Web of Science oraz Scopus) używając oficjalnych skrótów nazw czasopism,
- w artykułach publikowanych w innych czasopismach (zwłaszcza indeksowanych w bazach Web of Science oraz Scopus) cytować prace publikowane w IAPGOS – zwłaszcza posługując się numerami DOI, np.:
 Kluszczyński K. *Modelowanie – umiejętność czy sztuka?* Informatyka, Automatyka, Pomiary w Gospodarce i Ochronie Środowiska – IAPGOS, 1/2016, 4–15, DOI: 10.5604/20830157.1193833.

CONTENTS – SPIS TREŚCI

1. Johanna Ender, Jan Cetric Wagner, Georg Kunert, Fang Bin Guo, Roland Larek, Thorsten Pawletta Concept of a self-learning workplace cell for worker assistance while collaboration with a robot within the self-adapting-production-planning-system Koncepcja samouczącego się stanowiska pracy dla wspierania pracownika przy współpracy z robotem w układzie samoadaptacja-produkcja-planowanie.....	4
2. Michèle Schaub Data-based prediction of soot emissions for transient engine operation Przewidywanie emisji sadzy w przypadku przejściowej pracy silnika w oparciu o dane	10
3. Piotr Wójcicki, Tomasz Zientarski Application of the Lennard-Jones potential in modelling robot motion Zastosowanie potencjału Lennard-Jonesa do modelowania ruchu robotów	14
4. Artur Popko, Konrad Gauda Application of artificial neural network in the process of selection of organic coatings Zastosowanie sztucznej sieci neuronowej w procesie doboru powłok organicznych	18
5. Konrad Gauda, Kamil Pasierbiewicz Application of optical profilometry in the analysis of the destruction process of renovation organic coatings for the automotive industry Zastosowanie profilometrii optycznej w analizie procesu destrukcji renowacyjnych powłok organicznych dla przemysłu motoryzacyjnego	22
6. Tomasz Rymarczyk, Bartek Przystupa, Marcin Kowalski, Piotr Bednarczuk Analysis of data from measuring sensors for prediction in production processes control systems Analiza danych z czujników pomiarowych do predykcji w systemach kontroli procesów produkcyjnych	26
7. Barbara Tomaszewska-Wach, Mariusz R. Rząsa, Marcin Majer Measurement of two-phase gas-liquid flow using standard and slotted orifice Pomiar strumienia mieszaniny gaz-ciecz z wykorzystaniem kryzy standardowej i kryzy szczelinowej	30
8. Volodymyr Mashchenko, Valentine Krivtsov, Volodymyr Kvasnikov, Volodymyr Drevetskiy Determination of Young's dynamic modulus of polymer materials by resonance vibrating-reed method Określenie dynamicznego modułu Younga materiałów polimerowych za pomocą rezonansowej metody wibracyjnej	34
9. Adam Ryszard Zywicka, Marcin Ziolkowski Determination of the optimal scanning step for evaluation of image reconstruction quality in magnetoacoustic tomography with magnetic induction Określenie optymalnego kroku skanowania do oceny jakości rekonstrukcji obrazu w tomografii magnetoakustycznej ze wzbudzeniem indukcyjnym	38
10. Tomasz Rymarczyk, Michał Gołębek, Piotr Lesiak, Andrzej Marciniak, Mirosław Guzik Construction of an ultrasonic tomograph for analysis of technological processes in the field of reflection and transmission waves Budowa tomografu ultradźwiękowego do analizy procesów technologicznych w zakresie fal odbitych i transmisyjnych	43
11. Tomasz Rymarczyk, Krzysztof Polakowski, Jan Sikora A new concept of discretization model for imaging improving in ultrasound transmission tomography Nowa koncepcja dyskretyzacji modelu celem podniesienia jakości obrazowania w transmisyjnej tomografii ultradźwiękowej	48
12. Jacek Kryszyn, Damian Wanta, Waldemar T. Smolik Evaluation of the electrical capacitance tomography system for measurement using 3D sensor Ocena systemu elektrycznej tomografii pojemnościowej do pomiarów z wykorzystaniem sondy 3D	52
13. Oleg Avrunin, Yana Nosova, Ibrahim Younouss Abdelhamid, Oleksandr Gryshkov, Birgit Glasmacher Using 3D printing technology to full-scale simulation of the upper respiratory tract Wykorzystanie technologii drukowania 3D do modelowania górnych dróg oddechowych w pełnej skali	60
14. Olga Chaikovska, Oleksandr Ponomarenko, Olexandr Dovgan, Igor Rokunets, Sergii Pavlov, Olena Kryvoviaz, Oleg Oleg Vlasenko Concept and realization of backpack-type system for multichannel electrophysiology in freely behaving rodents Koncepcja i realizacja systemu plecakowego dla wielokanałowej elektrofizjologii u swobodnie zachowujących się gryzoni	64
15. Viktor Kifer, Nataliya Zagorodna, Olena Hevko Atrial fibrillation detection on electrocardiograms with convolutional neural networks Detekcja migotania przedsionków na elektrokardiogramach z wykorzystaniem konwolucyjnej sieci neuronowej	69
16. Sławomir Szymaniec, Sławomir Szymocha, Łukasz Miszuda The concept of a flying electromagnetic field measuring platform Koncepcja latającej platformy pomiarowej pola elektromagnetycznego	74
17. Andrzej Nowrot, Monika Mikołajczyk, Anna Manowska, Joachim Pielot, Antoni Wojacek Low cost solar thermoelectric water floating device to supply measurement platform Termoelektryczne urządzenie solarne do zasilania platformy pomiarowej	78
18. Łukasz Kwaśny Improving the dynamics of an inverter-based PV generator during load dumps Poprawa dynamiki przekształtnikowego generatora PV podczas zrzutu mocy	83
19. Arkadiusz Malek Measurement systems for the energy produced by the photovoltaic system and consumed by the building of the Lublin Science and Technology Park Systemy pomiaru energii produkowanej przez system fotowoltaiczny i pobieranej przez budynek Lubelskiego Parku Naukowo-Technologicznego	87
20. Katarzyna Zwarycz-Makles, Sławomir Jaszczak Design, construction and automatic control system of single-stage six-bed adsorption heat pump Projekt, budowa i system automatycznej regulacji jednostopniowej sześciokomorowej adsorpcyjnej pompy ciepła	93
List of reviewers cooperating with the journal in 2019 Lista recenzentów współpracujących z czasopismem w roku 2019	99

DOI: 10.35784/IAPGOS.36

CONCEPT OF A SELF-LEARNING WORKPLACE CELL FOR WORKER ASSISTANCE WHILE COLLABORATION WITH A ROBOT WITHIN THE SELF-ADAPTING-PRODUCTION-PLANNING-SYSTEM

Johanna Ender^{1,2}, Jan Cetric Wagner², Georg Kunert², Fang Bin Guo¹, Roland Larek², Thorsten Pawletta²

¹Liverpool John Moores University, Faculty of Engineering and Technology, Liverpool, United Kingdom,

²Hochschule Wismar, University of Applied Sciences: Technology, Business and Design, Faculty of Engineering, Wismar, Germany

Abstract. For some time, the focus of past research on industrial workplace designs has been the optimization of processes from the technological point of view. Since human workers have to work within this environment the design process must regard Human Factor needs. The operators are under additional stress due to the range of high dynamic processes and due to the integration of robots and autonomous operating machines. There have been few studies on how Human Factors influence the design of workplaces for Human-Robot Collaboration (HRC). Furthermore, a comprehensive, systematic and human-centred design solution for industrial workplaces particularly considering Human Factor needs within HRC is widely uncertain and a specific application with reference to production workplaces is missing.

The research findings described in this paper aim the optimization of workplaces for manual production and maintenance processes with respect to the workers within HRC. In order to increase the acceptance of integration of human-robot teams, the concept of the Assisting-Industrial-Workplace-System (AIWS) was developed. As a flexible hybrid cell for HRC integrated into a Self-Adapting-Production-Planning-System (SAPPS) assists the worker while interaction.

Keywords: human-robot collaboration, human factors, post-optimised reinforcement learning algorithm, self-adapting-production-planning-system

KONCEPCJA SAMOUCZĄCEGO SIĘ STANOWISKA PRACY DLA WSPIERANIA PRACOWNIKA PRZY WSPÓLPRACY Z ROBOTEM W UKŁADZIE SAMOADAPTACJA-PRODUKCJA-PANOWANIE

Streszczenie. Wcześniejsze badania nad projektami przemysłowych miejsc pracy koncentrowały się od pewnego czasu na optymalizacji procesów z technologicznego punktu widzenia. Ze względu na konieczność pracy ludzi w takim środowisku, proces projektowania musi uwzględniać potrzeby czynnika ludzkiego. Operatorzy znajdują się pod dodatkowym obciążeniem ze względu na zakres procesów o wysokiej dynamice, integrację robotów i autonomicznych maszyn roboczych. Stosunkowo niewiele badań dotyczy wpływu czynników ludzkich na projektowanie miejsc pracy na potrzeby układów Human-Robot Collaboration (HRC). Co więcej, wszechstronne, systematyczne i ukierunkowane na człowieka rozwiązanie projektowe dla przemysłowych zakładów pracy, szczególnie uwzględniające potrzeby czynnika ludzkiego w HRC, jest szeroko niepewne i brak jest konkretnego zastosowania w odniesieniu do miejsc pracy w produkcji.

Opisane w artykule wyniki badań mają na celu optymalizację miejsc pracy dla ręcznych procesów produkcji i utrzymania ruchu, w odniesieniu do pracowników w HRC. W celu zwiększenia akceptacji integracji zespołów ludzko-robotycznych opracowano koncepcję systemu wspomagania miejsca pracy (ang. Assisting-Industrial-Workplace-System, AIWS). Jako elastyczna komórka hybrydowa dla HRC zintegrowana z Samo-Adaptacyjnym Systemem Planowania Produkcji (ang. Self-Adapting-Production-Planning-System, SAPPS) pomaga pracownikowi podczas interakcji.

Słowa kluczowe: współpraca człowiek-robot, czynniki ludzkie, zoptymalizowany poprawiony algorytm uczenia się, układ samoadaptacja-produkcja-planowanie

Introduction

A major reason for the general change in the way of working particularly in industry, is the integration of machines, computers and smart devices [23, 31]. The term digitized industry will be used within this paper to refer to the merge of Industry 4.0 (I4.0) and the Industrial Internet of Things (IIoT). In this context, Cyber-Physical Systems (CPS) evolved as a significant element [23]. These systems contain autonomous operating machines and storage systems and a continuous exchange of information is typical [31]. Tasks within Human-Machine Interaction (HMI), in particular, the interaction with robots will be increasingly integrated into the work process in the future [8, 17].

Currently, there is still a strict separation between workers and robots through fences and safety systems, but further advances of coexistence, cooperation and collaboration of humans and robots have been classified [21]. Within cooperation, humans and robots work towards higher common goals; however, there is still a clear division of their tasks. In Human-Robot Collaboration (HRC) partial goals are also pursued together. To ensure this, the safe and comfortable collaboration of humans and robots is sought [24, 35].

In order to create a human-centred design solution to resolve issues identified within the digitized industry, Human Factors knowledge has been adopted to develop the concept of an Assisting Workplace Cell for HRC to minimise cognitive load, increase the acceptance of the worker and increase the productivity. To develop the concept of an Assisting-Industrial-Workplace-System (AIWS) the three level of ergonomics/human factors [36] have been investigated:

- Physical level – anthropometrics of the human body and physical interaction.
- Cognitive level – psychological perception.
- Organisational level – design of socio-technical systems.

The concept removes traditional input and output devices such as monitors, keyboard and PC-mouse and employs the surface of the table as an interface that is connected with a Self-Adapting-Production-Planning-System (SAPPS). In addition, to reduce strain, the integration of a post-optimization reinforcement learning algorithm within the workplace system will enable a situational adaptation of the spatial movements of the robot to the behaviour of the worker. The individual adaption of the AIWS to Human Factor needs will improve the well-being of the worker and increases the integration of HRC.

1. State of the research

Bullinger [4], Bullinger-Hoffmann and Mühlsted [5] show that the design of workplaces for HMI needs not only to consider the ergonomic requirements, but also psychological aspects to assist the operator.

Psychological influences have an effect on workers' health and wellbeing whilst working in an industrial environment. Goschke [9] cites the Yerkes-Dodson-law [28], according to which human performance in information processing depends on the complexity of the task and mental activation. A high level of nervous stimulation significantly lowers performance in solving complex tasks. This corresponds to Braseth's [3] suggestion that one of the main issues for designing visual interfaces is to avoid information overloading. The higher dynamics of processes within industry require a permanent interpretation of signals and adequate reactions of the operator. Endsley and Jones [7] outlined how the human brain becomes a bottleneck when the design of work equipment does not provide support for rapid information processing. An adequate design will help to overcome the bottleneck by promoting the rapid reception of information and supporting the interpretation process. Similarly, Bauernhansl [2]

draws attention to the flood of data resulting from global networking and ever-improving device technology and concludes that the support of the worker in the production plant is getting increasingly important. In the same way, the BMBF [34], refers to the importance of assistance systems within changing working environments.

Today, the character of industry is changing, and the role of product design has been altered. Sanders and Staplers [22] concluded that industry had been primarily manufacturing-driven and then shifted to technology-driven. Currently, the industry is motivated by the stagnation of the technology push and the user experience appears to be the focus of investigations. In the enquiry of the role of design within I4.0, IXDS Human Industries Venture [37] reports that design improves manufacturing processes when involving all stakeholders early. Accordingly, the user-centred design landscape is developing into an environment of co-creation, where workers are involved in the design process from the early stages [22]. Norman [20] believes that anyone can design, due to their own creative potential. In addition, Steelcase Inc. [39] requires supporting creativity at work so as to create value for business and society. Supporting this potential for creativity and new high-flexible forms of diverse cooperation teams will be the task of workplace design in the future. Given the discussions above, IXDS Human Industries Venture [37] declares that design will facilitate the development of systems to empower skilled operators and non-experts at the same time, and resulting in processes usable for a large number of worker.

Product design is not only concerned with the aesthetic design of the exterior form but also with the proper interfaces for users interacting with the system/environment. With the increasing automatization of the industry, Lee [16] suggests that consideration of Human Factors in design tends to be significant. Contemporary design takes all aspects of ergonomics into account, in particular, the psychological impact on employees.

A growing body of literature examines the features and requirements of the fast-changing production processes within the digitized industry; their findings [27] highlight the new quality of linking production systems as one of the main advantages of the digitized industry. On the other hand, the digitized industry is characterized by dynamic processes with increasing complexity. Approvingly, Acatech [31] comments that an equally important feature of digitised industry results from smart assistance systems which release workers from having to perform routine tasks, instead of focusing on creative and value-added activities. Given a panorama view of research on assistant scenarios, it provides different approaches that aim to support the worker within the industrial environment. In one example: researchers have developed the integration of guidance lights and projections within the workplace environment to instruct the worker [1, 32]. Other approaches focus on the integration of screens or wearables to support the worker in manual production processes [10] or on the interaction with CPS in general [29]. The integration of robots has aimed to reduce the strain of the workload [18, 19]. Sensitive robots facilitate interactions between the CPS and workers through physical contact instead of screens [30]. Furthermore, experts draw attention to machines which are able to increasingly adapt to individual abilities and needs of the worker [30, 33]. Self-learning algorithms process a large amount of data and accommodate the system to different environments [14].

Vogel-Heuser, Bauernhansl and ten Hompel [25] employed the term *versatility* to satisfy the requirements of unpredictable commerce changes and to highlight the value of production systems, which can be transformed according to the order situation with minimal effort. These versatile systems are also able to overcome the limitations of traditional production and maintenance systems in dealing with increasing customization

of products and small batch sizes. Individual customer requirements can be taken into account and even the industrialized manufacture of individual pieces and production for small batch sizes is profitable [31].

Given these discussions, ten Hompel and Henke [12] comment that a system needs to accommodate its circumstances at all times. The industrial plant of the future must be able to move its regional location effortlessly. Hackl, Wagner, Attmer and Baumann [11] emphasise that in response to technological and economic volatility, the expectations of employees in the 'New Work' have changed.

2. The concept of an Assisting Workplace Cell

The following section discusses how an appropriate product design helps to improve the performance and usability of an HRC-workplace system.

2.1. The Assisting Workplace as a hybrid cell: contribution to the flexible manufacturing

The concept of flexible manufacturing systems enables highly adaptable production [6, 38]. The principal value results from the flexibility of the configurable production cells, where robots are able to handle and add in parts. Tool magazines next to the robot supply the adaptation of the gripper to the work task. Material, parts and further tools are transferred from the warehouses and tool stores to the specific cell, i.e. using automated guided vehicles. Overall, the production is controlled by a decentralized intelligence that connects all parties and is able to communicate, e.g. over the Internet of Things. The workpieces, machines and the process constantly delivers and exchanges process data [38]. These flexible and scalable systems provide an attractive perspective on future production.

Nevertheless, this concept lacks integration of the workers and the adaptation of workplaces for the HMI / HRC regarding Human Factor needs.

2.2. AIWS integration within the production system

The research described in this paper provides a cell for hybrid teams. A cell contains an AIWS for HRC and supports workers interacting with the CPS, e.g. solving of assembly and maintenance tasks (Fig. 1, Fig. 2). The AIWS works as a hybrid cell which is developed based on a real-world scenario from the digitized industry.

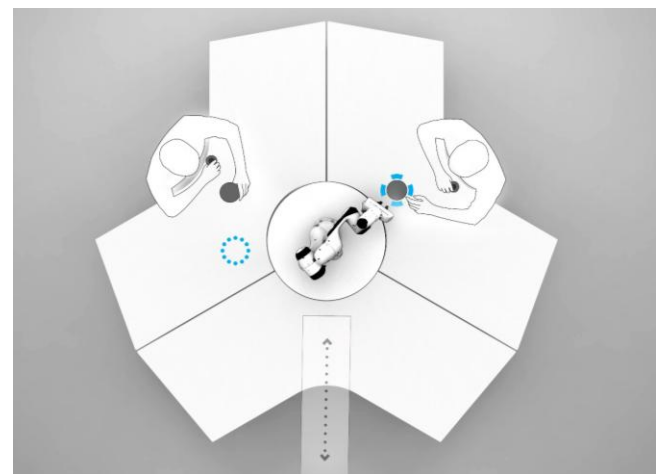


Fig. 1. The concept of the prototype of an assisting workplace for HRC. It includes an integrated Franka Emika robot handling tools and work-pieces which have been delivered by a conveyor belt



Fig. 2. AIWS – Concept rendering

Elements of automated production systems within a digitized factory include machines, tool stores, warehouses, manual workstations and HRC-workplaces. These are constantly networked together and sharing their current status. The AWIS extends flexible manufacturing systems by including workplaces for hybrid human-robot teams in order to promote manual tasks (Fig. 3, Fig. 4).

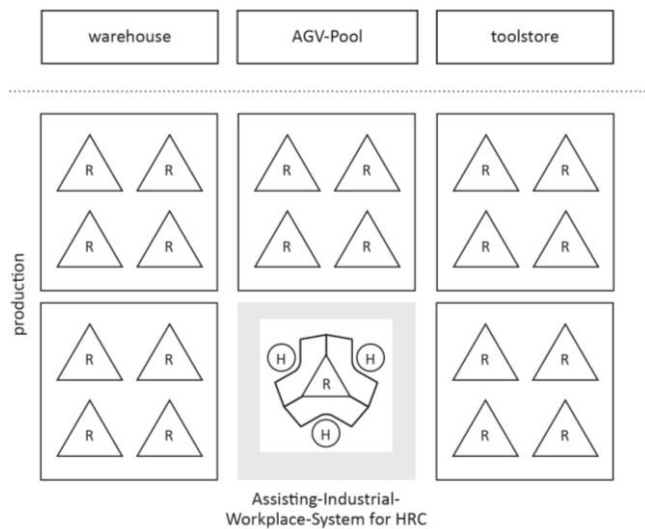


Fig. 3. Integration of the hybrid production cell for HRC as advance of the Matrix Production adapted from [20] (R – Robot; H – Human)

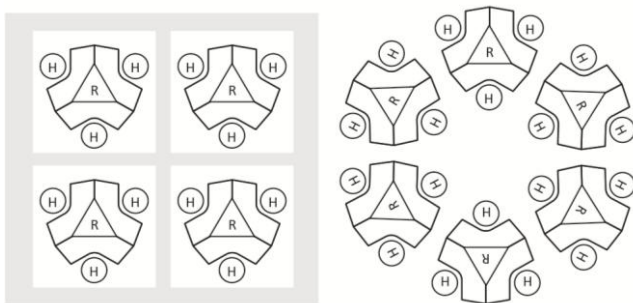


Fig. 4. AIWS – Composition variants of individual cells (R – Robot; H – Human)

In the background of the assisting workplace, an extended network plan (ENP) controls dynamically the work orders according to the order situation and existing resources [15]. It is a specification of a Self-Adapting-Production-Planning-System (SAPPS) that improves this workflow within the production system. The ENP demonstrates additionally to all steps that are necessary for products assembly, alternatives for several tasks [26]. Fig. 5 visualizes an example of ENP.

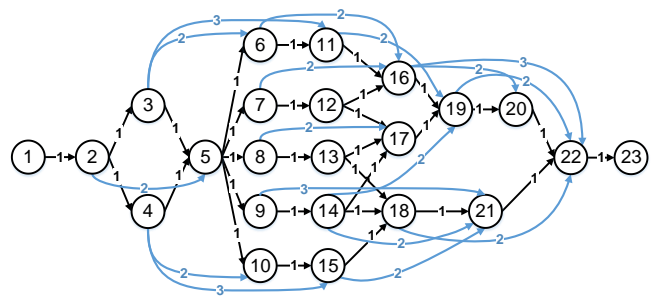


Fig. 5. The extended network plan – an example of an assembly sequence for an industrial production process

The arrows are weighted with a quantifier x ; $x = 1$ represents the ideal assembly process; all other arrows with $x \geq 2$ represents the alternatives. The ENP algorithm calculates these weights. All needed information like predecessors, successors, preconditions as well as possible alternatives for each job is stored in a database. Whereby, this system is able to respond to constantly changing conditions, e.g. failure of a machine or bottlenecks in the delivery of materials. In situations where alternatives are needed, it provides solutions to the worker which can be done instead of non-available jobs. The ENP algorithm analyses and evaluates the different alternatives based on several parameters such as preconditions, arrow weight and job relevance in the whole assembly process. In the future, the industry will be able to control both incoming and outgoing materials and available tools in tool stores via an automatic and networked storage system include conveyor belts, mobile and autonomous vehicles and robots. The required parts and tools are transferred to the specific homogeneous cells (Machine to Machine) or heterogeneous cells (HMI and HRC). At the workplaces for manual tasks in collaboration with the robot, this robot receives the delivery and handles it to the specific employee. The flexibility of this system is very high-level, including assembly, maintenance, testing, packaging. All work steps can now be performed on the same workbench system of that cell.

In addition, a hybrid form through the integration of machines within a section of the cell is feasible, e.g. two workers and one collaborative robot working with one machine.

2.3. The user experience concerning the AIWS

When starting work, an employee selects a free workplace randomly from one of the many islet cells in the production hall. Based on flexible office-organizational concepts such as the Co-Working Spaces, Collaboration Platform or Desk Sharing, the workplaces of a workbench system cell are freely available to every employee.

When the employee logs into the system through an electronic ID, the workbench will adjust the table height to the individual preferred and previously stored level, and the employee's specific settings such as lighting environment, colour preferences etc. In addition, the system recognizes the employee's skill description and offers suitable work tasks for the current order situation. The CPS adjusts itself independently, to support the specific work task, e.g. the required tools and work pieces are conveyed to the cell and then are supplied to the workplace with the help of the collaborative robot. Subsequently, the employee performs the work steps. The surface of the table serves as an interactive user interface (UI) and guides the employee through the assembly and/or maintenance process. The interface is also motivating during the day, it provides a positive visual response to work assignments completed and reminds the worker to observe break times. The robot assists employees in solving a wide variability of work tasks, for instance through the integrated measuring

equipment, the robot could assist with quality-relevant decisions for the reduction of subjective influences by the employee. The broad variety and adaptivity of the end-effectors of the robot offer the possibility of adapting to the requirements of the networked production lines and its current tasks. For example, determining the surface quality can be implemented by scanning the workpiece with a specific effector.

The concept allows a variety of degrees of freedom for the employees and enables and supports the intuitive interaction with the system:

- Free division of working time.
- Freedom in choosing the place of work.
- Freedom of selection of the scope of work.
- Adaptation of the work assignment to specific qualifications.

2.4. User Interface concept – Work-by-Light

Part of the AIWS is the development of a communication channel to support the interaction between worker, robot and network. The system will now be introduced by using the term *Work-by-Light (WbL)*.

Derived from the existing Pick-by-Light framework – where operators are directed to particular stock areas via light signals – the WbL system includes a UI that directs work tasks to the worker within the networked plant. The UI utilizes light displays to support operators conducting specific work tasks in collaboration with a robot (Fig. 6). In addition, the light signals give an indication of the future movements of the robot.

Light signals of the AIWS as a communication channel:

- Status display of the robot (active, inactive, error).
- Input and output interface (e.g. work instructions, switching on/ off/ pausing the system).
- Display of the direction of movement of the robot by marking relevant zones on the workbench.

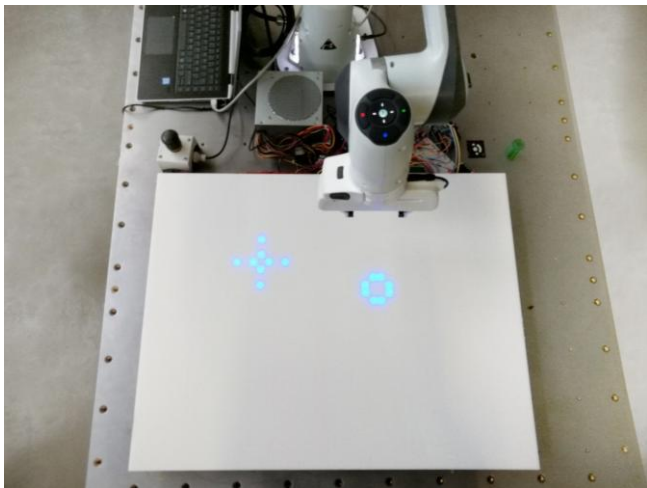


Fig. 6. The prototype of the UI framework which supports the worker during task solving

In order to minimize the cognitive overload of the worker and to create more free space at the workplace, the table surface itself will be the input and output device. The concept of an innovative and simplified display technology based on a LED-matrix connected with the high performance acrylic solid material was successfully developed. The translucent material is illuminated from below with LEDs. These LED-Matrix can be controlled via a microcontroller. It gets an RGB image from the control computer. The microcontroller extracts the individual pixel information from the image and generates the control of the individual LEDs.

Light signals inside the surface of the table are reduced to the minimum of information to support the rapid processing of the instruction through the worker in order to support the intuitive utilization of the interface and consequently reduces strain in HRC.

Since autonomous robot movement rhythms are generally not predictable, there are still barriers in the HRC that cause stress. The development of the light-guidance system will help the employee to forecast the movements of the robot, and reduce the need for these barriers.

2.5. Set up of the Demonstrator

The assistance system consists of different interconnected components. Fig. 7 demonstrates individual actuators within the concept layout. Based on this structural concept, the pilot workplace for running future experimental studies on user acceptance was already successfully set up at the laboratory of Hochschule Wismar (Fig. 8).

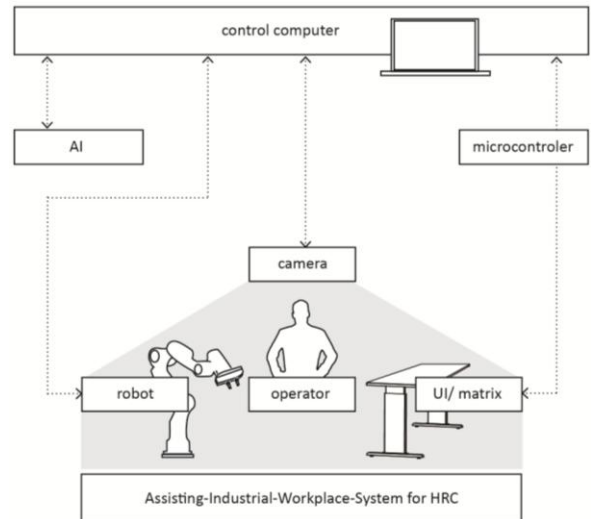


Fig. 7. Structure and communication of the single actuators of the AIWS for HRC

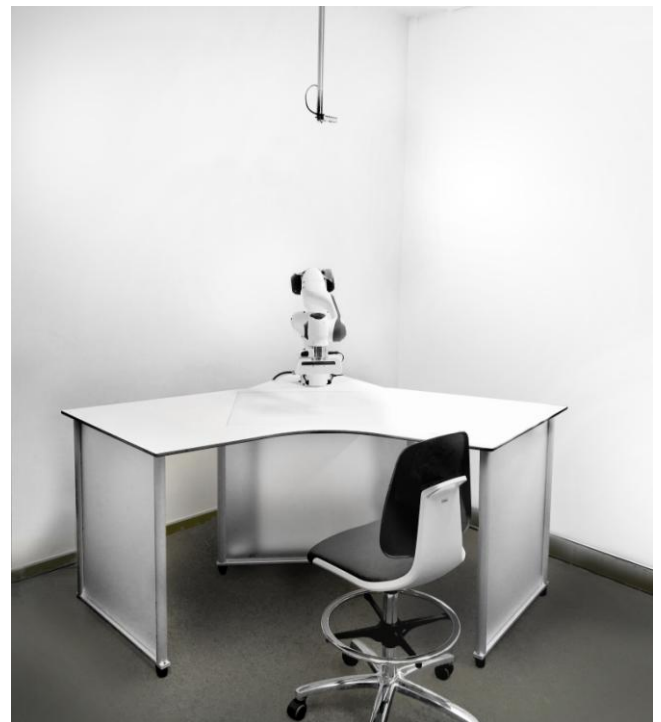


Fig. 8. Set up of the AIWS pilot workplace at the laboratory of Hochschule Wismar. A camera-system is attached to the ceiling and tracks the workplace

The operator inputs information through gestures tracked by the common camera-system. The control computer inspects the situation with the camera-system and makes its decision with help of a learned behaviour. If the situation is new to the control computer, it will transmit the situation to an artificial intelligence

(AI) component on a mainframe. The mainframe processes this data through post-optimizing reinforcement learning [13] and adjusting the behavioural strategy of the system; after that, the control computer receives the new behavioural strategy.

The control computer generates the robot control program from the learned behavioural strategy. The actions that are suggested from the control computer are positions and/or paths of the robot. The safety functions are still in the controller of the robot.

Moreover, in achieving this aim, the machine learning method will be employed to develop a highly flexible and self-learning robot control program. The program will be able to interact with the employee and production workflow independently, through a model-based learning pattern. The program is also expected to respond adequately to unknown circumstances. Thus, it is imperative that alternative sequences will be learned. The learning process consists of two steps: the real-world process will be simulated with a model and learned (i) offline with the post-optimizing reinforcement learning; then machine learning needs to improve (ii) online for the entire operating time.

The following system elements are derived from the concept and will be developed/implemented by the research group Computational Engineering and Automation (CEA) at the Hochschule Wismar, University of Applied Sciences: Technology, Business and Design:

- Autonomously learning robot control program, which is able to find an order of tasks for the assembly to receive a short production time using with the post-optimizing reinforcement learning [13].
- Secure movements, which do not hinder or distract the worker
- A robot control program, which proactively responds to the individual behaviour of the worker.

While learning, the Reinforcement Learning algorithm switches between exploration – acting randomly and finding new states, and exploitation – choosing the best so far known action to reaches as fast as possible the given target. By switching between these two modes, the algorithm learns alternative sequences for solving a problem. While learning offline, the control program always regards the security of the worker within the workplace environment.

After the control program has learned offline, the algorithm has to proactively learn online at the real environment. Even if a path of the robot is blocked by a human or by an obstacle, the algorithm independently chooses an alternative route for the robot to move to the targeted position without disturbing the worker.

However, the movements of the employee will be recorded with a camera-system and evaluated with a standard computer. The analysis of the picture (Fig. 9) marks the position and body dimensions of the worker on the surface of the workbench. Furthermore, images of objects, such as tools and workpieces, can be stored in a database and recognized afterwards within the real environment.

The robot control will use this data. Theoretically, calculating the behavioural strategy of the robot can be completed by any computer, however, it requires a lot of time for calculation. A mainframe computer is advisable for the calculation to process new/unknown states of the manufacturing process, so the control computer reacts adequately when these conditions are encountered again.

Accordingly, it is possible that the robot control program as well as the UI accommodates itself to the behaviour of the employee using the recorded data and calculated by the control computer.

Connected with the UI, the overall system will be able to accommodate the specific/inconstant behaviour and performance variability of each employee. For this purpose, the robot will proactively adapt the constantly changing movement model of the employee. Since it is impossible for the robot control program to simulate human's behaviour and as it is not predictable, a rigid control program will not be able to complete this task.

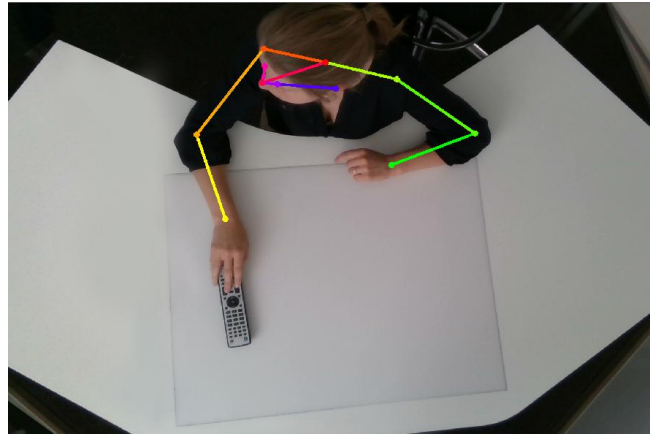


Fig. 9. Camera-Tracking at the demonstrator – The system recognizes the position and dimension of the human skeleton. As a result, the movements of the workers can be detected safely. A recognition and evaluation of gestures would also be possible in the future development – an integration in the pilot system is currently being tested for their relevance for use and implementability

3. Summary and outlook

The motivation of the research was to reduce the level of stress, physical and cognitive strain of the operators while working at assembly and maintenance tasks and support the integration of HRC within the digitized factory to increase the productivity. As a contribution to the flexible manufacturing system, the concept of AIWS for HRC has successfully developed as a flexible hybrid cell design.

The concept considers the three dimensions of Human Factors in design:

Physical level: The AIWS with an integrated robot will be able to accommodate behaviour patterns of the employee to satisfy ergonomic and HRC requirements using machine learning.

Cognitive level: The WbL-concept accelerates the reception of information and assisting the interpretation process to reduce strain during the HRC process.

Organisational level: The hybrid cell integrated into a SAPPs and combined with the advantages of the ENP enables the industry to transform according to the order situation with minimal effort and allows a variety of freedoms for the employees, e.g. division of working time.

Considerable progress has been made to the iterative development of the concept, the construction, and prototyping of a demonstrator. Further research will be investigating and exemplifying how the AIWS supports manufacturing tasks within an application scenario from digitized industry. Further works also include investigations of new technologies as smart glass and tablets that can be applied to the design of the AIWS. Finally, testing has been scheduled to organise potential users working on the system. The entire process will be monitored for data analysis and further discussion. Together with feedback interviews of operators will be undertaken to derive and validate the criteria for industrial workplaces design, in terms of satisfying ergonomic requirements and reducing stress while interacting between the use and the system; and resulting to a high acceptance of the HRC.

A considerable relief of the worker's strain is to be expected by the use of the system. This will be validated within a future pilot experiment, in which the subjectively perceived workload is determined.

References

- [1] Bannat A.: Ein Assistenzsystem zur digitalen Werker-Unterstützung in der industriellen Produktion. TU München, 2014.
- [2] Bauernhansl T., ten Hompel M., Vogel-Heuser B. (Eds.): Industrie 4.0 in Produktion, Automatisierung und Logistik: Anwendung, Technologien, Migration. Springer Vieweg, Wiesbaden 2014.
- [3] Braseth A. O.: Information-Rich Design: A Concept for Large-Screen Display Graphics: Design Principles and Graphic Elements for Real-World Complex Processes. Norwegian University of Science and Technology, 2015.
- [4] Bullinger H.-J.: Ergonomie: Produkt- und Arbeitsplatzgestaltung. Vieweg+Teubner Verlag, Wiesbaden 1994.

- [5] Bullinger-Hoffmann A. C., Mühlstedt J.: Homo Sapiens Digitalis – Virtuelle Ergonomie und digitale Menschmodelle. Springer Vieweg, Wiesbaden 2016.
- [6] Dostal W., Kamp A.-W., Lahner M., Seessle W. P.: Flexible Fertigungssysteme und Arbeitsplatzstrukturen. W. Kohlhammer GmbH, Stuttgart 1982.
- [7] Endsley M. R., Jones D. G.: Designing for situation awareness: An approach to user-centered design. CRC Press, Boca Raton 2011.
- [8] Freitag M., Molzow-Voit F., Quandt M., Spöttl G.: Aktuelle Entwicklung der Robotik und ihre Implikationen für den Menschen. In: Molzow-Voit F., Quandt M., Freitag M., Spöttl G. (Eds.): Robotik in der Logistik: Qualifizierung für Fachkräfte und Entscheider. Springer Gabler, Wiesbaden 2016, 9–20.
- [9] Goschke T.: Aktivierungstheoretische Ansätze: Motivation, Emotion, Volition. TU Dresden, 2013.
- [10] Grendel H., Larek R., Riedel F., Wagner J. C.: Enabling manual assembly and integration of aerospace structures for Industry 4.0 – methods. New Production Technologies in Aerospace Industry: MIC Proceedings 2017, Hannover 2017.
- [11] Hackl B., Wagner M., Attmer L., Baumann D.: New Work: Auf dem Weg zur neuen Arbeitswelt: Management-Impulse, Praxisbeispiele, Studien. Springer Gabler, Wiesbaden 2017.
- [12] ten Hompel M., Henke M.: Logistik 4.0. in SpringerLink, Industrie 4.0 in Produktion, Automatisierung und Logistik. In: Bauernhansl T., ten Hompel M., Vogel-Heuser B. (Eds.): Anwendung, Technologien, Migration. Springer Vieweg, Wiesbaden 2014, 615–624.
- [13] Kunert G., Pawletta T.: Generating of Task-Based Controls for Joint-Arm Robots with Simulation-based Reinforcement Learning. SNE 28(4), 2018, 149–156.
- [14] Kunert G., Pawletta T.: Generierung von Steuerungen für Gelenkarmroboter mit simulationsbasiertem Reinforcement-Learning. 24. Symposium Simulationstechnik ASIM 2018, 56, 2018.
- [15] Larek R., Grendel H., Wagner J. C., Riedel F.: Industry 4.0 in manual assembly processes – a concept for real time production steering and decision making. Procedia CIRP 79, 2019, 165–169.
- [16] Lee J. D., Wickens Ch. D., Liu Y., Boyle L. Ng: An introduction to human factors engineering: A beta version. CreateSpace Independent Publishing Platform, 2017.
- [17] Lorenz M., Rübmann M., Strack R., Lueth K. L., Bolle M.: Man and Machine in Industry 4.0: How Will Technology Transform the Industrial Workforce Through 2025? BCC The Boston Consulting Group, 2015.
- [18] Michalos G. et al.: ROBO-PARTNER: Seamless Human-Robot Cooperation for Intelligent, Flexible and Safe Operations in the Assembly Factories of the Future. Procedia CIRP 23, 2014, 71–76.
- [19] Molzow-Voit F., Quandt M., Freitag M., Spöttl G. (Eds.): Robotik in der Logistik: Qualifizierung für Fachkräfte und Entscheider. Springer Gabler, Wiesbaden 2016.
- [20] Norman D. A.: The design of everyday things. Basic Books, New York 2013.
- [21] Onnasch L., Maier X., Jürgensohn T.: Mensch-Roboter-Interaktion – Eine Taxonomie für alle Anwendungsfälle. Bundesanstalt für Arbeitsschutz und Arbeitsmedizin 2016.
- [22] Sanders E. B.-N., Stappers P. J.: Co-creation and the new landscapes of design. CoDesign 4(1), 2008, 5–18.
- [23] Spath D. et al. (Eds.): Produktionsarbeit der Zukunft – Industrie 4.0: Fraunhofer Verlag, 2013.
- [24] Stark J., Mota R. R.C., Sharlin E.: Personal Space Intrusion in Human-Robot Collaboration. Companion of the 2018 ACM/IEEE International Conference on Human-Robot Interaction – HRI '18, 2018, 245–246.
- [25] Vogel-Heuser B., Bauernhansl T., ten Hompel M.: Handbuch Industrie 4.0: Produktion. Springer-Verlag GmbH Deutschland, Berlin 2017.
- [26] Wagner J. C., Larek R., Nüchter A.: Der Maximalnetzplan als Neuinterpretation der Netzplantechnik. Proc. of Wismarer Wirtschaftsinformatik-Tage 11, 2018, 123–136.
- [27] Westkämper E., Spath D., Constantinescu C., Lentjes J.: Digitale Produktion. Springer-Verlag Berlin Heidelberg, Berlin 2013.
- [28] Yerkes R. M., Dodson J. D.: The relation of strength of stimulus to rapidity of habit-formation. J. Comp. Neurol. Psychol. 18(5), 1908, 459–482.
- [29] Ziegler J.: Wearables im industriellen Einsatz: Befähigung zu mobiler IT-gestützter Arbeit durch verteilte tragbare Benutzungsschnittstellen. 2015.
- [30] Acatech: Innovationspotenziale der Mensch-Maschine-Interaktion. Herbert Utz Verlag GmbH, Munich 2016.
- [31] Acatech: Umsetzungsempfehlungen für das Zukunftsprojekt Industrie 4.0: Abschlussbericht des Arbeitskreises Industrie 4.0. Deutschlands Zukunft als Produktionsstandort sichern. Apr. 2013.
- [32] AiF Projekt GmbH: ZIM-Erfolgsbeispiel: Exakt montiert – sicher verpackt – zufriedene Kunden. Jan. 2018.
- [33] Bundesministerium für Arbeit und Soziales Abteilung Grundsatzfragen des Sozialstaats, der Arbeitswelt und der sozialen Marktwirtschaft: WEISS BUCH Arbeiten 4.0: Arbeit weiter denken. 2017.
- [34] Bundesministerium für Bildung und Forschung: Zukunft der Arbeit: Innovationen für die Arbeit von morgen. 2016.
- [35] Fraunhofer IAO: Arbeitswelten der Zukunft: Jahresbericht. Fraunhofer-Gesellschaft 2017.
- [36] International Ergonomics Association IEA, Definition and Domains of Ergonomics. <https://www.iea.cc/> (Available: 25.02.2019).
- [37] IXDS Human Industries Venture: Without design, Industry 4.0 will fail: Six challenges where design accelerates successful digital transformation in manufacturing. 2018, <https://www.ixds.com/without-design-industry-4.0-will-fail> (Available: 27.06.2018).
- [38] KUKA AG: Hello Industrie 4.0 – we go digital. <https://www.nebbiolo.tech/wp-content/uploads/KUKA-Industrie-4.0.pdf> (Available: 19.06.2018).
- [39] Steelcase Inc.: 360°Focus_Creativity: Creativity, Work and the Physical Environment. 17-0005439, 2017.

Dipl.-Des. (FH) Johanna Ender

e-mail: johanna.ender@hs-wismar.de

Johanna Ender passed with distinction her graduation as Diplom Designer (FH) for product design in 2017 at the Hochschule Wismar, University of Applied Sciences: Technology, Business and Design. She has started her international and interdisciplinary Ph.D. research in June 2017 at the Liverpool John Moores University – Faculty of Engineering and Technology. Awards: Gottlob-Frege-Price 2017, Anja-Schaible Price 2017, Innovation-Price 2018, German Design Award Nominee 2018, Science Slam Winner 2019

ORCID ID: 0000-0002-6827-3270

**M. Eng. Jan Cetric Wagner**

e-mail: jan.wagner@hs-wismar.de

Cooperative Ph.D. student of Hochschule Wismar, University of Applied Sciences: Technology, Business and Design, and the Julius-Maximilians-University Würzburg. In 2016 he completed his master studies of mechanical engineering. He does research at the production engineering laboratory of the UAS Wismar in the research field of production organisation. His theory of the extended network plan helps to find alternative jobs in assembly tasks whereby downtimes can be reduced.

ORCID ID: 0000-0002-9236-2935

**M. Eng. Georg Kunert**

e-mail: georg.kunert@hs-wismar.de

Ph.D. student of Hochschule Wismar, University of Applied Sciences: Technology, Business and Design. In 2018 he completed his master studies of mechatronics. He is now researcher at the Research Group Computational Engineering & Automation. His research interest machine learning algorithms and robot control that enables proactively interaction within humans and machines.

Awards: Gottlob-Frege-Price 2018, Science Slam Winner 2017

ORCID ID: 0000-0002-7469-8435

**Dr. Fang Bin Guo**

e-mail: F.B.Guo@ljmu.ac.uk

Dr. Fang Bin Guo has been a senior industrial designer with over 20 years' experience in product/spatial design. He is currently teaching BSc Product Design Engineering and supervising Ph.D. students' research in arts, design and creative technologies. Meanwhile, he remains actively involved in academic research. His major researches incorporate identifications of contemporary role of design/designers, Human/user centred design; together with the studies of Human Factors and its application in new product development.

ORCID ID: 0000-0002-7442-7344

**Prof. Dr.-Ing. Roland Larek**

e-mail: roland.larek@hs-wismar.de

Prof. Dr.-Ing. Larek gained industrial experience among others at Airbus and a supplier to the wind power industry. Since 2013 he has been Professor for Production Engineering and Factory Planning at Hochschule Wismar, University of Applied Sciences: Technology, Business and Design. His research interest in the field of digital factory/Industry 4.0 has been documented in numerous publications.

ORCID ID: 0000-0003-2823-6237

**Prof. Dr.-Ing. Thorsten Pawletta**

e-mail: thorsten.pawletta@hs-wismar.de

Professor for Applied Computer Science at Hochschule Wismar, University of Applied Sciences: Technology, Business and Design, Germany. He is co-founder and member of the research group Computational Engineering & Automation. His research incorporates modeling & simulation theory and the application in engineering. He is member of the board of the German Simulation Society (ASIM) and member of the International Simulation Society (SCS).

ORCID ID: 0000-0003-1740-6560



otrzymano/received: 08.08.2019

przyjęto do druku/accepted: 06.12.2019

DATA-BASED PREDICTION OF SOOT EMISSIONS FOR TRANSIENT ENGINE OPERATION

Michèle Schaub

Wismar University of Applied Sciences, Faculty of Engineering, Maritime Department

Abstract. Global maritime transport is one of the causes of air pollution. Annex VI of the International Maritime Organisation's (IMO) International Convention for the Prevention of Pollution from Ships (MARPOL) refers to air pollution. Air pollution is mainly caused by the conversion of energy in internal combustion engines, in particular in the case of transient engine operation. The main pollutant is soot. It is an impure carbon substance of various sizes, resulting from incomplete combustion of hydrocarbons. This document concerns data-based modelling of soot emissions – the main component of exhaust particles – in transient engine operation. In a unique manoeuvring aid system, the prediction of exhaust emissions will become a new element. If the navigator knows the consequences of his actions, the human role will be strengthened in relation to the decision making on energy-efficient and emission-poor vessel traffic, in particular during manoeuvres. Thanks to the mathematical model, the soot formation process during stationary engine operation – at constant speed and load – will be mapped first. The model will then be extended to simulate engine operation and soot formation in the transition phase.

Keywords: ship emissions, data processing, predictive models

PRZEWIDYWANIE EMISJI SADZY W PRZYPADKU PRZEJŚCIOWEJ PRACY SILNIKA W OPARCIU O DANE

Streszczenie. Globalny transport morski jest jedną z przyczyn zanieczyszczenia powietrza. Załącznik VI do Międzynarodowej konwencji o zapobieganiu zanieczyszczeniu morza przez statki (MARPOL) Międzynarodowej Organizacji Morskiej (IMO) odnosi się do zanieczyszczeń powietrza. Zanieczyszczenie powietrza jest głównie powodowane przez konwersję energii w silnikach spalinowych, w szczególności w przypadku przejściowej pracy silnika. Głównym zanieczyszczeniem jest sadza. Jest to zanieczyszczona substancja węglowa różnej wielkości, będąca wynikiem niepełnego spalania węglowodorów. Niniejszy dokument dotyczy modelowania emisji sadzy – głównego składnika cząstek spalin, w pracy silnika w warunkach przejściowych w oparciu o dane. W unikalnym systemie wspomagania manewrów, przewidywanie emisji spalin stanie się nowym elementem. Jeżeli nawigator zna konsekwencje swoich działań, to rola człowieka zostanie wzmocniona w odniesieniu do podejmowania decyzji o energooszczędnym i ubogim w emisje spalin ruchu statków, w szczególności podczas manewrów. Dzięki modelowi matematycznemu, w pierwszej kolejności zostanie odwzorowany proces powstawania sadzy podczas stacjonarnej pracy silnika – przy stałych obrotach i obciążeniu. Następnie model ten zostanie tak rozszerzony, aby umożliwić symulację pracy silnika i powstawania sadzy w fazie przejściowej.

Słowa kluczowe: emisje ze statków, przetwarzanie danych, modele predykcyjne

Introduction

During ship manoeuvres the ship's longitudinal, transversal and rotational velocities are changing continuously. The cause of these changes are newly set rudder, engine or thruster commands or environmental influences as wind or current. All the external and internal impacts on the ship's motion have influence on the behaviour of the ship's engines. The ship's exhaust gas composition depends on the transient engine operation. They have to adapt rotational speed and torque in order to fulfil the required settings. The engine command sets the required engine speed (engine revolutions) or the propeller pitch. New thruster commands or rudder angle settings lead to a new resistance of the ship's hull and thus to a different propeller inflow and counter torque for the engine. To fulfil the required engine settings, the engine control unit (ECU) adapts the amount of injected fuel. The engine speed is the time-dependent integration of the difference between engine and propeller torque divided by the inertia of the powertrain (1).

$$n_{t+1} = n_t + \frac{M_E - M_P}{J} \times \Delta t \times \frac{60}{2\pi} \quad (1)$$

A disequilibrium between propeller and engine torque is the indicator of transient engine operation. The engine control unit has to act on the fuel injection in order to comply with the given order. During the transient engine operation when the load increases the air-fuel ratio becomes too small. This is the main cause which leads to an incomplete combustion of the injected fuel. Thus soot particles in different sizes arise [9]. This issue is widely described in literature, e.g. in [2], [8] and [11]. Whilst [2] reflects a forum on soot formation with various discussions on chemical and thermodynamic approaches, the latter two authors focussed on the application and improvement of existing thermodynamic soot models. Isermann et al. [11] considers the data-based emission modelling for high-speed diesel engines. One of those approaches was adopted for medium-speed ship diesel engines and is presented in this paper.

1. General Conditions

1.1. Regulations regarding particulate matters

Annex VI of the International Convention for the Prevention of Pollution from Ships (MARPOL) of the International Maritime Organisation (IMO) regulates the ship's air pollution. Regulations 13 and 14 [4] concern the nitrogen oxides (NO_x), the particulate matters (PM) as well as sulphur oxides (SO_x). For sea-going vessels built since 1st January 2016 with more than 130 kW per engine and sailing within Emission Control Areas (ECA) the nitrogen oxides must not exceed the requirements defined in TIER III.

Sulphur oxides are restricted by mass fraction of the used fuel oil whereas particulate matters, of which soot forms the significant part, are only mentioned in the regulation's header. A reduction of sulphur in the fuel oil leads to less PM. But nevertheless, low sulphur diesel still produces PM in rough amounts when combustion is incomplete.

The formation of the greenhouse gas CO₂ essentially depends on the total fuel oil consumption and on the type and carbon content of the used fuel oil. The Energy Efficiency Design Index (EEDI) should enable to monitor the CO₂ emissions. Most of the world's ocean-going vessels obtain their propulsion energy from diesel fuels of different quality. The presented method focusses on this kind of ships and takes the formation of PM to demonstrate the research work in an exemplary way. With little adaptation, the method can also be applied to NO_x emissions, for example.

1.2. Test bed engine and measurement equipment

An MAN 6L23/30 engine serves as test bed. The machine is located on the campus of Wismar University. It is a 4-stroke marine diesel engine. Its specification is shown in Table 1. The MAN 6L23/30 engine is mostly assigned for education of marine engineers.

Table 1. Test bed engine specification

Parameter	Test bed engines
	MAN B&W 6L23/30
Type	medium speed 4-stroke marine diesel engine
Bore	225 mm
Stroke	300 mm
Rated output	1050 kW
Rated speed	900 min ⁻¹
Compression Ratio	13.5 : 1
Fuel injection system	Unit injector System

For research purpose the fixed measurement equipment was enhanced by a portable Pegasor Mi3 particle sensor in order to measure PM during transient engine operation. The measuring principle is based on determining the number of particles smaller than 2.5 μm . By calibrating the equipment with a mean particle size, the corresponding mass in mg/m^3 is calculated. [10]

1.3. Ship model and engine module

For the integration of the data-based model an already existing simulation environment, called SAMMON, is used. SAMMON stands for Simulation Augmented Manoeuvring Design & Monitoring System [5]. The mathematical ship model represents movements with 3 degrees of freedom (DOF): longitudinal, transversal and rotational speeds around the vertical axis. It is based on a system of highly non-linear equations for representing the ship's hydrodynamic behaviour. Fig. 1 shows the online-prediction from a ferry ship entering a port. Even though the ship is still in straight forward motion, the prediction reacts on changed rudder or engine settings.

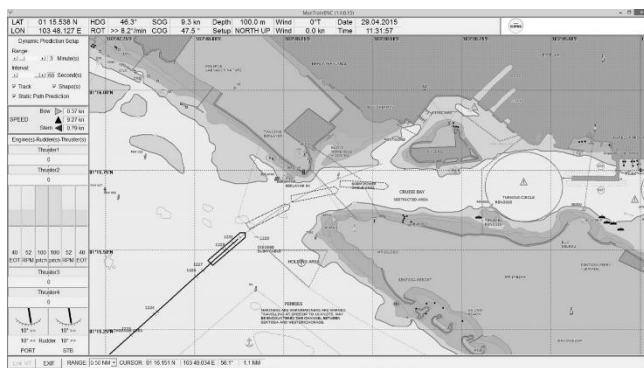


Fig. 1. Manoeuvring assistance software SAMMON for predicting and monitoring ship's behaviour in confined waters [10]

SAMMON Software allows to parameterize several ship types. It can be used for pre-planning of manoeuvre sequences, for online-monitoring or for debriefing after having completed manoeuvres.

The ship model is equipped with an engine interface. Currently, the engine module only consists of a lookup table where the target-actual-difference of engine speed enters. A new engine torque derives from it which is accurate enough to only simulate the ship's motion. To calculate fuel consumption and emissions, the calculated engine torque fails to be useful. Therefore, a PI controller algorithm is implemented which determines the amount of fuel injected in one time step. This is the basis for the calculation of soot emissions.

The proposed data-based modelling of soot will extend the SAMMON software in the future.

1.4. Rapid Advanced Prediction & Interface Technology (RAPIT)

The kernel of the above mentioned manoeuvring assistance software SAMMON is formed by a technology called Rapid Advanced Prediction & Interface Technology (RAPIT). RAPIT

is a kind of fast-time simulation which enables to calculate up to 24 minutes of the simulation process ahead in only one second of real time and to display the results in a sophisticated interface.

The data-based soot model shall fulfil these requirements. This is one of the reasons why an empirical, data-based model was chosen instead of a theoretical model. While a theoretical model must calculate every degree of crank angle and take into account mechanics, thermodynamics and reaction kinetics, an empirical data-based model can save a lot of computing time being a black- or greybox model. The disadvantage, however, is the high effort required to obtain sufficient data in a good quality.

2. Data acquisition for data-based modelling

2.1. Data origin

Soot is the main part of particulate matters (PM). PM are solid components of engine exhaust gas emissions, e.g. hydrocarbons and soot as well as inorganic sulphates. The diameter varies between less than 10 nanometers and more than 1 μm .

A chemical reduction takes place at the beginning of soot formation followed by a planar growth of polycyclic aromatic hydro-carbons. Van der Waals forces lead to soot nucleation which is followed by coagulation, accumulation and addition of sulphates. These formation steps are superimposed by soot oxidation. Soot oxidizes with OH radicals and O_2 at high temperatures in competition with carbon monoxide [3]. The difference between reduction and oxidation can be measured in the exhaust gas duct with a standard sampling rate of one second. By means of the already introduced Pegasor Mi3 particle sensor (see section 1.2), the measurements for particles took place. The measurement for the other relevant engine data was taken from the fixed measurement system of the machine laboratory.

Even though for reasons of better understanding theoretical, but time-consuming models are more substantiated, they are not applicable for the present studies. Apart of not being completely described and understood, they would still need too much computing time than RAPIT would allow for (see section 1.4).

2.2. Experimental design

For these studies, the test bed engine is not a shipborne diesel engine. Nevertheless, the experimental setup was designed with real ships in mind.

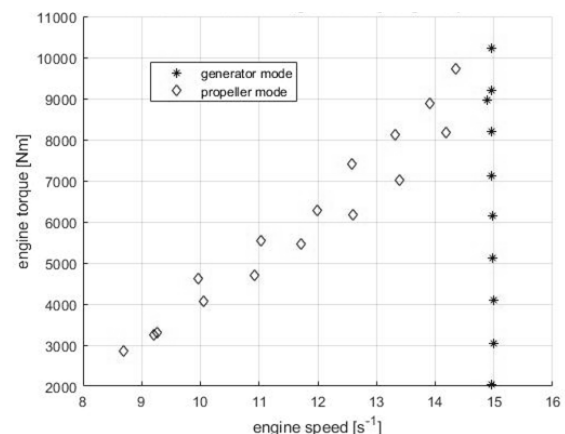


Fig. 2. Engine map with measurement points on two propeller curves (100% and 85%) and generator curve

First of all, the distinction between generator and propeller mode is of great importance:

- Propeller mode means that the torque/speed relation follows the propeller curve within the engine map. A load change leads to a change in torque and engine speed simultaneously.
- Generator mode requires a constant or nearly constant engine speed whereas load changes only affect the engine torque.

At a first step, these stationary measurements serve for establishing a stationary model, which can then be extended by transient parts. Attention is to be paid to numerous data of high quality covering as many input/output combinations as possible (Fig. 2).

The experimental design also provides for load changes of varying magnitude on each of the two propeller and the one generator curves as will be shown in Fig. 7.

2.3. Determination of model input and output

During the data analysis, existing measurement data were searched for which have a clear influence on the soot formation. Finally, the decision was made on the injected fuel mass (m_B) and current engine speed (n_{act}). Fig. 3 shows the combustion chamber in which soot is formed by the above described reduction and oxidation process. This process depends mainly on the currently injected fuel mass and the dwell time in the combustion chamber represented by the engine speed.

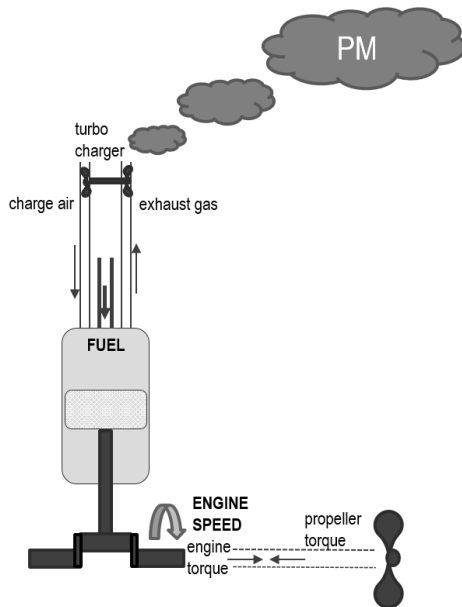


Fig. 3. Model sketch of combustion chamber and adjacent systems

These findings lead to the conclusion that a MISO (multiple input, single output) model with two inputs and one output will be necessary.

3. Static Artificial Neural Network (ANN)

3.1. Decision to implement an ANN

Data-based models do not need any information about physical, chemical or other laws and relationships that determine the processes to be modelled if they are purely black-box models. There are many data-based model architectures to be considered when facing a problem as the one described above [6].

An Artificial Neural Network (ANN) architecture has been chosen due to its relatively good interpolation characteristic and its flexibility regarding input dimensions. For a first approach to create a static network, the Multilayer Perceptron (MLP) being a widely known ANN architecture, has been implemented. Fig. 4 is a sketch of the ANN architecture used for calculating PM by entering the two inputs fuel mass and engine speed.

The q neurons of the hidden layer (h_1 to h_q) are called perceptrons. The two inputs m_B and n_{act} are each multiplied by one synapse weight when entering a perceptron in order to intensify or attenuate the effect on the neuron. All input signals are summed up and enter a nonlinear sigmoidal activation function. Therein, a transformation takes place which result is forwarded to the output layer, where the amount of PM is calculated out of the sum of all the perceptron outputs.

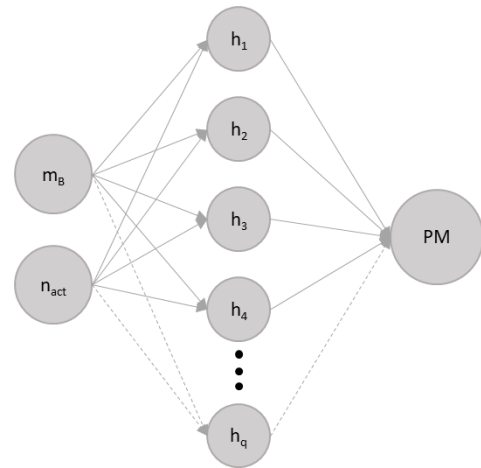


Fig. 4. MLP network with two inputs and one output. The number of neurons in the hidden layer (h) is to be determined

3.2. Determination of number of hidden neurons

The present MISO problem is only three dimensional for the static observation. The ANN must fit the measurement points in Fig. 5 as good as possible. The training of the ANN is done by backpropagation using the Levenberg-Marquardt algorithm.

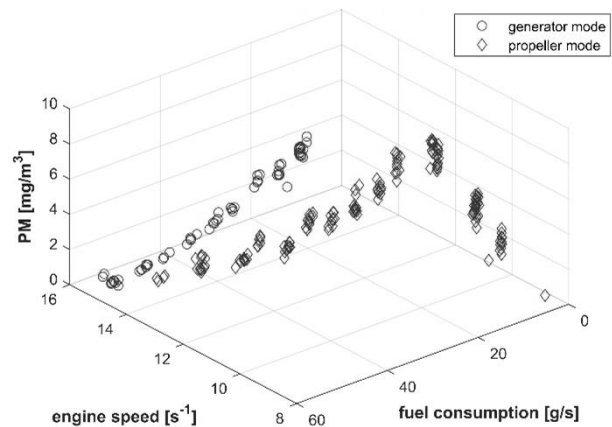


Fig. 5. Distribution of measurement data for input (m_B , n_{act}) and output variables (PM/soot)

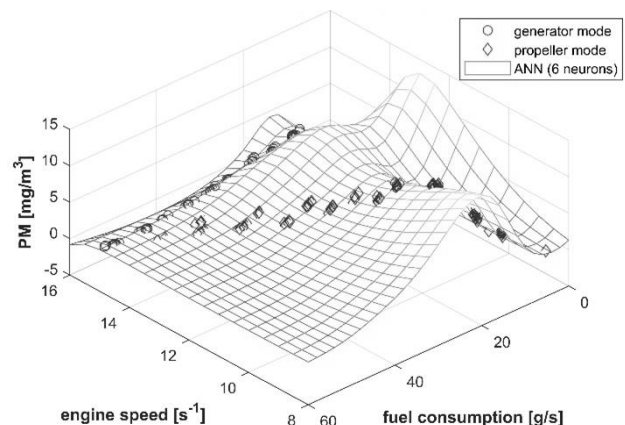


Fig. 6. Trained ANN with 6 neurons in the hidden layer

A k-fold cross validation took place in order to determine the necessary number of neurons. The smallest model error could be reached with 6 up to 15 neurons in the hidden layer. The absolute error in this range is about 0.3 mg/m^3 which corresponds with the scattering of measurement data, see Fig. 5. Fig. 6 shows the shape of the ANN with 6 neurons. More neurons mean also more curvature in the ANN and possibly more distance from a physically interpretable model.

3.3. Application for transient engine operation

A static ANN with 6 neurons has been used for simulation of the transient engine operation. The result shows the big difference between the development of PM in stationary and transient engine operation. The zoomed section in Fig. 7 is an example to show how close the stationary operation would be approached by the ANN and how dynamics are not yet implemented.

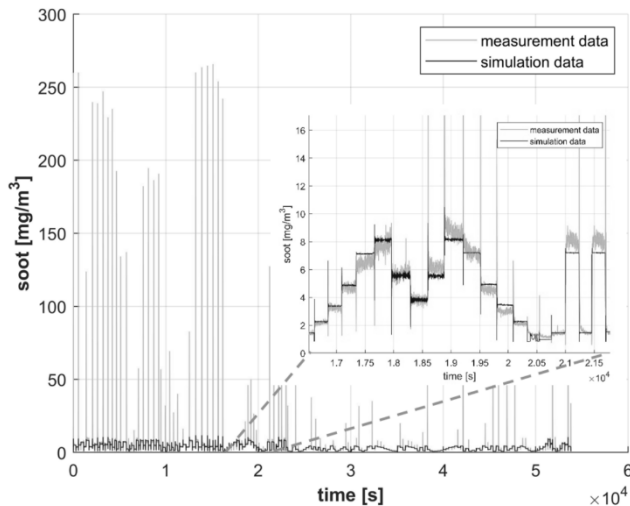


Fig. 7. Trying to simulate measured load changes by means of a static ANN

4. ANN with external dynamics – a lookout

In a first step, the external dynamics approach was chosen to simulate soot formation during transient operation. External dynamics means that the dynamic is generated by extension of the input space [7]. Each of the input parameters (herein m_B and n_{act}) needs a certain time history which is also entering the ANN. The following example takes into account each input parameter's values up to 100 seconds in the past, but only every second value is taken as additional input. Consequently, the number of inputs rises to one hundred considering m_B and n_{act} .

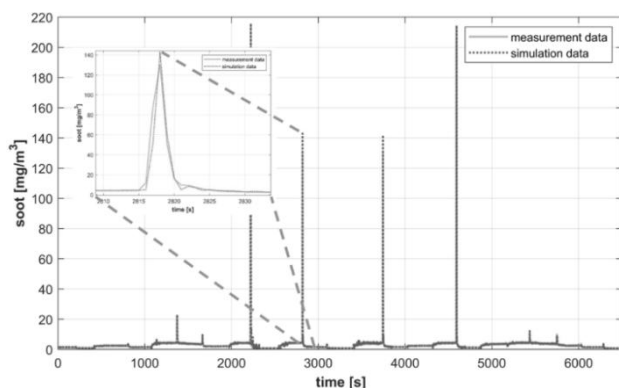


Fig. 8. Validation data set (light grey solid line) and simulation of this same data with trained ANN (dark grey dotted line)

The increased input number also requires an increased number of hidden neurons and training data. The optimum for the three setting parameters – the past values and their intervals as well as the number of hidden neurons – is still to be investigated for the present problem. So far, the following example shows an ANN with external dynamics taking the above described number

of input values and 20 hidden neurons. The training data set comprises 75% of the available data in generator mode. The remaining 25 % of measurement data was used for validation (Fig. 8). For a first attempt the ANN with external dynamics is able to identify the instationarities and to follow the characteristics of the soot peaks. By using different parameter settings, even better results might be expected.

5. Summary

In this paper, it was shown that soot produced during the transient operation of a 4-stroke marine diesel engine can be reproduced very well with the help of a stationary ANN that contains 6 up to 15 neurons in the hidden layer. Investigations on the use of an ANN with external dynamics for the simulation of transient engine operation are currently in progress and appear to be promising as suggested in the work of [6] for the application for high-speed diesel engines. Besides the different dynamic behaviour of a passenger car and a ship diesel engine, the biggest difference between the two engine types are the availability and the operational costs of testbed engines.

The next step will be the integration of the ANN into a suitable ship model and its use within the SAMMON software for verification of the entire method from testbed trials until the application in the prediction software. The perspective is to take measurement data from a real ship in order to simulate both, the ship's motion as well as its fuel consumption and emissions within the assistance software SAMMON.

References

- [1] Ayoubi M.: Nonlinear system identification based on neural networks with locally distributed dynamics and application to technical processes. VDI edition, Düsseldorf 1996.
- [2] Bockhorn H.: Soot formation in combustion. Springer edition, Berlin/Heidelberg 1994.
- [3] Dahms F., Reska M., Nocke J., Hassel E., Reißig M., Schaub M.: Characterizing of transient engine operating with investigation on particle size distribution on a four-stroke medium-speed engine. CIMAC 2019.
- [4] [http://www.imo.org/en/KnowledgeCentre/IndexofIMOResolutions/Marine-Environment-Protection-Committee-\(MEPC\)/Documents/MEPC.176\(58\).pdf](http://www.imo.org/en/KnowledgeCentre/IndexofIMOResolutions/Marine-Environment-Protection-Committee-(MEPC)/Documents/MEPC.176(58).pdf) (available: 24.07.2019).
- [5] <https://issims-gmbh.com/yoomla/products/sammon> (available: 24.07.2019).
- [6] Isermann R.: Engine Modeling and Control. Springer edition, Heidelberg 2014.
- [7] Nelles O.: Nonlinear System Identification. Springer, Heidelberg 2001.
- [8] Rohs H.: Simulation des transienten Betriebsverhalten von aufgeladenen Dieselmotoren. PhD Thesis, TH Aachen, 2006.
- [9] Schaub M., Finger G., Dahms F., Hassel E., Jeinsch T., Kirchhoff M.: Data-based prediction of particle emissions during manoeuvring of ships. IIPhW 2019.
- [10] Schaub M., Finger G., Riebe T., Dahms F., Hassel E., Baldauf M.: Data-based modelling of ship emissions and fuel oil consumption for transient engine operation. OCEANS 2019.
- [11] Wenzel S.P.: Modellierung der Ruß- und NO_x-Emissionen des Dieselmotors. PhD thesis, Otto-von-Guericke-Universität Magdeburg, 2006.

M.Sc. Michèle Schaub

e-mail: michele.schaub@hs-wismar.de

Michèle Schaub grew up in Switzerland. After finishing high school, she studied Comparative Religious Studies in Fribourg/CH before she discovered her passion for seafaring. 2006 she started her maritime studies at Wismar University (B.Sc.) and became a navigational officer on board a general cargo ship. After several years in practice, she began her work in maritime research at the Maritime Department of Wismar University accompanied by a distance learning course in environmental protection at University of Rostock (M.Sc.). She is currently working on her doctoral thesis, in which she combines seafaring and environmental protection.

ORCID ID: 0000-0002-3566-7572

otrzymano/received: 02.08.2019

przyjęto do druku/accepted: 06.12.2019



APPLICATION OF THE LENNARD-JONES POTENTIAL IN MODELLING ROBOT MOTION

Piotr Wójcicki, Tomasz Zientarski

Lublin University of Technology, Institute of Computer Science, Lublin, Poland

Abstract. The article proposes a method of controlling the movement of a group of robots with a model used to describe the interatomic interactions. Molecular dynamics simulations were carried out in a system consisting of a moving groups of robots and fixed obstacles. Both the obstacles and the group of robots consisted of uniform spherical objects. Interactions between the objects are described using the Lennard-Jones potential. During the simulation, an ordered group of robots was released at a constant initial velocity towards the obstacles. The objects' mutual behaviour was modelled only by changing the value of the interaction strength of the potential. The computer simulations showed that it is possible to find the optimal value of the potential impact parameters that enable the implementation of the assumed robotic behaviour scenarios. Three possible variants of behaviour were obtained: stopping, dispersing and avoiding an obstacle by a group of robots.

Keywords: swarm, Lennard-Jones potential, molecular dynamics simulation

ZASTOSOWANIE POTENCJAŁU LENNARD-JONESA DO MODELOWANIA RUCHU ROBOTÓW

Streszczenie. W artykule zaproponowano metodę kontrolowania ruchu grupy robotów za pomocą modelu stosowanego do opisu oddziaływań międzycząsteczkowych. Przeprowadzono symulacje metodą dynamiki molekularnej w układzie składającym się z ruchomych grup robotów oraz nieruchomych przeszkód. Zarówno przeszkody, jak i roboty składały się z jednolitych sferycznych obiektów. Oddziaływania między obiektami opisano za pomocą potencjału Lennard-Jonesa. Podczas symulacji, początkowo uporządkowana grupa robotów poruszała się ze stałą prędkością w kierunku przeszkód. Wzajemne zachowanie obiektów modelowano tylko poprzez zmianę wartości parametrów potencjału oddziaływań. Symulacje komputerowe wykazały, że możliwe jest znalezienie optymalnych wartości parametrów oddziaływania, które umożliwiają uzyskanie pożądanego zachowania robotów. W trakcie symulacji uzyskano trzy możliwe warianty zachowania: zatrzymywanie, rozpraszanie i omijanie przeszkód przez grupę robotów.

Słowa kluczowe: rój, potencjał Lennard-Jones, symulacja metodą dynamiki molekularnej

Introduction

Controlling multiple robots while maintaining a focused formation has been a major challenge for scientists for many years. The main inspiration for these applications is the observation of animals occurring in the natural environment in large groups [3, 14]. Ants, bees, birds and fish are examples of how simple individuals can succeed when working in groups. The interest in social animals stems from the fact that they show some kind of group intelligence [3]. Nature provides many examples of groups of animals in which there is a phenomenon described as group intelligence. As a result, a group is able to perform complex tasks that individual individuals are unable to perform. Complex behaviour is the result of the combined efforts of individuals with extremely limited intelligence (resources). These complex, collective behaviours are derived from a small set of simple behavioural rules using only low-level interactions between individuals and the environment. The field dealing with these issues is known as swarm intelligence [2, 4, 14]. It concerns solving optimisation problems in the traditional mathematical approach and proposes a new computational paradigm: the calculation of the hive [2, 14], in which there is no concept of central intelligence controlling the group. However, there are local interactions between individuals leading to the appearance of complex behaviours absent in the case of single objects [4, 10, 14]. Many algorithms used to control single robots or groups of robots are based on the behaviour of groups of animals. The algorithm presented in [14] is inspired by the natural behaviour of bats using echolocation to move around, avoid obstacles and detect crevices in the dark. Maintaining a formation centred around a point or curve is also a behaviour that occurs in groups of animals. For example, ants move one after the other to form a chain – new units can only join at the end of the chain. Works [7, 8] show examples of how to obtain such a formation. Another example of inspiration for animal behaviour is study [5], in which the authors present a developed algorithm of communication in a group of robots based on ants communicating by means of pheromones.

An alternative to control inspired by biology and behaviour of animals in the natural environment are physical phenomena. In the real world, objects interact with each other. To describe these

interactions, various equations are used with greater or lesser effect. One of the simplest is the Lennard-Jones equation proposed in 1924 [6]. It was used for the first time in computer simulations to describe the behaviour of so-called rigid spheres in 1957 [1]. Since then it has attracted continuous interest and has been applied in various fields of science. It was also used to describe the behaviour of a group of robots [9–12,15]. In paper [11] it was proposed to describe the motion of a group of robots based on the behaviour of particles in a liquid, partially using the Lennard-Jones potential. Many papers describe the use of the potential for group behaviour and self-organisation [7–10,12].

The research was undertaken to better understand the mechanisms used to self-organise robotic groups inspired by physical phenomena. For this purpose, the molecular dynamics method was used to describe the motion of robots in 2D space and the interactions in the system were described by the Lennard-Jones potential. The work consists of four parts: Introduction, Model, Results and Conclusions.

1. Model

Two-dimensional molecular dynamics simulations are carried out to study the behaviour of a group of robots. The simulation model is shown in Figure 1. It consists of several stationary obstacles and a moving group of robots. Both robots and obstacles are composed of spherical elements. To avoid "escape" of robots from the simulated area, system boundaries have been introduced.

The interactions between the objects in the system are described using the Lennard-Jones (LJ) potential (see Figure 2). It shows that depending on the selected parameters σ and ϵ and the mutual distance r , objects can repel or attract other objects. It was assumed that both robots and obstacles are unified and the interactions between them are assumed to be pairwise additive and the pair potential is represented by a truncated (12,6) Lennard-Jones potential:

$$U(r) = \begin{cases} 4\epsilon \left[\left(\frac{\sigma}{r}\right)^{12} - \left(\frac{\sigma}{r}\right)^6 \right], & r \leq r_{max} \\ 0, & r > r_{max} \end{cases} \quad (1)$$

where r is the distance between objects, ϵ is the strength of the interactions, and r_{max} is the cut-off distance, equal to about 10σ for both types of interactions.

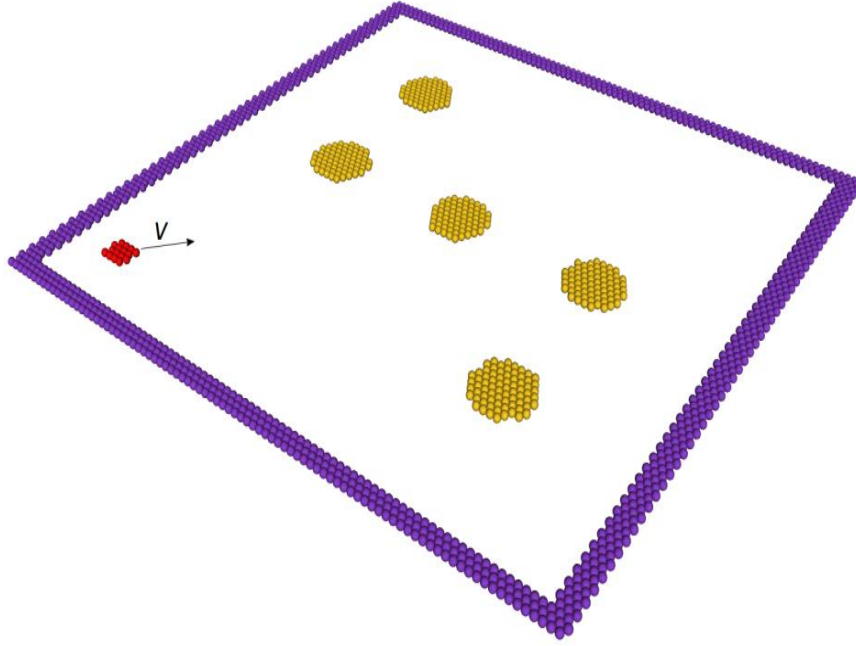


Fig. 1. Model of the simulation system. The obstacles are marked in yellow, the system border in purple and the robot group in red

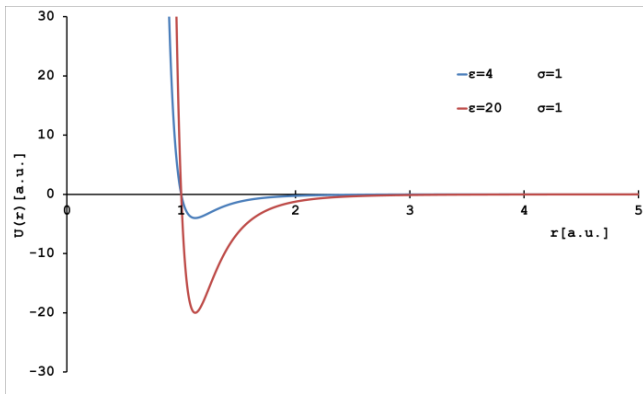


Fig. 2. Lennard-Jones potential for different values of the parameter ϵ

The resultant interaction (E) in the system is the sum of all interactions between all objects (2):

$$E(r) = \sum U_s(r) + \sum U_o(r) + \sum U_w(r) + \sum U_{so}(r) + \sum U_{sw}(r) + \sum U_{ow}(r) \quad (2)$$

where, U_s , U_o , U_w are the interactions between robots, obstacle objects and boundary objects. These interactions are characterised by the corresponding values of the parameters σ , ϵ . In addition, there are mixed interactions between different types of components U_{so} , U_{sw} and U_{ow} , where ϵ_{so} , ϵ_{sw} , ϵ_{ow} are the mixed interactions. We calculate them accordingly from the formula:

$$\epsilon_{ij} = \sqrt{\epsilon_i \epsilon_j} \quad (3)$$

Throughout this paper, all the distances and lengths are expressed in the units of σ , and the energy parameter ϵ of the potential (1) is the unit of energy. In addition, all objects have a unit weight. The trajectories of each object in the computational cell are obtained by integrating Newton's classical equation of motion. The integration is performed over finite time steps using a fifth-order predictor-corrector method. The time step used for solving Newton's equation of motion is 0.005 ps. The temperature during the simulation was kept fixed by periodical velocity rescaling and equal to 300 K. During the simulation, a group of robots was assigned the velocity $V = 20$ m/s and then released towards obstacles. In order to speed up the calculations, the influence of the environment on the moving objects was omitted. The Ovito environment was used to visualise model [13].

2. Results

In order to investigate the influence of the parameters determining the force of the impact of the LJ potential on the behaviour of a group of robots, three research scenarios were proposed. It was assumed that each time a group of robots would be released towards obstacles at a constant speed V . The objects in the group can move relative to each other and have a spherical shape. The other objects in the system are motionless. It has been assumed that all component elements of objects will have the same size:

$$\sigma = \sigma_s = \sigma_o = \sigma_w = 1.0$$

and the only variable parameter will be ϵ . The competitiveness of interactions will be the decisive factor determining the behaviour of objects.

Table 1 summarises the LJ potential parameters used in the simulation to model the behaviour of a group of robots. They made it possible to observe three types of behaviour.

Table 1. Summary of simulation parameters

Option	Strength of interaction		
	ϵ_s	ϵ_o	ϵ_{so}
I. Omission	2.2400	0.1120	0.501
II. Stopping	2.2400	0.0112	0.158
III. Dispersion	0.1120	0.1120	0.112

Figure 3 shows the results of the simulation for option I. It is observed that the group of robots initially moves along the planned trajectory. After sufficient approach to the obstacle, the group is internally reorganised and the obstacle is bypassed. The arrows show the successive stages of the movement of the group in relation to the obstacle. The influence of the obstacle is so big that the robots are not able to move too far away from it. The trajectory of the flight is curved. The kinetic energy is so high that at the final stage of the movement the robots are separated from the obstacle.

It turns out that reducing the ϵ_o parameter 10 times results in a behaviour change of the robot group. The calculated resultant value of ϵ_{so} is several times smaller than for option I and is $\epsilon_{so} = 0.158$. For the same values of the ϵ_s parameter it results in an increase of the robot's willingness to adhere to the obstacle. Decreasing the value of ϵ_o in effect results in an increase in the robots affinity to an obstacle. The observed behaviour is shown in Figure 4.

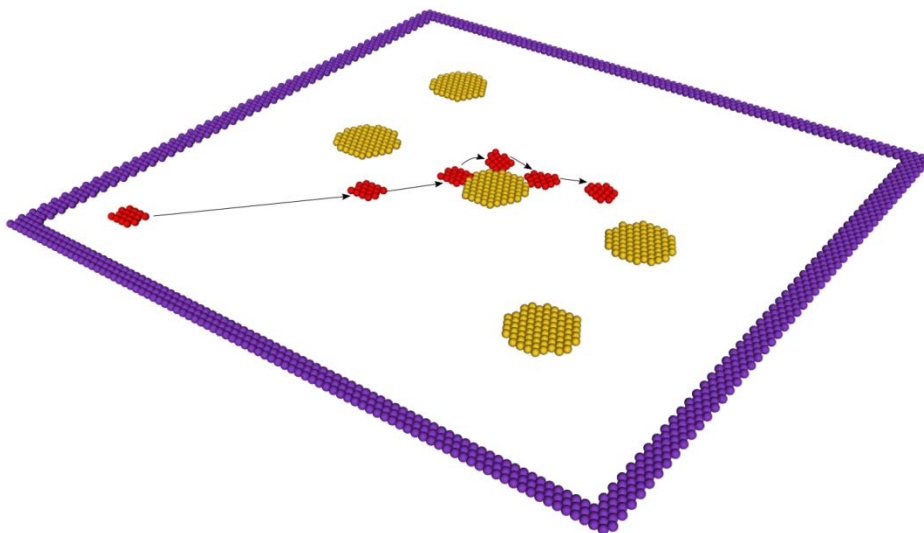


Fig. 3. Avoidance of an obstacle by a group of robots

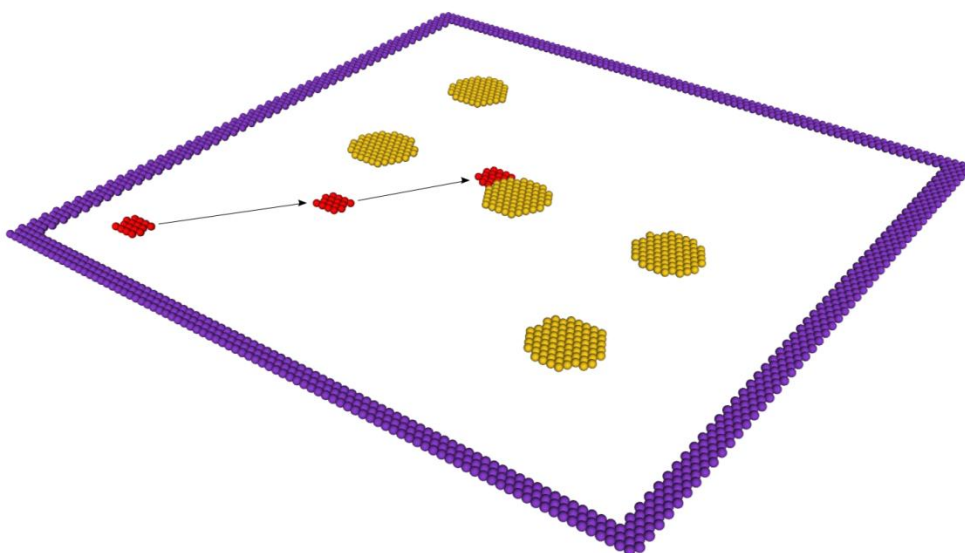


Fig. 4. Stopping a group of robots at an obstacle

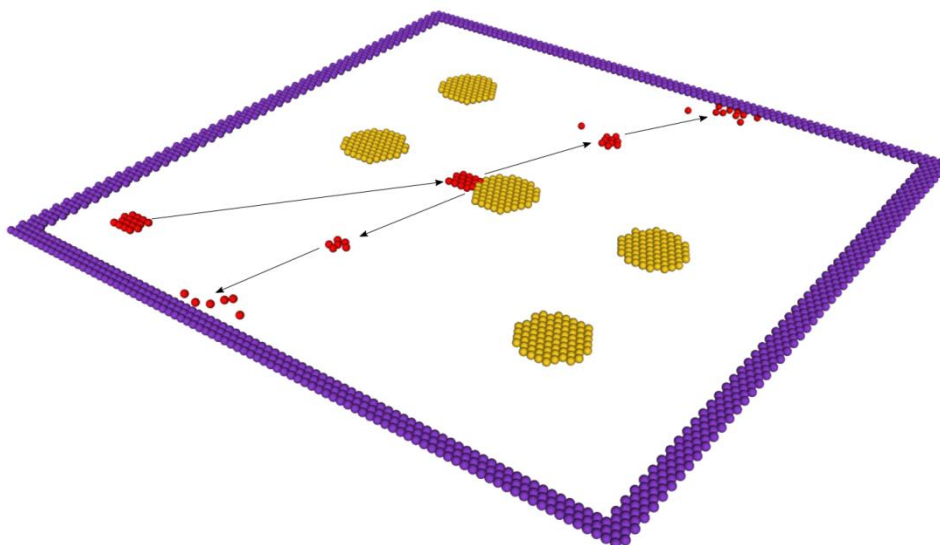


Fig. 5. Dispersal of the group on impact with an obstacle

A completely different situation was observed when $\varepsilon_s = \varepsilon_0 = \varepsilon_{s0}$. In this case, none of the interaction types is highlighted; all are equally weak. The group of robots after hitting an obstacle is dispersed. The kinetic energy delivered during the collision is sufficient to break up the group and scatter its elements. Additionally, a very small value of ε_s results in the inability to maintain the initial configuration of the robots and a dispersion of the group occurs. It has been noticed that the dispersion is multistage and one collision with an obstacle is not enough to completely break the formation. The situation described is shown in Figure 5.

Proper selection of parameters allows to keep the group in a focused configuration and bypass the obstacle. The presence of an obstacle on the trajectory of movement does not cause dispersion of group of robots. An incorrectly selected parameter of the strength of interaction ε causes either the group to be attached to an obstacle or the formation to be broken up immediately. An additional factor influencing the behaviour of robot formation is also the speed of moving robots and the associated kinetic energy. The smoothness of movement will be maintained when the balance of forces is maintained in the system.

3. Conclusion

Simulations show that it is possible to use the Lennard-Jones potential to model the motion of a robot group. The selection of parameters has a key influence on the behaviour of objects. Three predicted types of behaviour were obtained: avoiding an obstacle, breaking up the group by an obstacle and avoiding a collision and stopping at an obstacle. Unfortunately, it was not possible to restore the formation of the group after it was broken up. The aim of future research will be to modify the type of potential or take into account other factors acting in the system, such as the resistance of the environment in which the objects move.

M.Sc. Eng. Piotr Wójcicki
e-mail: p.wojcicki@pollub.pl

Piotr Wójcicki graduated from the Lublin University of Technology, where he now works as assistance in the Institute of Computer Science. His previous research is related to microelectronics, mobile robotics, IoT and applied computer science.



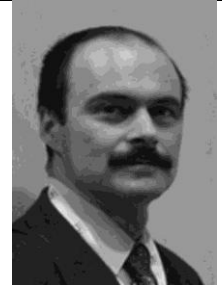
ORCID ID: 0000-0002-0522-6223

References

- [1] Alder B. J., Wainwright T. E.: Phase Transition for a Hard Sphere System. *Journal of Chemical Physics* 27/1957, 1208–1209, [DOI: 10.1063/1.1743957].
- [2] Blum C., Merkle D.: *Swarm Intelligence: Introduction and Applications*. Natural Computing Series. Springer 2008.
- [3] Brambilla M., Ferrante E., Birattari M., Dorigo M.: Swarm robotics: a review from the swarm engineering perspective. *Swarm Intelligence* 7/2013, 1–41, [DOI: 10.1007/s11721-012-0075-2].
- [4] Engelbrecht A. P.: *Computational Intelligence*, John Wiley and Sons. England 2007.
- [5] Farrelly C., Kell D. B., Knowles J.: *Ant Colony Optimization and Swarm Intelligence*. Springer 2008.
- [6] Jones J. E.: On the Determination of Molecular Fields. *Royal Society* 106/1924, 463–477, [DOI: 10.1098/rspa.1924.0082].
- [7] Maxim P. M., Spears W. M., Spears D. F.: *Robotic Chain Formations*. IFAC Proceedings Volumes 42/2009, 19–24.
- [8] Nouyan S., Dorigo M.: Chain Based Path Formation in Swarms of Robots. *ANTS Workshop 2006*, 120–131, [DOI:10.1007/11839088_11].
- [9] Olfati-Saberras R.: Flocking for multi-agent dynamic systems: algorithms and theory. *IEEE Transactions on Automatic Control* 51/2006, 401–420, [DOI: 10.1109/TAC.2005.864190].
- [10] Pinciroli C., Birattari M., Tuci E., Dorigo M., et al.: Self-Organizing and Scalable Shape Formation for a Swarm of Pico Satellites. *Proceedings of the 2008 NASA/ESA Conference on Adaptive Hardware and Systems (AHS 2008)*, 2008, 57–61, [DOI: 10.1109/AHS.2008.41].
- [11] Shimizu M., Ishiguro A., Kawakatsu T., Masubuchi Y., Doi M.: Coherent Swarming from Local Interaction by Exploiting Molecular Dynamics and Stokesian Dynamics Methods. *Proceedings 2003 IEEE/RSJ International Conference on Intelligent Robots and Systems (IROS 2003)*, 2003, 1614–1619, [DOI: 10.1109/IROS.2003.1248875].
- [12] Son J. H., Ahn H. S., Cha J.: Lennard-Jones potential field-based swarm systems for aggregation and obstacle avoidance. *International Conference on Control, Automation and Systems (ICCAS 2017)*, 2017, 1068–1072, [DOI: 10.23919/ICCAS.2017.8204374].
- [13] Stukowski A.: Visualization and analysis of atomistic simulation data with OVITO – the Open Visualization Tool. *Modelling and Simulation in Materials Science and Engineering* 18/2009, 015012, [DOI: 10.1088/0965-0393/18/1/015012].
- [14] Suárez P., Iglesias A., Gálvez A.: Make robots be bats: specializing robotic swarms to the Bat algorithm. *Swarm and Evolutionary Computation* 44/2019, 113–129, [DOI: 10.1016/j.swevo.2018.01.005].
- [15] Sydney N., Paley D.A., Sofge, D.: Physics-inspired motion planning for information-theoretic target detection using multiple aerial robots. *Autonomous Robots* 41/2017, 231–241, [DOI: 10.1007/s10514-015-9542-0].

D.Sc. Tomasz Zientarski
e-mail: t.zientarski@pollub.pl

Tomasz Zientarski is Head of the Department of Computer Science and Computer Modeling at the Lublin University of Technology. He is an associate professor there. His main scientific interests include computer simulation and modeling of physicochemical processes, industrial and mobile robotics, microelectronics, and wireless transmission.



ORCID ID: 0000-0002-1693-5316

otrzymano/received: 26.08.2019

przyjęto do druku/accepted: 06.12.2019

APPLICATION OF ARTIFICIAL NEURAL NETWORK IN THE PROCESS OF SELECTION OF ORGANIC COATINGS

Artur Popko, Konrad Gauda

University of Economics and Innovation in Lublin, Faculty of Transport and Computer Department of Transport and Computer Science, Lublin, Poland

Abstract. The structure of the artificial neural network (ANN) to support the selection of organic coatings was developed and verified, and its learning process was carried out. A simulation of the operation of the network was also carried out, which showed that programming of the coating system selection process can be much faster and more accurate, which is important for a system used in industrial conditions.

Keywords: artificial neural network, organic coatings

ZASTOSOWANIE SZTUCZNEJ SIECI NEURONOWEJ W PROCESIE DOBORU POWŁOK ORGANICZNYCH

Streszczenie. Opracowano i zweryfikowano strukturę sztucznej sieci neuronowej (SSN) służącej do wspomagania procesu doboru powłok organicznych oraz przeprowadzono jej proces uczenia. Dokonano również symulacji działania przedmiotowej sieci, która wykazała, że programowanie procesu doboru systemu powłokowego może być o wiele szybsze i dokładniejsze, co ma istotne znaczenie dla systemu użytkowanego w warunkach przemysłowych.

Słowa kluczowe: sztuczna sieć neuronowa, powłoki organiczne

Introduction

When choosing the type of protective and decorative coatings, it is particularly important to analyse the operational requirements determining the main destructive factors occurring during the use of the coating. Factors that determine the choice of coating type are primarily: the corrosive aggressiveness of the environment, the type of protected structure, the required degree of surface preparation, the life expectancy, the data of paint thickness limits, and data on the environment during application, etc. A comprehensive and meticulous analysis of all necessary data can be supported by an IT system based on an artificial neural network. Thanks to such a tool, programming of the coating system selection process can be much faster and more accurate.

1. Rules for the selection of protective and decorative coatings

The first stage when choosing paint sets should be the analysis of the operational requirements for coatings depending on the type of objects to be covered. These requirements determine the main destructive, climatic and corrosive factors occurring during operation, which decide the choice of coating [1–5].

Knowing the initial operating requirements for coatings to protect a particular object, you can proceed to the next selection stages. This selection, however, is very complex due to the need to take into account both the requirements for decorativeness and the coating's resistance to the effects of simultaneously occurring climatic and corrosive factors. In this selection, the size of the object, the material used for its manufacture, the method of assembly and the total cost of protection are also important. Therefore, the selection of a coating system for corrosion protection should be the result of a full technical and economic analysis [2, 9].

General rules for the selection of paint coatings are included in the relevant standards [6, 7]. Operating conditions were divided there into various macroclimate and microclimate taking into account additional factors (dust, steam, gases, and electrolytes), as well as corrosive aggressiveness of the environment and operational exposures: mechanical, temperature, physicochemical and biological. Most often, preliminary decisions regarding the choice of coverings are made just depending on environmental and operational exposures. The division and marking of exposures to products during exploitation that facilitate the selection of paint coatings is presented in Table 1.

Table 1. Selection of coatings depending on environmental exposures [9, 11]

Environmental exposures	Type of resin *						
	AK	CHK	PCW	ER	PU	SI	AR
Rural and urban environment	+	+	+	o	-	o	o
Acidic industrial environment	o	+	+	+	o	-	-
Alkaline environment	o	+	+	+	+	-	+
Acidic chemical environment	-	+	+	o	+	-	+
Chemical environment with traces of solvents	-	o	o	+	o	-	+
Water action – immersion	-	+	+	+	+	-	+
Water condensation	o	+	+	+	+	-	+
Temperature 80°C	+	+	+	+	+	+	+
Temperature 80÷140°C	+	-	-	+	+	+	+
Temperature 140÷200°C	-	-	-	+	+	+	+

*AK-alkyd; CHK – chlorinated rubber; PCW – polyvinyl chloride; ER-epoxy; PU – polyurethane; SI – silicone; AR – acrylic; + suitable; o sometimes suitable; - unsuitable

Epoxy paint has the most favourable properties. It is also worth paying attention to polyurethane and acrylic paints, which in addition to high temperature resistance and various corrosive environments are characterized by decorative properties, which is of great importance, e.g. in the automotive industry.

It should be noted, however, that these types are general. The durability and protective properties of the coating are determined not only by the film-forming resin but also to a large extent by other ingredients, primarily pigments [13, 14].

A comprehensive analysis of all necessary data can be supported by an IT system based on an artificial neural network. Thanks to such a tool, programming of the coating system selection process can be much faster and more accurate, especially in conditions when not all data is available, and therefore in industrial conditions.

2. Design of artificial neural network structure

As already mentioned, the analysis of necessary data can be supported by an IT system based on an artificial neural network. Boundary parameters for the ANN structure and their interrelationship were determined (Table 2).

Input parameters for ANN:

- Mechanical exposure (abrasion, impact, scratching) (0 – none, 1 – small, 2 – medium, 3 – large).
- Chemical exposure (0 – no exposure, 1 – contact with acids, 2 – contact with bases, 3 – contact with hydrocarbon solvents).
- Biological exposures (0 – no exposure, 1 – exposure caused by mould, bacteria, 2 – exposure caused by organisms, algae).
- Water action (humidity) (0 – none, 1 – low, 2 – high, 3 – immersion).
- Environment (0 – rural, 1 – urban, 2 – industrial, 3 – coastal).
- Corrosiveness of the atmosphere (0 – low, 1 – moderate, 2 – high, 3 – very high).
- Operating temperature (0 – up to 80 °C, 1 – 80–140°C, 2 – 140–200°C, 3 – above 200°C).
- Decorativeness of the coating (0 – no, 1 – yes).
- Substrate type (0 – steel, 1 – non-ferrous metals, 2 – wood, 3 – plastic).

Output parameters for ANN:

Choice of coating type (set number):

- 1 – alkyd, 2 – acrylic, 3 – waterborne acrylic (ecological), 4 – chlorinated rubber, 5 – epoxy, 6 – polyurethane, 7 – polyvinyl chloride, 8 – silicone.

Table 2. Relationship of I/O parameters [1, 11]

Output parameters	Input parameters								
	1 – mechanical	2 – chemical	3 – biological	4 – water	5 – environment	6 – corrosiveness	7 – temperature	8 – decorativeness	9 – type of substrate
1 AK	0, 1	0	0	0, 1	0, 1	0, 1	0, 1	1	0, 1, 2, 3
2 AR	0, 1, 2	0, 1, 2, 3	0	0, 1, 2, 3	0, 1, 2	0, 1, 2	0, 1, 2	1	0, 1, 2, 3
3 AR w	0, 1	0, 1, 2	0	0	0, 1	0	0, 1	1	1, 2, 3
4 CH K	0, 1	0, 1, 2	0	0, 1, 2, 3	0, 1, 2, 3	1, 2, 3	0	1	0, 1, 2, 3
5 ER	0, 1, 2	0, 1, 2, 3	0, 1, 2	0, 1, 2, 3	0, 1, 2, 3	1, 2, 3	0, 1	0	0, 1, 2, 3
6 PU	0, 1, 2, 3	0, 2, 3	0, 1, 2	0, 1, 2, 3	0, 1, 1, 2, 3	1, 2, 3	0, 1	1	0, 1, 2, 3
7 PC W	0, 1, 2	0, 2	0	0, 1, 2, 3	0, 1, 2, 3	2, 3	0	1	0, 1, 2, 3
8 SI	0, 1, 2	0	0	0, 1	0, 1	0, 1	2, 3	1	0, 1, 2, 3

On this basis, it was possible to develop the initial form of the artificial neural network structure required to support the selection of protective and decorative coatings (Fig. 1). The input and output data vectors specify the number of neurons in the input and output layers. The hidden ANN layer consists of neurons that are between the input layer and the output layer, and their number and organization can be treated as a "black box". Using additional layers of hidden neurons enables greater processing efficiency and increases the flexibility of the ANN system. This additional flexibility, however, increases the cost of complexity in the training algorithm. Too few hidden neurons, on the other hand, can prevent the system from properly matching the input data and reduce its resistance [8–10, 12]. Therefore, research was carried out to determine the optimal, final ANN structure and it was verified.

The required structure of the artificial neural network was developed in the MemBrain application environment.

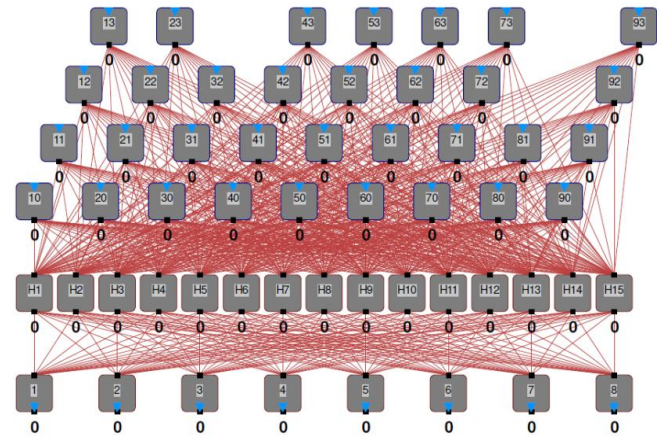


Fig. 1. Structure of the designed artificial neural network

3. The neural network learning process

The essence of the article was to determine and optimize the structure of the neural network, supporting the process of selecting organic coatings. The network's task will be to recognize eight visual patterns adequate to the types of organic coatings. The input and output vectors were generated using the "lesson editor" tool (Fig. 2). An example visualization of one pattern is shown in Figure 3. A training algorithm was used – standard backward propagation. The target network error was set at 0.01 (Fig. 4). To achieve proper results when teaching the network, it must be randomized beforehand – during the first teaching process. Network randomization means that all link weights and activation thresholds for neurons are initiated with small, randomly generated values (unless the corresponding connection or neuron properties are blocked). The values of errors made by the network during its learning were monitored using the "Net error viewer" tool (Fig. 5).

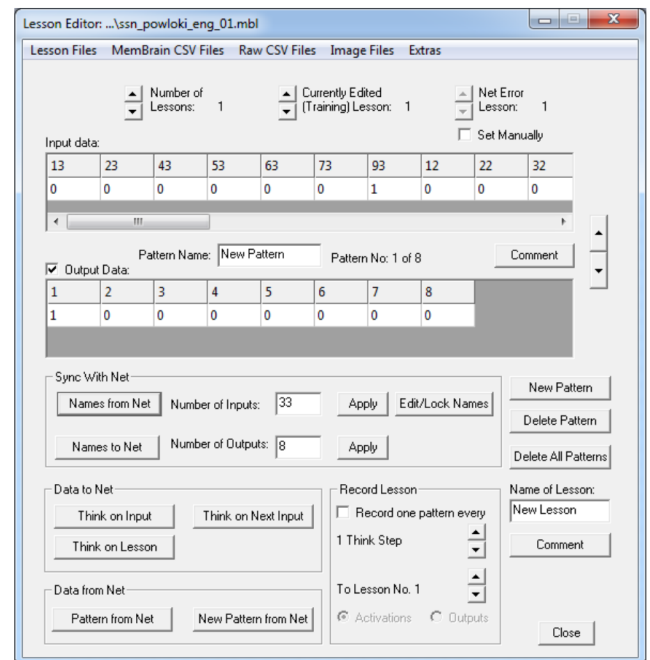


Fig. 2. View of the "lesson editor" tool

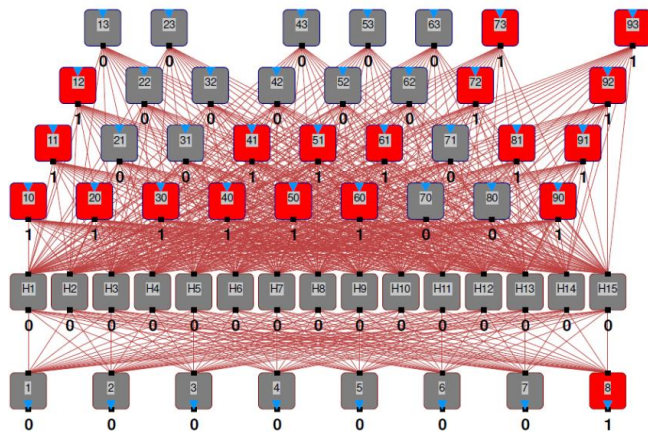


Fig. 3. Visualization of an exemplary vector pattern (silicone coating)

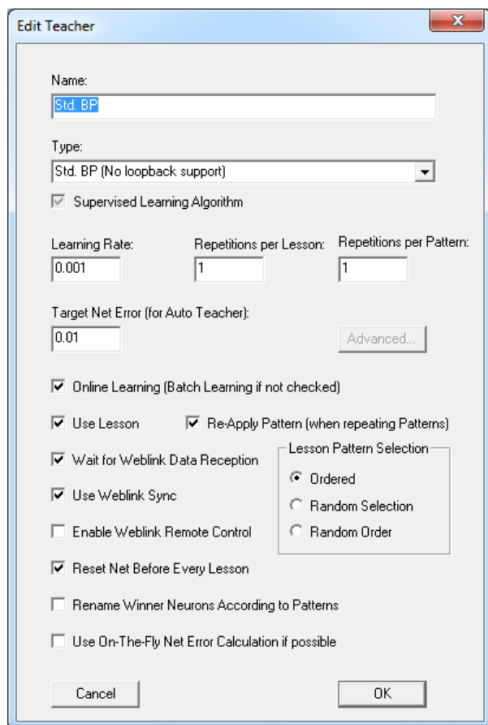


Fig. 4. View of the "Edit Teacher" tool

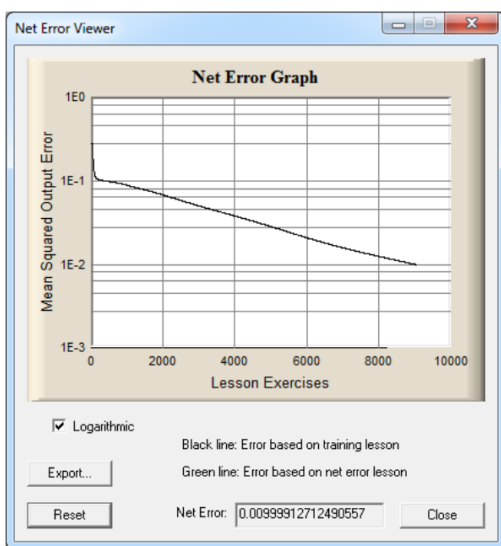


Fig. 5. View of the "Net error viewer" tool

The next stage of research was testing the network with the number of 4–30 neurons in the hidden layer. The results of ANN structure optimization are shown in Figure 6. A better result is obtained when the neural network requires less training cycles. The final resulting relationship between the number of exercises and the number of neurons in the hidden layer is shown in Figure 6. The most effective architecture of the tested ANN consists of 10 neurons in a hidden layer.

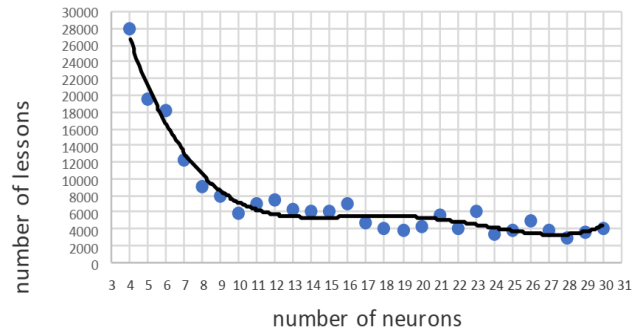


Fig. 6. Results of ANN structure optimization

4. Simulation of the network operation

The developed and tested neural network recognizes visual patterns flawlessly. The example presented in Figure 7 relates to supporting the process of selecting organic coatings when the input data is not complete. For the assumed task input parameters, the neural network indicates the solution, which consists in choosing a silicone coating.

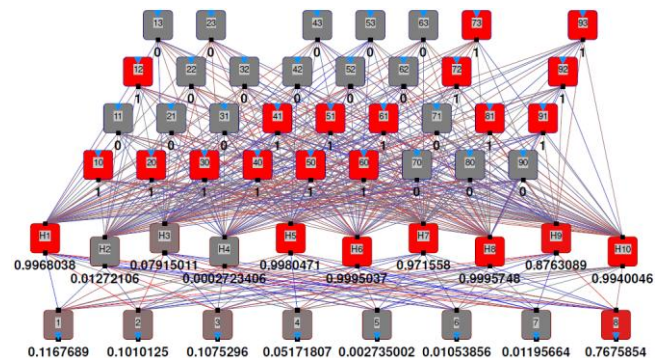


Fig. 7. An example of supporting the process of selecting organic coatings

5. Summary

An artificial neural network project was developed to support the selection of organic coatings. The most adequate initial architecture of the studied ANN consists of 51 neurons, of which 10 contained in a hidden layer. The developed form of an artificial neural network was based on a structure containing only one hidden layer of neurons of the type of standard back propagation without feedback. Network learning was carried out using the "with the teacher" method with the target network error adopted. The learning process was carried out based on a sequential system, using appropriate standards.

The conducted research shows that the adopted assumptions are fully correct. The developed and verified form of the artificial neural network supports solving the problem of choosing the type of organic protective and decorative coatings in a highly effective manner. In addition, the problems described in the study, and in particular the methodology for the implementation of artificial neural networks in the presented range can be successfully used to support similar processes.

References

- [1] Gauda K.: Wodorozcieńczalne powłoki organiczne w przemyśle maszynowym. Lubelskie Towarzystwo Naukowe, Lublin 2011.
- [2] Gauda K., Lenik K., Zinowicz Z.: The possibility of use of waterborne epoxy coatings for the protection of machine and device elements. International Conference: Advances in Coatings Technology, Warsaw 2004.
- [3] Hryniewicz T.: Technologia powierzchni i powłok. Wydawnictwa Uczelniane PK, Koszalin 1999.
- [4] Lenik K., Gauda K., Lenik Z.: Forecasting of durability of waterborne coatings in the machine industry. The Worldwide Journal of Achievements in Materials and Manufacturing Engineering 37(2)/2009, 102–109.
- [5] Miodek A.: Zabezpieczenie antykorozyjne wielkogabarytowych konstrukcji stalowych w aspekcie analizy kosztowej. Lakiernictwo Przemysłowe 6/2001, 12–19.
- [6] PN-EN ISO 12944-1:2001 Farby i lakiery – Ochrona przed korozją konstrukcji stalowych za pomocą ochronnych systemów malarskich.
- [7] PN-EN ISO 9223:2012 Ochrona materiałów metalowych przed korozją – ryzyko korozji w warunkach atmosferycznych – klasyfikacja, określanie i ocena korozyjności atmosfery.
- [8] Popko A.: Multilayer neural network for visual object identification. International Conference on Humanity and Social Science. Guangzhou 2014.
- [9] Popko A., Gauda K.: Sztuczna sieć neuronowa jako innowacyjne narzędzie wspomagania doboru powłok ochronno-dekoracyjnych. Edukacja – Technika – Informatyka 1(23)/2018, 77–82.
- [10] Popko A., Jakubowski M., Wawer R.: Membran neural network for visual pattern recognition, Advances In Science and Technology. Postępy Nauki i Techniki 7(18)/2013, 54–59.
- [11] Rodzyńkiewicz-Rudzińska J. (Ed.): Powłoki malarsko-lakiernicze. Poradnik. Wydawnictwa Naukowo-Techniczne, Warszawa 1983.
- [12] Tadeusiewicz R.: Sieci Neuronowe. Problemy Współczesnej Nauki i Techniki, Informatyka. Akademicka Oficyna Wydawnicza, Warszawa 1999.
- [13] Zinowicz Z., Gauda K.: Powłoki organiczne w technice antykorozyjnej. Wydawnictwo Politechniki Lubelskiej, Lublin 2003.
- [14] Zubielewicz M.: Działanie ochronne powłok z farb wodorozcieńczalnych w zależności od rodzaju pigmentów antykorozyjnych. Lakiernictwo przemysłowe 1/2002, 15–17.

D.Sc. Eng. Artur Popko

e-mail: artur.popko@wsei.lublin.pl

Associate Professor WSEI, Ph.D. D.Sc. Eng. Artur Popko defended his doctoral thesis at the Faculty of Working Machines and Transport of the Poznan University of Technology in 1997. He defended his habilitation thesis at the Faculty of Production Engineering of the University of Life Sciences in Lublin in 2012. He developed, among others methods of computer-aided processes using systems based on artificial neural networks.

ORCID ID: 0000-0001-8882-0545

Ph.D. Konrad Gauda

e-mail: konrad.gauda@wsei.lublin.pl

A graduate of doctoral studies organized at the Faculty of Mechanical Engineering of the Lublin University of Technology. His scientific interests mainly include surface engineering and computer-aided learning process. He is the author or co-author of 2 monographs and over 30 articles in the field of organic coatings research and the use of computer science in technology and education.

ORCID ID: 0000-0002-7300-6978

*otrzymano/received: 29.08.2019**przyjęto do druku/accepted: 06.12.2019*

APPLICATION OF OPTICAL PROFILOMETRY IN THE ANALYSIS OF THE DESTRUCTION PROCESS OF RENOVATION ORGANIC COATINGS FOR THE AUTOMOTIVE INDUSTRY

Konrad Gauda, Kamil Pasierbiewicz

University of Economic and Innovation in Lublin, Lublin, Poland

Abstract. The article concerns the evaluation of the possibility of using the optical profilometry method in the analysis of the destruction process of acrylic coatings exposed at a climate station in an industrial-urban atmosphere. It was found that the observed changes do not allow to clearly assess the durability of the tested coatings. It seems that the method used may play a supporting role in assessing the quality of the coatings because the surface maps show the number and size of pores in the coating. Therefore, this method can be used, for example, to help determine the optimal parameters of the coating process (e.g. spray pressure).

Keywords: optical profilometer, organic coating, automotive

ZASTOSOWANIE PROFILOMETRII OPTYCZNEJ W ANALIZIE PROCESU DESTRUKCJI RENOWACYJNYCH POWŁOK ORGANICZNYCH DLA PRZEMYSŁU MOTORYZACYJNEGO

Streszczenie. Artykuł dotyczy oceny możliwości wykorzystania metody profilometrii optycznej w analizie procesu destrukcji renowacyjnych powłok akrylowych przeznaczonych dla przemysłu motoryzacyjnego eksponowanych na stacji klimatycznej w atmosferze przemysłowo-miejskiej. Stwierdzono, że zaobserwowane zmiany nie pozwalają jednoznacznie ocenić trwałości badanych powłok. Wydaje się, że zastosowana metoda może odgrywać rolę pomocniczą w ocenie jakości powłok, ponieważ mapy powierzchni wyraźnie pokazują liczbę i wielkość porów w powłoce. Można więc zastosować tę metodę przykładowo jako wspomagającą ustalenie optymalnych parametrów procesu nakładania powłok (np. ciśnienia natrysku).

Słowa kluczowe: profilometr optyczny, powłoka organiczna, motoryzacja

Introduction – outline of optical profilometry method

The operation of the optical profilometer is based on the principle of light wave interferometry. This means that when the waves of the same frequency and amplitude overlap, a characteristic result wave is created, the amplitude of which depends on the mutual phase shift of the input waves

When both streams are in the amplitude phase, they add up, while when both waves are offset by 180° , a zero amplitude wave is created. This summation and drift property is called interference or superposition and creates a set of dark and bright stripes known as interference fringes when observed on screen or through a microscope [13, 15] (Fig. 1).

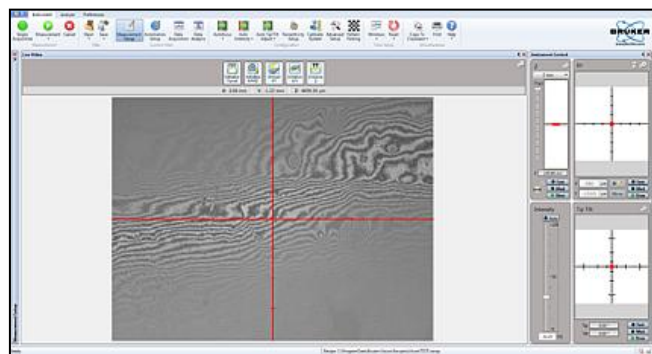


Fig. 1. Interference fringes on the sample surface displayed in Vision 64 application

To use the phenomenon of interference for surface topography analysis, the light beam is divided into two tracks. One of them is undisturbed, while the other one, after reflection from surface irregularities, undergoes phase shifts. After superimposing the disturbed and reference waves, the changes caused by the differences in the height of the tested surface topography can be analyzed.

Figure 2 shows a simplified schematic of the optical profilometer. The wave emitted by the light source is split into two tracks in a special splitter. Each of the beams moves in the direction of the reference mirror and the second mirror, which is the tested surface of the sample. After reflection, phase shifts

of the waves are created depending on the distance of the mirrors. Then the reflected beams are put back on each other in the splitter, and the resulting wave is recorded by a detector that measures the intensity of light during sample movement and finds maximum interference.

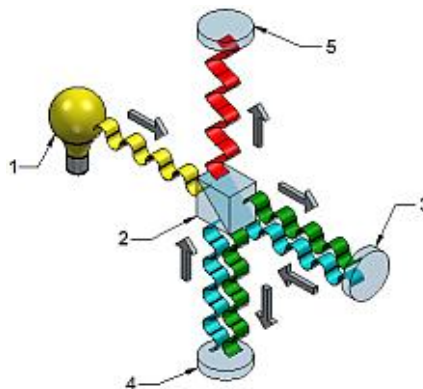


Fig. 2. Simplified diagram of optical interferometer operation [13]: 1 – light source, 2 – splitter, 3 – reference mirror, 4 – sample tested, 5 – detector

The measurement method, in contrast to the traditional (contact measurement), allows non-contact measurement and achieves accuracy up to 1nm, which is important for organic coatings testing [1].

1. Research methodology

The samples were prepared in accordance with the PN-EN ISO 1514: 2006 standard [11]. Based on the analysis of the literature, standard and the paint materials market, Dupont's organic renovation coatings for the automotive industry based on acrylic resin with the trade designation CS 920 were qualified for testing. Multilayer systems (primer – base varnish – colorless varnish) were applied to steel plates (so-called car body sheet) using the pneumatic spraying method (pressure 7 bar), with the average thickness of a single layer was $50 \mu\text{m}$ [2–5] (Fig. 3).

Samples were labeled with SKxB and SKxC symbols (where: CS-climate station, x – sample number, W – white coating (AM1 pigment), B – black coating (AM5 pigment)).

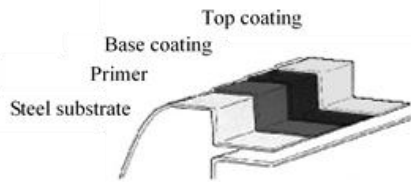


Fig. 3. Multilayer system tested (single layer thickness $50 \pm 5 \mu\text{m}$)

The samples prepared in this way were analyzed using an optical profilometer, while a Bruker profilometer was used in the tests (Fig. 4).

Using the profilometer, basic surface roughness parameters and their 2/3 D maps were obtained (initial imaging), with several areas of 1 mm^2 analyzed (Fig. 5, Fig. 6).

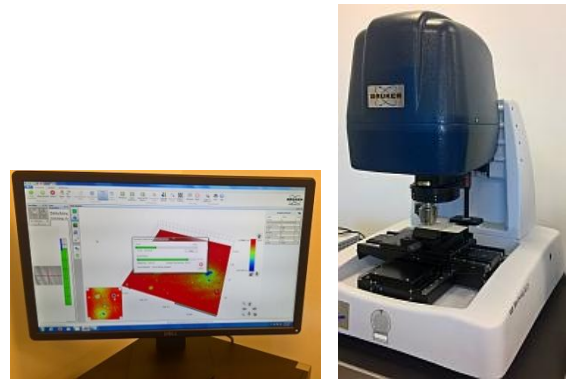


Fig. 4. View of the "Edit Teacher" tool

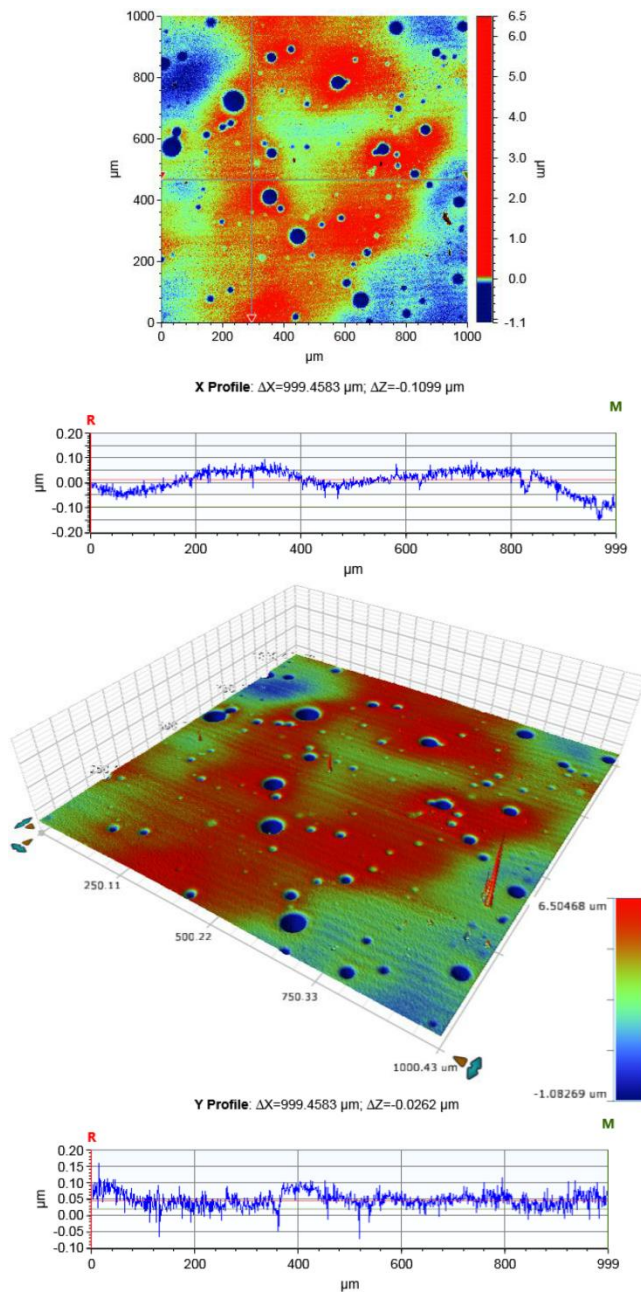


Fig. 5. Preliminary imaging – 2D/3D maps and profilograms of sample fragments of the coating surface – $R_a = 0.053 \mu\text{m}$ (sample CS2W)

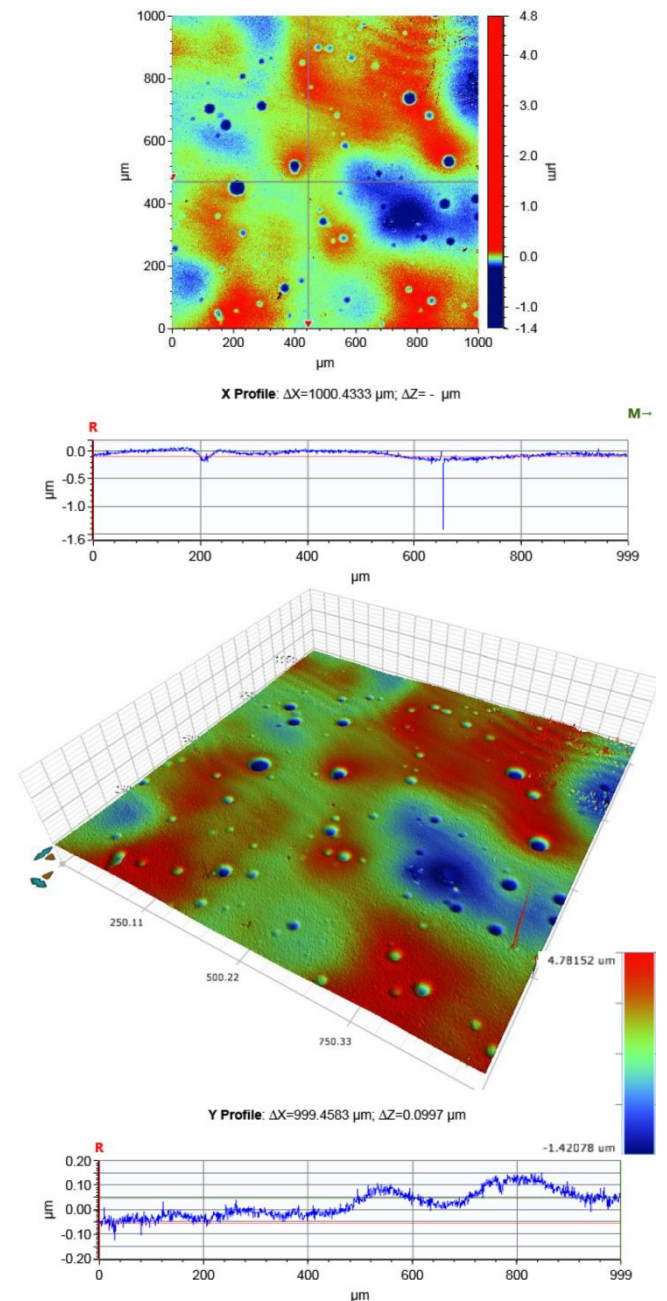


Fig. 6. Preliminary imaging – 2D/3D maps and profilograms of sample fragments of the coating surface – $R_a = 0.064 \mu\text{m}$ (sample CS3B)

Samples with coatings were then exposed at a climate station for 34 weeks in the autumn-winter-spring period in an industrial and urban atmosphere (according to PN-EN ISO 2810: 2005) (Fig. 7) [12].

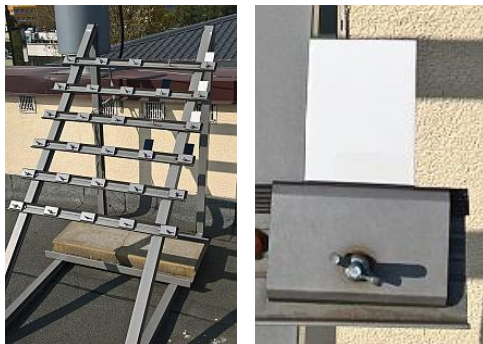


Fig. 7. View of the climate station and method of sample attachment

The average daily temperature during the exposure period was 8.3°C, humidity 73%, and the amount of precipitation 20.3 mm [14].

2. Test results

After the exposure, the surface condition of the coatings was again monitored and the basic roughness parameters were assessed (Fig. 8, Fig. 9, Tab. 1). In order to assess the variability of the R_a parameter, a K factor was introduced, which is a percentage of the ratio of the current value from a given measurement of y_n to the initial value of y_0 described by the following relation (1):

$$K = \frac{y_n}{y_0} \cdot 100[\%] \quad (1)$$

This factor allows the assessment of the degree of change in the R_a parameter of the tested coatings in relation to the initial value obtained at the beginning of the test cycle (coatings before exposure at a climate station – "new").

Table 1. Summary of measurement results

Parameter	Multilayer system (average values)			
	white		black	
	before exposure	after exposure	before exposure	after exposure
Number of Data Points [%]	99.9	99.9	99.9	99.9
R_a [μm]	0.053	0.087	0.072	0.134
The K-factor [%]	164.2		186.1	

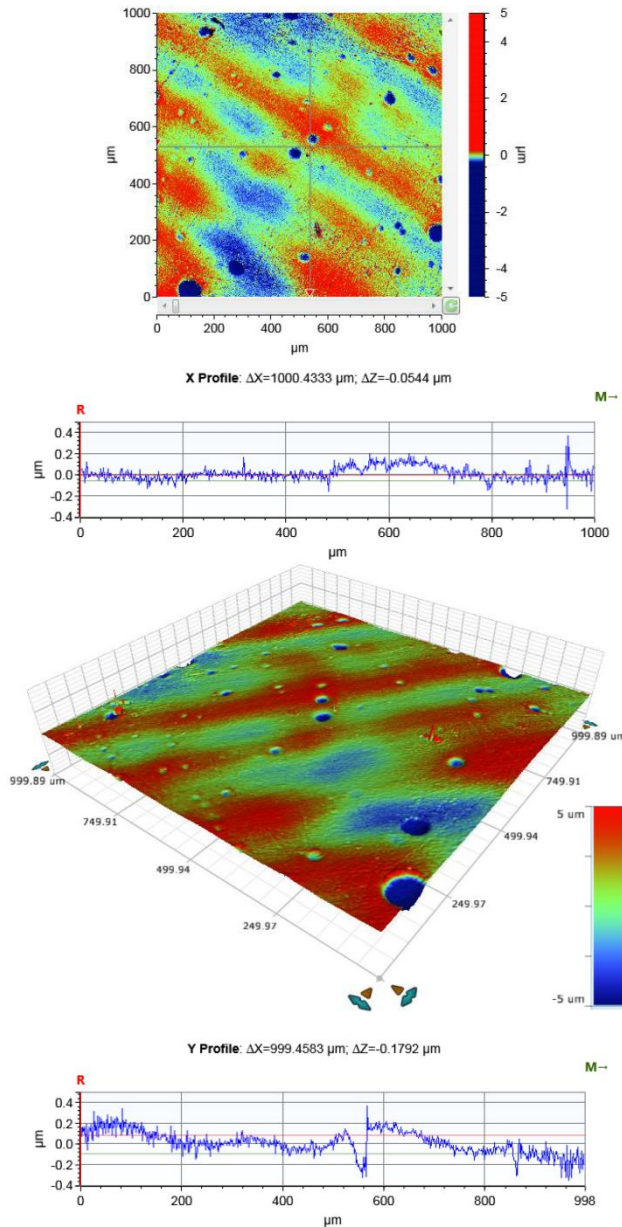


Fig. 8. Final imaging – 2D/3D maps and profilograms of sample fragments of the coating surface – $R_a = 0.087 \mu\text{m}$ (sample CS2W)

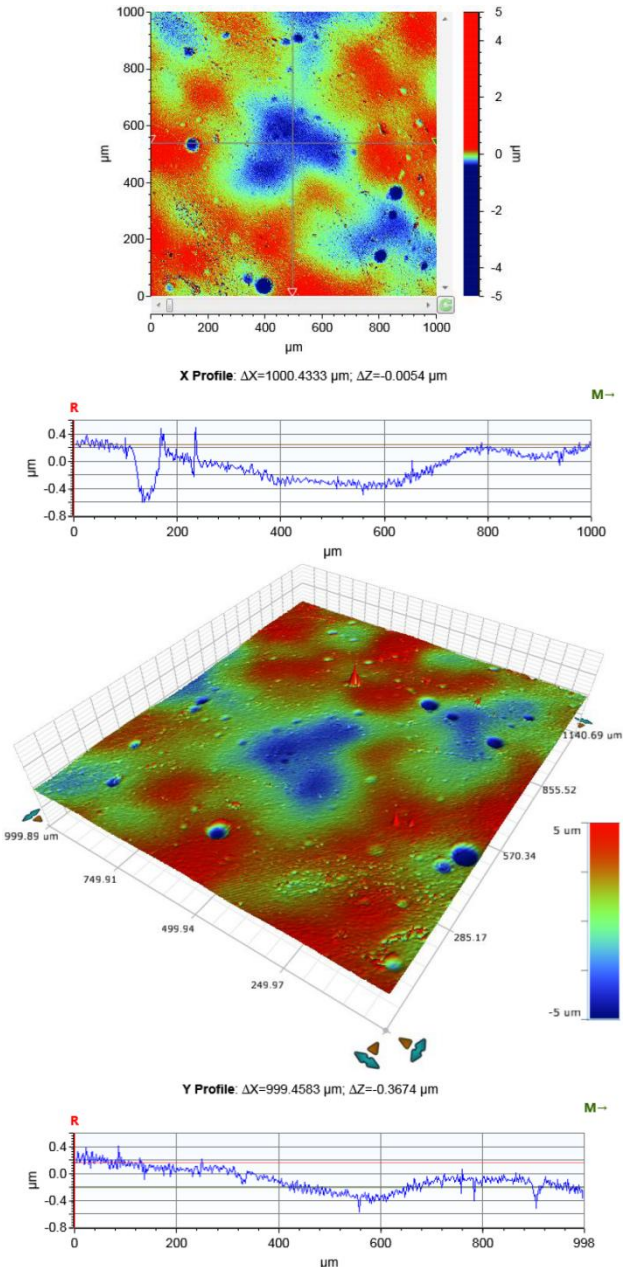


Fig. 9. Final imaging – 2D/3D maps and profilograms of sample fragments of the coating surface – $R_a = 0.127 \mu\text{m}$ (sample CS3B)

3. Summary

As a result of the analysis of the obtained images and profilograms of a number of samples, it can be concluded that:

- the sensitivity of the profilometer is most adequate for testing organic coatings – the average number of collected measurement points of the tested surface fragments was over 99.9%, and the measurement accuracy of Ra parameter was ± 1 nm,
- no visible differences were found in the obtained surface maps of the coatings before and after exposure – similar size and number of coating pores,
- the value of Ra parameter of the coatings exposed at the climatic station increased, which may indicate the initiation of the destruction process,
- the color of the coating, and thus the type of pigment used may influence the speed of the process of destru – the factor of variation K for black coatings was 186.1% and was higher than white coatings by nearly 22%.

Nevertheless, the observed changes do not allow to clearly assess the durability of the tested coatings. The reason for this may be that the exposure time of the samples is too short. Therefore, this time should be extended or intensified by destructive factors using the aging chamber for research, which will be the subject of further studies. An unfavorable factor in this type of research is also the contamination of the coating after the exposure period, which may affect the results [5–8].

It seems that the method used may have an auxiliary/supplementary role in assessing the quality of coatings due to the fact that surface maps clearly show the number and size of pores in the coating. Therefore, this method can be used, for example, as a supporting optimization of the coating process (spray pressure, temperature, drying speed). In the case of determining the durability of coatings, it would be advisable to additionally support the tests of mechanical properties, especially the scratch hardness or adhesion to the substrate, or additionally measure the gloss of the coatings and prepare photographic documentation [3–10].

References

- [1] Dokumentacja techniczna profilometru firmy Bruker (technical documentation)
- [2] Gauda K.: Badania korozyjne akrylowych powłok organicznych w komorze solnej. *Postępy Nauki i Techniki* 15, 2012, 170–179.
- [3] Gauda K.: Wodorozcieńczalne powłoki organiczne w przemyśle maszynowym. Monografia. Lubelskie Towarzystwo Naukowe, Lublin 2011.
- [4] Gauda K.: Wpływ oddziaływań smaru maszynowego na właściwości mechaniczne powłok akrylowych o zróżnicowanej zawartości lotnych związków organicznych. *Postępy Nauki i Techniki* 9, 2011, 145–158.

- [5] Gauda K.: Prognozowanie zmian połysku lustrzanego powłok organicznych jako metoda szacowania trwałości pokryć. *Postępy Nauki i Techniki* 4, 2010, 114–129.
- [6] Kotlík P., Doubravová K., Horálek J., Kubáč L., Akma J.: Acrylic copolymer coatings for protection against UV rays. *Journal of Cultural Heritage* 15, 2014, 44–48.
- [7] Kotnarowska D., Sirak M.: Destrukcja nawierzchniowych powłok akrylowych starzonych promieniowaniem UV. *Autobusy: technika, eksploatacja, systemy transportowe* 6 (18), 2017, 816–821.
- [8] Kotnarowska D., Sirak M.: Wpływ czynników środowiska na destrukcję powłok akrylowych. *Ochrona przed Korozją* 9, 2017, 300–305.
- [9] Lenik K., Gauda K., Lenik Z.: Forecasting of durability of waterborne coatings in the machine industry. *Archives of Materials Science and Engineering* 37(2), 2009, 102–109.
- [10] Pintus V., Wei S., Schreiner M.: Accelerated UV ageing studies of acrylic, alkyd, and polyvinyl acetate paints influence of inorganic pigments. *Microchemical Journal* 124, 2016, 949–961.
- [11] PN-EN ISO 1514:2006 – znormalizowane płytki do badań.
- [12] PN-EN ISO 2810:2005 – powłoki w naturalnych warunkach atmosferycznych – ekspozycja i ocena.
- [13] Patorski K. (ed.): *Interferometria laserowa z automatyczną analizą obrazu*. Wydawnictwo OWPW, Warszawa 2005.
- [14] www.meteoblue.com (weather archive for Lublin).
- [15] Zhang S.(ed.): *Handbook of 3D machine vision. Optical metrology and imaging*. CRC Press, 2013.

Ph.D. Konrad Gauda

e-mail: konrad.gauda@wsei.lublin.pl

A graduate of doctoral studies organized at the Faculty of Mechanical Engineering of the Lublin University of Technology. His scientific interests mainly include surface engineering and computer-aided learning process. He is the author or co-author of 2 monographs and over 30 articles in the field of organic coatings research and the use of computer science in technology and education.

ORCID ID: 0000-0002-7300-6978

M.Sc. Eng. Kamil Pasierbiewicz

e-mail: kamil.pasierbiewicz@wsei.lublin.pl

Specialist in the field of laboratories devices at the University of Economic and Innovation in Lublin. Ph.D. student at the Lublin University of Technology at the Department of Materials Engineering.

ORCID ID: 0000-0003-4365-7363

otrzymano/received: 10.09.2019

przyjęto do druku/accepted: 06.12.2019



ANALYSIS OF DATA FROM MEASURING SENSORS FOR PREDICTION IN PRODUCTION PROCESS CONTROL SYSTEMS

Tomasz Rymarczyk^{1,2}, Bartek Przysucha³, Marcin Kowalski², Piotr Bednarczuk²

¹Research and Development Centre, Netrix S.A., Lublin, Poland, ²University of Economics and Innovation in Lublin, Lublin, Poland,

³Lublin University of Technology, Lublin, Poland

Abstract. The article presents a solution based on a cyber-physical system in which data collected from measuring sensors was analysed for prediction in the production process control system. The presented technology was based on intelligent sensors as part of the solution for Industry 4.0. The main purpose of the work is to reduce data and select the appropriate covariate to optimise modelling of defects using the Cox model for a specific mechanical system. The reliability of machines and devices in the production process is a condition for ensuring continuity of production. Predicting damage, especially its movement, gives the ability to monitor the current state of the machine. In a broader perspective, this enables streamlining the production process, service planning or control. This ensures production continuity and optimal performance. The presented model is a regressive survival analysis model that allows you to calculate the probability of failure occurring over a given period of time.

Keywords: Cox model, time to failure prediction, production control, intelligent platform

ANALIZA DANYCH Z CZUJNIKÓW POMIAROWYCH DO PREDYKCJI W SYSTEMACH KONTROLI PROCESÓW PRODUKCYJNYCH

Streszczenie. Artykuł przedstawia rozwiązanie oparte na systemie cyber-fizycznym, w którym analizowano dane zbierane z czujników pomiarowych do predykcji w systemie kontroli procesów produkcyjnych. Przedstawiona technologia została oparta na inteligentnych czujnikach pomiarowych jako element rozwiązania dla Przemysłu 4.0. Głównym celem pracy jest redukcja danych i wybór odpowiedniego kowariantu w celu optymalizacji modelowania usterek za pomocą modelu Coxa dla konkretnego układu mechanicznego. Niezawodność pracy maszyn i urządzeń w procesie produkcyjnym jest warunkiem zapewnienia ciągłości produkcji. Przewidywanie uszkodzenia, a zwłaszcza jego momentu daje możliwość monitorowania bieżącego stanu maszyny. W szerszej perspektywie umożliwia to usprawnienie procesu produkcji, planowania serwisu, czy kontroli. Zapewnia to utrzymanie ciągłości produkcji i optymalnej jej wydajności. Przedstawiony model jest regresyjnym modelem analizy przeżycia, który pozwala na obliczanie prawdopodobieństwa wystąpienia awarii w określonym czasie.

Słowa kluczowe: model Coxa, predykcja uszkodzeń, sterowanie produkcją, inteligentna platforma

Introduction

The article presents the results of research on the use of sensors for the analysis of technological processes using measuring devices [17]. Control of production processes and advanced automation and play an important role in industry. Production lines are an important element of production companies, where with the use of measuring and control systems it is possible to optimise technological processes that can provide high flexibility and quick adaptation of production processes, safety and efficiency at optimal costs. The presented concept consists in the use of cyber-physical systems and devices of the Internet of Things. The integration of business devices and processes gives greater opportunities and increases the efficiency of technological lines [16]. Modern production systems are based on the latest achievements in the field of information and measuring technologies (Fig. 1). There are many methods for solving optimisation problems [2, 5–12, 13–23]. Autonomy, optimisation and integration of analytical approaches is related to the operation of sensor networks, large amounts of data, analysis and interpretation of information, taking into account security aspects [1, 13–15].



Fig. 1. Industrial automation system

An important condition for ensuring continuity of production is the reliability of the equipment in the production process. Predicting damage time allows you to monitor the current status of the device and improve the planning process for inspections and service. In order to maintain production continuity and optimal production efficiency, the Cox model was used to determine the expected failure time. The presented solution is a regressive survival analysis model that allows you to calculate the probability of failure occurring at a given time or the average time of failure occurrence, etc. [3, 4, 24, 25].

1. Model of fault prediction

One of the most popular models for determining the expected failure time is the Cox model, which is a regressive model for survival analysis. It allows you to calculate the probability of failure occurring within a specified time. The main idea of the Cox model, the proportional threat is that devices age with time. The specific degradation process may depend on many factors that can be permanent.

In the Cox model, the proportional hazard is defined by the following terms:

The survival function is called the function given by:

$$S(x) = P(T \geq x) = 1 - F(x^-) \quad (1)$$

F – lifetime distributor, f – lifetime density. Specifies the probability that the object will live longer than x time.

The hazard function is defined as the following relationship:

$$h(t) = \lim_{\Delta t \rightarrow 0} \frac{P[(t \leq T < t + \Delta t) | (T \geq t)]}{\Delta t} \quad (2)$$

Indicates the probability that a given object will live longer than the time t .

Cumulative risk – the cumulative hazard function is expressed by the formula:

$$H(t) = \int_0^t h(u) du \quad (3)$$

For time-dependent hazard function, covariants can be divided into time-dependent and constant.

Then the function is determined by

$$h(\mathbf{x}_i, t) = h_0(t) \exp \left[\sum_{j=1}^{p_1} x_{ij} b_j + \sum_{j=1}^{p_2} x_{ij}(t) b_j \right] \quad (4)$$

x_{ij} – time-fixed covariates, $x_{ij}(t)$ – time-varying covariates.

A Cox proportional hazard model with time dependent variables is described:

$$h(t, \mathbb{x}_l(t), \beta) = h_0(t) \exp(\mathbb{x}_l(t)\beta) \quad (5)$$

Where $\beta = (\beta_1, \beta_2, \dots, \beta_n)$ – model parameter vector (in the Cox proportional model it is assumed that this vector is constant in time), $h_0(t)$ – baseline hazard function.

The hazard rate is given

$$HR(t, x_1, x_2) = \frac{h(t, \mathbb{x}_1(t), \beta)}{h(t, \mathbb{x}_2(t), \beta)} \quad (6)$$

In the event of a fault occurring at specific time intervals, when the failure times are approximate by the same amount, determining parameter estimates is complicated. It is helpful to use the algorithm proposed by Breslow:

$$l = \prod_{l=1}^m \frac{\exp(\mathbb{x}_{(l)+}\beta)}{[\sum_{j \in R(t_l)} \exp(\mathbb{x}_{(j)}\beta)]^{d_l}} \quad (7)$$

d_l – number of objects with survival time $t_{(l)}$,

$$\mathbb{x}_{(l)+} = \sum_{j \in D(t_{(l)})} \mathbb{x}_j \quad (8)$$

In the PHM model, the estimation of the basic hazard function takes place irrespective of the parameter model estimation. The most common form of primary threat is Weibull or exponential, Gompertz. The Weibull distribution is one of the most frequently used distributions in modelling the time of failure occurrence. He assumes that the intensity of damage is a monotonic variable. The Gompertz distribution is used when the population divides the cause of the fault into two parts. Devices or units at a young age are primarily prone to random events or diseases, while for advanced age natural resistance in people or parts wear in the case of machines decreases, which is included in the function in the form of parameters.

The Weibull distribution function looks like this:

$$h_0(t) = \frac{f(t)}{S(t)} \quad (9)$$

$$f(t) = \frac{\alpha}{\gamma} \left(\frac{t}{\gamma}\right)^{\alpha-1} \exp\left\{-\left(\frac{t}{\gamma}\right)^\alpha\right\} \quad (10)$$

$$S(t) = 1 - F(t) = \exp\left\{-\left(\frac{t}{\gamma}\right)^\alpha\right\} \quad (11)$$

where α – shape parameter, γ – scale parameter.

The shape parameter tells us about the change in the probability of a fault occurring over time. For $\gamma > 1$ the probability of occurrence of a fault increases with time, for $\gamma = 1$ the probability of occurrence of a fault is constant, for $\gamma < 1$ the probability of a fault decreases with time. The scale parameter is related to the time the fault occurred.

Therefore, the hazard function is ensured by:

$$h_0(t) = \frac{\alpha}{\gamma} \left(\frac{t}{\gamma}\right)^{\alpha-1} \quad (12)$$

After estimating the model parameters, you can test the statistical significance of the parameters. For this purpose, for example, the partial probability test or Wald test is used.

The partial likelihood ratio test statistics are provided by:

$$G = 2\{L(\hat{\beta}) - L(0)\} \quad (13)$$

$$L(0) = -\sum_{l=1}^p \ln(n_l) \quad (14)$$

where n_l is the number of objects in the risk set.

With the null hypothesis that the tested coefficient is equal to zero, it is statistics with distribution χ^2 .

Wald's Test:

This test assumes that the ratio of the estimated ratio to the standard error will have a normal distribution

$$z = \frac{\hat{\beta}}{SE(\hat{\beta})} \quad (15)$$

Partial probability tests are usually recommended.

The value of the standard deviation of the model parameters is estimated based on the inverse of Fisher's information matrix.

$$\mathbb{I}(\hat{\beta}) = -\frac{\partial^2 L(\beta)}{\partial \beta^2} \Big|_{\beta=\hat{\beta}} \quad (16)$$

On the other hand, the variance and standard deviation of the data are given in the formulas:

$$\widehat{Var}(\hat{\beta}) = \mathbb{I}(\hat{\beta})^{-1} \quad (17)$$

$$\widehat{SE}(\hat{\beta}) = \sqrt{\widehat{Var}(\hat{\beta})} \quad (18)$$

The model assumptions are tested by verifying four basic assumptions:

- Violation of the proportional threat determination,
- Appropriate functional form of accompanying variables,
- Remote observations,
- Influential observations.

Testing the correctness of the model is checked by testing the probability distribution of so-called Cox-Snell residues.

Schoenfeld's residuals

For the vector covariates $\mathbb{x}_{(l)}$ calculated at time t_l , $k = 1, \dots, p$. Schoenfeld's residuals are:

$$\hat{r}_k(\hat{\beta}) = \mathbb{x}_{(k)} - E(\mathbb{x}_{(k)} | R_k), \quad k = 1, \dots, p \quad (19)$$

where set R_k – a set of those objects that remain endangered until, t_k . In the event that Cox regression model assumptions are met rather than asymptotically $E(\hat{r}_k) = 0$. When fixing $\hat{r}_k(\hat{\beta})$ instead of β we take $\hat{\beta}$.

2. Results and data analysis

For each covariant, the maximum percentage of significant models can be observed depending on the length of the time window. Both too short time windows and too long give lower percentages of significant models. Optimal values are obtained for a time window from 10 sec to 12 sec depending on the type of covariant. The least favourable case can be observed for the minimum, where the percentages of significant models decrease rapidly for all sample sizes. For the maximum, the percentage levels decrease in the least significant way, then for the average the situation is worse while for the median and for the minimum the worst. Based on this criterion, the optimal selection of a covariant in terms of choosing a time window is a maximum of the 10 seconds RMS time series.

An analysis of the selection of the covariant was also made due to the criterion of the percentage of statistically significant models depending on the sample size. The relationships between the covariant are presented in the graphs Fig 2–Fig 6.

In the selection of the covariant that gives the largest percentage of significant models depending on the time window length, the worst case is the covariant which is the minimum RMS value from the time window of the given length. From the graphs it can be seen that the larger the window size, the percentage of significant models is getting smaller just for the minimum with RMS, while the percentage of significant models does not differ significantly for other covariant.

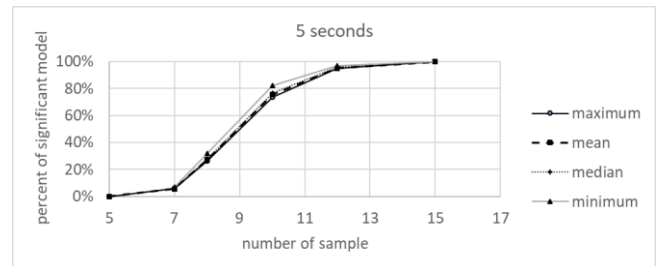


Fig. 2. Percentage of relevant models depending on the sample size for a 5-second time period

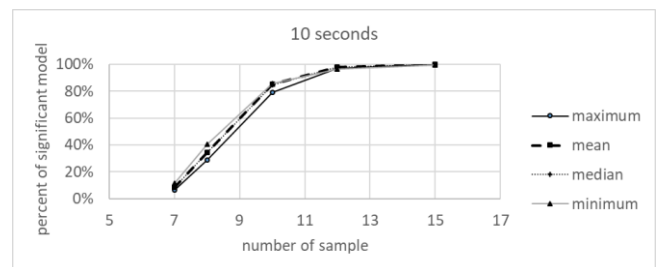


Fig. 3. Percentage of relevant models depending on the sample size for a 10-second time period

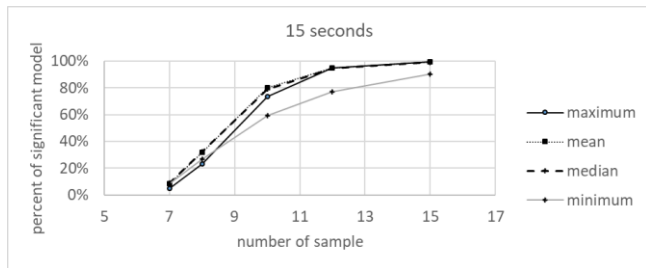


Fig. 4. Percentage of relevant models depending on the sample size for a 15-second time period

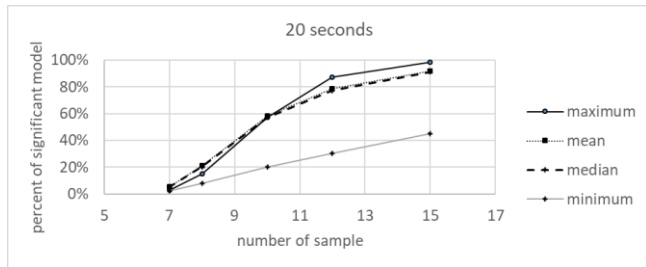


Fig. 5. Percentage of relevant models depending on the sample size for a 20-second time period

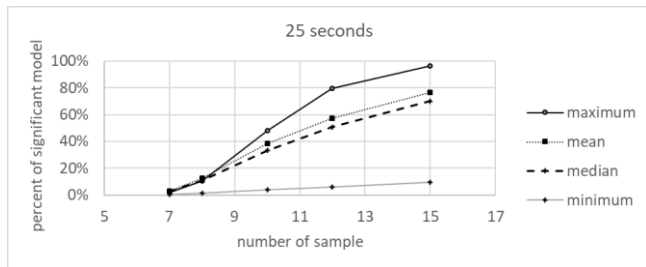


Fig. 6. Percentage of relevant models depending on the sample size for a 25-second time period

The quality of model fit depending on the covariant form was also analysed by examining the sum of standard parameter errors for the covariant. The results are shown in Fig. 7 to Fig 11.

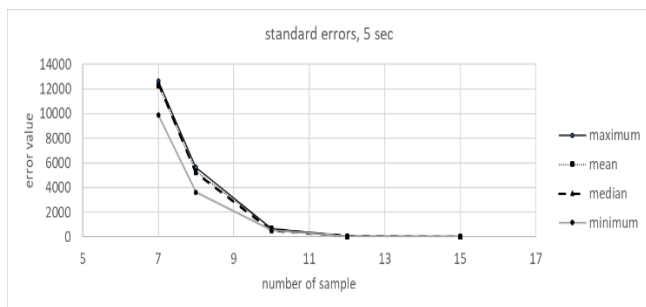


Fig. 7. Graph of the sum of standard errors of the parameter at the covariance in the Cox model depending on the sample size at the set time window length $d = 5$ sec

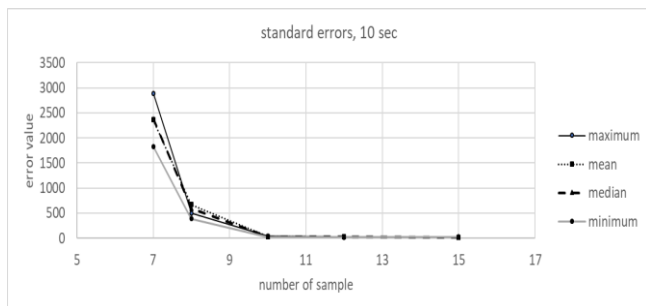


Fig. 8. Graph of the sum of standard errors of the parameter at the covariance in the Cox model depending on the sample size at the set time window length $d = 10$ sec

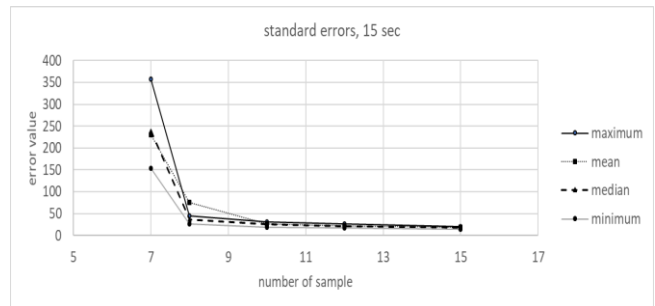


Fig. 9. Graph of the sum of standard errors of the parameter at the covariance in the Cox model depending on the sample size at the set time window length $d=15$ sec

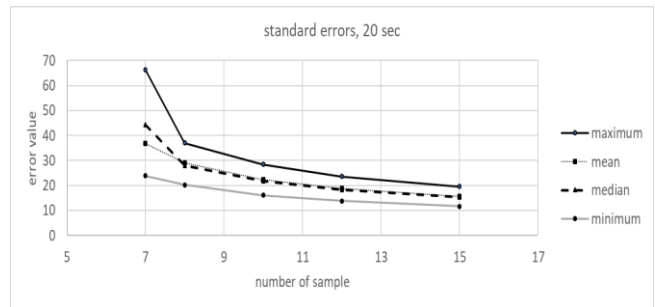


Fig. 10. Graph of the sum of standard errors of the parameter at the covariance in the Cox model depending on the sample size at the set time window length $d=20$ sec

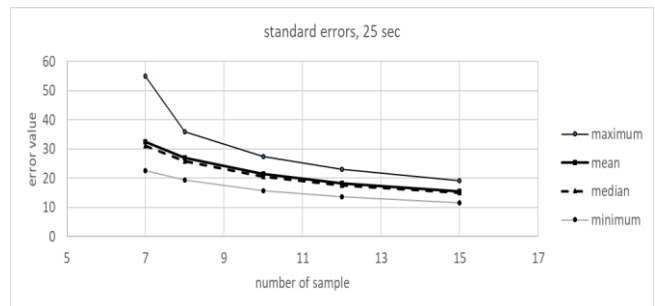


Fig. 11. Graph of the sum of standard errors of the parameter at the covariance in the Cox model depending on the sample size at the set time window length $d=25$ sec

It can be seen from the graphs that the maximum RMS in a given time window generates the largest estimation errors. The smallest generates the minimum. The median and average generate error values between the maximum and minimum values.

3. Conclusion

The article presents the problem of choosing covariates in the Cox model and data reduction in order to optimise the quality of the obtained models. Data collected from measuring sensors for prediction in the production process control system. The presented technology was based on intelligent measuring sensors from an experiment consisting in introducing a defect in the mechanical shaft alignment system. Based on the received data, damage simulations were performed. Based on the generated time series data, the impact of the length of the data reduction time window on the quality of the model was examined. The maximum percentage of significant models can be observed depending on the time window length. For models where we care about the smallest estimation error, the most appropriate covariate will be the minimum RMS in the time interval. For 15-element samples, 99.9 percent of the models appear significant. For 5-element samples, no model turned out to be significant. For 7-element samples, significant models are beginning to appear, but this is only a few percent of all models. For models in which we are interested in maximizing the percentage of significant models, the best covariate will be the maximum RMS in the time window.

References

- [1] Bergweiler S.: Intelligent Manufacturing based on Self-Monitoring Cyber-Physical Systems. UBICOMM 2015 The Ninth International Conference on Mobile Ubiquitous Computing, Systems, Services and Technologies, 2015.
- [2] Chen B., Abascal J., Soleimani M.: Electrical Resistance Tomography for Visualization of Moving Objects Using a Spatiotemporal Total Variation Regularization Algorithm. *Sensors* 18(2018), 1704.
- [3] Cox D., Snell E.: A general definition of residuals. *Journal of the Royal Statistical Society Series B (Methodological)* 30(1968), 248–275.
- [4] Deszyńska A.: Modele hazardów proporcjonalnych Coxa. *Matematyka stosowana* 13(54)/2011.
- [5] Dušek J., Hladký D., Mikulka J.: Electrical Impedance Tomography Methods and Algorithms Processed with a GPU. *PIERS Proceedings* 2017, 1710–1714.
- [6] Goetzke-Pala A., Hoła A., Sadowski L.: A non-destructive method of the evaluation of the moisture in saline brick walls using artificial neural networks. *Archives of Civil and Mechanical Engineering* 18(4)/2018, 1729–1742.
- [7] Grudzien K., Romanowski A., Chaniecki Z., Niedostatkiwicz M., Sankowski D.: Description of the silo flow and bulk solid pulsation detection using ECT. *Flow Measurement and Instrumentation* 21(3)/2010, 198–206.
- [8] Kozłowski E., Mazurkiewicz D., Kowalska B., et al.: Binary Linear Programming as a Decision-Making Aid for Water Intake Operators. 1st International Conference on Intelligent Systems in Production Engineering and Maintenance (ISPEM), Wrocław 2017.
- [9] Korzeniewska E., Walczak M., Rymaszewski J.: Elements of Elastic Electronics Created on Textile Substrate. *Proceedings of the 24th International Conference Mixed Design of Integrated Circuits and Systems – MIXDES 2017*, 2017, 447–454.
- [10] Kowalska A., Banasiak R., Romanowski A., Sankowski D.: Article 3D-Printed Multilayer Sensor Structure for Electrical Capacitance Tomography. *Sensors* 19/2019, 3416.
- [11] Kryszyn J., Smolik W.: Toolbox for 3d modelling and image reconstruction in electrical capacitance tomography. *Informatyka, Automatyka, Pomiary w Gospodarce i Ochronie Środowiska – IAPGOŚ* 7(1)/2017, 137–145.
- [12] Kozłowski E., Mazurkiewicz D., Żabiński T., Prucnal S., Sęp J.: Assessment model of cutting tool condition for real-time supervision system. *Eksploatacja i Niezawodność – Maintenance and Reliability* 21(4)/2019, 679–685.
- [13] Monostori L. Cyber-physical production systems: Roots, expectations and R&D challenges. *Procedia CIRP* 17, 2014, 9–13.
- [14] Mosorov V., Grudzien K., Sankowski D.: Flow velocity measurement methods using electrical capacitance tomography. *Informatyka, Automatyka, Pomiary w Gospodarce i Ochronie Środowiska – IAPGOŚ*, 7(1)/2017, 30–36.
- [15] Qian F., Xu G., Zhang L., Dong H.: Design of Hybrid NC Control System for Automatic Line. *International Journal of Hybrid Information Technology* 8(4)/2015, 185–192.
- [16] Repta D., Sacala I., Moisesescu M., Stanescu A.: Towards the development of a Cyber-Intelligent Enterprise System Architecture. 19th World Congress The International Federation of Automatic Control, Cape Town 2014.
- [17] Rymarczyk T., Przysucha, B.: Intelligent sensor platform for multi-source data analysis for monitoring and control of technological systems. *Applications of Electromagnetics in Modern Engineering and Medicine, PTZE 2019*, 171–175.
- [18] Rymarczyk T., Filipowicz S.F., Sikora J.: Level Set Method for Inverse Problem Solution In Electrical Impedance Tomography. *Journal Proceedings of the XII International Conference on Electrical Bioimpedance & V Electrical Impedance Tomography*, 2004, 519–522.
- [19] Rymarczyk T., Klosowski G.: Innovative methods of neural reconstruction for tomographic images in maintenance of tank industrial reactors. *Eksploatacja i Niezawodność – Maintenance and Reliability* 21(2)/2019, 261–267.
- [20] Rymarczyk T., Kozłowski E., Klosowski G., Niderla K.: Logistic Regression for Machine Learning in Process Tomography. *Sensors* 19/2019, 3400.
- [21] Rymarczyk T.: Characterization of the shape of unknown objects by inverse numerical methods. *Przegląd Elektrotechniczny* 88(7b)/2012, 138–140.
- [22] Rymarczyk T., Adamkiewicz P., Polakowski K., Sikora J.: Effective ultrasound and radio tomography imaging algorithm for two-dimensional problems. *Przegląd Elektrotechniczny* 94(6)/2018, 62–69.
- [23] Rymarczyk T., Szumowski K., Adamkiewicz P., Tchórzewski P., Sikora J.: Moisture Wall Inspection Using Electrical Tomography Measurements. *Przegląd Elektrotechniczny* 94/2018, 97–100.
- [24] Schoenfeld D.: Partial residuals for the proportional hazards regression model. *Biometrika* 69/1980, 239–241.
- [25] Xue Y., Schifano E. D.: Diagnostic for Cox model. *Communications for statistical Applications and Methods* 24(6)/2017, 583–604.

Ph.D. Eng. Tomasz Rymarczyk

e-mail: tomasz@rymarczyk.com

He is the director in Research and Development Centre in Netrix S.A. and the director of the Institute of Computer Science and Innovative Technologies in the University of Economics and Innovation, Lublin, Poland. He worked in many companies and institutes developing innovative projects and managing teams of employees. His research area focuses on the application of non-invasive imaging techniques, electrical tomography, image reconstruction, numerical modelling, image processing and analysis, process tomography, software engineering, knowledge engineering, artificial intelligence and computer measurement systems.

ORCID ID: 0000-0002-3524-9151

Ph.D. Przysucha Bartosz

e-mail: b.przysucha@pollub.pl

He is a doctor of mechanics AGH University of Science and Technology, and master of mathematic – Maria Curie-Skłodowska University in Lublin. He is a head of the Department of Quantitative Methods in Management in Lublin University of Technology. His research area focuses on acoustic, uncertainty measurement, statistical modelling and machine learning.

ORCID ID: 0000-0002-1117-8088

Ph.D. Eng. Marcin Kowalski

e-mail: marcin.kowalski@wsei.lublin.pl

He is the researcher in the Institute of Computer Science and Innovative Technologies in the University of Economics and Innovation, Lublin, Poland. He also works in IT department in a company of an energy sector. His research area focuses on the data bases, data analysis and methods of an optimisation of the SQL and PL/SQL code. He graduated in Electrotechnics at Technical University in Lublin. He has been post graduated in Data Bases and Data Analysis in Business.

ORCID ID: 0000-0002-1644-0612

Ph.D. Eng. Piotr Bednarczuk

e-mail: Piotr.Bednarczuk@wsei.lublin.pl

He is a doctor in the Institute of Computer Science at the University of Economics and Innovation in Lublin. He supports his scientific knowledge with professional practice gained in one of the leading IT companies, where he has been working for over 15 years, currently as the head of the database solutions department in the mobile systems department. His research area focuses on the software engineering web base systems, mobile-device systems and databases and data warehouses.

ORCID ID: 0000-0003-1933-7183

otrzymano/received: 30.10.2019

przyjęto do druku/accepted: 06.12.2019



MEASUREMENT OF TWO-PHASE GAS-LIQUID FLOW USING STANDARD AND SLOTTED ORIFICE

Barbara Tomaszewska-Wach¹, Mariusz Rząsa¹, Marcin Majer²

¹Opole University of Technology, Department of Thermal Engineering and Industrial Facilities, Opole, Poland, ²Opole University of Technology, Department of Parallel Systems and Artificial Intelligence, Opole, Poland

Abstract: The differential pressure of gas measurement is very often used in industrial measurements. During the gas flow, liquid condensation often occurs. The result is that when measuring a gas flow, the gas-liquid mixture is essentially measured. Errors in the indications of measuring instruments are starting to appear due to a change in the properties of the continuous phase, which is gas. In addition, the appearance of liquid droplets leads to flow disturbances and pressure pulsations. Therefore, new methods and tools for measuring the flow of gas-liquid mixture are being sought. The work involves the use of slotted orifices for measuring gas-liquid mixtures. An analysis of the influence of the slotted orifice geometry on the measurement of the biphasic mixture stream was carried out. Standard orifice and three slotted orifices of various designs. The experiment included measuring the air flow with a small amount of water dispersed in the form of drops.

Keywords: standard orifice, slotted orifice, mixture gas-liquid

POMIAR STRUMIENIA MIESZANINY GAZ-CIECZ Z WYKORZYSTANIEM KRYZY STANDARDOWEJ I KRYZY SZCZELINOWEJ

Streszczenie. Pomiar gazu metodą zwężkową jest bardzo często stosowany w pomiarach przemysłowych. Podczas przepływu gazu bardzo często dochodzi do wykroplenia się cieczy. Powoduje to, że mierząc przepływ gazu w zasadzie mierzy się mieszaninę gaz – ciecz. Zaczynają pojawiać się błędy wskazań przyrządów pomiarowych wynikających ze zmiany właściwości fazy ciągłej, którą jest gaz. Dodatkowo pojawienie się kropelek cieczy prowadzi do powstawania zaburzeń przepływu i pulsacji ciśnienia. W związku z tym poszukuje się nowych metod i narzędzi do pomiaru przepływu mieszaniny gaz-ciecz. Praca obejmuje zastosowanie kryz szczelinowych do pomiaru mieszanin gaz-ciecz. Przeprowadzono analizę wpływu geometrii kryzy szczelinowej na pomiar strumienia mieszaniny dwufazowej. Badaniom kryzę standardową oraz trzy kryzy szczelinowe o różnych konstrukcjach. Eksperyment obejmował pomiar przepływu powietrza z niewielką ilością wody rozproszonej w postaci kropelek.

Słowa kluczowe: kryza standardowa, kryza szczelinowa, mieszanina gaz-ciecz

Introduction

Orifice meters are employed in flow measurements in many branches of industry. When a particular industrial application involves the transport of gas, we often have to do with the conditions when liquids carried with gas are condensed inside a tube. The existence of small liquid droplets leads to the measurement errors resulting from variable physical properties of the flow in the conditions when measurements are performed using orifice meters. Such phenomena occur as a consequence of the loss of the homogeneity of the gas phase flow. In such cases, gas takes the form of a two-phase mixture comprising gas and liquid phases. As a result of using standard methods in the measurements of homogeneous fluids, significant levels of measurement error are encountered. For these reasons, some of the currently challenging problems facing flow metrology are associated with the measurements of two-phase mixtures. The measurements concerned with mass flow rates of gas-liquid mixtures play an important role in many branches of engineering, for example power sector as well as applications in petrochemical and chemical areas [4]. This stems from fact that the occurrence of a dispersed phase results in the variations of the physical parameters of the continuous phase [5].

The approach to measurements outlined above can also be applied in the areas where natural gas is saturated with liquid. Wet gas provides a common example of such flow, i.e. gas in which the liquid phase does not exceed 5% of the volume fraction [7]. As a result of the economic feasibility of extracting gas from various inaccessible sources, such as mining in sea beds, desert and arctic areas, as well as other remote places, there is a need to develop reliable, small size and low cost metering systems [7, 8]. Another area in which the principle of differential measurement can be employed, includes waste composting [2], where the flows of wet gas occurs. Research has been conducted over the past years in many research centers and scientific institutions with the purpose of improving existing techniques and developing new ones to be applied in the metering of two-phase mixture flows. It is common for such measurements to employ equipment with large dimensions, complex structure and high cost of performance. Therefore, a current challenge facing engineering is associated with the need to design metering equipment with a simple design

that can be built and assembled at a low cost. Differential pressure meters provide some of the examples of cheap flow measurement solutions with high performance. AS a result of their simple design, low cost of production, they are suitable for applications in industry. Recent reports include a variety of examples giving the applications of orifice plate meters in the measurement involving mixtures comprising gas and small amounts of liquids [6, 14].

1. Measurements of flow mixture by differential pressure flowmeters

The measurements of the fluid flow rates by application differential pressure flowmeter consist in the use of a constriction of the flow cross-section. This constriction leads to an increase in the fluid velocity, and along with the change in the velocity, the static pressure decreases and a differential pressure is developed at the orifice. The resulting differential pressure ΔP forms a reliable source serving for determination of the fluid mass or volume [5]. Among the orifices meters, we can distinguish: orifice plates, nozzles and Venturi tubes [10]. In this work, various types of orifice meters were applied in experimental research.

1.1. Standard orifice

A vast proportion of metering systems apply standard orifices as the simplest and reliable equipment for measuring fluid flow. The standard orifice is also characterized by considerable strength and lack of moving parts. The standard orifice can be successfully applied in measurements involving liquids, gas and suspensions, as they perform measurements well in extreme operating conditions, over a wide range of pressures and temperatures [5].

Differential pressure flowmeters are designed for measuring single-phase fluids, ensuring high measurement accuracy. However, when these types of flow meters are used in wet gas applications, due to the presence of liquids in the flow, the results tend to have a positive bias in the flow measurement. The presence of liquid droplets in the flowing gas results in an increase in the differential pressure Δp [7, 8, 14]. Therefore, we can state a general remark that differential pressure flowmeters indicate an overestimated value of the gas mass flow. The uncorrected gas stream is often called the superficial gas flow.

1.2. Special orifice

The differential pressure flowmeter may be used to measure the gas – liquid droplet flow, however it is necessary to use the appropriate measuring orifice construction. Over the years, many researchers, including Hall, Geng, Morrison, and Kumar, have presented various design solutions that are a modification of the standard orifice, Fig. 1. Such orifices are called special orifices, and you can distinguish, among others, slotted, perforated or other [1, 3, 7–9, 11, 12]. In the literature, you can also find orifices with various hole shapes, e.g. square, triangular, oval, longitudinal.

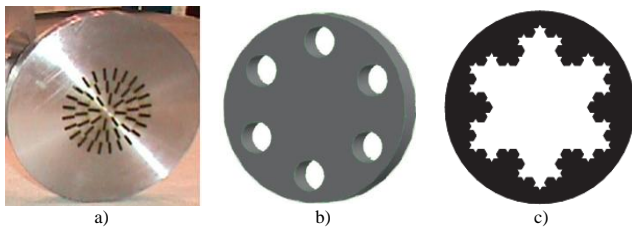


Fig. 1. Examples of special orifices: a) slotted orifice [7, 8], b) perforated orifice [3, 9], c) fractal orifice [1]

The reason for wet gas formation is often associated with a decrease in temperature or pressure, and when condensation processes are encountered in the pipeline, this leads to accumulation of small amounts of liquid in the form of droplets that are condensed on the pipeline walls. And it is known that even small amounts of liquid in the flow of gas can lead to flow disturbance.

The Lockhart-Martinelli parameter forms one of the most commonly applied characteristic that can be used to define the relative fraction of liquid in a two-phase flow. It is defined by the formula [6–8]:

$$X_{LM} = \frac{m_L}{m_G} \sqrt{\frac{\rho_G}{\rho_L}} \quad (1)$$

where: m_L and m_G are mass flow rates of the liquid and gas phases, respectively, and ρ_L , ρ_G are the liquid and gas densities. For the wet gas, the value of the X_{LM} parameter does not exceed 0.35.

2. Experimental setup

The diagram of the setup applied in the testing the flow of gas-liquid mixture is presented in Figure 2. The purpose of the tests was to determine the effect of the slotted orifice geometry on the resulting pressure difference measured for the flow of the gas-liquid mixture.

The air into this installation was fed via a compressor. The air was routed for the experiment via a throttling valve, which provided a constant pressure value of 0.5 bar. The flow rate of the air was regulated by a valve. The parameters of the air flow were controlled by a measuring system comprising a pressure sensor and a temperature sensor and an orifice plate. Water was supplied from the water network to a chamber in which the two-phase mixture was formed, and the flow rate was regulated by a valve. The flow rate of the water was measured by a rotameter (VEB MLW Prüfgeräte – Werk) and its measuring range was equal to 0.2–0.6 m³/h). The horizontal section of the pipeline comprised a system designed for testing slotted orifice plates that could be removed and replaced. The differential pressure resulting from the installation of the slotted orifice plates was measured with a differential pressure transducer (Aplisens typ PR-50G) and the measuring range was -10 kPa–10 kPa. The static pressure value in the pipeline was measured with a sensor (TRUCK typ PC001-Gi1/4A1M-U8X-H114), measuring range 0–1 bar. A separator was applied to remove the air from the liquid at the end of the measuring section in the installation. The values of signals from the measurement sensors were recorded continuously by a dedicated card on a PC throughout the duration of the experiment.

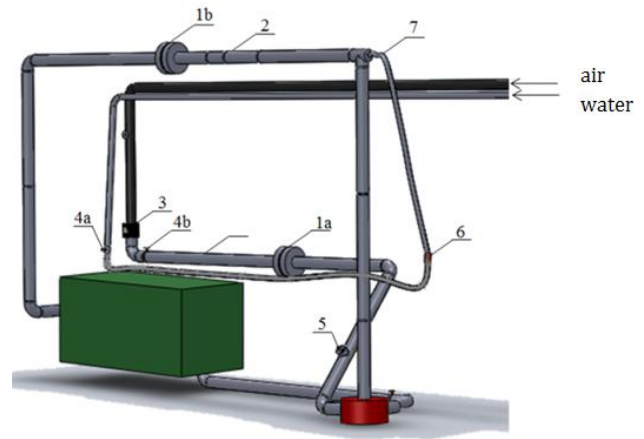


Fig. 2. Diagram of the experimental setup: 1a, 1b – differential pressure meter, 2 – pressure sensor, 3 – reducing valve, 4a – liquid flow regulating valve, 4b – air flow regulating valve, 5 – temperature sensor, 6 – rotameter, 7 – water spray nozzle, a – air, w – water

The measurements were carried out for two mass flow rates of air, which were equal to 216 kg/h and 313 kg/h, respectively. After the gas flow was stabilized, water was fed into the installation in the range of flow rates from 216 kg/h to 576 kg/h.

In experimental research, the orifices were used: standard and three variants of slotted orifices. Diagrams of the orifices used in the experimental studies are shown in the figure 3.

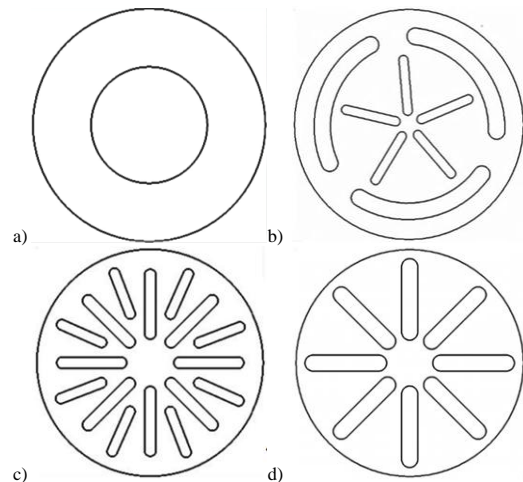


Fig. 3. Orifice plates applied in the experimental research: a) standard orifice, b) slotted orifice 1, c) slotted orifice 2, c) slotted orifice 3

Slotted orifices were designed by the authors of this work. The design of the slots in the slotted orifice is selected in such a way that the mass flow rate can pass through the entire diameter of the pipeline. The slots in slotted orifice 2 and 3 are arranged radially, with the only difference that the geometry of the slots is such that in comparison to orifice no. 2, the slots in orifice no. 3 are wider and longer. The purpose of this geometry was to check which design can offer better flow characteristics. In addition to the slots with radial arrangement, slotted orifice no. 1 has three arc-shaped slots, which are arranged concentrically close to the wall of the pipeline. The dimensions of the slots in the slotted orifices were chosen so that the surface area of these slots was equal to the area of the orifice hole. The orifice ratio of all orifices was the same and was $\beta = 0.5$.

The β ratio is determined by the formula:

$$\beta = \sqrt{\frac{A_{slots}}{A_{pipe}}} \quad (2)$$

where: A_{slots} – surface area of the slots, A_{pipe} – cross-sectional area of the pipe.

3. Results of experimental research

Figure 4 contains the results of the measurements of the differential pressure as a function of the mass fraction of liquid in the constant gas flow rates, for 216 kg/h and 313 kg/h, respectively. The values in terms of the mass fraction of the liquid were determined on the basis of the measurements of gas and liquid flows by application of the following relations:

$$\alpha = \frac{m_L}{m_L + m_G} \quad (3)$$

where: m_L and m_G are mass flow rates of the liquid and gas, respectively.

The analysis of the results in Figure 4 demonstrates that the distortions in differential pressure in the orifice due to the presence of the liquid phase in the constant air flow. The value of differential pressure in this case is due to greater fraction of the liquid in the air flow. The distribution of the differential pressure is non-linear. We can note that for the case of slotted orifice, lower values of differential pressure are generated by the mixture comprising air and water compared to the standard orifice. The study demonstrated that slotted orifice with a radial of slot arrangement has the lowest sensitivity to fluctuations in the mass fractions of the liquids.

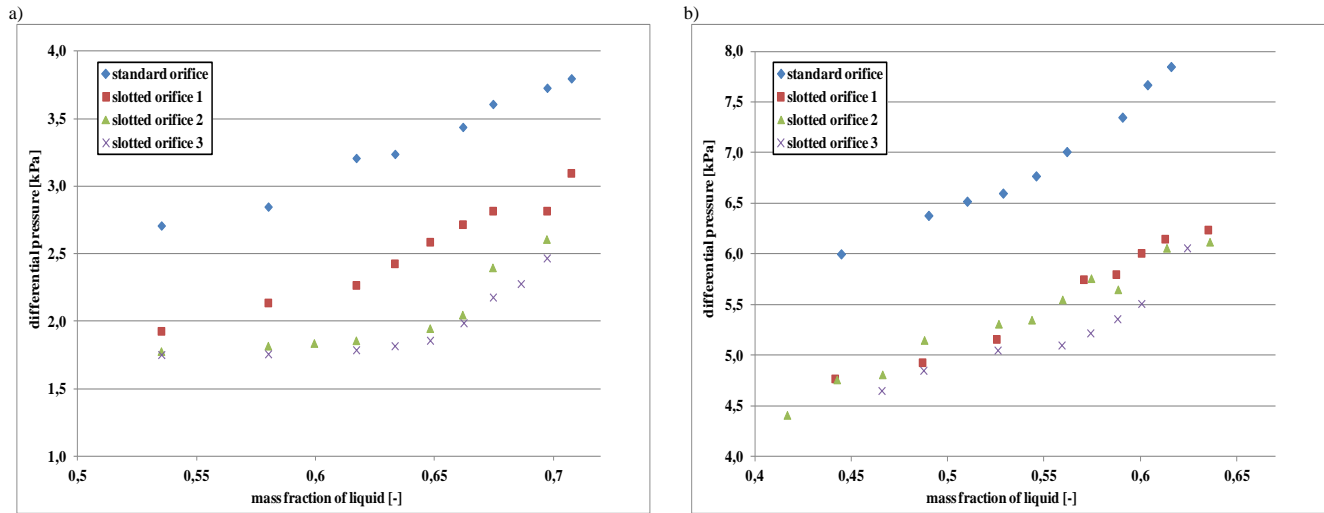


Fig. 4. Dependence between the differential pressures and water mass fraction for the airflow rates equal to: a) 216 kg/h, b) 313 kg/h

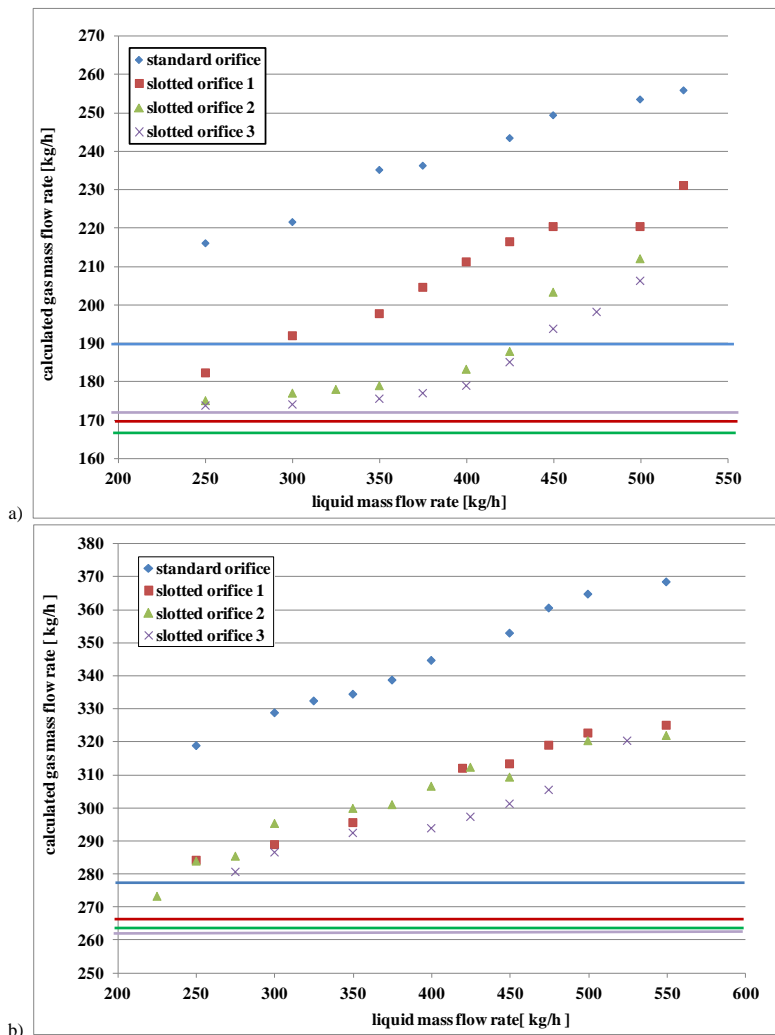


Fig. 5. Dependence between the calculated gas mass flow rate and liquid mass fraction for the airflow rates equal to: a) 216 kg/h, b) 313 kg/h

In such conditions, gas containing liquid droplets is carried over through the obstacle, and only a small proportion of the liquid is separated near the orifice. The slots arranged on the cross-section of the pipe result in the entrainment of the liquid along with the gas flow. In a standard orifice, some of the liquid is held up downstream of the orifice, leading to liquid accumulation and additional flow distortions.

The chart in Fig. 5 contains the results of the comparison of the mass flow rate of the gas taking into account the differential pressure during wet gas flow and flow of pure gas.

The results of a comparison between the mass flow rates of gas and one for water that was measured in the investigated orifices plates are presented in a graphical form in Fig. 5. The formula derived from the norm (ISO 5167) formed the basis for the calculation of the mass flow rate of the gas phase to account for the differential pressure that accompanies the gas-liquid flow. The horizontal lines on the diagrams denote the mass flow rates for the case of single-phase gas flow. The blue line marks the mass flow rate of gas for the standard orifice, red refers to the slotted orifice 1, whereas the green and violet ones relate to the gas mass flow rate measured for the slotted orifices 2 and 3, respectively. We can note that in the chart above marked by a, the green and violet lines follow the same course.

We can remark here that the increase in the flow rate of water leads to the greater value of the error of the measured gas flow rate. As a result of the application of the standard orifice in the flow of gas-small amount of liquid, the measurements of the flow rate of gas that account for the gas-liquid differential pressure give 18–32% greater values in comparison to the case of the single-gas flow through the pipeline. For the slotted orifices numbered 1, 2, 3, the range of this error is 11–30%, 10–25% and 5–23% respectively.

4. Conclusions

The results of the research reported in this paper demonstrate that the surface profiles and the geometric details of the perforations on slotted orifices have an effect on the length of the region needed for the flow to stabilize and affect the value of permanent pressure drop. The process responsible for this is associated with the separation of the mixture into several smaller fluxes. In the case when flow metering applies a slotted orifice, recirculation zone is not normally developed. The use of the common standard orifice forms the reason for the occurrence of flow distortions leading to the generation of energy losses. However, the length of the hydraulic stabilization region in the flow is dependent to a large extent on the design of the slotted orifices and its value takes on smaller value compared to the case of a standard orifice. Moreover, the results of the study have demonstrated that the existence of perforations on the surface of the slotted orifice meters has a positive effect on homogenization of the flow and decrease of pressure pulsations, which form the major sources of the measurement error. Nevertheless, a disadvantage of slotted orifices is associated with the decrease of the differential pressure, leading to a limited sensitivity of flow measurements. This area needs further analysis associated with an attempt to strike a balance between the above advantages and disadvantages of the use of various slotted orifice designs in particular engineering applications. In this aspect, studies need to be concerned with the determination of the suitable arrangement of slots suitable in specific applications.

References

- [1] Abou El-Azm Aly A., Chong A., Nicolleau F., Beck S.: Experimental study of pressure drop after fractal-shaped orifice in turbulent pipe flow. *Experimental Thermal and Fluid Science* 34, 2010, 104–111.
- [2] Anders D., Rząsa M. R.: The possibility of composting animal waste products. *Environment Protection Engineering* 33(2), 2007, 7–15.
- [3] Bayazit Y., Sparrow M., Joseph D.: Perforated plates for liquid management: Plate geometry effects and flow regime. *International Journal of Thermal Sciences* 85, 2014, 101–111.
- [4] Bertani C., De Salve M., Malandrone M., Monni G., Panella B.: State-of-Art and selection of techniques in multiphase flow measurement. Report RdS/2010/67, Torino 2010.
- [5] Falcone G., Hewitt G., Alimonti C.: *Multiphase Flow Metering: Principles and Applications (Developments in Petroleum Science 54)*. Elsevier Science, 2009.
- [6] Fang L., Zhang T., Jin N.: A comparison of correlations used for Venturi wet gas metering in oil and gas industry. *Journal of Petroleum Science and Engineering* 57, 2007, 247–256.
- [7] Geng Y., Zheng J., Shi T.: Study on the metering characteristics of a slotted orifice for wet gas flow. *Flow Measurement and Instrumentation* 17, 2006, 123–128.
- [8] Hua C., Geng Y.: Wet gas metering technique based on slotted orifice and swirlmeter. *Flow Measurement and Instrumentation* 30, 2013, 138–143.
- [9] Huang S., Ma T., Wang D., Lin Z.: Study on discharge coefficient of perforated orifices as a new kind of flowmeter. *Experimental Thermal and Fluid Science* 46, 2013, 74–83.
- [10] ISO/TR 15377:2007: Measurement of fluid flow by means of pressure-differential devices- Guidelines for the specification of orifice plates, nozzles and Venturi tubes beyond the scope of ISO 5167, 2007.
- [11] Morrison G. L., Hall K. R., Holste J. C., DeOtte R. E., Macek M. L., Ihfe L. M.: Slotted Orifice Flowmeter. *AIChE Journal* 40(10), 1994, 1757–1760.
- [12] Morrison G. L., Hall K. R., Holste J. C., Macek M. L., Ihfe L. M., De Otte R. E., Terracina D.: Comparison of orifice and slotted plate flowmeters. *Flow measurement and Instrumentation* 5(2), 1994, 71–77.
- [13] Morrison G. L., Terracina D., Brewer C., Hall K.R.: Response of a slotted orifice flow meter to an air/water mixture. *Flow Measurement and Instrumentation* 12, 2001, 175–180.
- [14] Steven R., Hall A.: Orifice plate meter wet gas flow performance. *Flow Measurement and Instrumentation* 20, 2009, 141–151.

M.Sc. Eng. Barbara Tomaszewska-Wach
e-mail: b.tomaszewska@po.edu.pl

Assistant in the Department of Thermal Technology and Industrial Equipment at the Faculty of Mechanical Engineering of the Opole University of Technology. In scientific work I deal with research on the flow of single-phase and two-phase fluid through orifices of various geometric shapes. Areas of interest are issues related to experimental and numerical fluid mechanics.

ORCID ID: 0000-0002-9796-1013

Ph.D., Eng. Mariusz R. Rząsa
e-mail: m.rzasa@po.opole.pl

Graduated from the Faculty of Electrical Engineering, Automatic Control and Informatics at Opole University of Technology, specializing in automation and electrical metrology. Employed in the Department of Thermal Engineering and Industrial Facilities at Opole University of Technology. Received a Ph.D. degree with the specialization in the Construction and Operation of Machines. Habilitation obtained at the Faculty of Mechanical Engineering and Computer Science, Częstochowa University of Technology. Scientific work in the field of two-phase flow measurement

ORCID ID: 0000-0002-3461-2131

M.Sc. Eng. Marcin Majer
e-mail: m.majer@po.edu.pl

Faculty of Electrical Engineering, Automatic Control and Informatics Institute of Computer Science Scientific interests focused around broadly defined computer science and automation related to algorithmics, parallel programming, optimization, and the use of computer clusters.

ORCID ID: 0000-0003-1411-209X

otrzymano/received: 27.08.2019

przyjęto do druku/accepted: 06.12.2019



DETERMINATION OF YOUNG'S DYNAMIC MODULUS OF POLYMER MATERIALS BY RESONANCE VIBRATING-REED METHOD

Volodymyr Mashchenko¹, Valentine Krivtsov², Volodymyr Kvasnikov³, Volodymyr Drevetskiy⁴

¹Odessa State Academy of Technical Regulation and Quality, Department of Metrology and Metrological Support, Odessa, Ukraine, ²Rivne State Humanitarian University, Department of Physics, Rivne, Ukraine, ³National Aviation University, Department of Computerized Electrical Systems and Technologies, Kiev, Ukraine, ⁴National University of Water and Environmental Engineering, Department of Automation, Electrotechnical and Computer-integrated Technologies, Rivne, Ukraine

Abstract. The paper deals with its own oscillations of a rectangular rod with a cross section of a rectangular shape. The method of determining real part of Young's dynamic modulus and tangent of mechanical loss of samples in the form of rods of a number of polymer materials by means of resonant vibrating-reed method are proposed. Experimental setup, algorithm and software for determining the amplitude of the sample oscillations are developed. The accuracy of measurements was determined and a comparative analysis of results was performed with data obtained by other methods.

Keywords: oscillation amplitude, frequency measurements, acoustic and viscoelastic properties

OKREŚLENIE DYNAMICZNEGO MODUŁU YOUNGA MATERIAŁÓW POLIMEROWYCH ZA POMOCĄ REZONANSOWEJ METODY WIBRACYJNEJ

Streszczenie. W pracy opisano wahań własne prostokątnego sworznia o przekroju prostokątnym. Zaproponowano metodę wyznaczenia za pomocą metody rezonansowej wibracyjnej rzeczywistej części dynamicznego modułu Younga i tangensa kąta mechanicznych strat wzorców w postaci sworzniów z szeregu materiałów polimerowych. Opracowano eksperyment, algorytm i oprogramowanie dla określenia amplitudy wahań wzorca. Określono precyzję pomiarów i przeprowadzono porównawczą analizę wyników z rezultatami otrzymanymi innymi metodami pomiarów.

Słowa kluczowe: amplituda oscylacji, pomiary częstotliwości, właściwości akustyczne i lepkościowe

Introduction

Requirements for reducing the mass of structures operating in the same dynamic fields of stresses that occur during impulse loading due to polymer materials are an urgent task of modern professional equipment making. However, an important factor is to determine the physical and mechanical properties of such structural materials with high reliability of results. The elastic properties of polymer material are determined by the speeds of propagation of ultrasonic waves, the deformation properties at high deformation rates, and the relaxation characteristics at short time intervals. The experimental values of Young's modulus (E) will be fully reliable only when obtained from wave-based and quasi-static experiments corresponding to the loading time of the order of a few microseconds – time of passing of the ultrasonic pulse through a polymer material sample. The results of mechanical tests using resonance methods that correspond to time intervals in the millisecond range can be used to refine or complement each other at such relatively high time intervals. Resonance methods in different modifications are often used to define Young's modulus in PVC materials [1–3, 5, 7]. However, they do not always ensure essential accuracy or require additional theoretical calculations [8]. Therefore, new methods development or renovation of already existing ones are rather a pertinent issue.

1. Resonance method for determining dynamic modulus of elasticity and mechanical loss factor

Young's complex dynamic modulus (E^*) and tangent of mechanical losses ($tg\delta$) of a number of polymer materials, the method of forced resonant oscillations of a fixed sample was used as a rod of rectangular shape at sound frequencies [1, 2].

The essence of method is to measure oscillation amplitude (A) of free end of the rod when changing frequency of driving force applied to the other fixed end. According to $|A|$ sample measurements of transverse oscillations at different frequencies, a resonance curve is constructed, which parameters are frequency of oscillations (f) and ratio of amplitudes ($|A|/|A_{max}|$), where A_{max} is the maximum value of the amplitude corresponding to principal resonant frequency (f_r). For f_r determines the width of

resonance curve (Δf_r) at the level $\frac{|A_{max}|}{\sqrt{2}}$.

The behaviour of a sample of a polymer material (Fig. 1) during oscillations under the disturbing force is described by the following differential equation [4]:

$$\rho \frac{\partial^2 u(x,t)}{\partial t^2} + E^* \chi^2 \frac{\partial^4 u(x,t)}{\partial x^4} = 0, \quad (1)$$

where $u(x,t)$ is function of dependence of points transverse displacements of the rod axis on coordinate x and time t ; ρ is the density of polymer material.

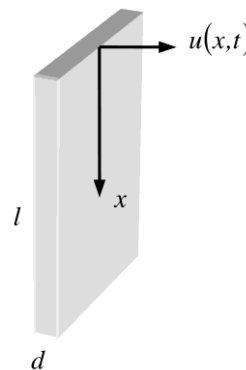


Fig. 1. Specimen and its vibrating coordinate system

The solution of equation (1) is represented as a harmonic function

$$u(x,t) = X(x)e^{i\omega t}, \quad (2)$$

then, we get

$$\frac{d^4 X(x)}{dx^4} + kX(x) = 0, \quad (3)$$

where k^* complex wave number of oscillations per bend; where ω cyclic frequency ($\omega = 2\pi f$).

The general solution of equation (3) is as follows

$$X(x) = A_1 \cos kx + A_2 \sin kx + A_3 \cosh kx + A_4 \sinh kx, \quad (4)$$

where A_i arbitrary constants.

The boundary conditions for our problem are as follows

$$\begin{aligned} X(0) &= X'(0) = 0; \\ X(l) &= X'(l) = 0, \end{aligned} \quad (5)$$

where l is the sample length.

The integral of equation (3) satisfying the conditions at the end $x = 0$ has following form:

$$X(x) = \frac{1}{2} A_3 (ch_k x - \cos_k x) + \frac{1}{2} A_4 (sh_k x - \sin_k x), \quad (6)$$

The conditions at end $x = l$ are expressed by the following equations

$$A_3 (ch_k l + \cos_k l) + A_4 (sh_k l + \sin_k l) = 0 \quad (7)$$

where

$$(ch_k^* l + \cos_k^* l)^2 - (sh_k^* l - \sin_k^* l) = 0, \quad (8)$$

or

$$ch_k^* l \cos_k^* l + 1 = 0. \quad (9)$$

Putting $k^* l = a + ib$ at resonance of the rod in conditions of $a = a_i; b = 0$, enables to obtain a ratio for the sample amplitude oscillations

$$X_i(x) = C \left(cha_x - cosa_x - \frac{(sha_x - sina_x)^2}{cha_x + cosa_x} \right), \quad (10)$$

where a_i roots of the equation (9), C some constant.

The values a and b are defined as follows

$$a \cong \frac{\omega^2 l}{\left(\frac{E \chi^2}{\rho} \right)^{\frac{1}{4}}}, \quad (11)$$

$$b \cong \frac{1}{4} \frac{\omega^2 l}{\left(\frac{E \chi^2}{\rho} \right)^{\frac{1}{4}}} tg \delta, \quad (12)$$

moreover, for a rectangular rod $\chi = \frac{d}{\sqrt{12}}$, d is the thickness of the sample.

The first four roots of equation

$$kl = 1,8751; 4,6941; 7,8548; 10,9965. \quad (13)$$

In this case, at fundamental resonant frequency f_r , which corresponds to the smallest root of equation (9), we obtain following relation for E'

$$E' = \frac{48\pi^2 \rho l^4 f_r^2}{1,8751^4 d^2}. \quad (14)$$

For the value of $tg \delta$ we have

$$tg \delta = \frac{\Delta f_r}{f_r}. \quad (15)$$

Accordingly, imaginary part (E'') of complex E^* is defined as follows

$$E'' = E' tg \delta. \quad (16)$$

In this case, we can determine value of E^* in the following way:

$$E^* = \left(E'^2 + E''^2 \right)^{\frac{1}{2}}. \quad (17)$$

2. Experimental setup and measurement technique

Measurement A for the construction of resonance curves and determination of f_r was performed on installation, a block diagram which is shown in Fig. 2.

In experimental setup, a sample of polymer material 4 is placed into an air heat chamber 2 where it is rigidly fixed at one end to the thrust of mechanical oscillator 4 by means of a clamp. Thermal camera has viewing windows for optical observation

of amplitude oscillations of closed and free ends of sample. In the middle of camera a light-emitting diode backlight is placed. Mechanical oscillation of the sample is performed by field-relay, which is supplied from generator of audio frequency range 1 (Siglent SDG1010). The sample oscillation amplitude clamped end is governed by generator output voltage. In order to eliminate effects of power supply voltage fluctuations, a sound generator is connected via a ferroresonance voltage stabilizer.

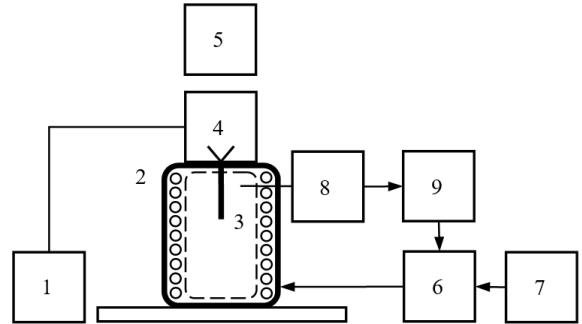


Fig. 2. Installation block diagram to study viscoelastic properties of polymer materials via resonance method

Measurement of resonance oscillations amplitude can be carried out at different temperatures of polymer sample to the glass transition temperature. Heating of camera is electric provided by auto-transformer 7 through solid-state Crydom H12D4825 6. Temperature mode in thermal chamber is supported by means of thermal sensor 8 and microprocessor controller 9 MTP-8. To determine amplitude of oscillations A special software is developed that recognizes image of the sample oscillation using webcam 5 with an optical zoom.

Using oscillator, f changes the sample oscillations in range of 10–140 Hz in 0.5 Hz increments and determine A .

2.1. Algorithm for determining sample amplitude oscillations using software

Using program interface (Fig. 3), two vertical and one horizontal lines define the sample oscillation region.

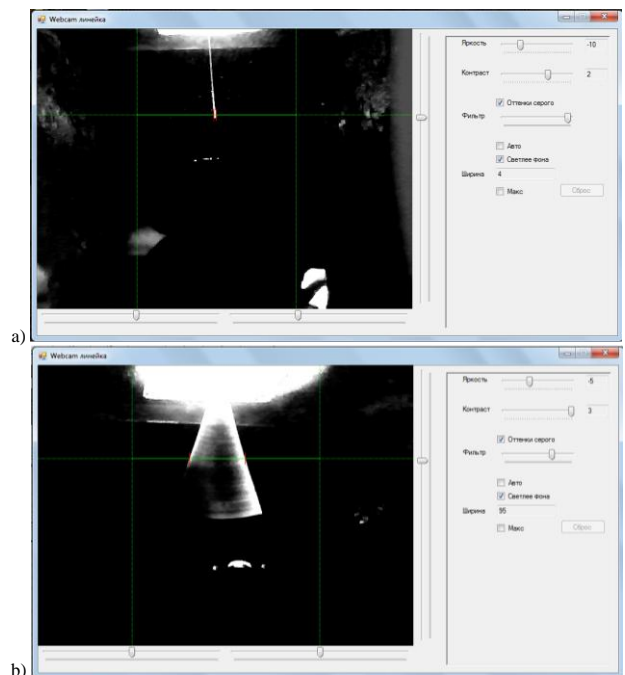


Fig. 3. Program interface used to determine sample oscillation amplitude from an image of an installation web camera to study resilient properties of polymer materials

The program that automatically determines brightness threshold as an average brightness of points on a horizontal segment. By comparing brightness of two adjacent pixels, the program independently searches limits of sample oscillations. If brightness of i pixel is lower than specified brightness threshold, and brightness of $i + 1$ pixel is higher than brightness threshold, then we obtain left limit of oscillation, conversely, if $i + 1$ pixel is darker than brightness threshold, and – lighter than this threshold, we get right limit of oscillation.

The program constantly compares determined left limit of oscillation with previously found one, selects the far left, coordinate of which is smaller relatively to vertical zero position. The obtained right boundary is also compared with the previously found boundary, and the extreme right is chosen, coordinate of which is larger relatively to vertical zero position. Magnitude of the sample oscillation will be automatically determined by the program and equal to $2A$.

An optical zoom webcam allows you to zoom in on a sample 10 times. In this case, measurement error A does not exceed 2%.

3. Results and discussion

Experimental studies were performed on polymer samples of polyvinyl chloride (PVC), polystyrene (PS), high density polyethylene (HDPE) and low density polyethylene (LDPE).

Density of polymer materials was determined by hydro-static weighing. According to the latter, ρ sample immersed in thermostatic fluid will be determined as follows

$$\rho = \frac{m}{m - m_1}(\rho_1 - \rho_2) + \rho_2 \quad (18)$$

where m, m_1 – mass of sample in air and liquid; ρ_1, ρ_2 are densities of liquid and air.

Resonance curve for PVC sample in frequency range 10–140 Hz is presented in Fig. 3. The curve has several resonance peaks in frequency range of 10–40 Hz and a maximum peak corresponding to fundamental resonance frequency in the region of 113 Hz. Fundamental resonant frequency can be changed by sample factor (l/d).

Similar resonance curves were obtained for PS, HDPE and LDPE. Density, form factor and thickness of the samples are presented in table 1. Resonance curves in the region of principal resonant frequencies for each polymer at 293 K are presented in Fig. 4. The results of measurements $f_r, \Delta f_r$ are presented in table 1.

Analysis of obtained data shows that main resonant frequencies increase in a number of LDPE, HDPE, PS, PVC and lie in the range 105–113 Hz. Accordingly, width varies from 8 Hz for LDPE to 12 for PS. For HDPE and PVC, Δf_r value is 10 Hz.

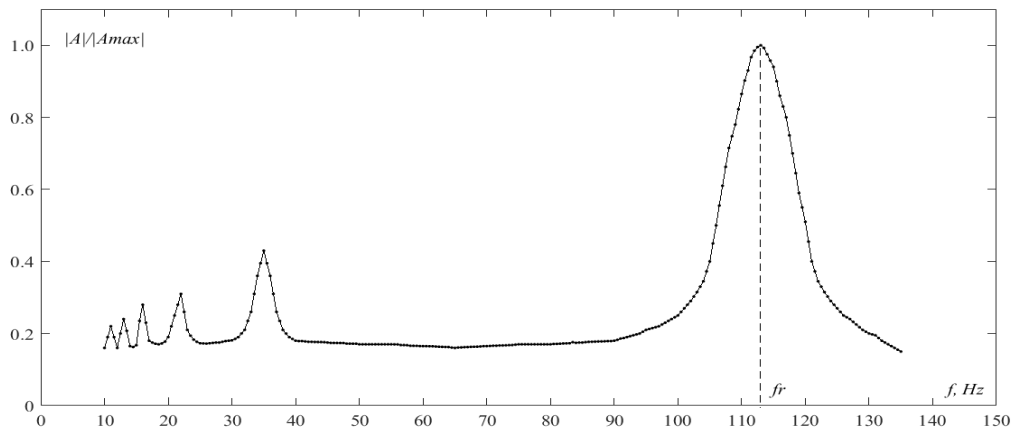


Fig. 4. Resonance curve for PVC in the frequency range 10–140 Hz

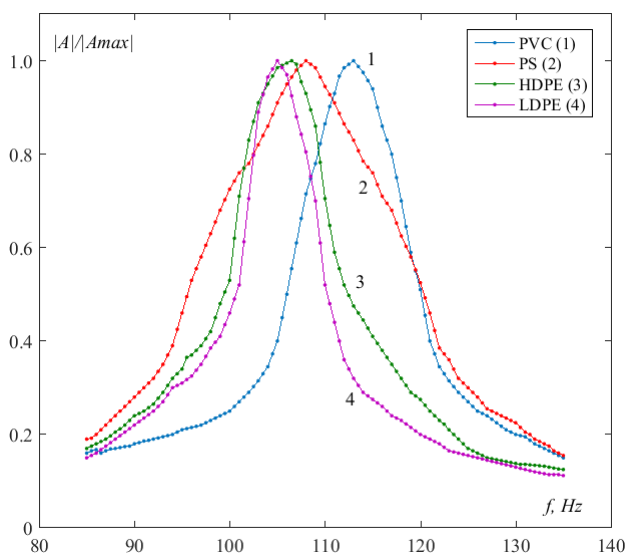


Fig. 5. Resonance curves for basic resonance frequencies for polymer samples: 1 – PVC, 2 – PS, 3 – HDPE, 4 – LDPE.

The calculations of values of E' , $tg\delta$, E'' and E^* by relations (14)–(17) are presented in table 1.

Magnitude of E' increases in a number of LDPE, HDPE, PS, PVC and lies in range $(2.24\text{--}3.56)\cdot 10^9$ N/m². The $tg\delta$ value is minimal for LDPE 0.07 and increases to 0.11 for PS. For HDPE and PVC, mechanical loss factor is 0.09. Similarly a change in value of $tg\delta$ change values of E'' . Values of Jung's E^* complex modulus of a number of polymer materials follow tendency of changing its real part of E'' .

Table 1. Measurement results

Value	Polymers			
	PVC	PS	HDPE	LDPE
$\rho, \text{kg/m}^3$	1396	1040	950	915
l/d	40.541	44.188	42.857	42.857
d, mm	0.74	0.66	0.70	0.70
f_r, Hz	113	108	106.5	105
$\Delta f_r, \text{Hz}$	10	12	10	8
$E' \cdot 10^{-9}, \text{N/m}^2$	3.55	3.04	2.40	2.24
$tg\delta$	0.09	0.11	0.09	0.07
$E'' \cdot 10^{-8}, \text{N/m}^2$	3.05	3.25	2.17	1.67
$E^* \cdot 10^{-9}, \text{N/m}^2$	3.57	3.06	2.41	2.25

Accuracy of installation is determined by an error in generator frequency settings as well as in determining density and dimensions of the sample. For the Siglent SDG1010, in frequency range 10–140 Hz the error does not exceed $10^{-5}\%$.

We estimate fractional error of E' value determination by following relation:

$$\varepsilon_{E'} = \varepsilon_{\rho} + 4 \frac{\Delta l}{l} + 2 \frac{\Delta d}{d} + 2 \frac{\Delta f}{f_r} + \varepsilon_{Const}, \quad (19)$$

where ε_{ρ} fractional error of a sample density measurement; Δl , Δd maximum instrumental errors in measuring length and thickness of specimen; Δf absolute error in determining fundamental resonant frequency; ε_{Const} relative error in determining constants in ratio (14).

The fractional error of hydrostatic weighing method is $\varepsilon_{\rho} = 0.2\%$. The Fractional error of constants ε_{Const} determination does not exceed 0.05%.

Measuring samples thickness with up to 1.5%, leads to determining fractional error of E' value.

An estimate of relative error $\varepsilon_{E'}$ by relation (19) shows that it does not exceed 1.9%.

Let us compare values of Young's modulus by determining velocity of propagation of longitudinal ultrasonic waves (ultrasonic method), mechanical methods [6, 9] and vibrating reed method (Table 2).

Table 2. Young's modulus of polymer materials are defined by different methods

Polymer	$E \cdot 10^{-9}, \text{N/m}^2$		
	Ultrasonic Method	Vibrating-reed method	Mechanical method
LDPE	4.3–4.4	2.25	0.7
HDPE	5.5–6.2	2.41	0.8
PS	5.7	3.06	3–3.5
PVC	7.4	3.57	2.4–3.1

Analysis of presented data shows that values of E for a number of polymers determined by vibrating-reed method are smaller than values obtained by the ultrasonic method. For LDPE and PS on average 1.9 times, for HDPE respectively – 2.3–2.6 times, for PVC – 2.1. In this case, values of the Young's modulus determined by the vibrating-reed method are higher than those obtained by mechanical methods for LDPE, HDPE, PVC, respectively, 3.2 and 3 times and 1.2–1.5 times, respectively. For PS, value of E coincides with lower bound and less than 0.9 times upper bound.

Ph.D. Volodymyr Mashchenko

e-mail: volodymyr_mashchenko@ukr.net

Doctoral student at the Odessa State Academy of Technical Regulation and Quality.
Main scientific direction – development of methods and instruments for measuring the physical and mechanical parameters of polymer materials.

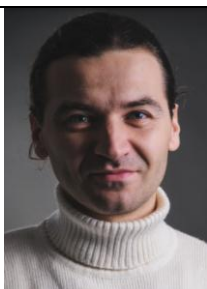


ORCID ID: 0000-0001-6968-762X

Ph.D. Valentine Krivtsov

e-mail: labor.relax@gmail.com

Associate Professor of Physics, Rivne State Humanitarian University, Department of Physics.
Main scientific direction – spectroscopy of polymer materials.



ORCID ID: 0000-0002-8338-645X

4. Conclusion

Experimental studies and comparative analysis showed that resonant vibration method has the prospects of technological application in metro-logical control bodies to create database of structural polymer materials. Usage of software to determine sample amplitude of oscillations in frequency range of measurement allows to minimize error in determining the fundamental resonant frequency. Error determination of Young's modulus of structural polymer materials is determined by measurements of sample geometric dimensions and depends on equipment instrumental error. Application of resonance vibrating method and analysis of resonance curve to control Young's modulus and mechanical loss factor at this stage is limited mainly by laboratory testing of polymer material samples. Implementation perspectives of the method are shown to investigate the influence of plastification, filling, radiation, orientation, heat treatment and other factors on viscoelastic properties of high-molecular mass compounds, and to define dependence between their static and dynamic properties.

References

- Caracciolo R., Gasparetto A., Giavagnoni M.: Application of causality check and the reduced variable method for experimental of Young's modulus of viscoelastic material. *Mechanic of materials* 33/2001, 693–703.
- Ferry J. D.: *Viscoelastic properties of polymers*. John Wiley & Sons Inc., New York/Chichester/Brisbane/Toronto/Singapore 1980.
- Gamboia F., Corona J. E., Hoy-Benitez J.A., Aviles F., Oliva A. I., Sosa V.: Simple vibrating reed apparatus for determination of thin film elastic modulus. 1st International Congress on Instrumentation and Applied Sciences 2014, https://www.researchgate.net/publication/265975755_Simple_vibrating_reed_apparatus_for_determination_of_thin_film_elastic_modulus (available: 15.09.2019).
- Kolupaev B. B., Krivtsov V. V., Malynovs'kiy E. V.: The acoustic spectroscopy of the PVC-based composition materials in audio frequency range. *Acoustic bulletin* 16(2)/2013–2014, 3–7.
- Lin K., Yu Y., Xi J., Li H., Guo Q., Tong J., Su L.: A Fiber-coupled self-nixing laser diode for the measurement of Young's modulus. *Sensors* 16, 2016, 928 [DOI: 10.3390/s16060928].
- Mashchenko V.: Determination of elasticity modulus of constructional and heterogeneous materials by ultrasonic method. *Scientific notes* 65, 2019, 165–169.
- Pintelon R., Guillaume P., De Belder K., Rolain Y.: Measurement of Young's modulus via modal analysis experiment: a system identification approach. 13th IFAC Symposium on System Identification, 2003, 389–394.
- ISO 18437-1:2012 Mechanical vibration and shock – Characterization of the dynamic mechanical properties of viscoelastic materials – Part 1: Principles and guidelines, <https://www.iso.org/standard/35585.html> (available: 15.09.2019)
- The Engineering Toolbox http://www.engineeringtoolbox.com/young-modulus_417.html. (available: 15.09.2019).

Prof. Volodymyr Kvasnikov

e-mail: kvp@nau.edu.ua

President of Engineering Academy of Ukraine, Head of Computerized electrical systems and technologies department (NAU).
Main scientific direction – development of methods and instruments for measuring mechanical quantities and metro-logical support for measurement processes.



ORCID ID: 0000-0002-6525-9721

Prof. Volodymyr Drevetskiy

e-mail: westra@rv.ua.net

Vice president of Engineering Academy of Ukraine, Head of Automation, electrical and computer-integrated technologies department (NUWEE).
Main scientific direction – development of methods and devices for continuous automatic monitoring of physical and mechanical parameters of fluids and polymers materials.



ORCID ID: 0000-0001-8999-2226

otrzymano/received: 01.10.2019

przyjęto do druku/accepted: 06.12.2019

DETERMINATION OF THE OPTIMAL SCANNING STEP FOR EVALUATION OF IMAGE RECONSTRUCTION QUALITY IN MAGNETOACOUSTIC TOMOGRAPHY WITH MAGNETIC INDUCTION

Adam Ryszard Zywica, Marcin Ziolkowski

West Pomeranian University of Technology, Faculty of Electrical Engineering, Department of Electrical and Computer Engineering, Szczecin, Poland

Abstract. *Magnetoacoustic Tomography with Magnetic Induction (MAT-MI) is a new hybrid imaging modality especially dedicated for non-invasive electrical conductivity imaging of low-conductivity objects such as e.g. biological tissues. The purpose of the present paper is to determine the optimal scanning step assuring the best quality of image reconstruction. In order to resolve this problem a special image reconstruction quality indicator based on binarisation has been applied. Taking into account different numbers of measuring points and various image processing algorithms, the conditions allowing successful image reconstruction have been provided in the paper. Finally, the image reconstruction examples for objects' complex shapes have been analysed.*

Keywords: image reconstruction, image processing algorithms, medical diagnostic imaging, magnetoacoustic effects, magnetoacoustic tomography with magnetic induction

OKREŚLENIE OPTIMALNEGO KROKU SKANOWANIA DO OCENY JAKOŚCI REKONSTRUKCJI OBRAZU W TOMOGRAFII MAGNETOAKUSTYCZNEJ ZE WZBUDZENIEM INDUKCYJNYM

Streszczenie. *Tomografia magnetoakustyczna ze wzbudzeniem indukcyjnym (MAT-MI) to nowa hybrydowa technika obrazowania dedykowana szczególnie do nieinwazyjnego obrazowania obiektów o niskiej konduktywności elektrycznej, takich jak na przykład tkanki biologiczne. Celem niniejszej pracy jest określenie optymalnego kroku skanowania zapewniającego najlepszą jakość rekonstrukcji obrazu. W celu rozwiązania tego problemu zastosowano specjalny wskaźnik jakości rekonstrukcji obrazu bazujący na binaryzacji. W artykule przedstawiono warunki umożliwiające pomyślne zrekonstruowanie obrazu biorąc pod uwagę różną liczbę punktów pomiarowych oraz różne algorytmy przetwarzania obrazu. W końcowym etapie pracy przeanalizowano przykłady rekonstrukcji obrazu dla obiektów o bardziej złożonych kształtach.*

Słowa kluczowe: rekonstrukcja obrazu, algorytmy przetwarzania obrazu, diagnostyczne obrazowanie medyczne, efekty magnetoakustyczne, tomografia magnetoakustyczna ze wzbudzeniem indukcyjnym

Introduction

Magnetoacoustic Tomography with Magnetic Induction (MAT-MI) is a new hybrid modality dedicated for non-invasive imaging of low-conductivity objects' internal structure, especially designated to use in medical diagnostics or in non-destructive testing of materials. MAT-MI is characterised by a good spatial resolution, high contrast and overcomes the unwanted screening effect which is often found in other tomographic techniques [5, 8, 10].

The MAT-MI method can be divided into two main parts, namely: so-called *forward* and *inverse* problems. The result of the first part is obtaining and recording the sound pressure generated inside the low-conductivity object. The ultrasonic signals are collected by piezoelectric transducers (during an experiment) or calculated at measuring points – which in a present simulation study are the transducers' equivalents. The latter part consists of two steps, i.e. reconstructing the distribution of the Lorentz force divergence, and finally, the imaging of the electrical conductivity distribution [5, 9].

MAT-MI, in the principle, uses electromagnetic and acoustic field theory. In this technique an object to be imaged is placed in static and time-varying (pulsed) external magnetic fields (an arrangement schematically has been shown in Fig. 1). Accordingly, due to the electromagnetic induction, eddy currents are induced. Consequently, the object emits acoustic waves through the Lorentz force generated as result of interaction between static magnetic field and eddy currents. The propagated acoustic waves are used for electrical conductivity image reconstruction [5].

The purpose of the presented study is to determine the optimal *scanning step* which is the equivalent of ultrasonic pressure measuring points' number. In order to resolve this problem a special image reconstruction quality indicators based on binarisation have been applied. Finally, the image reconstruction examples for objects' complex shapes have been analysed and the reconstruction of the Lorentz force divergence has been achieved. Taking into account different numbers of measuring points and various image processing algorithms, the conditions allowing successful image reconstruction have been provided.

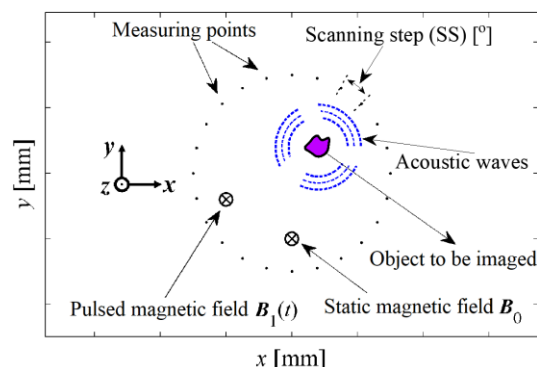


Fig. 1. Schematic diagram of 2D MAT-MI concept

1. Image reconstruction quality

In order to determine the conditions allowing for successful image reconstruction an assessment of the quality of the reconstructed images must be made. In this case, the image reconstruction quality should be understood by the similarity between the reconstructed image and the original image of an object. There are two kinds of quality assessment: *subjective assessment* (a method based on estimation of image quality by a human) and *objective assessment* (considered in this paper) where the goal is to implement and use *quality indicator* that can predict perceived image quality automatically. In practice, an objective image quality metric can be employed to determine the optimal value of scanning step SS which determines a required minimal scanning resolution assuring the best quality of image reconstruction. Finally, information obtained during the simulation studies can be used subsequently in experiments to properly calibrate a measuring system [7].

In tomography, various approaches and correlated indicators are commonly used in image processing approaches, e.g. an image feature extraction (shape, curve, texture and histogram). In this paper a straight image comparison, based on comparing binary images globally, has been applied [1]. The block diagram of a quality estimation of an image reconstruction is shown in Fig. 2.

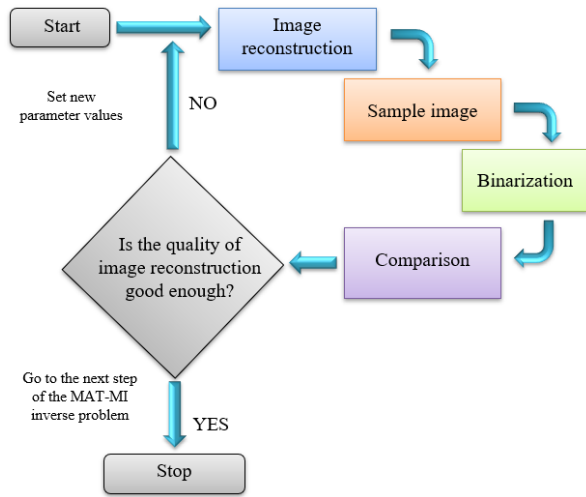


Fig. 2. Block diagram of reconstruction quality evaluation algorithm

In order to obtain sample images, the first step of the MAT-MI inverse problem ought to be conducted. The Lorentz force divergence can be reconstructed using time reversal technique which is one of the ultrasound imaging modalities [5, 9]. The resulting sample images (stored in grayscale) are subjected to a binarisation and then compared with the original image of the object. The binarisation process has been performed with the help of Matlab's function *imbinarize*. The function uses Otsu's method, which chooses the threshold value to minimize the interclass variance of the threshold black and white pixels (global thresholding method) [6].

The most appropriate and natural ways to compare binary images is the statistical approach using such indicators as: positive predictive value (PPV, precision), negative predictive value (NPV), true positive rate (TPR, sensitivity), true negative rate (TNR, specificity or selectivity) and accuracy (ACC) which are derivatives from so-called *confusion matrix* (also called as *error matrix*). PPV, NPV, TPR, TNR and ACC can be determined by the following expressions [4]:

$$PPV = \frac{TP}{TP + FP}, \quad (1)$$

$$NPV = \frac{TN}{TN + FN}, \quad (2)$$

$$TPR = \frac{TP}{TP + FN}, \quad (3)$$

$$TNR = \frac{TN}{TN + FP}, \quad (4)$$

$$ACC = \frac{TP + TN}{TP + TN + FP + FN}, \quad (5)$$

where: TP (true positive) and FP (false positive) are the numbers of foreground image reconstruction pixels (black pixels, pixels of the reconstructed object) consistent with model object's pixels and inconsistent with model object's pixels, respectively; TN (true negative) and FN (false negative) are the numbers of background image reconstruction pixels (white pixels) consistent with model background pixels and inconsistent with model background pixels, respectively.

Besides a confusion matrix approach, others measures are also used to evaluate the similarity of two images, e.g. pixel-to-pixel matching (MPxP), peak signal-to-noise ratio (PSNR) and correlation (COR). MPxP is the method in which each pixel from reconstructed image is compared to the corresponding pixel from the original image. Secondly, peak signal-to-noise ratio (PSNR) is the image quality measure which is simple to calculate, has clear physical measuring but does not match well with the human perception. In practice, the higher PSNR generally the higher image reconstruction quality.

The PSNR is defined as (in dB) [4]:

$$PSNR = 20 \log_{10} \left(\frac{MAX}{\sqrt{MSE}} \right) \quad (6)$$

Where: MAX is the maximum possible pixel value of the image, MSE is the mean squared error.

Lastly, correlation (COR) is the Pearson correlation coefficient. COR is used to measure of the linear correlation between the reconstructed image and the original image of an object as a measurement of the similarity of these two images. In this case, COR is defined as [2-3]:

$$COR = \frac{\sum_m \sum_n [f(m+i, n+j) - \bar{f}][g(m, n) - \bar{g}]}{\sqrt{\sum_m \sum_n [f(m+i, n+j) - \bar{f}]^2 \sum_m \sum_n [g(m, n) - \bar{g}]^2}}, \quad (7)$$

Where: $f(m, n)$ is the pixel intensity at a point (m, n) in the original image, $g(m, n)$ is the pixel intensity at a point (m, n) in the reconstructed image, \bar{f} and \bar{g} are mean values of the intensity of the images f and g , respectively.

2. Study

The MAT-MI forward problem has been performed with the help of Comsol Multiphysics based on the finite element method (FEM). In order to reconstruct the acoustic source as the Lorentz force divergence, i.e. $\nabla \cdot (\mathbf{J} \times \mathbf{B}_0)$, the time reversal algorithm has been used. It should be noted, that the layers are acoustically homogeneous without any reflections, dispersion and attenuation. Moreover, all the studies are ideal and therefore the recorded signals are considered as a noise-free.

The original images of the two exemplary objects under test are shown in Fig. 3. On the left, the so-called a simple-shaped object (hereinafter referred to as a *simple object*), and to the right a compound-shaped object (hereinafter referred to as a *complex object*) are presented. The 2D geometry of the simple object consists of two separate spots, while the complex object to be imaged consists of inner and outer layers with the irregular shapes. The electrical conductivity of smaller spot of the simple object and inner layer of the complex object has been set to 8 S/m. The electrical conductivities of the bigger spot of the simple object and outer layer of the complex object have been set to 6 S/m. Moreover, the conductivity of the white background in both pictures has been set to 0 S/m.

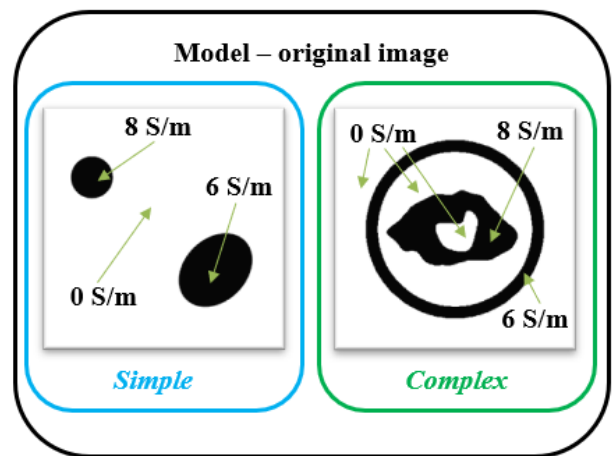


Fig. 3. The objects' view: simple (left, blue frame) and complex (right, green frame)

Results of the reconstruction for four different exemplary number of MP (6, 12, 24 and 36) have been presented in the Fig. 4 and Fig. 5 for the simple and complex object, respectively. In order to reduce the computation time, the size of images has been rescaled to 300×300 pixels.

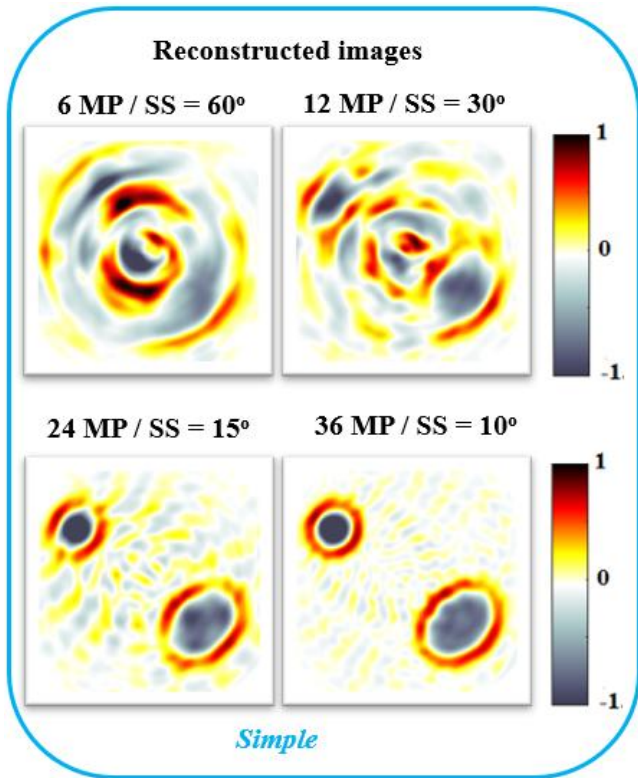


Fig. 4. Normalized acoustic pressure: reconstructed images of the simple object for different number of MP

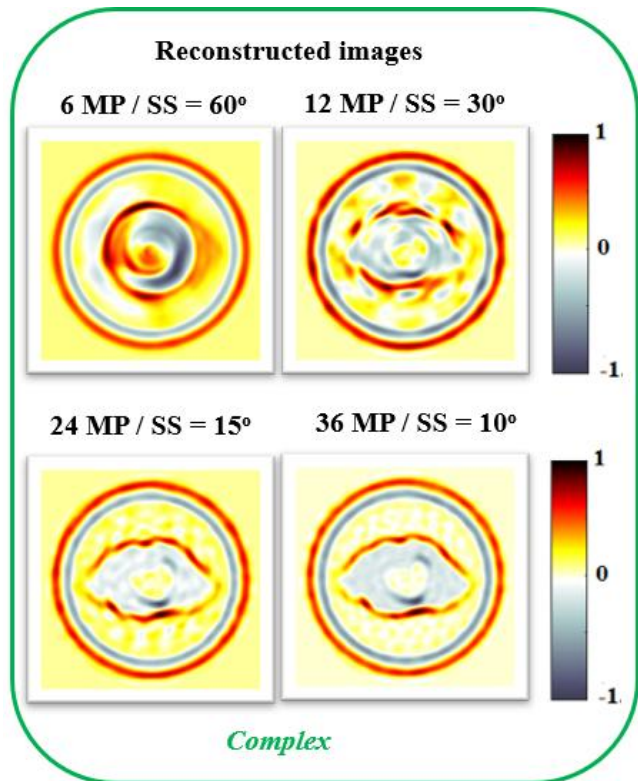


Fig. 5. Normalized acoustic pressure: reconstructed images of the complex object for different number of MP

Next, two groups of the binary images from reconstructed images of the simple and complex object have been made, called 'case A' and 'case B', respectively. The former is made after binarisation from the grayscale image reconstruction of the object with full range of values. In turn, the latter is made after binarisation from the grayscale image reconstruction of the object without positive values. Results of image binarisation of exemplary source images presented already in Fig. 4 and Fig. 5 are shown in Fig. 6.

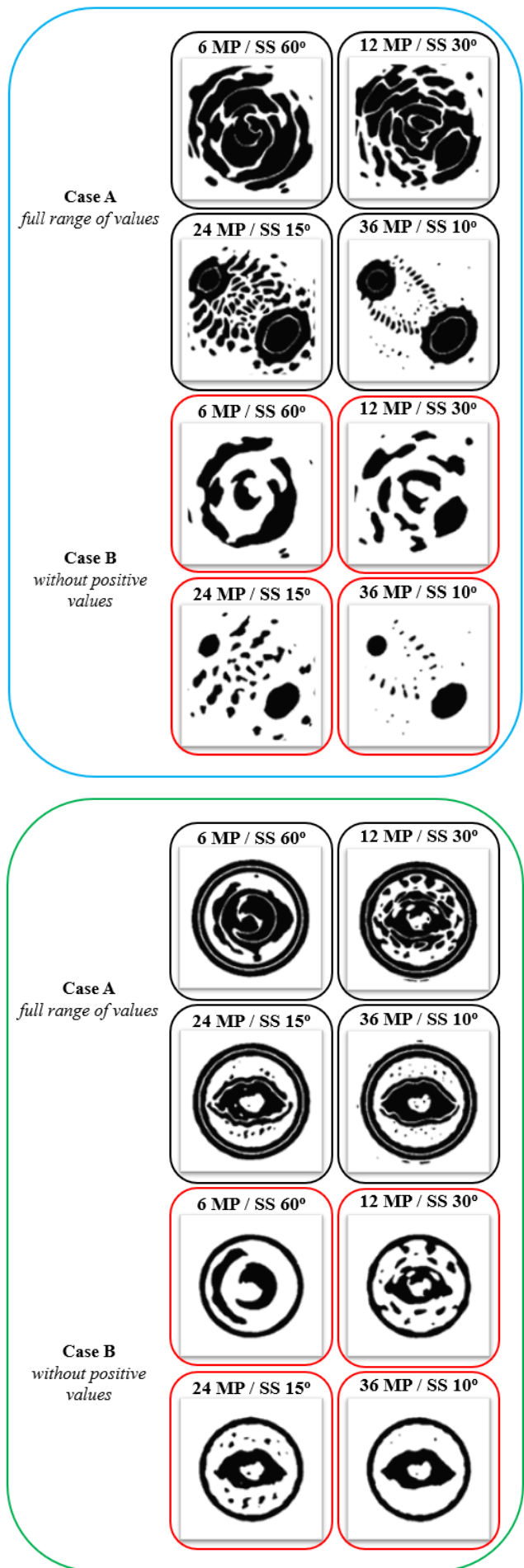


Fig. 6. Exemplary results of binarisation of the simple (blue frame, upper part) and complex (green frame, lower part) object for case A and case B

The subjective assessment is undoubtedly pointing at a greater similarity of the images in case B to object image than in case A for the both objects. For example, for 6 MP the external ring was properly reconstructed but not much information about the inner part of the complex object is revealed. With 12 MP, some of the inner basic features of the complex object start to emerge but still blurring artefacts around and between the inner and outer part of the complex object can be observed. Finally, for 36 MP the reconstructed acoustic source positions almost exactly correspond to the actual locations of the complex object. However, the same thing happens for the simple object. Generally, the greater number of measuring points, the better quality images with less time reversal noise can be observed.

3. Results

The straight image comparison (globally) has been chosen which seems best adapted for this case. During the full calculations, the following nine MP numbers have been analysed, i.e.: 6, 12, 24, 36, 60, 90, 120, 180 and 360. The binary images have been compared without using feature extension (feature comparison). In order to evaluate the reconstruction quality properly, some of the statistical and the other mentioned above indicators have been calculated for the case A and B for the simple and complex object. Curves obtained for PPV and TPR are shown in Fig. 7 and Fig. 8 but values of all calculated indicators for the both objects and the both cases have been summarised in Tab. 1 and Tab. 2.

Table 1. Values of the indicators used to compare the images of the simple object for case A and case B for different number of measuring points MP

Case A of the simple object										
SS [°]	MP	PPV	NPV	TPR	TNR	ACC	MPxP [%]	PSNR [dB]	COR	
60	6	0.978	0.177	0.524	0.895	0.562	52.41	51.71	0.254	
30	12	0.978	0.181	0.541	0.891	0.577	54.09	51.86	0.262	
15	24	0.990	0.238	0.657	0.941	0.689	65.68	53.15	0.369	
10	36	0.994	0.416	0.848	0.954	0.859	84.76	56.62	0.573	
6	60	0.995	0.514	0.896	0.962	0.903	89.63	58.26	0.661	
4	90	0.995	0.518	0.898	0.963	0.905	89.78	58.33	0.665	
3	120	0.996	0.520	0.899	0.965	0.905	89.85	58.37	0.667	
2	180	0.996	0.521	0.899	0.965	0.906	89.89	58.39	0.668	
1	360	0.996	0.521	0.899	0.965	0.906	89.90	58.39	0.669	
Case B of the simple object										
SS [°]	MP	PPV	NPV	TPR	TNR	ACC	MPxP [%]	PSNR [dB]	COR	
60	6	0.954	0.261	0.783	0.671	0.772	78.33	54.54	0.312	
30	12	0.958	0.306	0.823	0.686	0.809	82.28	55.31	0.366	
15	24	0.959	0.398	0.884	0.671	0.862	88.43	56.75	0.445	
10	36	0.963	0.800	0.981	0.668	0.949	98.09	61.04	0.806	
6	60	0.963	1.000	1.000	0.665	0.966	99.89	62.78	0.867	
4	90	0.963	1.000	1.000	0.664	0.966	99.89	62.78	0.869	
3	120	0.963	1.000	1.000	0.664	0.966	99.89	62.78	0.869	
2	180	0.963	1.000	1.000	0.665	0.966	99.89	62.78	0.872	
1	360	0.963	1.000	1.000	0.665	0.966	99.89	62.78	0.872	

Table 2. Values of the indicators used to compare the images of the complex object for case A and case B for different number of measuring points MP

Case A of the complex object										
SS [°]	MP	PPV	NPV	TPR	TNR	ACC	MPxP [%]	PSNR [dB]	COR	
60	6	0.945	0.476	0.733	0.851	0.759	73.32	54.32	0.496	
30	12	0.938	0.466	0.729	0.831	0.752	72.88	54.18	0.475	
15	24	0.942	0.538	0.797	0.829	0.804	79.69	55.21	0.548	
10	36	0.955	0.555	0.802	0.866	0.816	80.22	55.49	0.583	
6	60	0.956	0.566	0.810	0.868	0.823	81.04	55.65	0.594	
4	90	0.956	0.560	0.805	0.870	0.819	80.48	55.56	0.590	
3	120	0.956	0.566	0.810	0.870	0.823	81.00	55.66	0.596	
2	180	0.956	0.568	0.811	0.870	0.824	81.11	55.68	0.597	
1	360	0.957	0.568	0.811	0.871	0.824	81.11	55.69	0.598	
Case B of the complex object										
SS [°]	MP	PPV	NPV	TPR	TNR	ACC	MPxP [%]	PSNR [dB]	COR	
60	6	0.912	0.726	0.926	0.686	0.873	92.61	57.08	0.624	
30	12	0.925	0.771	0.938	0.735	0.893	93.77	57.82	0.684	
15	24	0.946	0.876	0.967	0.806	0.932	96.74	59.78	0.797	
10	36	0.950	0.946	0.987	0.819	0.950	98.67	61.10	0.850	
6	60	0.953	0.950	0.988	0.830	0.953	98.77	61.37	0.859	
4	90	0.952	0.952	0.988	0.827	0.952	98.81	61.35	0.858	
3	120	0.954	0.952	0.988	0.831	0.953	98.80	61.43	0.861	
2	180	0.954	0.952	0.988	0.832	0.954	98.81	61.46	0.862	
1	360	0.954	0.952	0.988	0.831	0.953	98.82	61.48	0.865	

The results present the high similarity of the compared binary images in both cases for the both objects. However, the lesser difference between PPV and TPR for case B than case A indicates that the cut off of positive values from the grayscale image reconstruction is resulted in a distinct improvement in the match

of the reconstruction to the model. Significant image reconstruction improvement takes place when the number of measuring points begins by 36 for case A and case B also for the both objects, respectively. What is more, further increment of measuring points' number does not change the image crucially.

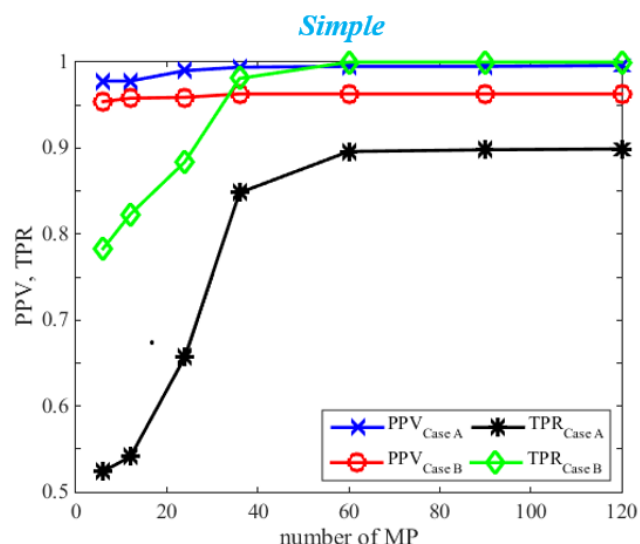


Fig. 7. Value of some confusion matrix indicators obtained for the case A and case B for the simple object

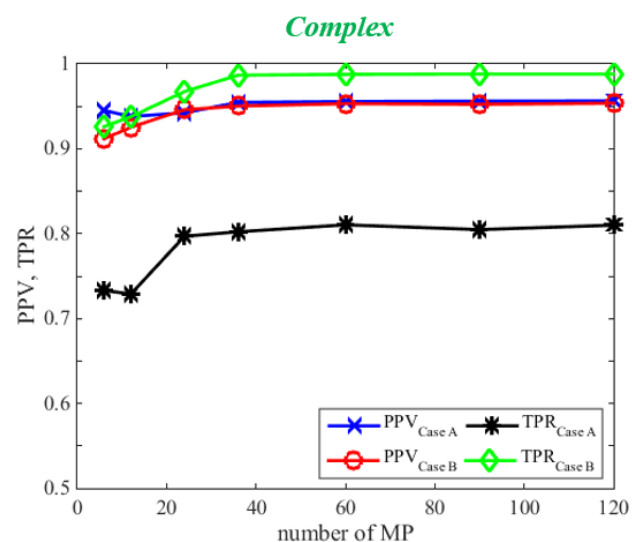


Fig. 8. Value of some confusion matrix indicators obtained for the case A and case B for the complex object

Taking into account three other indicators i.e. pixel-to-pixel matching (MPxP), PSNR and correlation (COR), it can be observed that the results present the great similarity of the compared binary images in both cases for the both objects. As in previous situation (statistical approach), significant image reconstruction improvement occurs when the number of measurement points starts at 36 for both cases also for the both objects. The high values of the indicators for the both cases are due to the fact that the images are compared globally. In addition, large fragments of images near their edges, consisting only of pixels of white colour, also have a large share in inflating the values. Another element that enhances this effect is the lack of a large number of smaller sized artefacts that were cleared during the binarisation.

4. Conclusions

In this paper, the influence of MAT-MI scanning resolution on the image reconstruction quality has been studied in detail. In order to evaluate properly the image reconstruction quality, the set of quality indicators has been used. The main task of the indicators is to determine the perceived image quality automatically allowing to benchmark and to optimize scanning resolution and parameter

settings in the simulations studies. The information obtained after the simulation tests will allow for accurate matching of the experimental conditions and to properly calibrate the measuring system. Taking into account the subjective and objective assessment of image reconstruction quality, among all the indicators we used to determine the similarity between the reconstructed image and the original image, the correlation gives the best results.

It should be noted that the obtained values of the indicators depend on the resolution of the compared images. However, this resolution is related to the sampling time occurring in the MAT-MI forward problem. This aspect will be studied in the next article.

References

- [1] Baudrier E., Nicolier F., Millon G., Ruan S.: Binary-image comparison with local dissimilarity quantification. *Pattern Recognition* 41/2008, 1461–1478, [doi:10.1016/j.patcog.2007.07.011].
- [2] Bourke. P.: *Cross Correlation. Auto Correlation and 2D Pattern Identification*. Research Paper. Oxford University, Oxford 1996.
- [3] Fastowicz J., Bąk D., Mazurek P., Okarma K.: Estimation of Geometrical Deformation of 3D Prints Using Local Cross-Correlation and Monte Carlo Sampling. *Advances in Intelligent Systems and Computing* 681/2018 [DOI: 10.1007/978-3-319-68720-9_9].
- [4] Lech P., Okarma K.: Optimization of the Fast Image Binarisation Method Based on the Monte Carlo Approach. *Elektronika ir Elektrotechnika* 20/2014, 63–66 [DOI: 10.5755/j01.eee.20.4.6887].
- [5] Li X., Yu K., He B.: Magnetoacoustic tomography with magnetic induction (MAT-MI) for imaging electrical conductivity of biological tissue: a tutorial review. *Physics in Medicine & Biology* 61/2016, 249–270 [DOI: 10.1088/0031-9155/61/18/R249].
- [6] Michalak. H., Okarma K.: Region Based Approach for Binarisation of Degraded Document Images. *Advances in Soft and Hard Computing* 889/2019, 433–444 [DOI: 10.1007/978-3-030-03314-9_37].
- [7] Rymarczyk T., Kłosowski G., Kozłowski E.: A non-destructive system based on electrical tomography and machine learning to analyze the moisture of buildings. *Sensors* 18(7)/2018, 2285 [DOI: 10.3390/s18072285].
- [8] Stawicki K., Gratkowski S., Komorowski M., Pietrusiewicz T.: A new transducer for magnetic induction tomography. *IEEE Transactions on Magnetics* 45/2009, 1832–1835 [DOI: 10.1109/TMAG.2009.2012799].
- [9] Wang Z., Sheikh H. R., Bovik A.: Objective video quality assessment. Chapter 41 in *The Handbook of Video Databases: Design and Application*, Furht B. and Marqure O., CRC Press 2003, 1041–1078.
- [10] Zywica A. R.: Magnetoacoustic tomography with magnetic induction for biological tissue imaging: numerical modelling and simulations. *Archives of Electrical Engineering* 65(1)/2015, 141–150 [DOI: 10.1515/ae-2016-0011].

M.Sc. Adam Ryszard Zywica
e-mail: adam.zywica@zut.edu.pl



Adam Ryszard Zywica received the M.Sc. degree in Electrical Engineering Faculty from West Pomeranian University of Technology, Szczecin, Poland in 2014. Since October 2014, he is a Ph.D. student at the Department of Electrical and Computer Engineering, Electrical Engineering Faculty, West Pomeranian University of Technology, Szczecin, Poland. His main research interests include non-destructive testing of materials. His hobbies are chess, modern history, football, tennis.

ORCID ID: 0000-0003-2598-0052

D.Sc. Marcin Ziolkowski
e-mail: marcin.ziolkowski@zut.edu.pl



Marcin Ziolkowski received M.Sc., Ph.D. and D.Sc. (Habilitation) degrees in Electrical Engineering from the Szczecin University of Technology, Szczecin, Poland and West Pomeranian University of Technology, Szczecin, Poland in 2001, 2006 and 2012, respectively. Since 2008, he has been working with the Department of Electrical and Computer Engineering, Electrical Engineering Faculty, West Pomeranian University of Technology, Szczecin, Poland. His main research interests include numerical calculations and visualization of EM fields, inverse problems, electromagnetic field shielding and non-destructive testing of materials.

ORCID ID: 0000-0002-2773-2565

otrzymano/received: 02.08.2019

przyjęto do druku/accepted: 06.12.2019

DOI: 10.35784/IAPGOS.569

CONSTRUCTION OF AN ULTRASONIC TOMOGRAPH FOR ANALYSIS OF TECHNOLOGICAL PROCESSES IN THE FIELD OF REFLECTION AND TRANSMISSION WAVES

Tomasz Rymarczyk^{1,2}, Michał Gołąbek¹, Piotr Lesiak², Andrzej Marciniak², Mirosław Guzik²

¹Research and Development Center, Netrix S.A., Lublin, Poland, ²University of Economics and Innovation in Lublin, Lublin, Poland

Abstract. This article presents the ultrasonic structure for the analysis of technological processes in the field of reflective and transmission waves. Ultrasound tomography enables the analysis of processes occurring in the examined object without interfering with its interior through appropriate acquisition and analysis of data. The design goal is to verify the repeatability of measurement results by eliminating laboratory equipment. The ultrasonic tomograph has been designed in a modular way and consists of a motherboard connected to an analog signal conditioning board, a liquid crystal display with an integrated graphics processor and a high voltage pulser with a 64 channel multiplexer. The solution was designed for tomographic measurements of technological process properties.

Keywords: ultrasound tomography, sensors, measurements

BUDOWA TOMOGRAFU ULTRADŹWIĘKOWEGO DO ANALIZY PROCESÓW TECHNOLOGICZNYCH W ZAKRESIE FAŁ ODBITYCH I TRANSMISYJNYCH

Streszczenie. W niniejszym artykule przedstawiono konstrukcję tomografu ultradźwiękowego do analizy procesów technologicznych w zakresie fal odbitych i transmisyjnych. Tomografia ultradźwiękowa umożliwia analizowanie procesów zachodzących w badanym obiekcie bez ingerencji w jego wnętrze poprzez odpowiednią akwizycję i analizę danych. Celem konstrukcyjnym jest weryfikacja powtarzalności wyników badań pomiarowych poprzez wyeliminowanie sprzętu laboratoryjnego. Tomograf ultradźwiękowy został zaprojektowany w sposób modułowy i składa się z płyty głównej połączonej z płytą kondycjonowania sygnału analogowego, wyświetlacza ciekłokrystalicznego ze zintegrowanym procesorem graficznym oraz impulsatora wysokiego napięcia wraz z 64 kanałowym multiplexerem. Urządzenie zostało zaprojektowane do tomograficznych pomiarów właściwości procesów technologicznych.

Słowa kluczowe: tomografia ultradźwiękowa, sensory, pomiary

Introduction

Ultrasound tomography can be used to analyze the processes taking place in the facility without interfering with the production, analysis or detection of obstacles, defects and various anomalies. The article describes the measuring system has a specially designed measuring structure. The application allows you to choose the right method of image reconstruction thanks to knowledge of the features of each solution. The process of identifying optimization or synthesis, in which the goal is to specify parameters describing the data field, is solved by the inverse problem. The designed system for data acquisition and analysis enables monitoring and control of technological processes related to the processing of data obtained from various sensors. The idea of measuring in ultrasonic tomography is shown in Fig. 1.

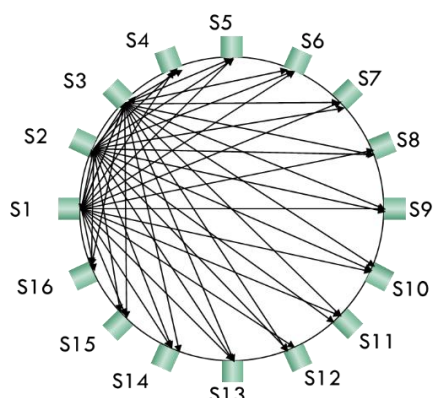


Fig. 1. The principle of ultrasonic measurement by transmission mode

Measuring technologies are still being improved. There is a clear tendency to implement more optimal solutions with an emphasis on active control and optimization [11–15, 25–27]. There are many numerical methods [1–4, 17, 24, 28, 29], but in order to solve the inverse problem, ultrasound tomography [5–10, 16] can be used.

The principle of operation is that one of the active probes sends an ultrasonic signal, the other probes are in the receiving

mode. The number of signal periods sent will depend on the type and size of the object being tested. For the container tested, four periods are sufficient. Active probes measure time individually from the moment the signal is sent to when it is picked up by individual transducers. This is the time when ultrasound travels the distance between probes.

1. Measurement system

The reflective ultrasound tomograph has been designed in a modular way (Fig. 2–4). The first module consists of a motherboard connected to an analog signal conditioning board and a liquid crystal display with an integrated FT811CB graphics processor. The second module consists of a high voltage pulse generator with a 64-channel multiplexer.

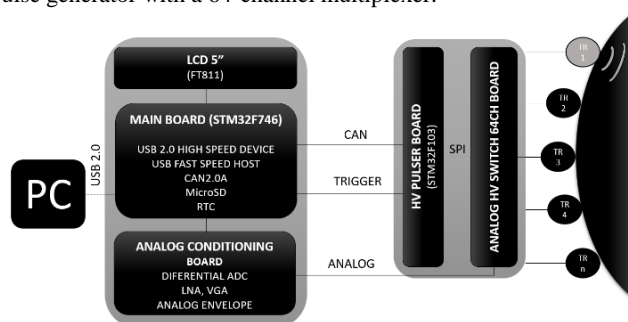


Fig. 2. Block diagram of an ultrasonic reflective tomograph

When designing the main module of the device, great emphasis was placed on its universality. The size of the printed circuit board depends on the dimensions of the FT811CB display. The main module board itself will be mounted under the display. The board allows you to connect external storage media: micro SD cards, portable drives to the USB Fast Speed port. The board has a spare RTC battery, spare registers, EEPROM memory. Communication with the computer can be implemented in the USB High Speed 2.0 standard. The debugger connector and serial port are connected. CAN, SPI, RS485 buses are output via the standard Cat 6a connector. Other I/O ports come from popular terminal blocks.

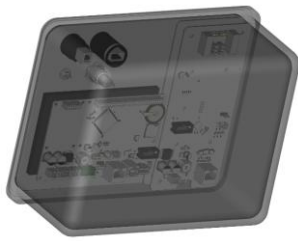


Fig. 3. Device model



Fig. 4. Ultrasound tomograph

The device is a closed structure that needs several control signals:

- CAN 2.0A bus
Setting device parameters such as:
 - Channel number to which the extortion is given,
 - Channel number from which the analogue signal is fed to the A / C converter,
 - The number of pulses generated,
 - Frequency of pulses generated,
 - Time of output shorting to ground after keying,
 - Brightness levels of RGB channels with backlit company logo.
- TRIGGER
This is a differential signal that triggers the bipolar excitation signal generator.
- ANALOG
The analog signal output from the multiplexer is protected by a high voltage cut-off system.

To generate waveforms to control the MOSFET key, use three cascade-connected hardware counters operating in One Pulse mode. In Figure 5 the exact way to connect the counters. The generator cycle begins by receiving a signal at the differential input of the TRIGGER line, which generates an interruption in the microcontroller during the execution of the ENA-BLE line is set to high, and also TIM1 is started (OUTA, OUTB), after the TIM1 countdown, the hardware called TIM2, the countdown for the first

counting period, after which the equipment sets the low state on OUTA, OUTB lines and starts TIM3. The third timer counts down the time by one TX output is topped with something that starts the interrupted program statement of the ENABLE line in the low state. Which causes MD1822 to set up secure tables on MOSFET TC8220 high-voltage key exchange control lines.

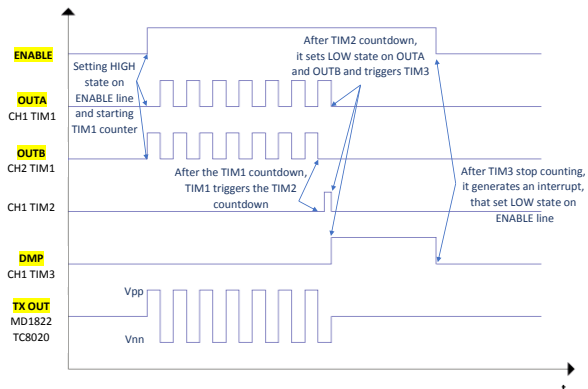


Fig. 5. MOSFET key control method for high voltage generator

User interface

Tomography software, including the user interface at the current stage of work is still being developed. The screenshots below are illustrative (Fig. 6).

Measuring parameters that can be changed:

- First probe number – the number of the probe from which the measurement sequence begins,
- Last probe number – the probe number at which the measurement sequence ends,
- Number of pulses – the number of bipolar pulses generated by the excitation system,
- Short to ground after transmission – the time for which the excitation system closes the ground lines after the transmission,
- Frequency – the frequency of the excitation signal,
- Input gain – amplification of the first stage of signal processing (12 bit),
- Output gain – amplification of the second stage of signal processing (signal envelope path, 8 bit),
- Measurement method – a method of performing measurements: reflection / transmission,
- Number of samples – the number of samples collected by the analog to digital converter,
- Sampling [ns] – signal sampling,
- A/D converter selection – selection of a/c converter (measurement of signal envelope or measurement of unprocessed signal).

The START button starts the measurement cycle during which data is sent via USB to the computer in binary form.

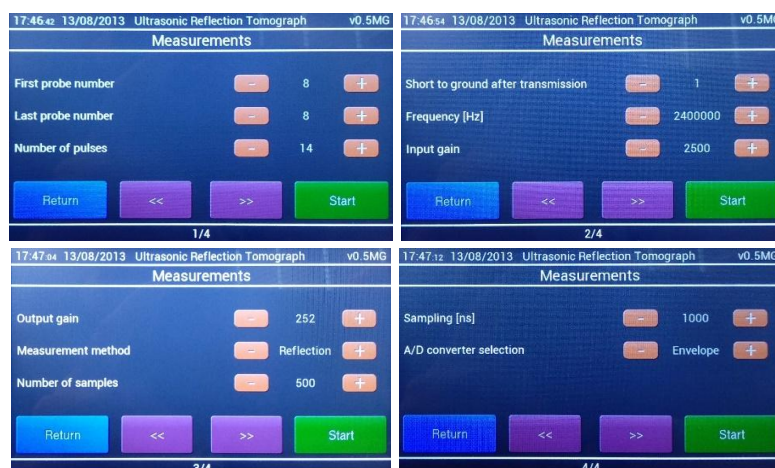


Fig. 6. Device measuring interface

2. Measurement tests

Measurements were made using 8 ultrasonic probes designed in the laboratory. The probes made by us work with a resonance frequency of 2.4 MHz. Due to the low resonance impedance of the transducers (approx. 2 Ohm), each probe has a 49 Ohm series resistor protecting the tomograph against damage. The ultrasonic transducers used, depending on the specimen, show varying sensitivity to signal reflections (Fig. 7).

The measurements were carried out in a plastic vessel with a diameter of 34 cm with full immersion of the sensor in water, a plastic bottle filled with water was used as a phantom (Fig. 8).

Tomograph settings:

- Number of pulses: 16,
- First level strengthening: 2332/4095,
- Second degree gain (envelope): 252/255,
- Measurement method: reflective,
- Number of samples: 500,
- Sampling: 1 us.



Fig. 7. Ultrasonic probe

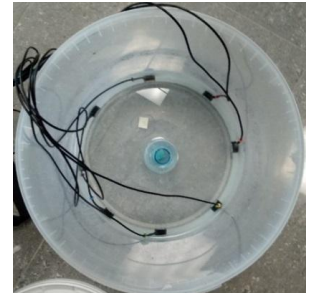
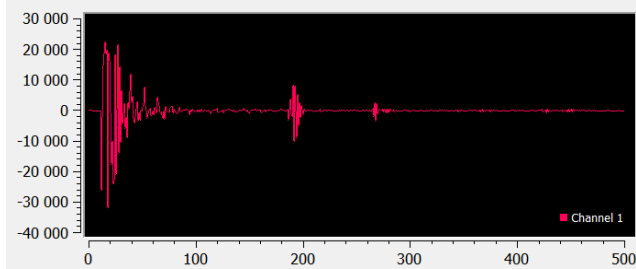
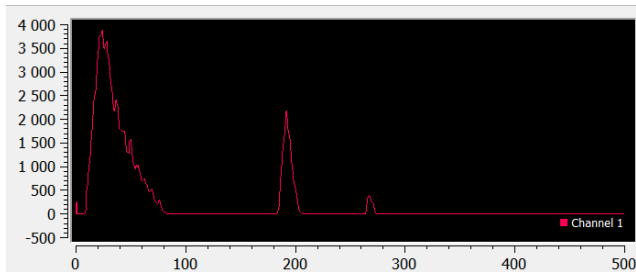


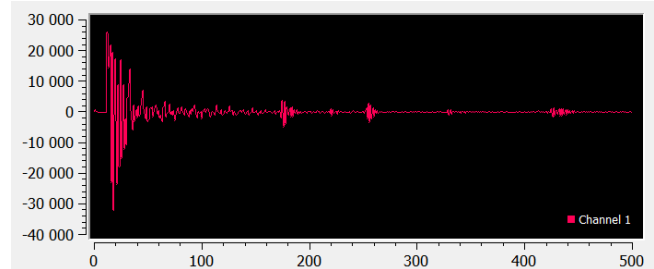
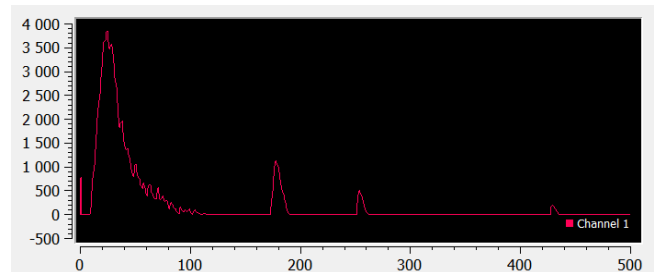
Fig. 8. Measuring object

The captured waveforms for each of the probes are shown below, and for comparison the waveforms captured without converting to boundaries (Fig. 9). From the measurements it is possible to observe a very high wave direction at such a high frequency. For example, the same bottle slightly tilted would not be visible through all probes, because the wave reflected from it directly would not return back to the inverter.

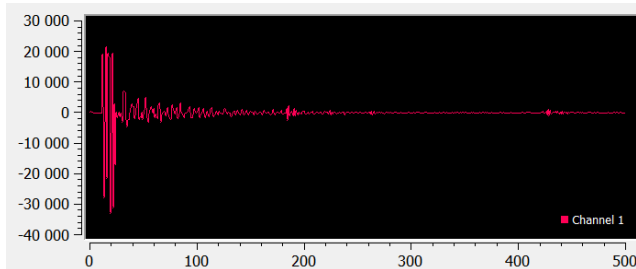
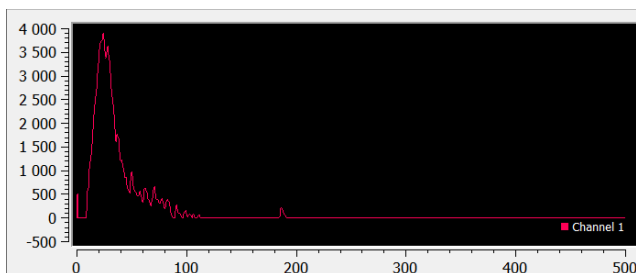
Sensor 1



Sensor 3



Sensor 2



Sensor 4

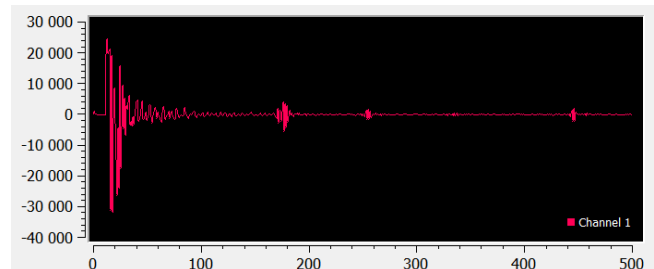
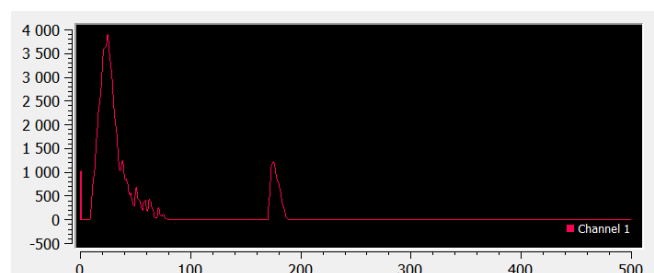


Fig. 9 (part 1). Waveforms for each probe and for comparison waveforms captured without processing into boundaries

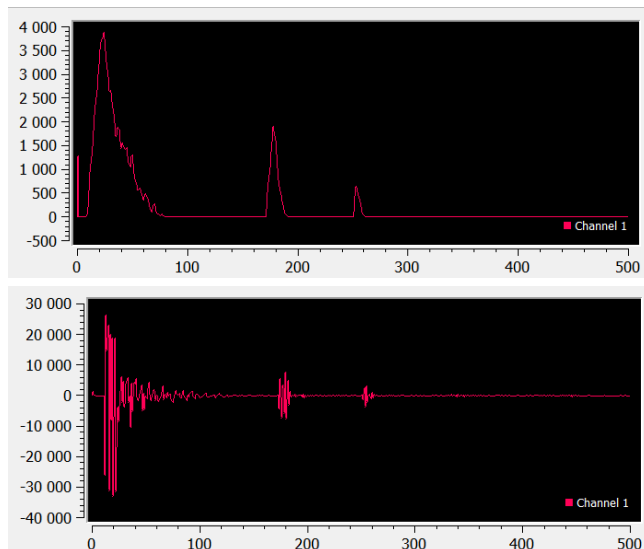
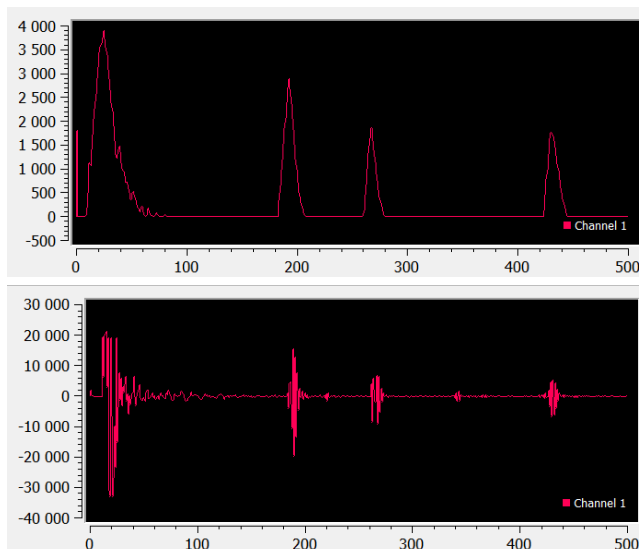
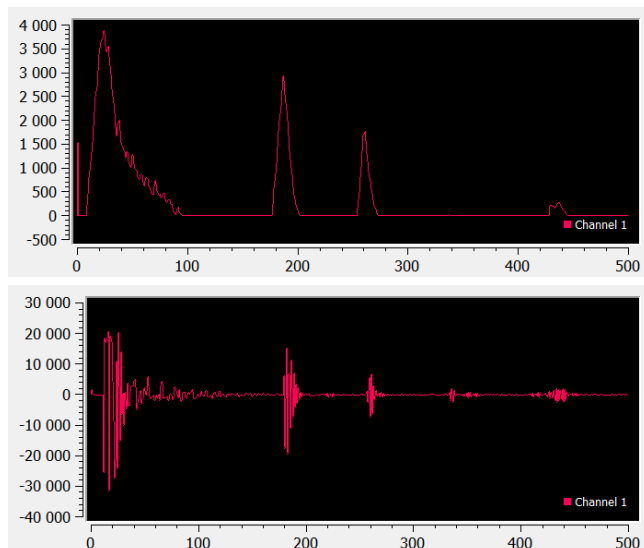
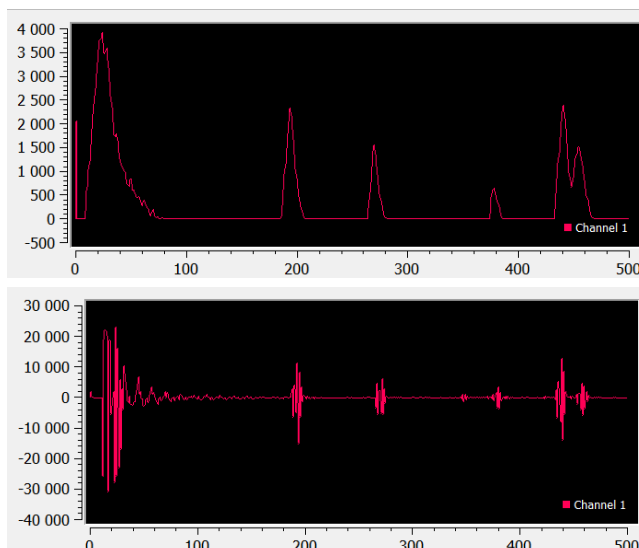
Sensor 5**Sensor 7****Sensor 6****Sensor 8**

Fig. 9 (part 2). Waveforms for each probe and for comparison waveforms captured without processing into boundaries

3. Conclusion

The article presents the construction of the device based on ultrasonic tomography. An original tomograph was designed for measuring ultrasonic waves and processing data obtained from various sensors. The ultrasonic tomograph has been designed in a modular way and consists of a motherboard connected to an analogue signal conditioning board, a liquid crystal display with an integrated graphics processor and a high voltage pulser with a 64 channel multiplexer. The device allows you to analyse the properties of various technological processes. Measurements were carried out in a plastic vessel with the sensor fully immersed in water, a plastic bottle filled with water was used as a phantom. Waveforms for each of the probes are presented and for comparison waveforms captured without processing into boundaries, where very high directionality of the wave can be observed at such a high frequency.

References

[1] Babout L., Grudzień K., Wiącek J., Niedostatkiwicz M., Karpiński B., Szkodo M.: Selection of material for X-ray tomography analysis and DEM simulations: comparison between granular materials of biological and non-biological origins. *Granul. Matter* 20(3)/2018, 38.

[2] Chaniecki Z., Romanowski A., Nowakowski J., Niedostatkiwicz M.: Application of twin-plane ECT sensor for identification of the internal imperfections inside concrete beams Grudzien. *IEEE Instrumentation and Measurement Technology Conference 2016*, 7520512.

[3] Duda K., Adamkiewicz P., Rymarczyk T., Niderla K.: Nondestructive Method to Examine Brick Wall Dampness. *International Interdisciplinary PhD Workshop, Brno, 2016*, 68–71.

[4] Fiala P., Drexler P., Nešpor D., Szabó Z., Mikulka J., Polívka J.: The Evaluation of Noise Spectroscopy Tests. *Entropy* 18(12)/2016, 1–16.

[5] Gudra T., Opieliński K. J.: The multi-element probes for ultrasound transmission tomography. *Journal de Physique* 4(137)/2006, 79–86.

[6] Golabek M., Rymarczyk T., Adamkiewicz P.: Construction of ultrasonic reflection tomograph for analysis of technological processes, Applications of Electromagnetics in Modern Engineering and Medicine. *XXIX Sympozjum PTZE 2019*, 47–51.

[7] Herman G.T.: *Image Reconstruction from Projections: The Fundamentals of Computerized Tomography*. Academic Press, New York 1980.

[8] Jiang Y., Soleimani M., Wang B.: Contactless electrical impedance and ultrasonic tomography, correlation, comparison and complementary study. *Measurement Science and Technology* 30/2019, 114001.

[9] Kaczmarz S.: *Angenäherte Auflösung von Systemen Linearer Gleichungen*. *Bull. Acad. Polon. Sci. Lett. A*, 6–8A/1937, 355–357.

[10] Kak A. C., Slaney M.: *Principles of Computerized Tomographic Imaging*. IEEE Press, New York 1999.

[11] Kryszyn J., Wanta D. M., Smolik W. T.: Gain Adjustment for Signal-to-Noise Ratio Improvement in Electrical Capacitance Tomography System EVT4. *IEEE Sens. J.* 17(24)/2017, 8107–8116.

[12] Kryszyn J., Smolik W.: Toolbox for 3d modelling and image reconstruction in electrical capacitance tomography. *Informatyka, Automatyka, Pomiar w Gospodarce i Ochronie Środowiska – IAPGOŚ 7(1)/2017*, 137–145.

- [13] Lopato P., Chady T., Sikora R., Ziolkowski M.: Full wave numerical modelling of terahertz systems for nondestructive evaluation of dielectric structures. *COMPEL – The international journal for computation and mathematics in electrical and electronic engineering* 32(3)/2013, 736–749.
- [14] Majchrowicz M., Kapusta P., Jackowska-Strumillo L., Sankowski D.: Optimization of Distributed Multi-node, Multi-GPU, Heterogeneous System for 3D Image Reconstruction in Electrical Capacitance Tomography. *Image processing & communications* 21(3)/2016, 81–90.
- [15] Nowakowski J., Ostalczyk P., Sankowski D.: Application of fractional calculus for modelling of two-phase gas/liquid flow system. *Informatyka, Automatyka, Pomiary w Gospodarce i Ochronie Środowiska – IAPGOŚ* 7(1)/2017, 42–45.
- [16] Polakowski K., Sikora J.: *Podstawy matematyczne obrazowania ultradźwiękowego*. Politechnika Lubelska, Lublin 2016.
- [17] Romanowski A., Luczak P., Grudzień K.: X-ray Imaging Analysis of Silo Flow Parameters Based on Trace Particles Using Targeted Crowdsourcing. *Sensors* 19(15)/2019, 3317.
- [18] Rymarczyk T., Kłosowski G.: Innovative methods of neural reconstruction for tomographic images in maintenance of tank industrial reactors. *Eksploatacja i Niezawodność – Maintenance and Reliability* 21(2)/2019, 261–267.
- [19] Rymarczyk T., Filipowicz S. F., Sikora J.: Level Set Method for Inverse Problem Solution In Electrical Impedance Tomography. *Journal Proceedings of the XII International Conference on Electrical Bioimpedance & V Electrical Impedance Tomography*, 2004, 519–522.
- [20] Rymarczyk T., Kozłowski E., Kłosowski G., Niderla K.: Logistic Regression for Machine Learning in Process Tomography. *Sensors* 19/2019, 3400.
- [21] Rymarczyk T., Szumowski K., Adamkiewicz P., Tchórzewski P., Sikora J.: Moisture Wall Inspection Using Electrical Tomography Measurements. *Przegląd Elektrotechniczny* 94/2018, 97–100.
- [22] Rymarczyk T., Nita P., Vejar A., Stefaniak B., Sikora J.: Electrical tomography system for Innovative Imaging and Signal Analysis. *Przegląd Elektrotechniczny* 95(6)/2019, 133–136.
- [23] Soleimani M., Mitchell C. N., Banasiak R., Wajman R., Adler A.: Four-dimensional electrical capacitance tomography imaging using experimental data. *Progress in Electromagnetics Research* 90/2009, 171–186.
- [24] Szczepny A., Korzeniewski E.: Selection of the method for the earthing resistance measurement. *Przegląd Elektrotechniczny* 94(12)/2018, 178–181.
- [25] Vališ D., Hasilová K., Forbelská M., Vintř Z.: Reliability modelling and analysis of water distribution network based on backpropagation recursive processes with real field data. *Measurement* 149/2020, 107026.
- [26] Wajman R., Fiderek P., Fidos H., Sankowski D., Banasiak R.: Metrological evaluation of a 3D electrical capacitance tomography measurement system for two-phase flow fraction determination. *Measurement Science and Technology* 24(6)/2013, 065302.
- [27] Wang M.: *Industrial Tomography: Systems and Applications*. Elsevier 2015.
- [28] Ye Z., Banasiak R., Soleimani M.: Planar array 3D electrical capacitance tomography. *Insight: Non-Destructive Testing and Condition Monitoring* 55(12)/2013, 675–680.
- [29] Ziolkowski M., Gratkowski S., Zywicka A. R.: Analytical and numerical models of the magnetoacoustic tomography with magnetic induction. *COMPEL – The international journal for computation and mathematics in electrical and electronic engineering* 37(2)/2018, 538–548.

Ph.D. Eng. Tomasz Rymarczyk

e-mail: tomasz@rymarczyk.com

He is the director in Research and Development Centre in Netrix S.A. and the director of the Institute of Computer Science and Innovative Technologies in the University of Economics and Innovation, Lublin, Poland. He worked in many companies and institutes developing innovative projects and managing teams of employees. His research area focuses on the application of non-invasive imaging techniques, electrical tomography, image reconstruction, numerical modelling, image processing and analysis, process tomography, software engineering, knowledge engineering, artificial intelligence and computer measurement systems.

ORCID ID: 0000-0002-3524-9151

M.Sc. Eng. Michal Golabek

e-mail: michal.golabek@netrix.com.pl

He is embedded software developer and electrical engineer employed in Research and Development Department of Netrix S.A. Currently he is working on ultrasound tomography project. He graduated with Master of Engineering in Electrical Engineering with specialization "Microprocessor drives in industrial automation" on Lublin University of Technology.

ORCID ID: 0000-0002-2696-505X

D.Sc. Eng. Piotr Lesiak

e-mail: piotr.lesiak@wsei.lublin.pl

The Faculty of Transport and Computer Science, University of Economics and Innovation in Lublin. His research interests include technical diagnostics and smart systems measurements in railway transport.

ORCID ID: 0000-0002-9792-3463

D.Sc. Eng. Andrzej Marciniak

e-mail: andrzej.marciniak@wsei.lublin.pl

The Faculty of Transport and Computer Science, University of Economics and Innovation in Lublin. His research interests include data analysis, graph databases and machine learning methods.

ORCID ID: 0000-0002-2718-4802

Ph.D. Eng. Mirosław Guzik

e-mail: miroslaw.guzik@wsei.lublin.pl

The Faculty of Transport and Computer Science, University of Economics and Innovation in Lublin. His research interests include reverse engineering, rapid prototyping and 3D systems measurements in mechanical engineering.

ORCID ID: 0000-0003-3351-9039

otrzymano/received: 30.10.2019

przyjęto do druku/accepted: 06.12.2019

DOI: 10.35784/IAPGOS.131

A NEW CONCEPT OF DISCRETISATION MODEL FOR IMAGING IMPROVING IN ULTRASOUND TRANSMISSION TOMOGRAPHY

Tomasz Rymarczyk^{1,2}, Krzysztof Polakowski³, Jan Sikora^{1,2}¹Research & Development Centre Netrix SA, Lublin, Poland, ²University of Economics and Innovation in Lublin, Faculty of Transport and Informatics, Lublin, Poland,³Warsaw University of Technology, Warsaw, Poland

Abstract. In this paper a new version of discretisation model for Ultrasonic Transmission Tomography is presented. The algorithm has been extensively tested for synthetic noisy data on various configurations of internal objects. In order to improve the imaging quality, the pixels/voxels have been enlarged compared to the figures inscribed in pixels/voxels however no more than figures described on the standard square pixels or cubic voxels. The proposed algorithm provides better quality of imaging.

Keywords: Ultrasound Transmission Tomography, image reconstruction, constrained optimisation, circular pixels, spherical voxels

NOWA KONCEPCJA DYSKRETYZACJI MODELU CELEM PODNIESIENIA JAKOŚCI OBRAZOWANIA W TRANSMISYJNEJ TOMOGRAFII ULTRADŹWIĘKOWEJ

Streszczenie. W tym artykule zaproponowano nową wersję dyskretyzacji modelu dla Ultradźwiękowej Tomografii Transmisyjnej. Przedstawiony algorytm był wszechstronnie przetestowany dla danych syntetycznych zaszumionych dla różnych konfiguracji obiektów wewnętrznych. W celu poprawienia jakości obrazowania, piksele/woksele zostały powiększone w stosunku do figur wpisanych w piksele/woksele, jednak nie więcej niż figury opisane na standardowych kwadratowych pikselach lub sześciennych wokselach. Proponowany algorytm zapewnia lepszą jakość obrazowania.

Słowa kluczowe: Transmisyjna Tomografia Ultradźwiękowa, obrazowanie, optymalizacja z ograniczeniami, piksele kołowe, woksele kuliste

Introduction

The discretisation model with circle space elements [12, 14, 15] instead of classical square pixels or cuboid voxels simplifies numerical calculations on the one hand [13], but on the other hand causes complications. Under assumption that the rays have infinitely thin, some rays passing through square pixels or cubic voxels do not pass through their circular – spherical equivalents.

The area fill factor for the entered figures is suitable for 2D and 3D spaces;

$$W_{2D}=\pi/4 \text{ and } W_{3D}=\pi/6 \quad (1)$$

So in the case of 2D space less than 80% of the area is covered with circular pixels and for 3D space less than 55% of the volume is covered with a new voxels. It is obvious that this situation is a source of imaging errors.

This defect is especially visible for 3D space. To alleviate this problem, one can slightly enlarge the circular pixels or spherical voxels, moving from the figures inscribed to the figures described (see Fig. 1 and Fig. 2). The visualisation presented in Fig. 1 was made using isometric axonometry. This figure shows a cube-shaped voxel and the spheres inscribed and described on it with the common points of the projection ray and the voxel walls. Those common points were named P_c (with standard cuboid like voxel), P_{So} with sphere described and P_{Si} with sphere inscribed.

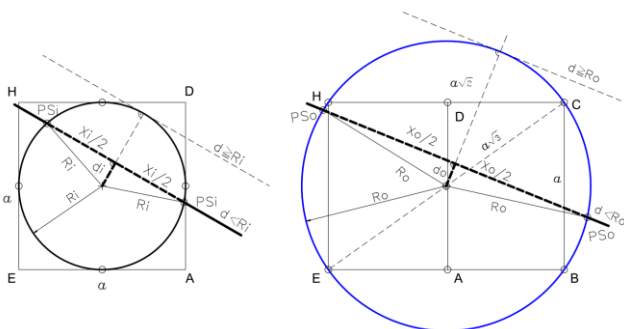


Fig. 1. A projection of a sphere inscribed in a cube and described on a cube

The radius of the sphere described R_o is $\sqrt{3}$ times greater than the radius of the sphere inscribed R_i in a cubic voxel (see Fig. 1).

If instead of the inscribed figures, the figures described were applied, then the whole space would be filled, but unfortunately the voxels would overlap, causing additional difficulties and errors resulting from this fact.

Therefore, a compromise solution was proposed consisting in increasing the radius in such a way as to fill the largest possible area of the imaged space, while at the same time the surface/volume of the overlapping pixels/voxels is as small as possible. The value of the radius increased by about 30% in relation to the inscribed radius was determined by means of a numerical experiment. Then the fill factor of the area for figures with radii increased by 30% in relation to the entered figures is respectively for 2D and 3D spaces:

$$W_{2D}=\pi/4 \cdot 1.3^2=1.327 \text{ and } W_{3D}=\pi/6 \cdot 1.3^3=1.15 \quad (2)$$

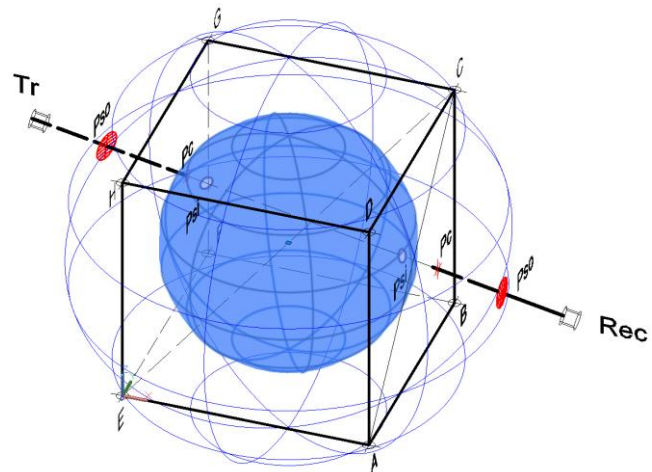


Fig. 2. Replacement of a cubic voxel with a sphere inscribed in a cube or described on a cube

1. Modifications in 2D space

In the 2D space, the square pixel has been replaced by a circular pixel inscribed in the square and then described on the square. In order to make the figures clear only the first row was shown in Fig. 3. The arc in this figure represents the edge of the region under consideration.

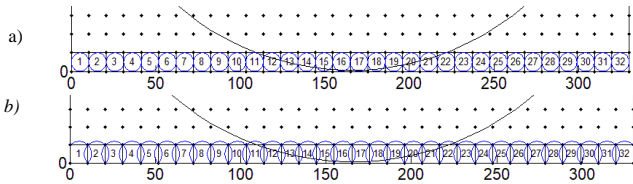


Fig. 3. Only the first row of square pixels replaced by: a) circular pixel inscribed, b) circular pixel described

In order to check the proximity effect, two closely placed objects were considered, presented in Fig. 4. The 32 sensors fixed on the perimeter of the region were considered as it was done in our previous works see for example [13]. The Algebraic Reconstruction Technique (ART) was used to formulate the system of algebraic equations [1–6, 8–10] solved by Singular Value Decomposition (SVD) [7]. The distribution of the singular values of the coefficient matrix is shown in Fig. 4b [7]. For both cases, i.e. the standard circular pixel and the increased circular pixel, the distribution practically did not differ much.

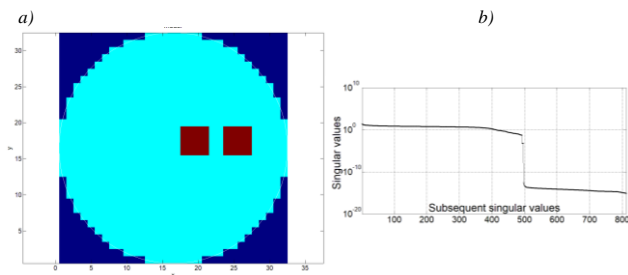


Fig. 4. Image of the model b) singular value distribution

In previous works [11, 13] for noise free signal correctness of the novel discretisation was proved. To demonstrate the advantages of pixel enlargement, a synthetic signal with 5% noise was considered, as shown in Fig. 5.

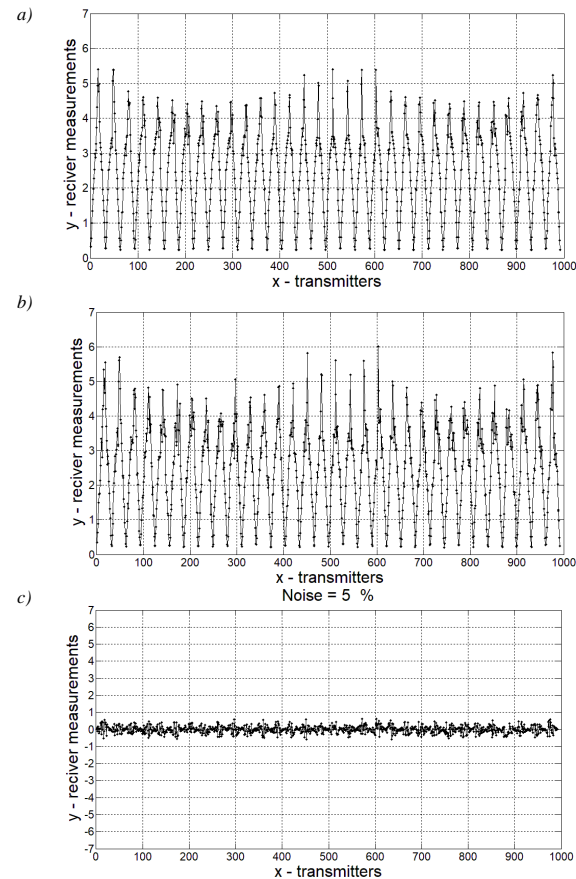


Fig. 5. "Measured" signal: a) noisy free, b) the signal with 5% noise, c) the noise

Imaging results for a standard circular pixel are presented in Fig. 6a and for a circular pixel enlarged in Fig. 6b.

In both cases, the image is acceptable, however, the pixel enlargement has improved the quality of imaging, in particular the pixel closer to the centre of the considered area, where the sensitivity of the material factor to the measuring signal is the lowest.

The obtained results may not be spectacular, which could be explained by a much higher fill factor for 2D space than for 3D space in case of inscribed pixels (see eq. 1). For this reason, the authors believe that this method will be particularly useful in matters of 3D space.

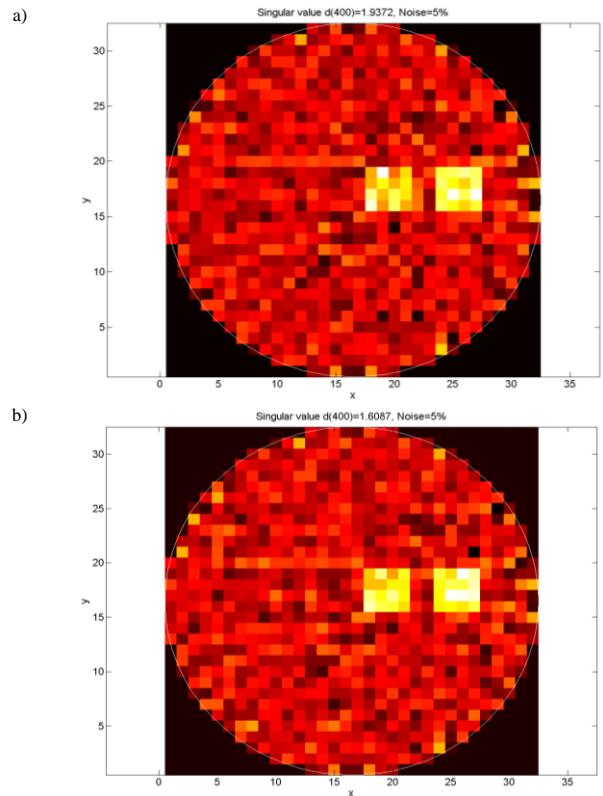


Fig. 6. Imaging results: a) for a circular pixel inscribed, b) for a circular pixel described on a square pixel

2. Modifications in 3D space

In 3D space as shown in Fig. 7, the replacement of cubic voxels with spherical voxels causes that some voxels in the path of certain rays may be omitted.

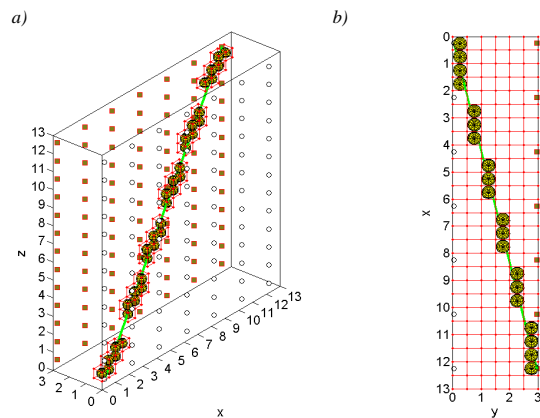


Fig. 7. Missing spherical voxels in the path of the selected ray

This problem may be alleviated by an enlarged radius, but this will result in overlapping of adjacent spherical voxels as shown in Fig. 8.

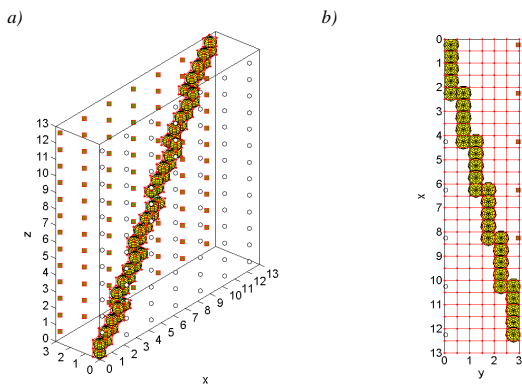


Fig. 8. Enlarged voxels along the selected ray

Let's consider a single object placed asymmetrically inside a rectangular container as shown in Fig. 9a. The sixty and four sensors were placed on the edge of the container in two layers (see Fig. 9b). To study the effect of sensor placement on imaging quality, different sensor spacing was placed in the upper and lower layers (see Fig. 9a and Fig. 9b).

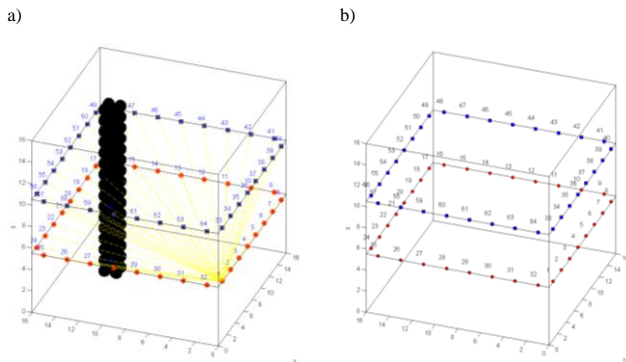


Fig. 9. Container with an internal object and two layers of sensors on its walls, the rays radiating from the first sensor are marked in yellow

To facilitate imaging, the ratio of background to material factor is 1:10 (see Fig. 10). In the same drawing, the material factor distribution is depicted in the middle of the container height.

Numerical experiments are designed to examine the effect of overlapping voxels on imaging results for transmission ultrasonic tomography in the case of synthetic data.

As can be seen in Fig. 11, the structure of the coefficient matrix changed slightly in favour of enlarged voxels, since the pseudo-order of the matrix [7] increased (see Fig. 11b).

As shown in Fig. 12 and Fig. 13 as a result of imaging, a view was obtained only of the part of the model that was in the space covered by the sensors located on the edge of the volume.

For voxels enlarged by about 30%, we see, especially in the colour map image (see Fig. 13). Clear improvement of the imaging quality could be observed. In addition, due to the change in the volume of the voxel, the matrix pseudo-order increased so that it was possible to reject 56 singular values less than for inscribed voxels [7, 11].

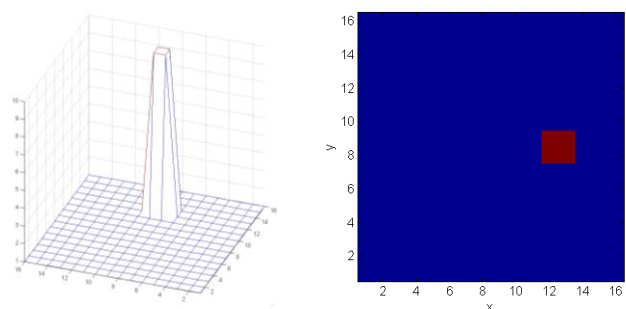


Fig. 10. In the middle of the tank height, its cross section is presented in 3D and as a coloured map

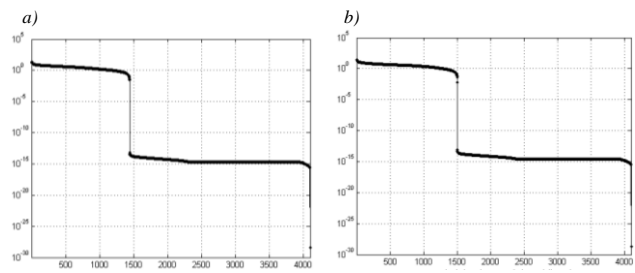


Fig. 11. Distribution of the singular values (vertical axis) versus subsequent singular values: a) for standard spherical voxels and b) enlarged radius of the spherical voxels

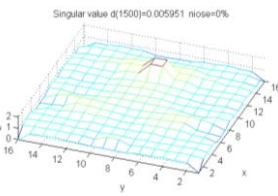
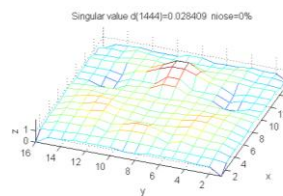
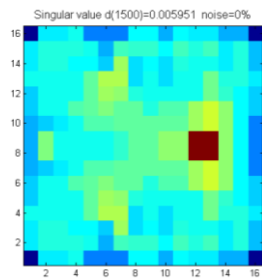
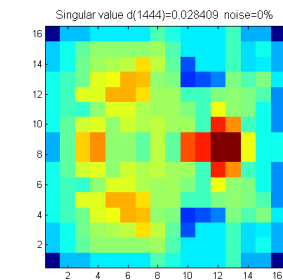
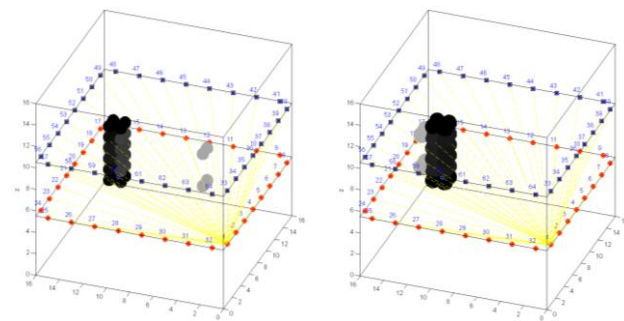


Fig. 12. Imaging results for a spherical voxel inscribed in a cubic voxel

Fig. 13. Imaging results for a spherical voxel radius increased by 30%

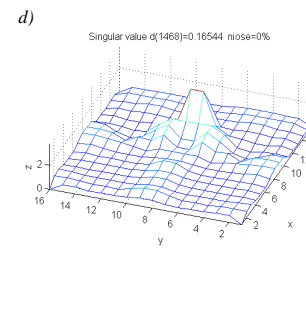
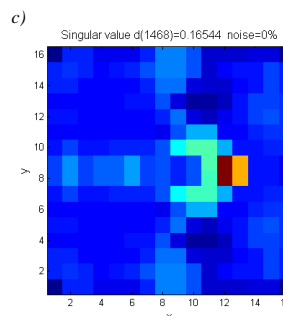
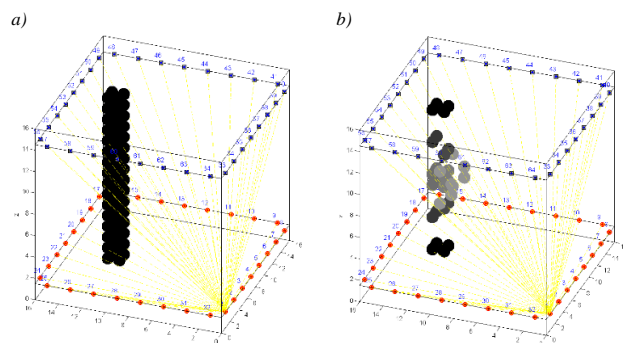


Fig. 14. Influence of spacing between sensor layers on imaging quality

The greater the distance between the sensor layers, the greater the length of the imaged internal object (see Fig. 14b), but the imaging quality deteriorates (see Fig. 14c and compare with Fig. 13).

In Fig. 14b there are significant gaps in the imaging of the internal object. But as the voxel radius is enlarged (compare Fig. 14a and Fig. 15a), the image quality has improved (compare Fig. 14b and Fig. 15b).

At the same time, an increase in the sensitivity of imaging quality to the choice of matrix pseudo-order can be observed (see Fig. 14c & d and Fig. 15c & d).

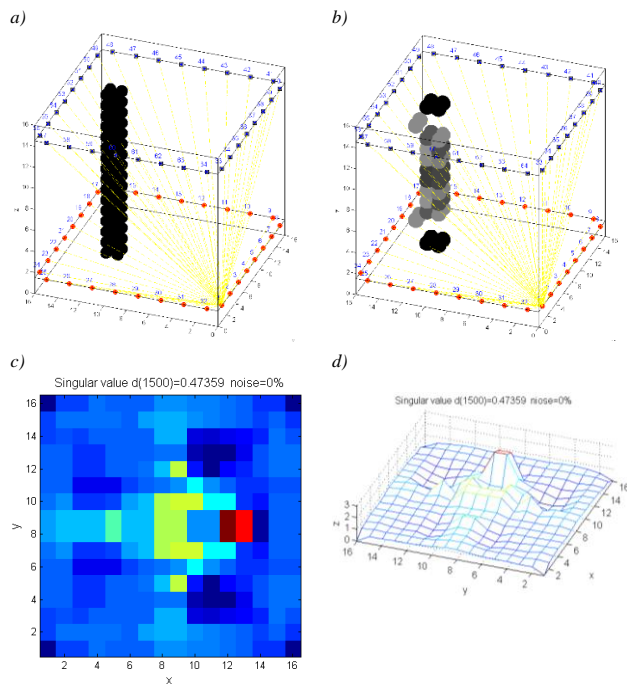


Fig. 15. Influence of spacing between sensor layers on imaging quality

3. Conclusion

In this paper a new algorithm for Ultrasound Transmission Tomography was presented. Based on experiments with synthetic noisy data conclusion can be stated as follows:

1. The algorithm with overlapped pixels/voxels provides stable and precise images,
2. For 2D space the results for enlarged pixels are not so impressive since the fill coefficient is much higher (see eq. 1) than for 3D space. So, there is not much space for improvement of ART method in this case.
3. Scale of enlargement of the radiuses for the pixels or voxels depends on the object or objects inside of the region and must be carefully selected depending on the case.

The authors would like to state that all figures were drawn with the aid of MATLAB [16].

References

- [1] Bartušek K., Drexler P., Fiala P., et al.: Magnetoinductive Lens for Experimental Mid-field MR Tomograph. Progress in Electromagnetics Research, Cambridge, 5–8 July 2010, 1047–1050.
- [2] Dušek J., Hladký D., Mikulka J.: Electrical Impedance Tomography Methods and Algorithms Processed with a GPU. PIERS Proceedings (Spring) 2017, 1710–1714.
- [3] Kak A. C., Slaney M.: Principles of Computerized Tomographic Imaging. IEEE Press, New York 1999.
- [4] Klosowski G., Rymarczyk T.: Using Neural Networks and Deep Learning Algorithms in Electrical Impedance Tomography. Informatyka, Automatyka Pomiar w Gospodarce i Ochronie Środowiska – IAPGOS 3/2017, 99–102.
- [5] Klosowski G., Rymarczyk T., Gola A.: Increasing the Reliability of Flood Embankments with Neural Imaging Method. Applied Sciences 8(9)/2018, 1457.

- [6] Koulountzios P., Rymarczyk T., Soleimani M.: Ultrasonic Tomography for automated material inspection in liquid masses. 9th World Congress on Industrial Process Tomography, Bath, Great Britain, 2–6 September 2018.
- [7] Lawson Ch. L., Hanson R. J.: Solving Least Squares Problems. Classics in Applied Mathematics 15/1995.
- [8] Mikulka J.: GPU–Accelerated Reconstruction of T2 Maps in Magnetic Resonance Imaging. Measurement Science Review 4/2015, 210–218.
- [9] Ming Y., Schlager H. I., Hoyle B. S., Beck M. S., Lenn C.: Real-Time Ultrasound Process Tomography for Two-Phase Flow Imaging Using a Reduced Number of Transducers. IEEE Transactions on Ultrasonics, Ferroelectrics, and Freq. Control 46(3)/1999.
- [10] Opieliński K. J., Gudra T.: Ultrasonic Transmission Tomography in Industrial and Biological Tomography: Theoretical Basis and Applications. Electrotechnical Institute, 2010, 265–338.
- [11] Rymarczyk T.: Tomographic Imaging in Environmental, Industrial and Medical Applications. Innovatio Press Publishing House, 2019.
- [12] Rymarczyk T., et al.: Sposób i układ do prowadzenia pomiarów w elektrycznej tomografii pojemnościowej. Patent P.418304, data zgłoszenia: 12.08.2016.
- [13] Rymarczyk T., Sikora J., Polakowski K., Adamkiewicz P.: Efektywny algorytm obrazowania w tomografii ultradźwiękowej i radiowej dla zagadnień dwuwymiarowych. Przegląd Elektrotechniczny 94(6)/2018, [DOI: 10.15199/48.2018.06.11].
- [14] Smolik W.: Forward Problem Solver for Image Reconstruction by Nonlinear Optimisation in Electrical Capacitance Tomography. Flow Measurement and Instrumentation 21/2010, 70–77.
- [15] Soleimani M., Mitchell C. N., Banasiak R., Wajman R., Adler A.: Four-dimensional electrical capacitance tomography imaging using experimental data. Progress in Electromagnetics Research 90/2009, 171–186.
- [16] <http://www.mathworks.com/products/matlab/> (access: June 2018).

Ph.D. Eng. Tomasz Rymarczyk

e-mail: tomasz@rymarczyk.com

He is the director in Research and Development Centre in Netrix S.A. and the director of the Institute of Computer Science and Innovative Technologies in the University of Economics and Innovation, Lublin, Poland. He worked in many companies and institutes developing innovative projects and managing teams of employees. His research area focuses on the application of non-invasive imaging techniques, electrical tomography, image reconstruction, numerical modelling, image processing and analysis, process tomography, software engineering, knowledge engineering, artificial intelligence and computer measurement systems.

ORCID ID: 0000-0002-3524-9151

D.Sc. Eng. Krzysztof Polakowski

e-mail: kp@zkue.ime.pw.edu.pl

Krzysztof Polakowski graduated from Warsaw University of Technology Faculty of Electrical Engineering. During the last year of his studies He was employed in the department of Electrical Machines of the WUT, where he defended his PhD and DSc degree. His scientific interest concentrated on 3D modelling with the aid of CAD and also on electro-mobility. Also he is interested in tomography application in the car industry. He is cofounder of specialisation devoted the Car Electricity in Warsaw University of Technology.

ORCID ID: 0000-0002-2301-4910

Prof. Jan Sikora

e-mail: sik59@wp.pl

Prof. Jan Sikora (Ph.D. D.Sc. Eng.) graduated from Warsaw University of Technology Faculty of Electrical Engineering. During 44 years of professional work he has proceeded all grades, including the position of full professor at his alma mater. Since 1998 he has worked for the Institute of Electrical Engineering in Warsaw. In 2008, he has joined Electrical Engineering and Computer Science Faculty in Lublin University of Technology. During 2001–2004 he has worked as a Senior Research Fellow at University College London in the prof. S. Arridge's Group of Optical Tomography. His research interests are focused on numerical methods for electromagnetic field. He is an author of 8 books and more than 180 papers published in the international journals and conferences.

ORCID ID: 0000-0002-9492-5818

otrzymano/received: 10.09.2019

przyjęto do druku/accepted: 06.12.2019



EVALUATION OF THE ELECTRICAL CAPACITANCE TOMOGRAPHY SYSTEM FOR MEASUREMENT USING 3D SENSOR

Jacek Kryszyn, Damian Wanta, Waldemar T. Smolik

Warsaw University of Technology, Division of Nuclear and Medical Electronics, Institute of Radioelectronics and Multimedia Technology, Warsaw, Poland

Abstract. Further tests of EVT4 data acquisition system for electrical capacitance tomography are presented. The modular system, which can have up to 32 channels with an individual analogue to digital converter, was designed to ensure small uncertainty of capacitance measurement at high speed of imaging. The system's performance in the context of 3D imaging was experimentally verified. In particular, we show that the measurement of changes in capacitance due to a small change of an electric permittivity distribution for the most distant electrodes in a suitably designed 3D sensor is possible using our system. Cross-plane measurements together with the measurements for the pairs of most distant electrodes are essential for accurate reconstruction of 3D distributions. Due to sensitivity of capacitance measurements obtained in the hardware, the measurements for all electrode pairs can be used in the inverse problem – the system of equations can be extended. Although the numerical condition number of a matrix of such a system is high, image reconstruction is possible from the data obtained in our system. The results of 3D image reconstruction for simple test objects are shown.

Keywords: electrical capacitance tomography, image reconstruction, capacitance measurement, inverse problems, numerical stability

OCENA SYSTEMU ELEKTRYCZNEJ TOMOGRAFII POJEMNOŚCIOWEJ DO POMIARÓW Z WYKORZYSTANIEM SONDY 3D

Streszczenie. Przedstawiono dalsze testy systemu akwizycji danych EVT4 do elektrycznej tomografii pojemnościowej. Modułowy system, który może mieć do 32 kanałów z indywidualnym przetwornikiem analogowo-cyfrowym, został zaprojektowany w celu zapewnienia małej niepewności pomiaru pojemności przy dużej prędkości obrazowania. Wydajność systemu w kontekście obrazowania 3D została zweryfikowana eksperymentalnie. W szczególności pokazujemy, że możliwy jest pomiar zmian pojemności wywołanych niewielką zmianą rozkładu przenikalności elektrycznej dla najbardziej odległych elektrod odpowiednio zaprojektowanego czujnika 3D przy pomocy naszego systemu. Pomiarzy międzypłaszczyznowe wraz z pomiarami par elektrod najbardziej odległych są niezbędne do dokładnej rekonstrukcji rozkładów 3D. Ze względu na wrażliwość pomiarów pojemności uzyskanych w opracowanym urządzeniu, pomiary dla wszystkich par elektrod mogą być wykorzystane w problemie odwrotnym – układ równań może zostać rozszerzony. Choć współczynnik uwarunkowania numerycznego macierzy takiego układu jest wysoki, możliwa jest rekonstrukcja obrazu z wykorzystaniem danych uzyskiwanych w naszym systemie. Pokazane są wyniki rekonstrukcji obrazu 3D dla prostych obiektów testowych.

Słowa kluczowe: elektryczna tomografia pojemnościowa, rekonstrukcja obrazów, pomiar pojemności, problem odwrotny, stabilność numeryczna

Introduction

Electrical capacitance tomography (ECT) enables visualization of a spatiotemporal distribution of electric permittivity [8]. High frame rate which can be provided by the hardware makes this technique an important research tool in chemical and process engineering [4]. The application of ECT is limited by low spatial resolution resulting from poor spatial sampling i.e. small number of sensing electrodes in the tomographic sensor [35]. The number of electrodes cannot be increased due to a very low value of mutual capacitance of opposite electrodes. Particularly, in case of a three dimensional electrode layout in the tomographic sensor, the capacitance value of most distant electrodes is very low, of the order of a few femtofarads. A problem of measurement of extremely low capacitance values in a 3D sensor is the major barrier in the development of 3D ECT [1, 31].

Although feasibility of 3D ECT (or electrical capacitance volume tomography – ECVT) is an open question [34], 3D process visualization using ECT raises interest [16, 22, 23, 29, 32]. The theoretical advantage of 3D ECT lies in correct modelling of inherently 3D electric field distribution in a tomographic sensor that assures correctness of the model used in solving of the ECT inverse problem. Single plane measurements enable only coarse approximation of electric permittivity distribution in a cross section of an examined volume.

Specialized measurement methods were elaborated by several groups to overcome problems with very small capacitance measurement in ECT [5, 7, 10, 17, 33]. New ECT and EIT hardware was developed to increase the throughput of contemporary data acquisition systems [3, 9, 28, 30, 38]. The state of the art in measurement methods and data acquisition systems development for ECT together with performance comparison was presented in [13] and [24].

The construction of hardware for ECT has been developed in our laboratory for two decades [2, 21]. The EVT4 data acquisition

system – our latest design – is a modular system which can have up to 32 channels [13]. Theoretically, due to the number of channels and the high signal to noise ratio (SNR) it can be used for measurements with a 3D tomographic sensor. In this paper an experimental verification of performance of our tomographic system working with a 3D sensor is presented. The suitability of EVT4 data acquisition system for 3D tomography is analyzed.

1. Methods

1.1. Small capacitance measurement method in EVT4 data acquisition system

The architecture of the EVT4 hardware is based on fast programmable devices [13]. The multi-channel system is modular and can have from 4 to 32 channels (Fig. 1). An individual analogue to digital converter in each channel and multi gigabit serial transmission enable high data throughput required in dynamic imaging.



Fig. 1. EVT4 data acquisition system for ECT

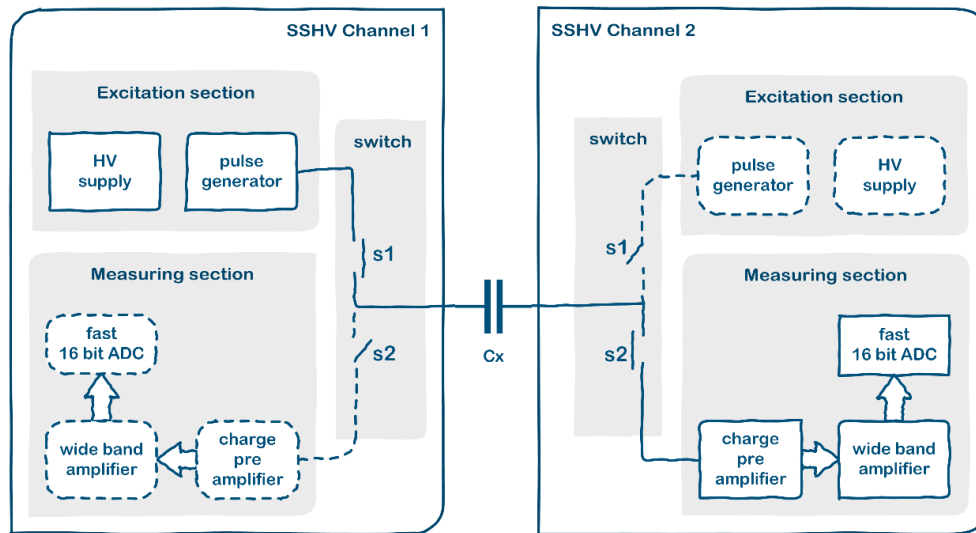


Fig. 2. Channel of the front-end board with the excitation and measuring section

EVT4 system performance is determined by a method used for the capacitance measurement. In the single-shot high voltage (SSHV) method [24], a single pulse excitation increases the speed of the measurement, whereas a high amplitude of the excitation and oversampling of the output signal preserve high signal to noise ratio. The current is integrated using a charge preamplifier while a voltage pulse is applied to the measured capacitance (Fig. 2). The height of the output pulse is proportional to the value of measured capacitance. The output signal is sampled using a fast ADC 14 μ s before the pulse, during the pulse which lasts 14 μ s and 14 μ s after, giving the measurement time below 50 μ s. Nevertheless, an additional time (about 20 μ s) is needed to adjust the gain of the first and second stage amplifiers. With measurement duration of about 62 μ s the theoretical speed of tomographic imaging is equal to about 500 frames per second (fps) for a multichannel tomographic system working with a sensor with 32 electrodes. Currently, each excitation is additionally delayed, so the whole measurement takes 100 μ s which results in 312 fps for a 32-channel tomographic sensor.

The SSHV circuit is linear in the range from about 1 fF to 1 pF. The signal to noise ratio (SNR) is equal from 61 dB for the capacitance value of about 1 pF to 13 dB for 1 fF with constant, lowest gain in the preamplifier. With the gain adjustment in the first amplifier stage, the SNR increases to 22 dB for measured value of 1 fF [12]. The capacitance resolution corresponds to the root mean square (rms) of noise equal to about 0.76 fF/bit and 0.013 fF/bit for the smallest and highest gain in the preamplifier, respectively.

1.2. 3D sensor design

A typical 3D capacitance sensor has a cylindrical shape and electrodes arranged in a few rings [26, 32], however different shapes and layouts of electrodes were proposed in the literature [20]. Comparison of various three-dimensional probes were made in [25] on the basis of numerical simulation. The authors considered various topologies and the number of electrodes, from one ring with 8 electrodes up to a cubic sensor consisting of 54 electrodes surrounding the entire imaged area. To equalize the sensitivity in the whole visualized area, a three-dimensional sensor of a unique structure was proposed in [1]: a different number of electrodes in the rings (6 electrodes in the outer rings, 10 electrodes in the inner rings). The analysis of the number of electrodes of three-dimensional sensor was presented in [27]. The results obtained for various test objects shown that a 24-electrode three-dimensional probe always gives better results than a 12-electrode three-dimensional sensor. It is often proposed to move the rings relative to each other by a certain angle like in [37]. To increase the number of measurements, a multi-electrode excitation can be used [18]. In such a way the signal-to-noise ratio

will be increased, but the spatial sampling frequency will be still small. A similar idea was proposed in [19]. The conditioning of the sensitivity matrix depends on the geometry of the electrodes. As shown in [15], the ratio of electrode lengths in Z axis to their angular widths equal to 0.75 is the best for a probe having 4 rings of 6 electrodes. The influence of a 3D sensor geometry on sensitivity maps has been discussed also in [39, 40]. The more radical strategy in 3D ECT implementation is to eliminate the electrode combinations for which the measurement is not possible because of the signal value below the noise level [14].

The 3D sensor design is important from the measurement and image reconstruction points of view. Too long electrodes in Z axis make the capacitance measurement using pairs of electrodes from different outer rings impossible. Too short electrodes cause the signal-to-noise ratio to be bad for all measurements. A large measurement range of capacitance values has a reflection in a very bad condition number of the sensitivity matrix (system function) which makes the inverse problem very ill posed [14].

The 3D tomographic sensor used in the experiment was designed using the principles mentioned above. The sensor was a cylindrical tube with 32 rectangular electrodes arranged in 4 rings with 8 electrodes in each ring (Fig. 3). The inner diameter of the cylinder was 152 mm and the height was 195 mm (265 mm with the guard electrodes). The electrode geometry was adjusted heuristically to the capacitance measurement range of the EVT4 hardware. The aspect ratio of the electrode dimensions and the distance between the electrodes was selected to avoid capacitance values larger than 500 fF for adjacent electrodes (when the sensor is fully filled with a material of maximum permittivity value) and smaller than a few fF for the opposite electrodes from outermost rings (when the sensor is empty). To limit the range of capacitance values, the distance between the adjacent in-ring electrodes was relatively large (half of the electrode width). To increase the mutual capacitance of the electrodes from the outermost rings, the height of the electrodes in these rings was enlarged (doubled) compared with the height of the electrodes from the central rings. The distance between rings was minimized. The smallest value of cross-ring mutual capacitance is about 2 fF for an empty sensor. To increase sampling on the circumference [18] the electrodes in adjacent rings were shifted by a half distance between electrodes (Fig. 3a).

The electrodes were made of copper foil (200 μ m) mounted inside the PVC cylinder. The electrodes were insulated from the field of view of the sensor by the transparent PVC foil with the thickness equal to 0.8 mm. PVC has dielectric breakdown voltage equal to 40 kV/mm which means that the foil is thick enough to avoid electrical breakdown when using 200 V in the measurement circuit. The guard electrodes were mounted outside the four rings of electrodes. The sensor was shielded using a grounded steel wire mesh surrounding the PVC tube.

An absolute value of mutual capacitance of electrodes for the built model of a 3D sensor was calculated from measurements made using a voltage divider. A known impedance was added for the time of measurements to eliminate the influence of stray impedance on the results. The sinusoidal signal of frequency equal to 10 kHz and known amplitude and phase was used as an excitation signal in the calibration circuit. A lock-in amplifier was used to measure real and imaginary parts of the output voltage. The uncertainty of capacitance value estimation was below 3%.

The mutual capacitance of electrodes was also measured using the selected channel of the EVT4 hardware. The lowest gain in the preamplifier was used. The real value of the voltage to capacitance gain was estimated using a standard capacitor of the value equal to 100 fF. The capacitance value in farads was calculated from the ADC value using the formula:

$$C_x = \frac{1}{0.341} \left[\frac{pF}{V} \right] \times 4.096[V] \times \frac{adc_value}{32767} \quad (1)$$

where 0.341 V/pF is the gain of the measurement circuit, 4.096V is a half of reference voltage of ADC, 32768 is a half of range of ADC. The uncertainty of single measurement of capacitance was from 1 % for 300 fF to 50 % for 1 fF.

The plot of mutual capacitance values of electrode number 1 with other electrodes of the sensor is shown in Fig. 4. In the case of measurements made using the EVT4 system, the mean value from 100 measurements is taken. A characteristic U-curve for circular sensor is repeated 4 times for four rings of electrodes. The data obtained with EVT4 data acquisition system (the mean value from 100 measurements) are in accordance with the calibration measurements except the range of the smallest values.

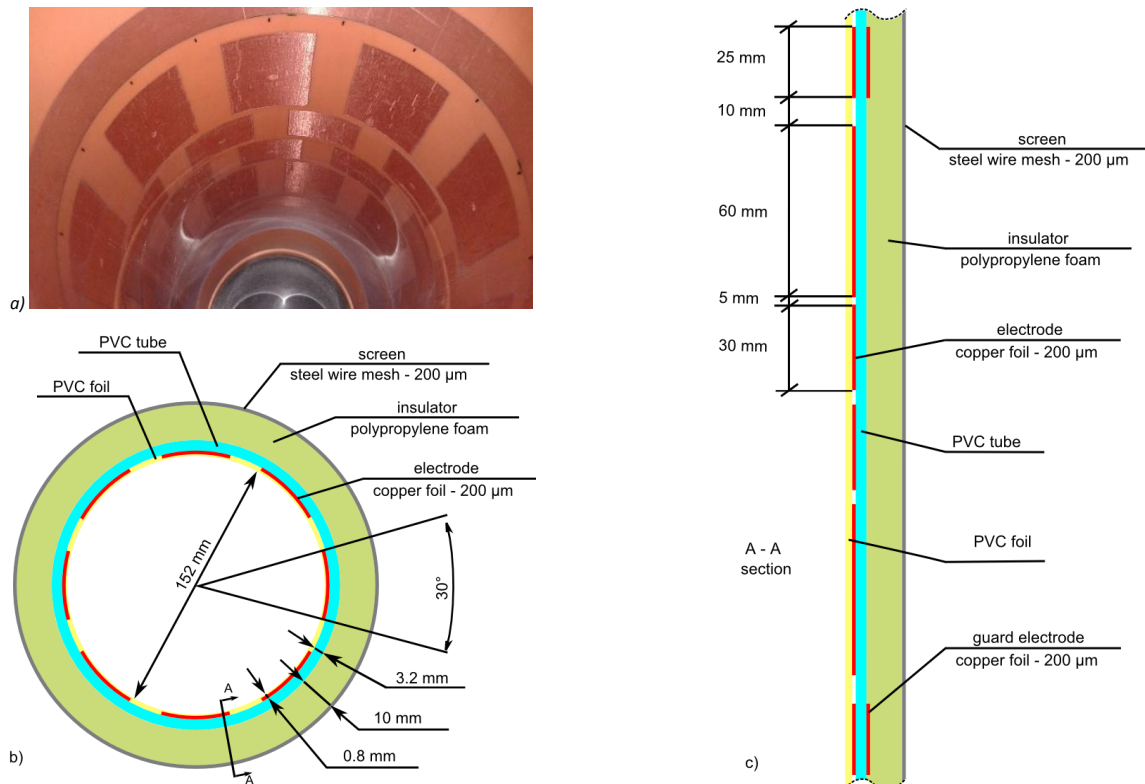


Fig. 3. 3D sensor. 32 electrodes (4 rings of 8 electrodes each). a) View of the interior of the sensor. b) Sketch of an axial cross-section. c) Sketch of a longitudinal cross-section. The size of the field of view of the sensor is not in scale with reference to other dimensions for sketch clarity

1.3. Experimental verification of measurement sensitivity

To evaluate the possibility of applying the EVT4 data acquisition system for three dimensional (3D) tomography, the sensitivity of capacitance measurements was verified experimentally. The sensitivity of mutual capacitance values of electrodes on a small change of permittivity value in a small volume defined as $\partial C/\partial \epsilon$ was measured by perturbing a uniform permittivity distribution by means of using a small object with low permittivity. The mutual capacitance values of electrode number 1 and the other electrodes of the sensor were measured without and with a perturbation. The cylinders of the same width and height equal to 10, 20 and 30 mm were used. The cylinders were made of different materials: Teflon (Polytetrafluoroethylene, PTFE), Kepital (Polyoxymethylene, POM) and alumina (Aluminium oxide). The relative permittivity of these materials is given in Table 1. Because the sensitivity map for a given pair of electrodes is not uniform, the objects were placed in the region of small sensitivity i.e. in the center of the sensor and in the region of high sensitivity, near the measuring electrode. Four positions near the opposite electrode to the electrode 1 (the excitation electrode) in each of four rings of the 3D sensor were selected as shown in Fig. 5.

Table 1. Relative electric permittivity of test objects

Material	Relative permittivity
Polytetrafluoroethylene (PTFE) (Teflon)	2.1
Polyoxymethylene (POM) (Kepital F30-03)	3.9
Aluminium oxide (alumina) 96%	9.3 – 11.5

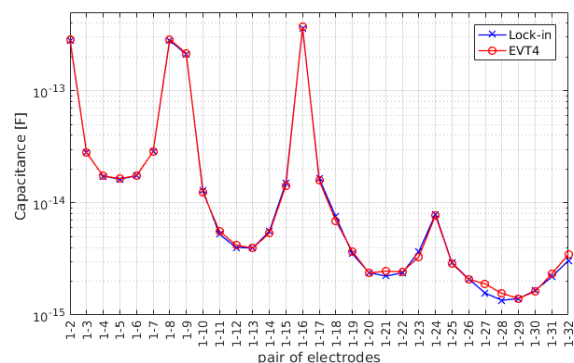


Fig. 4. Mutual capacitance of electrodes in the empty 3D sensor. Capacitance values measured using the lock-in amplifier and one selected channel of the EVT4 system (mean value from 100 EVT4 measurements)

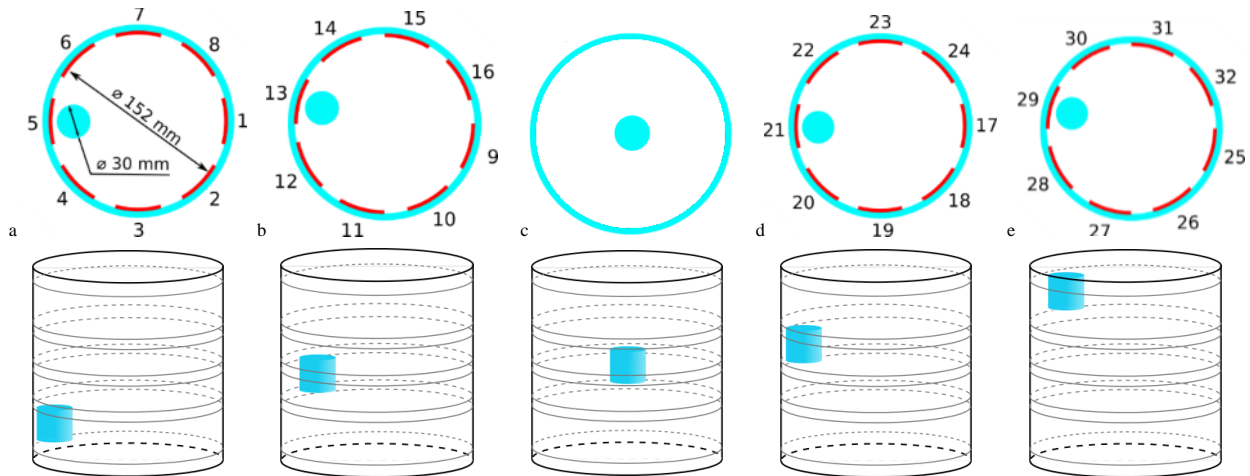


Fig. 5. Positions of the test object (cylinder of the height equal to the width) in the plane outlined by the ring of electrodes: a) top plane, b) second plane, c) third plane, d) bottom plane, e) center of sensor

All obtained measurement data were presented with normalization using minimum and maximum measurements. The empty sensor and the sensor fully filled with a material were measured to determine a range of changes in mutual capacitance of the 3D sensor electrodes. The maximum value of capacitance was registered when the sensor was filled with the granules of polyoxymethylene (POM).

1.4. Image reconstruction

The linear approximation of nonlinear problem existing in ECT was assumed in image reconstruction. Therefore, tomographic measurement can be described using formula:

$$\Delta c = S \Delta \varepsilon \quad (2)$$

where Δc is the vector of measured capacitance change, S is the sensitivity matrix (Jacobian matrix) and $\Delta \varepsilon$ is the vector of permittivity change in the points of a three dimensional discrete grid. The length of data vector Δc is determined by combinations of 2 electrodes from $K=32$ sensor electrodes and equals $N=K(K-1)/2=496$. Because the spatial sampling in measurement is limited, the size of the three dimensional grid of a reconstructed spatial distribution of electrical permittivity was selected to $16 \times 16 \times 24$ voxels, each of size $9 \text{ mm} \times 9 \text{ mm} \times 9 \text{ mm}$, in the X-, Y- and Z-axis of the cylinder, respectively. This gives $M=4968$ unknowns (a cylinder inscribed in a cuboid). The ratio of the number of measurements to the number of unknowns equals 0.1, what is a bit less than 0.14 in case of 2D reconstruction of 32×32 image matrix using 120 measurements from 16 electrodes (804 points of a circle inscribed in a square). Thus the 3D inverse problem is a little more underdetermined.

The numerical model of the sensor was built and electrical field modelling was performed using ECTsim 3.0 toolbox for Matlab [11, 41]. The computed 3D sensitivity maps for capacitance measurements give the sensitivity matrix of linearized model which dimensions equal to $M \times N$. The condition number of the sensitivity matrix was $1.05e7$ what indicates extreme ill-conditioning.

Because of channel-to-channel variability of parameters in a multichannel device, it is a good practice to normalize the measured values to the minimum-maximum in the channel. Thus, all equations of this linear system were normalized using the difference between minimal and maximal values of capacitance i.e. for the empty sensor and the sensor fully filled with the material. This procedure not only corrects channel variability but also acts as a matrix preconditioning and decreases the condition number of the sensitivity matrix to $5.82e5$ [36].

To show that the cross-plane measurements together with the values for the pairs of most distant electrodes contain useful information, image reconstruction was performed using complete and incomplete data model. Complete data are the measurements for all electrode combinations ($N_c=496$). The incomplete model was built by elimination of the rows of the linear system for the

measurements of pairs of electrodes for which the distance between rings is more than 2. For given electrode, the mutual capacitance of this electrode and the electrodes in the same ring and the adjacent ring are measured only. $N_{in}=304$ pairs of electrodes are included into a model with this distance. The advantage of this procedure is that the elimination of the measurements of the smallest values i.e. the most distant cross-planes electrodes from the system significantly reduces condition number to $4.77e3$.

A unique solution of severely underdetermined problem given by (2) was found by solving minimum norm least square problem. The minimum norm solution was calculated using truncated singular value decomposition (TSVD) due to the ill-conditioning of the sensitivity matrix. The value of regularization parameter (truncation level) was calculated using the L-curve method for the incomplete model [6]. For the complete model the shape of the L-curve did not look like an L-letter but rather as rotated W-letter with two corners. Because of this, the value of the regularization parameter was determined manually by selecting the value from the correct corner of the curve.

1.5. Results

The normalized capacitances (31 values for pairs with electrode no 1) measured for the test cylinder made of POM (Kepital) are shown in the Fig. 6. The data for a different diameter of the cylinder are presented in separated charts. The capacitances were normalized using maximum and minimum values obtained for the fully filled with POM and empty sensor, respectively. Five curves for five positions of the test object are plotted. The peak in each curve corresponds to the position of the test object near the receiving electrode (5th, 13th, 21th and 29th electrode) located in one of four rings of the sensor. For the position of the object in the center of the sensor, the change of the capacitance is noticeable for many electrodes, but mainly for the electrodes adjacent to the electrodes: 5th, 13th, 21th and 29th.

Other changes in the presented curves (positive and small negative) correspond to the spatial distribution of capacitance measurement sensitivity on permittivity change in a small element of space. For some electrode pairs the permittivity change (a cylindrical test object) was located in the region of positive sensitivity, but for other electrode pairs this perturbation was placed in the region of negative sensitivity. The value of the highest positive peak for each of four positions of the test object is different because of the different sensitivity distribution and different size of the electrodes. The phantom covers less of the area of the receiving electrode in case of positioning it next to the 5th and 29th electrodes, hence the normalized capacitance change is smaller in those cases. The ratio of permittivity perturbation to the electrode pair capacitance is smaller in a case of the electrode pair 1-5 than in a case of the electrode pair 1-29 so the relative change of the capacitance is also smaller.

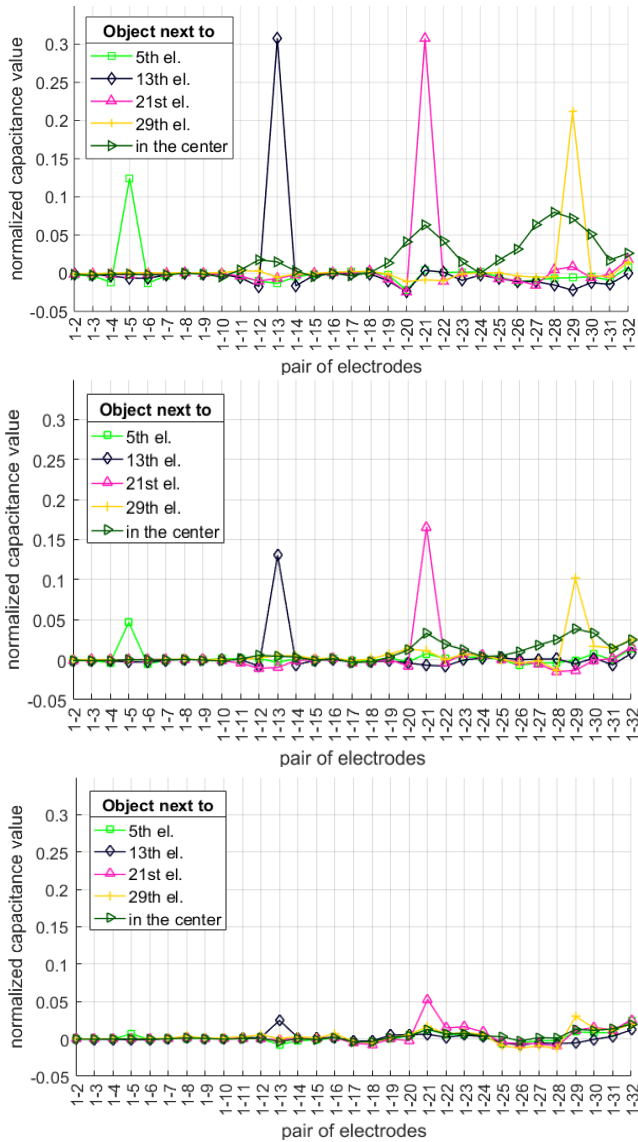


Fig. 6. Mutual capacitance of electrodes in the 3D sensor for five positions of the test object (POM cylinder) of the different diameter: a) 30 mm, b) 20 mm; c) 10 mm

Normalized capacitance value in a function of object size for different materials is shown in Fig. 7. The perturbation of a permittivity distribution in form of a small object causes a noticeable change of capacitance value for all tested materials. Even for the material with the lowest permittivity value it is possible to observe a change of capacitance value for all electrodes (Fig. 7c).

The three-dimensional image reconstruction of the relative permittivity distribution was performed using the measurement data registered using the EVT4 system. The cross-axial (XY plane) and longitudinal (XZ plane) slices through the 3D volume of the sensor were obtained for different positions of the test object. Additionally, the 3D visualization of reconstructed object was generated. The object surface was found by thresholding segmentation of relative permittivity distribution. The value of the threshold was selected heuristically. Fig. 8 and Fig. 9 show the reconstruction results obtained for the different size of the test cylinder: 30 and 10 mm, accordingly. The position of the objects can be identified for all their positions however the spatial resolution is too poor to reconstruct the shape of the object. The position can be identified even for the smallest object of 10 mm size.

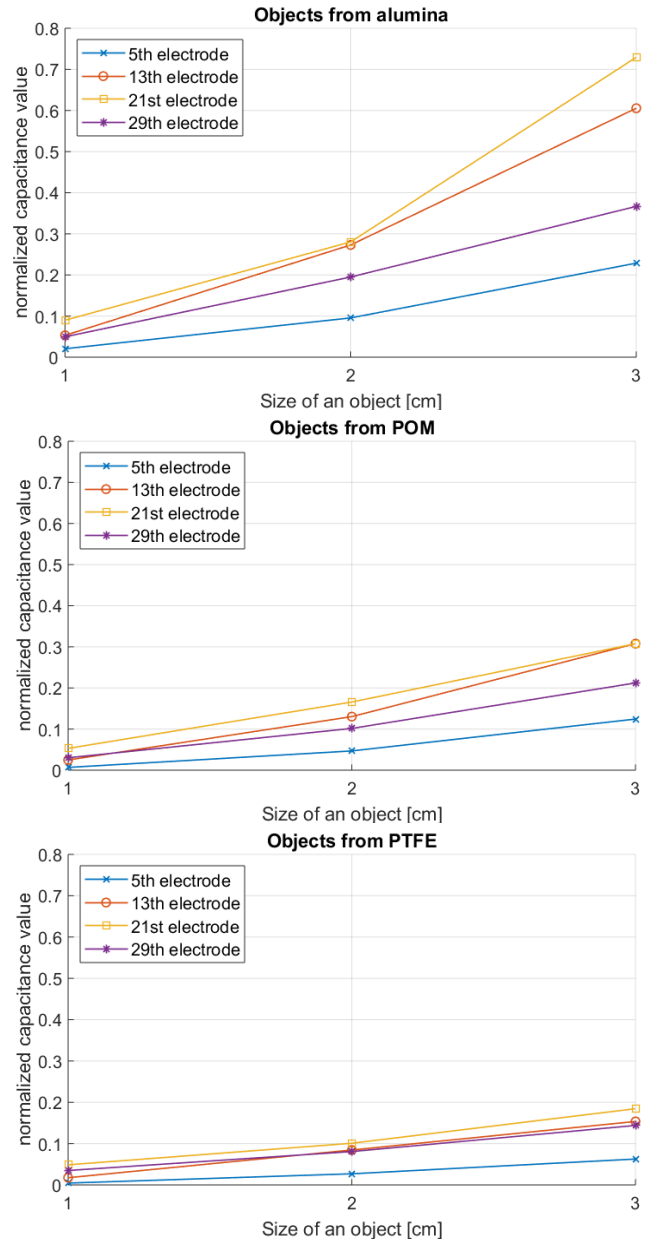


Fig. 7. Normalized mutual capacitance of electrodes in the 3D sensor in function of size of the test cylinders. Three charts for objects made of: a) Teflon, b) Kevlar and c) alumina. Plots for four positions of the test objects

Fig. 10 and Fig. 11 show the reconstruction results obtained for the complete set and incomplete set of measurements, 496 and 304 equations in the linear system accordingly. The slices and isosurfaces are presented for the 20 mm cylinder. As for the 30 and 10 mm objects, the shape of the object was not reconstructed well enough but the position of the object can be identified. The quality of presented images for the complete set and incomplete set is comparable, however the image reconstruction error is smaller for the images obtained using the complete model (Table 2).

Table 2. Image reconstruction error. L2 distance of the reconstructed image to the true permittivity distribution

Material	Number of measurements	
	496	304
near the 5th electrode	0.0268	0.0332
near the 13th electrode	0.0446	0.0697
at center	0.0266	0.0282
near the 21th electrode	0.0870	0.0633
near the 29th electrode	0.0433	0.0546

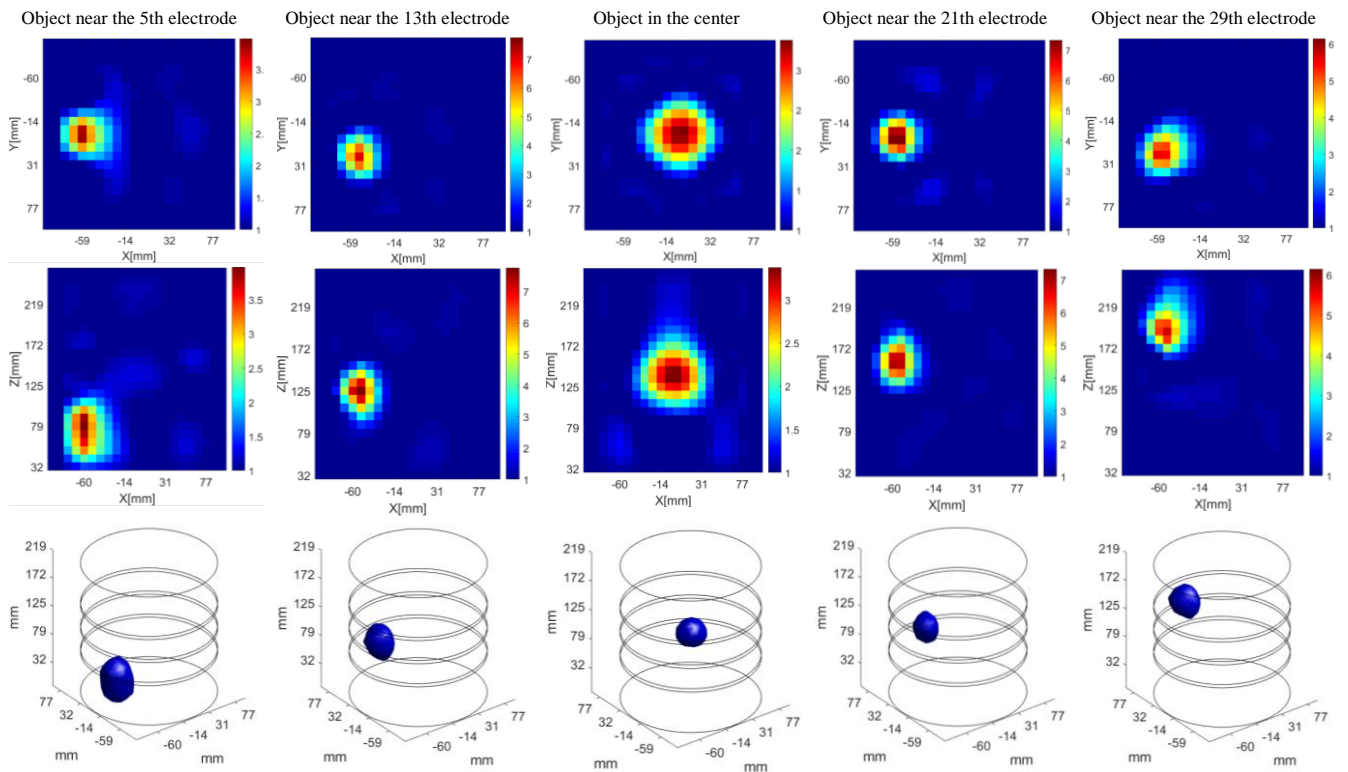


Fig. 8. 3D relative permittivity distribution obtained for a cylinder (width and height equal to 30 mm) in different positions in the sensor. Upper row: XY cross-sections. Middle row: XZ cross-sections. Bottom row: Isosurface determined by threshold segmentation, shaded by the Phong method

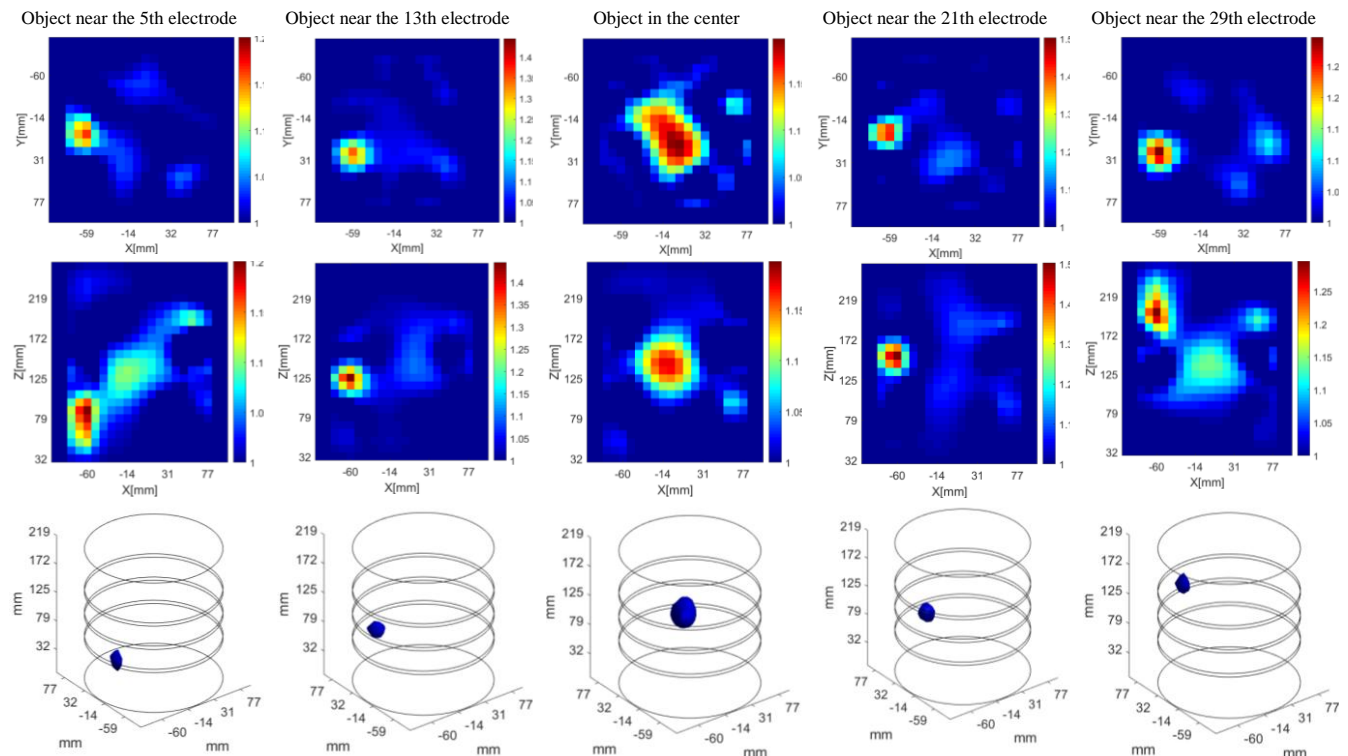


Fig. 9. 3D relative permittivity distribution obtained for a cylinder (width and height equal to 10 mm) in different positions in the sensor. Upper row: XY cross-sections. Middle row: XZ cross-sections. Bottom row: Isosurface determined by threshold segmentation, shaded by the Phong method

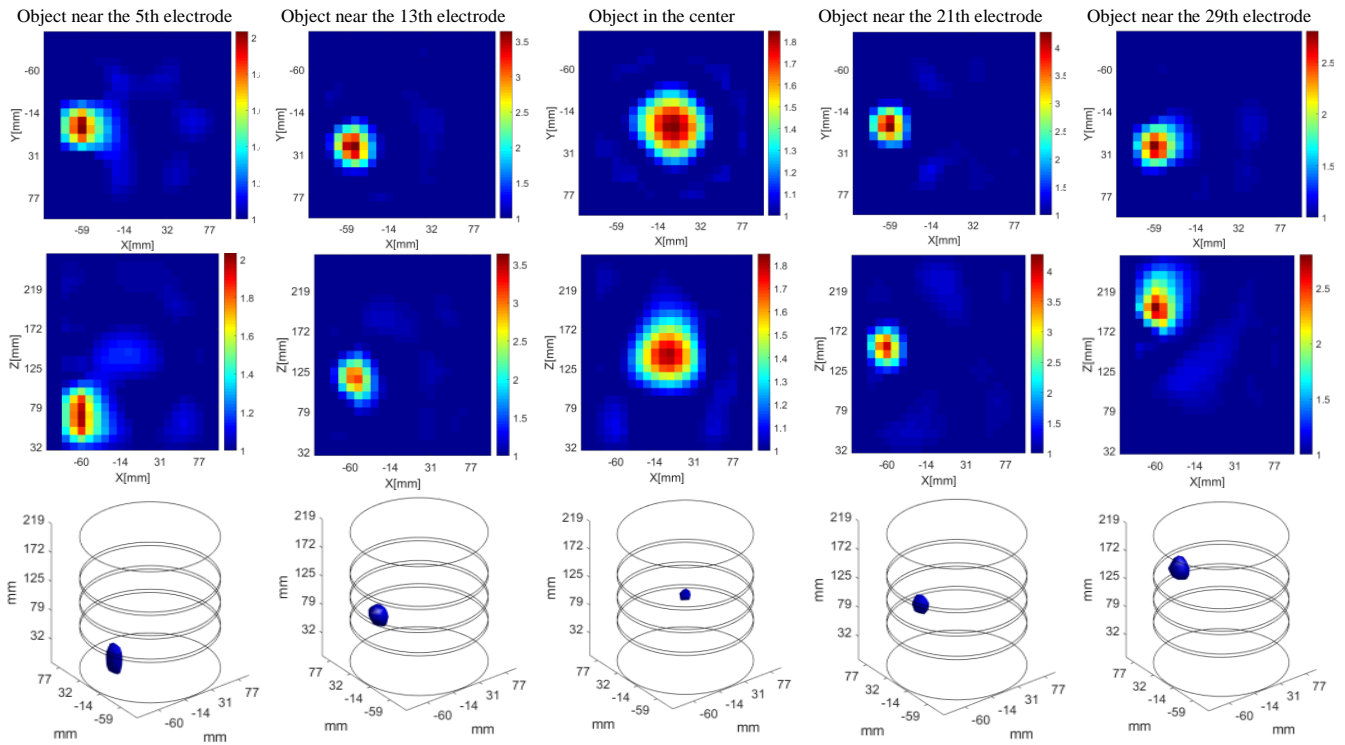


Fig. 10. 3D relative permittivity distribution obtained for a cylinder (width and height equal to 20 mm) in different positions in the sensor. Inverse problem solved using the complete set of measurements (496). Upper row: XY cross-sections. Middle row: XZ cross-sections. Bottom row: Isosurface determined by threshold segmentation, shaded by the Phong method

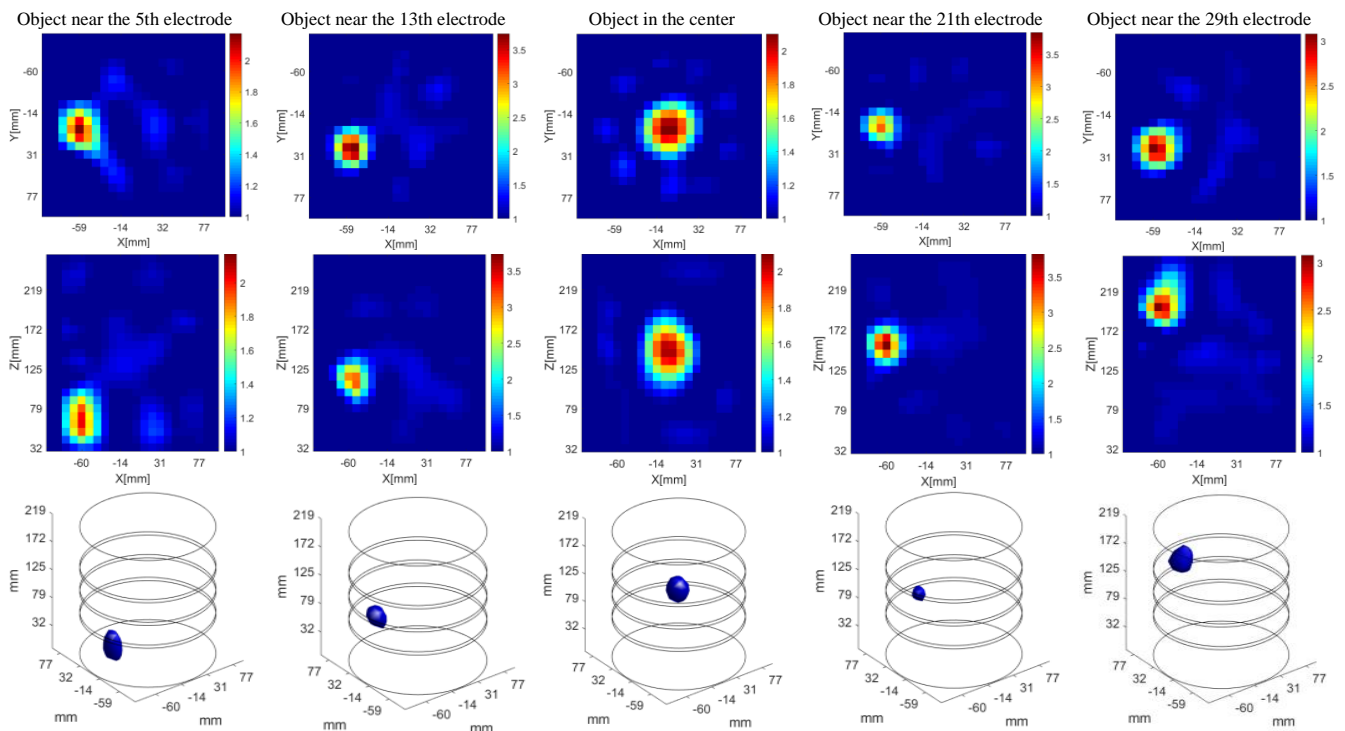


Fig. 11. 3D relative permittivity distribution obtained for a cylinder (width and height equal to 20 mm) in different positions in the sensor. Inverse problem solved using selected measurements (304). Upper row: XY cross-sections. Middle row: XZ cross-sections. Bottom row: Isosurface determined by threshold segmentation, shaded by the Phong method

2. Conclusions

We verified a 32-channel system in a context of application for 3D electrical capacitance tomography. The 3D sensor was designed for experiments using principles presented in the literature. The aspect ratio of the electrode dimension and the distance between the electrodes of the 3D sensor can be selected in such a way that the difference in capacitance values between pair of adjacent electrodes and pair of the opposite electrodes will fit in the range of a measuring circuit.

The SNR of capacitance measurements in presented hardware is sufficient to measure changes in capacitance for the most distant

electrodes in a suitably designed 3D 32-electrode sensor. The sensitivity of capacitance measurements was tested using objects which size is about 10% of the field of view of the sensor. The sensitivity of capacitance measurements is sufficient to detect such a permittivity change. Interestingly, the normalized sensitivity of capacitance measurement for the cross-plane electrodes is comparable to the sensitivity for in-plane electrodes for the designed 3D sensor and the selected position of the permittivity perturbation (on the edges of the field of view).

The reconstruction error for images reconstructed using the complete model is slightly, but noticeably smaller than the error obtained using the incomplete model, in which the pairs of

electrodes between not adjacent rings are excluded. The obtained results showed that cross-plane measurements together with the measurements for the pairs of most distant electrodes are useful for accurate reconstruction of 3D distributions. In comparison to incomplete model, the reconstruction from complete model is more difficult from numerical point of view because of severely ill-conditioned Jacobian matrix. Applied preconditioning procedure i.e. normalization of matrix rows and adjustment of regularization parameter made the reconstruction possible.

References

- [1] Banasiak R., Wajman R., Betiuk J., Soleimani M.: Feasibility study of dielectric permittivity inspection using a 3D capacitance CT method. *NDT & E International* 42, 2009, 316–322.
- [2] Brzeski P., Mirkowski J., Olszewski T., Plaskowski A., Smolik W. T., Szabatin R.: Multichannel capacitance tomograph for dynamic process imaging. *Optoelectronics Review* 11(3), 2003, 175–180.
- [3] Cui Z., Wang H., Chen Z., Xu Y., Yang W.: A high-performance digital system for electrical capacitance tomography. *Measurement Science and Technology* 22, 2011, 055503.
- [4] Dyakowski T., Jeanmeure L. F., Jaworski A. J.: Applications of electrical tomography for gas-solids and liquid-solids flows – a review. *Powder Technology* 112, 2000, 174–192.
- [5] Fan Z., Gao R. X.: A new sensing method for Electrical Capacitance Tomography. *IEEE Instrumentation & Measurement Technology Conference Proceedings*, 2010, 48–53.
- [6] Hansen P. C.: Regularization Tools version 4.0 for Matlab 7.3. *Numerical Algorithms* 46, 2007, 189–194.
- [7] Hu X., Katsouras M., Yang W., Huang S.: Further analysis of charge/discharge capacitance measurement circuit used with tomography sensors. *Sensors and Transducers* 80(6), 2007, 1246–1256.
- [8] Huang S. M., Plaskowski A. B., Xie C. G., Beck M. S.: Capacitance-based tomographic flow imaging system. *Electronics Letters* 24(7), 1988, 418–419.
- [9] Khan S., Manwaring P., Borsic A., Halter R. J.: FPGA-Based Voltage and Current Dual Drive System for High Frame Rate Electrical Impedance Tomography. *IEEE Transactions on Medical Imaging* 34, 2015, 888–901.
- [10] Kryszyn J., Smolik W. T., Radzik B., Olszewski T., Szabatin R.: Switchless charge-discharge circuit for electrical capacitance tomography. *Measurement Science and Technology* 25, 2014, 115009.
- [11] Kryszyn J., Smolik W. T., Szabatin R.: 3D image reconstruction in electrical capacitance tomography. *7th World Congress in Industrial Process Tomography*, 2013, 411–419.
- [12] Kryszyn J., Wanta D., Smolik W. T.: Gain Adjustment for Signal-to-Noise Ratio Improvement in Electrical Capacitance Tomography System EVT4. *IEEE Sensors Journal* 17(24), 2017, 8107–8116.
- [13] Kryszyn J., Wróblewski P., Stosio M., Wanta D., Olszewski T., Smolik W. T.: Architecture of EVT4 data acquisition system for electrical capacitance tomography. *Measurement* 101, 2017, 28–39.
- [14] Li Y., Holland D. J.: Fast and robust 3D electrical capacitance tomography. *Measurement Science and Technology* 24, 2013, 105406.
- [15] Li Y., Holland D. J.: Optimizing the geometry of three-dimensional electrical capacitance tomography sensors. *IEEE Sensors Journal* 15(3), 2015, 1567–1574.
- [16] Liao A., Zhou Q., Zhang Y.: Application of 3D electrical capacitance tomography in probing anomalous blocks in water. *Journal of Applied Geophysics* 117, 2015, 91–103.
- [17] Lu D., Shao F., Guo Z.: A high voltage method for measuring low capacitance for tomography. *Review of Scientific Instruments* 80, 2009, 053704.
- [18] Mao M., Ye J., Wang H., Zhang J., Yang W.: Evaluation of excitation strategy with multi-plane electrical capacitance tomography sensor. *Measurement Science and Technology* 27, 2016, 114008.
- [19] Marashdeh Q. M., Teixeira F. L., Fan L.-S.: Adaptive Electrical Capacitance Volume Tomography. *IEEE Sensors Journal* 14, 2014, 1253–1259.
- [20] Nurge M. A.: Electrical capacitance volume tomography with high contrast dielectrics using a cuboid sensor geometry. *Measurement Science and Technology* 18, 2007, 1511–1520.
- [21] Olszewski T., Brzeski P., Mirkowski J., Plaskowski A., Smolik W. T., Szabatin R.: Capacitance tomograph – Design and preliminary results. *Proc. 2nd International Symposium on Process Tomography in Poland*, 2002, 159–168.
- [22] Rymarczyk T.: New methods to determine moisture areas by electrical impedance tomography. *International Journal of Applied Electromagnetics and Mechanics* 52(1-2), 2016, 79–87.
- [23] Rymarczyk T., Kłosowski G., Kozłowski E.: A Non-Destructive System Based on Electrical Tomography and Machine Learning to Analyze the Moisture of Buildings. *Sensors* 18(7), 2018, 2285.
- [24] Smolik W. T., Kryszyn J., Radzik B., Stosio M., Wróblewski P., Wanta D., Dańko L., Olszewski T., Szabatin R.: Single-shot high-voltage circuit for electrical capacitance tomography. *Measurement Science and Technology* 28, 2017, 025902.
- [25] Soleimani M., Wang H., Li Y., Yang W.: A comparative study of three dimensional electrical capacitance tomography. *International Journal for Information & Systems Sciences* 3(2), 2007, 292–306.
- [26] Wajman R., Fiderik P., Fidos H., Jaworski T., Nowakowski J., Sankowski D., Banasiak R.: Metrological evaluation of a 3D electrical capacitance tomography measurement system for two-phase flow fraction determination. *Measurement Science and Technology* 24, 2013, 065302.
- [27] Wang A., Marashdeh Q. M., Teixeira F. L., Fan L.-S.: Electrical Capacitance Volume Tomography: a Comparison Between 12- and 24-Channels Sensor Systems. *Progress in Electromagnetics Research M* 41, 2015, 73–84.
- [28] Wang B., Ji H., Huang Z., Li H.: A high-speed data acquisition system for ECT based on the differential sampling method. *IEEE Sensors Journal* 5, 2005, 308–311.
- [29] Wang F., Marashdeh Q., Fan L.-S., Warsito W.: Electrical Capacitance Volume Tomography: Design and Applications. *Sensors* 10, 2010, 1890–1917.
- [30] Wang Mi, Ma Yixin, Holliday N., Dai Yunfeng, Williams R. A., Lucas G.: A high-performance EIT system. *IEEE Sensors Journal* 5(2), 2005, 289–299.
- [31] Warsito W., Fan L.-S.: Development of 3-Dimensional Electrical Capacitance Tomography Based on Neural Network Multi-criterion Optimization Image Reconstruction. *3rd World Congress on Industrial Process Tomography*, 2003.
- [32] Warsito W., Fan L.-S.: Dynamics of spiral bubble plume motion in the entrance region of bubble columns and three-phase fluidized beds using 3D ECT. *Chemical Engineering Science* 60, 2005, 6073–6084.
- [33] Xu L., Zhou H., Cao Z.: A recursive least squares-based demodulator for electrical tomography. *Review of Scientific Instruments* 84, 2013, 044704.
- [34] Yang W.: Design of electrical capacitance tomography sensors. *Measurement Science and Technology* 21, 2010, 042001.
- [35] Yang W. Q.: Hardware design of electrical capacitance tomography systems. *Measurement Science and Technology* 7, 1996, 225–232.
- [36] Yang W. Q., Peng L.: Image reconstruction algorithms for electrical capacitance tomography. *Measurement Science and Technology* 14, 2003, R1–R13.
- [37] Ye J., Mao M., Wang H., Yang W.: An evaluation of the rotation of electrodes in multi-plane electrical capacitance tomography sensors. *Measurement Science and Technology* 26, 2015, 125404.
- [38] York T. A., Phua T. N., Reichelt L., Pawłowski A., Kneer R.: A miniature electrical capacitance tomograph. *Measurement Science and Technology* 17, 2006, 2119–2129.
- [39] Zeeshan Z., Teixeira F., Marashdeh Q.: Sensitivity map computation in adaptive electrical capacitance volume tomography with multielectrode excitations. *Electronics Letters* 51, 2015, 334–336.
- [40] Zhao J., Zou X., Fu W.: Sensitivity Map Analysis of Adaptive Electrical Capacitance Volume Tomography Using Nonuniform Voltage Excitation Envelopes. *IEEE Sensors Journal* 17, 2017, 105–112.
- [41] ECTsim3D web page, <http://ectsim.ire.pw.edu.pl>

Ph.D. Eng. Jacek Kryszyn

e-mail: J.Kryszyn@ire.pw.edu.pl

Jacek Kryszyn was born in Warsaw, Poland, in 1986. He received his M.Sc. degree in electronics and computer engineering and the Ph.D. degree from Warsaw University of Technology, Warsaw, Poland in 2012 and 2018, respectively. He is an assistant professor at the Institute of Radioelectronics and Multimedia Technology, Electronics and Information Technology Faculty, Warsaw University of Technology since 2019. His field of interest covers Electrical Capacitance Tomography, especially small capacitance measurement methods.

ORCID ID: 0000-0002-0042-0473

M.Sc. Eng. Damian Wanta

e-mail: D.Wanta@ire.pw.edu.pl

Damian Wanta was born in Starogard Gdański, Poland, in 1991. He received the M. Sc. degree in biomedical engineering from Warsaw University of Technology, Warsaw, Poland in 2016. He is Ph.D. student in the Nuclear and Medical Electronics Division, Institute of Radioelectronics and Multimedia Technology, Electronics and Information Technology Faculty, Warsaw University of Technology. His current research interests include Imaging of Magnetic Nanoparticles, Electrical Capacitance Tomography and Partial Reconfiguration.

ORCID ID: 0000-0002-1596-6524

Prof. Waldemar T. Smolik

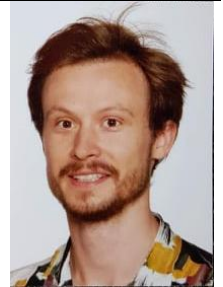
e-mail: W.Smolik@ire.pw.edu.pl

Waldemar T. Smolik was born in Otwock, Poland, in 1966. He received the M.Sc., Ph.D. and D.Sc. degrees in electronics engineering from Warsaw University of Technology (WUT), Warsaw, Poland in 1991, 1997 and 2014, respectively. Since 2016, he is a Professor at the Institute of Radioelectronics and Multimedia Technology, Electronics and Information Technology Faculty, WUT. He is the head of the Information Acquisition and Processing Systems Laboratory at the Division of Nuclear and Medical Electronics. His main research interests are computer engineering, computed tomography and medical imaging. He has published over 70 scientific papers. Mr. Smolik was a recipient of the best poster award at IEEE International Workshop on Imaging Systems and Techniques in 2009.

ORCID ID: 0000-0002-1524-5049

otrzymano/received: 16.09.2019

przyjęto do druku/accepted: 06.12.2019



DOI: 10.35784/IAPGOS.681

USING 3D PRINTING TECHNOLOGY TO FULL-SCALE SIMULATION OF THE UPPER RESPIRATORY TRACT

Oleg Avrunin¹, Yana Nosova¹, Ibrahim Younouss Abdelhamid¹, Oleksandr Gryshkov², Birgit Glasmacher²

¹Kharkiv National University of Radio Electronics, Kharkiv, Ukraine; ²Institute for Multiphase Processes of the Leibniz University of Hannover, Hannover, Germany

Abstract. The project "Implementation of rapid prototyping for modelling the upper respiratory tract in normal and typical pathologies" investigates the urgent problem of improving the reliability of diagnosis and effectiveness of treatment of disorders of the nasal breathing. Possibilities of modern 3D-printing technology for creation of individual natural anatomical models of the upper respiratory tract and determination of their aerodynamic characteristics are considered. The characteristics of the laminar boundary layer of the air flow in the parietal region of the nasal cavity are investigated under different modes of breathing in normal and with typical disorders of the nasal breathing. The concept of investigation of the aerodynamic indices of the anatomical structures of the respiratory system by the results of test tests of individual full-scale 3D models, obtained by the data of spiral computed tomography, is being developed. Theoretical bases of the method of computer planning of restorative rhinosurgical interventions in patients with chronic diseases of the nasal cavity are grounded, based on the change of the configuration of the anatomical structures of the nasal cavity taking into account the aerodynamic parameters of respiration. Modern distance learning and testing tools are being created to demonstrate the technology developed, to provide theoretical knowledge, practical skills and to solve situational tasks for a wide range of specialists. Development and research of natural patterns of the upper respiratory tract allows for supplementing and expanding the knowledge about the aerodynamic characteristics of the nasal cavity, to make decisions about therapy in a short period of time. Experience of the Laboratory of the Institute for Multiphase Processes (IMP) of the Leibniz Universität Hannover (LUH) in the development and use of rapid prototyping capabilities in biotechnology will provide technical support to the project.

Keywords: rhinomanometry, nasal breathing, full-scale models, tomography, virtual model

WYKORZYSTANIE TECHNOLOGII DRUKOWANIA 3D DO MODELOWANIA GÓRNYCH DRÓG ODDECHOWYCH W PEŁNEJ SKALI

Streszczenie. Projekt „Wdrożenie szybkiego prototypowania do modelowania górnych dróg oddechowych w normalnych i typowych patologiach” bada pilny problem poprawy wiarygodności diagnozy i skuteczności leczenia zaburzeń oddychania przez nos. Rozważane są możliwości nowoczesnej technologii druku 3D do tworzenia indywidualnych naturalnych modeli anatomicznych górnych dróg oddechowych i określania ich właściwości aerodynamicznych. Charakterystyka laminarnej warstwy granicznej przepływu powietrza w okolicy ciemieniowej jamy nosowej jest badana w różnych trybach oddychania w normalnym i typowym zaburzeniu oddychania przez nos. Opracowywana jest koncepcja badania wskaźników aerodynamicznych struktur anatomicznych układu oddechowego na podstawie wyników testów testowych poszczególnych pełnoskalowych modeli 3D, uzyskanych z danych spiralnej tomografii komputerowej. Podstawy teoretyczne metody komputerowego planowania rekonstrukcyjnych interwencji nosorożców u pacjentów z przewlekłymi chorobami jamy nosowej są oparte na zmianie konfiguracji struktur anatomicznych jamy nosowej z uwzględnieniem parametrów aerodynamicznych oddychania. Tworzone są nowoczesne narzędzia do nauki na odległość i testowania w celu zademonstrowania opracowanej technologii, zapewnienia wiedzy teoretycznej, umiejętności praktycznych i rozwiązywania zadań sytuacyjnych dla szerokiego grona specjalistów. Opracowanie i badanie naturalnych wzorów górnych dróg oddechowych pozwala uzupełnić i poszerzyć wiedzę na temat właściwości aerodynamicznych jamy nosowej w celu podjęcia decyzji o terapii w krótkim okresie czasu. Doświadczenie laboratorium Instytutu Procesów Wielofazowych (IMP) Leibniz Universität Hannover (LUH) w zakresie rozwoju i wykorzystania możliwości szybkiego prototypowania w biotechnologii zapewni wsparcie techniczne dla projektu.

Słowa kluczowe: rhinomanometria, oddychanie przez nos, modele w pełnej skali, tomografia, model wirtualny

Introduction

One of the most present actual social problems in all industrially developed countries around the world is the development and introduction of new medical technologies to improve quality of health care, which is confirmed, in particular, by the priority areas of the 7th Framework Program of the European Union and its continuation – the program EU "Horizon 2020". The use of modern information technologies in medicine can significantly improve the quality of diagnosis and treatment of various pathologies by providing the clinician with additional, advanced information about the disease process.

Rhinology is one of the least well-conclusive means of functional diagnostics fields of medicine, but in industrialized countries, according to statistical data, only rhinosinusitis affects approximately 10% of the population. It appears that there is no clear correlation between subjective sensations of the patient and characteristics of nasal airflow, communication of respiratory and olfactory functions, etc. In spite of the possibilities of the modern rhinomanometry equipment and related specialized software that can define and calculate the aerodynamic performance with high accuracy [2, 5–7, 9].

The basic laws of the aerodynamics of the upper respiratory tract are studied well enough. However, at this stage, it is advisable to assess not only the macro-indicators of airflow but also to explore the near-wall flows. Their indicators directly affect the mucosa of the nasal cavity with its morpho-functional features and located in the nervous limbs that will allow for a more

detailed assessment of the impact of air flow in the pathogenesis of several rhinology diseases. On the basis of these data, by means of computer methods of planning surgical interventions and modelling of the nasal cavity required configuration it is possible to predict functional outcome operation.

1. Analysis of recent research and publications

In diseases of the upper respiratory tract, there are often violations of the configuration of the airways (nasal passages) and anastomosis of the paranasal sinuses. A fairly large number of publications has been devoted to studying the spatial arrangement of anatomical objects and to studying the aerodynamics of the nasal cavity [8, 10, 14]. However, the problem of visualizing this area in the context of surgical planning procedures is only at the initial stage of development. Traditionally, introspective diagnosis of diseases of the nasal cavity was performed using X-ray. At the present stage, to determine the configuration of the upper respiratory tract, it is advisable to use the data of X-ray spiral computed tomography (CT), which allows us to identify the bone and airborne structures with a spatial resolution of less than 1 mm [7, 8]. Determining the morphometric parameters of these structures from flat tomographic slices in an interactive (manual) mode is a rather time-consuming procedure, which also provides a small amount of information about their spatial configuration. Therefore, the development of algorithms for automated segmentation and spatial visualization of the airways of the upper respiratory tract are relevant [1, 11].

The introduction of rapid prototyping technologies into rhinology allows us to base and predict the functional result of the operation, not only according to mathematical modelling of the process of air flow through the nasal cavity during breathing, but also taking into account the analysis of full-scale aerodynamic models of the studied area. The introduction of such simulation technologies takes the planning process of surgical operations to a qualitatively new level and improves the reliability of the results of procedures associated with predicting the functional results of surgical interventions [3, 4, 13, 15].

2. The aim of the study

The proposed work is aimed at the study of parietal air currents in normal and typical pathologies on spatial models of upper respiratory tract, obtained by the 3D prototyping technology according to tomographic studies of specific patients, taking into account individual variability, which will allow to reveal the possible effects of air flow shell of the nasal cavity and increase the reliability of functional diagnostics of disorders of the nasal breathing and increase the effectiveness of conducting com planning of rhinosurgical interventions.

3. Experimental

The object of research is the development and analysis of the aerodynamic characteristics of the individual natural of 3D-models of the upper respiratory tract created by rapid prototyping technology (3D-printing) according to CT.

The problem of research is improving the reliability of diagnosing disorders of nasal breathing by means of the analysis of the aerodynamic characteristics of the near wall air flow based on production and natural studies of the individual 3D-models of the upper respiratory tract (Fig. 1).

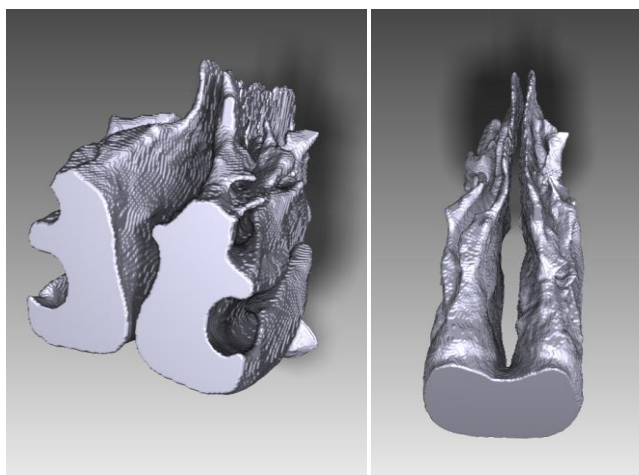


Fig. 1. 3D model of upper respiratory tract

The present international study is based on the experience of scientific and practical developments of the project participants.

The task of creating an implant model using rapid prototyping tools according to the spiral computed tomography consists of 6 main stages:

- segmentation – the selection on the images of tomographic sections of bone structures,
- determination of the location and selection of the bone defect replacement method,
- creation of a large implant reconstruction,
- preparation of data for prototyping in stl format,
- creating a layer-by-layer model of the implant in the G-code format for 3D printing on specific equipment,
- 3D printing of the full-scale model.

4. Results and discussion

The main working hypothesis is to study the impact of the near-wall flow (laminar boundary layer) air to the mucosal surface anatomical structures of the upper airway disorders in the diagnosis of nasal breathing [12].

The scientific basis of the work is the application of boundary-layer theory to identify the negative influence of air flow to the nasal cavity walls at various modes of breathing.

On the basis of the conducted researches it is planned to develop the theoretical bases of computer planning of restorative rhinosurgical interventions in patients with chronic diseases of the nasal cavity, based on the change of the configuration of the anatomical structures of the nasal cavity with taking into account the aerodynamic parameters of breathing during verification of the full-scale models. (Fig. 2).

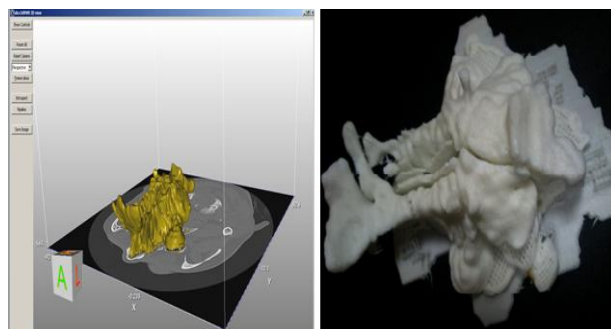


Fig. 2. Personalized Upper Airway Model according to spiral computed tomography: a) virtual model; b) full-scale model

The initial data for the studies are sets of images of axial tomographic sections with a thickness of 1 mm, obtained using a Siemens Somatom + Emotion tomograph according to the scanning protocol parallel to the plane of the skull base with standard patient laying.

The image of the tomographic slice is represented by a discrete function of intensity $B(i, j) [0.255]$ for $i, j [0.255]$, which determines the degree of X-ray absorption in each element of the raster. The total number of N slices was determined based on the spatial characteristics of the upper respiratory tract and amounted to about 60 slices ($N \approx 60$).

For spatial visualization of tomographic data, it is necessary to perform a complex of transformations of coordinate systems, performed, for the purpose of universality, in matrix form. So, for n -dimensional coordinate systems with bases (k_1, k_2, \dots, k_n) and (m_1, m_2, \dots, m_n) , the coordinate transformation problem can be represented as transformations:

$$\begin{cases} m_1 = f_1(k_1, k_2, \dots, k_n); \\ m_2 = f_2(k_1, k_2, \dots, k_n); \\ m_N = f_N(k_1, k_2, \dots, k_n), \end{cases}$$

where f_i is the function of recalculating the i -th coordinate, and the arguments of this function are the coordinates of the object in the basis k_i .

Accordingly, the inverse coordinate transformation problem is written as follows:

$$\begin{cases} k_1 = F_1(m_1, m_2, \dots, m_N); \\ k_2 = F_2(m_1, m_2, \dots, m_N); \\ k_n = F_n(m_1, m_2, \dots, m_N), \end{cases}$$

where F_i is the inverse transformation function with arguments – the coordinates of the object in the basis m_i .

If the transformation functions are linear and the dimensions of the coordinate systems coincide, then such transformations are called affine. For visualization, an important condition for the unambiguous transformation of coordinates is the coincidence of the dimensions of the coordinate systems.

Affine coordinate transformations are visually written in the matrix form:

$$\begin{bmatrix} m_1 \\ m_2 \\ \vdots \\ m_N \end{bmatrix} = \begin{bmatrix} a_{11} & a_{12} & a_{1N} \\ a_{21} & a_{22} & a_{2N} \\ \vdots & \vdots & \vdots \\ a_{31} & a_{32} & a_{3N} \end{bmatrix} * \begin{bmatrix} k_1 \\ k_2 \\ \vdots \\ k_N \end{bmatrix}$$

and are calculated using the formula:

$$m_i = \sum_{j=1}^N a_{ij} \cdot k_j$$

For the purpose of universality, when performing matrix affine transformations, points and vectors are conveniently represented in homogeneous coordinates. Thus, the coordinates of a vector in homogeneous coordinates are specified as:

$$\begin{bmatrix} x \\ y \\ z \\ 0 \end{bmatrix}$$

and coordinates of the point

$$\begin{bmatrix} x \\ y \\ z \\ 1 \end{bmatrix}$$

The transformation of the coordinates of the point can be represented in the analytical:

$$\begin{cases} X = Ax + By + Cz + D; \\ Y = Ex + Fy + Gz + H; \\ Z = Kx + Ly + Mz + N, \end{cases}$$

or in the matrix form using a uniform representation:

$$T = M \cdot T' = \begin{bmatrix} X \\ Y \\ Z \\ 1 \end{bmatrix} = \begin{bmatrix} A & B & C & D \\ E & F & G & H \\ K & L & M & N \\ P & R & Q & S \end{bmatrix} \cdot \begin{bmatrix} x \\ y \\ z \\ 1 \end{bmatrix}$$

where A, B, \dots, N are the constants.

Display in the surgical field is performed in the coordinate system of the surgical field (X_{op}, Y_{op}, Z_{op}) using the transformation matrix:

$$\begin{bmatrix} 1 & 0 & 0 & X_{op} \\ 0 & 1 & 0 & Y_{op} \\ 0 & 0 & 1 & Z_{op} \\ 0 & 0 & 0 & 1 \end{bmatrix}$$

where X_{op}, Y_{op}, Z_{op} are the coordinates of the base point of the object in the coordinate system of the surgical field.

Moving the object on dx, dy, dz is respectively performed using the transfer matrix:

$$\begin{cases} X = x - dx; \\ Y = y - dy; \\ Z = z - dz; \end{cases} \begin{bmatrix} 1 & 0 & 0 & -dx \\ 0 & 1 & 0 & -dy \\ 0 & 0 & 1 & dz \\ 0 & 0 & 0 & 1 \end{bmatrix}$$

Next, the coordinate system of the operating field is transformed into the coordinate system of the display using the projective transformation. As a type of projection, a parallel orthographic projection is selected, the transformation matrix for which it is specified in the form:

$$\begin{bmatrix} \frac{2}{x_r - x_l} & 0 & 0 & -\frac{x_r + x_l}{x_r - x_l} \\ 0 & \frac{2}{y_t - y_b} & 0 & -\frac{y_t + y_b}{y_t - y_b} \\ 0 & 0 & \frac{-2}{z_f - z_n} & -\frac{z_f + z_n}{z_f - z_n} \\ 0 & 0 & 0 & 1 \end{bmatrix}$$

where $x_r, x_l, y_t, y_b, z_f, z_n$, the bounding coordinates of the three-dimensional region of visibility along the x, y, z axes, respectively. These actions are performed using the OpenGL

glortho library procedure. The procedure is called with the parameters glortho (-2.5, 2.5, -2.5, 2.5, -12, 12), clamping the output region with a width and height of 5 relative units, and the distance between the front and rear clipping planes is 24 relative units.

Further, the picture plane is displayed on the graphic output window using the procedure. glViewport (), the first two parameters of which specify the initial coordinates of the output area, and the last two – the width and height of the output area. The output is carried out on the standard component VCL TPanel (graphic panel) with the properties panel1.Width, panel1.Height. Accordingly, the glViewport () procedure call is performed as follows: glViewport (0, 0, panel1.Width, panel1.Height).

For the implementation of a comprehensive multi-angle visualization, it is necessary to provide for the implementation of geometric transformations.

Then, geometric transformations are performed, associated with additional movements, rotations, and scaling.

The scaling operation is performed using the glScalef (kx, ky, kz) command, the parameters of which determine the scale factors along the corresponding coordinate axes. The corresponding transformation matrix is given below:

$$\begin{cases} X = x / k_x, \\ Y = y / k_y, \\ Z = z / k_z, \end{cases} \begin{bmatrix} 1/k_x & 0 & 0 & 0 \\ 0 & 1/k_y & 0 & 0 \\ 0 & 0 & 1/k_z & 0 \\ 0 & 0 & 0 & 1 \end{bmatrix}$$

Turns are carried out using the trigonometric functions in the coefficients of the transformation matrix. The universal OpenGL library procedure for executing rotations is glRotatef (ϕ, x, y, z), the first parameter of which indicates the magnitude of the rotation angle, the other three specify the axis relative to which the rotation is performed. Consider the rotation matrix relative to the main coordinate axes.

Rotation around the axis x by an angle ϕ (see Fig. 3).

$$\begin{cases} X = x, \\ Y = y \cos \phi - z \sin \phi, \\ Z = y \sin \phi + z \cos \phi, \end{cases} \begin{bmatrix} 1 & 0 & 0 & 0 \\ 0 & \cos \phi & -\sin \phi & 0 \\ 0 & \sin \phi & \cos \phi & 0 \\ 0 & 0 & 0 & 1 \end{bmatrix}$$

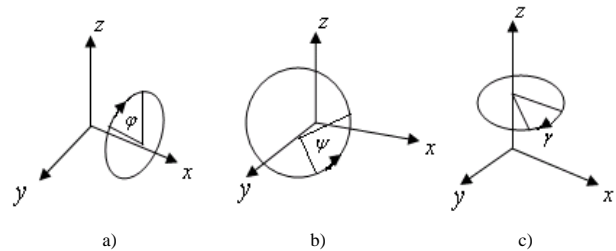


Fig. 3. Rotation: a) the rotation around the axis x by an angle ϕ ; b) the rotation by an angle ψ around the axis y ; c) the rotation around the axis z by an angle γ

The rotation around the axis y by an angle ψ

$$\begin{cases} X = x \cos \psi - z \sin \psi, \\ Y = y, \\ Z = x \sin \psi + z \cos \psi, \end{cases} \begin{bmatrix} \cos \psi & 0 & -\sin \psi & 0 \\ 0 & 1 & 0 & 0 \\ \sin \psi & 0 & \cos \psi & 0 \\ 0 & 0 & 0 & 1 \end{bmatrix}$$

The rotation around the axis z by an angle γ

$$\begin{cases} X = x \cos \gamma - y \sin \gamma, \\ Y = x \sin \gamma + y \cos \gamma, \\ Z = z, \end{cases} \begin{bmatrix} \cos \gamma & -\sin \gamma & 0 & 0 \\ \sin \gamma & \cos \gamma & 0 & 0 \\ 0 & 0 & 1 & 0 \\ 0 & 0 & 0 & 1 \end{bmatrix}$$

Development and research of natural patterns of the upper respiratory tract allows for supplementing and expanding the knowledge about the aerodynamic characteristics of the nasal cavity and to make decisions about therapy in a short period of time. Experience of the Laboratory of the Institute for Multiphase Processes (IMP) of the Leibniz Universität Hannover (LUH) in the development and use of rapid prototyping capabilities in

biotechnology will provide technical support to the project. In addition, the project participants have already gained considerable experience in the development of methods and models in the subject area. Considering the modern high technology and technogenic approach to the diagnosis and treatment of diseases, it is advisable to introduce the ability to showcase a wider audience of the proposed methods professionals wishing to develop new scientific approaches both in theoretical and practical terms.

5. Conclusions

Project implementation is based on the results of scientific and practical research of the participants, which were obtained as a consequence of the executed joint international programs: DAAD project "Eastern Partnership" and Erasmus+ Program Key Action 1 – Mobility for learners and staff – Higher Education Student and Staff Mobility during the years 2016–2018.

Perspective of work. Considering the modern high technology and technogenic approach to the diagnosis and treatment of diseases, it is advisable to introduce the ability to showcase a wider audience of the proposed methods professionals wishing to develop new scientific approaches both in theoretical and practical terms. To do this, it is possible to use the opportunities of Massive open online course (MOOC) service for remote e-learning theoretical knowledge, mathematical demonstration and natural (obtained using rapid prototyping technology) models as well as the acquisition of practical skills through the analysis of clinical cases and test solutions of situational problems. We plan to produce a pneumatic test stand to define the aerodynamic characteristics of the upper airway and corresponding theoretical and experimental parameters according to the data from the pressure transducer and the air flow situated in the received control natural positions models.

Acknowledgments

The exchange program with East European Countries funded by DAAD (Ostpartnerschaften, project number 54364768) and joint Ukraine-Germany project MESU-BMBF 2019-2020 "3D-Model – Implementation of rapid prototyping to design and model the upper respiratory tract in normal and typical pathologies".

References

- [1] Abizov R. A., Pavlishin Yu. D.: Disturbances in the functions of the olfactory analyzer and practical aspects of their research methodology and further tactics of conducting such patients. *Family Medicine* 4(48), 2013, 100–102.
- [2] Al_Omari A. K., Saied H. F. I., Avrunin O. G.: Analysis of Changes of the Hydraulic Diameter and Determination of the Air Flow Modes in the Nasal Cavity. *Image Processing and Communications Challenges 3. Advances in Intelligent and Soft Computing* 102, 2011, 303-310 [DOI: 10.1007/978-3-642-23154-4_34].
- [3] Aras A., Akay M., Cukurova I. et al.: Dimensional changes of the nasal cavity after transpalatal distraction using bone-borne distractor: an acoustic rhinometry and computed tomography evaluation. *J. Oral Maxillofac. Surg.* 68(7), 2010, 1487–1497.
- [4] Cole P., Fenton R.: Contemporary rhinomanometry. *Otolaryngol.* 35(2), 2006, 83–87.
- [5] Fyrmpas G., Kyrmizakis D., Vital V., Constantinidis J.: The value of bilateral simultaneous nasal spirometry in the assessment of patients undergoing septoplasty. *Rhinology* 49(3), 2011, 297–303.
- [6] Govidaraj S.: Endoscopic sinus surgery: evolution and technical innovations. *J. Laryngol. Otol.* 24(3), 2010, 242–250.
- [7] Halawi A. M., Smith S. S., Chandra R. K.: Chronic rhinosinusitis: epidemiology and cost. *Allergy Asthma Proc.* 34(4), 2013, 328–334.
- [8] Ismail Saied H. F., Al_Omari A. K., Avrunin O. G.: An Attempt of the Determination of Aerodynamic Characteristics of Nasal Airways. *Image Processing and Communications Challenges 3. Advances in Intelligent and Soft Computing* 102, 2011, 311–322. [DOI: 10.1007/978-3-642-23154-4_35].
- [9] Nosova Ya. V., Faruk Kh. I., Avrunin O. G.: A tool for researching respiratory and olfaction disorders. *Telecommunications and Radio Engineering* 77(15), 2018, 1389–1395. [DOI: 10.1615/TelecomRadEng.v77.i15.90].
- [10] Tingelhoff K., Moral A. I., Kunkel M. et al.: Comparison between manual and semi-automatic segmentation of nasal cavity and paranasal sinuses from CT images. 29th Annual International Conference of the IEEE Engineering in Medicine and Biology Society, 2007, 5505–5508. [DOI: 10.1109/IEMBS.2007.4353592].
- [11] Vogt K., Jalowayski A. A.: 4-Phase-Rhinomanometry Basics and Practice. *Rhinology* 21, 2010, 1–50.
- [12] Wójcik W., Pavlov S., Kalimoldayev M.: *Information Technology in Medical Diagnostics II.* Taylor & Francis Group, CRC Press, London 2019, [DOI: 10.1201/9780429057618].
- [13] Zambetti G., Moresi M., Romeo R., Filiaci F.: Study and application of a mathematical model for the provisional assessment of areas and nasal resistance, obtained using acoustic rhinometry and active anterior rhinomanometry. *Clin. Otolaryngol. Allied Sci.* 26(4), 2001, 286–293.
- [14] Zhang G., Fenton R., Rival R., Solomon P., Cole P., Li Y.: Correlation between subjective assessment and objective measurement of nasal obstruction. *Chinese journal of otorhinolaryngology head and neck surgery* 43(7), 2008, 484–489.
- [15] Zhang G., Solomon P., Rival R. et al.: Nasal airway volume and resistance to airflow. *Am. J. Rhinol.* 22(4), 2008, 371–375.

Prof. Avrunin Oleg

e-mail: oleg.avrunin@nure.ua

Doctor of Technical Sciences, professor, head of Biomedical Engineering Department, Kharkiv National University of Radio Electronics, Ukraine. Scientific supervisor of research work on research of theoretical and technical principles of diagnostics, assessment and correction of medical and social human conditions. Invited Professor in Gottfried Wilhelm Leibniz Universität Hannover (Germany) and Harbin Engineering University (China).

ORCID ID: 0000-0002-6312-687X



Ph.D. Nosova Yana

e-mail: yana.nosova@nure.ua

Assistant of the Department of Biomedical Engineering, Kharkiv National University of Radio Electronics, Ukraine. As part of the team of authors of the patent "Device for the testing of respiratory disorders of smell" was awarded the diploma of the winner of the All-Ukrainian contest "Invention of the Year – 2016" in the nomination "Best invention in Kharkiv region". Research Interests: biomedical signal processing and images.

ORCID ID: 0000-0003-4310-5833



M.Sc. Ibrahim Younouss Abdelhamid

e-mail: ibrahim.younouss.abdelhamid@nure.ua

Ph.D. Student, Department of Biomedical Engineering, Kharkiv National University of Radio Electronics, Ukraine. Research Interests: biomedical signal processing and images, functional diagnostics of nasal breathing.

ORCID ID: 0000-0003-2611-2417



Ph.D. Oleksandr Gryshkov

e-mail: gryshkov@imp.uni-hannover.de

PostDoc, Ph.D., Leibniz University of Hannover, Institute of Multiphase Processes, Hannover, Germany. Research Interests: Tissue engineering and biomaterials; cell therapies based on encapsulation of stem cells and cellular therapeutics in alginate 3D micro-environment; Medical implant engineering / 3D Printing; novel medical implants based on Magnesium and Silicon-Carbide porous ceramics; new methods for generating bioactive and bioinert coatings for medical applications.

ORCID ID: 0000-0002-3116-8792



Prof., Dr.-Ing. Birgit Glasmacher

e-mail: secretariat@imp.uni-hannover.de

Head of the Institute for Multiphase Processes of the Leibniz University of Hannover, Germany. Research Interests: Tissue engineering and biomaterials; cell therapies based on encapsulation of stem cells and cellular therapeutics in alginate 3D micro-environment; Medical implant engineering / 3D Printing; novel medical implants based on Magnesium and Silicon-Carbide porous ceramics; new methods for generating bioactive and bioinert coatings for medical applications.

ORCID ID: 0000-0002-2452-1666



otrzymano/received: 09.11.2019

przyjęto do druku/accepted: 06.12.2019

DOI: 10.35784/IAPGOS.688

CONCEPT AND REALIZATION OF BACKPACK-TYPE SYSTEM FOR MULTICHANNEL ELECTROPHYSIOLOGY IN FREELY BEHAVING RODENTS

Olga Chaikovska¹, Olexandr Ponomarenko¹, Olexandr Dovgan¹, Igor Rokunets¹, Sergii Pavlov², Olena Kryvoviaz¹, Oleg Vlasenko¹

¹National Pirogov Memorial Medical University, Vinnytsia, Ukraine; ²Vinnytsia National Technical University, Vinnytsia, Ukraine

Abstract. Technologies for multichannel electrophysiology are experiencing astounding growth. Numbers of channels reach thousands of recording sites, systems are often combined with electrostimulations and optic stimulations. However, the task of design the cheap, flexible system for freely behaving animals without tethered cable are not solved completely. We propose the system for multichannel electrophysiology for both rats and mice. The system allows to record unit activity and local field potential (LFP) up to 32 channels with different types of electrodes. The system was constructed using Intan technologies RHD 2132 chip. Data acquisition and recordings take place on the DAQ-card, which is placed as a back-pack on the animal. The signal is amplified with amplifier cascade and digitalized with 16-bit ADC. Instrumental filters allow to filter the signal in 0.1–20000 Hz bandwidth. The system is powered from the mini-battery with capacity 340 mA/hr. The system was validated with generated signals, in anaesthetized rat and showed a high quality of recordings.

Keywords: multichannel electrophysiology, freely behaving rodents, unit activity, local field potential

KONCEPCJA I REALIZACJA SYSTEMU PLECAKOWEGO DLA WIELOKANALOWEJ ELEKTROFIZJOLOGII U SWOBODNIE ZACHOWUJĄCYCH SIĘ GRYZONI

Streszczenie. Technologie elektrofizjologii wielokanalowej odnotowują zdumiewający wzrost. Liczba kanałów dociera do tysięcy miejsc rejestracji, systemy często łączone są z elektrostymulacjami i stymulacjami optycznymi. Jednak zadanie zaprojektowania taniego, elastycznego systemu pozwalającego na swobodne zachowania zwierząt bez przywiązania kabla nie zostało całkowicie rozwiązane. Zaproponowano system wielokanalowej elektrofizjologii zarówno dla szczurów, jak i myszy. System pozwala rejestrować aktywność jednostki i potencjał pola lokalnego (LFP) do 32 kanałów z różnymi rodzajami elektrod. System został zbudowany przy użyciu technologii Intan RHD 2132. Akwizycja danych i nagrania odbywają się na karcie DAQ, która została umieszczona w plecaku zwierzęcia. Sygnał jest wzmacniany kaskadą wzmacniaczy i digitalizowany za pomocą 16-bitowego przetwornika ADC. Filtry pozwalają filtrować sygnał w paśmie 0,1–20000 Hz. Zasilany jest z mini-baterii o wydajności 340 mA/godz. System został zwalidowany generowanymi sygnałami u znieczulonego szczura i wykazał wysoką jakość nagrań.

Słowa kluczowe: elektrofizjologia wielokanalowa, gryzonie swobodnie zachowujące się, aktywność jednostkowa, potencjał pola lokalnego

Introduction

Nervous system works and codes information in the form of various electrical events: series of individual spikes, local potentials and up to complex brain oscillations. Today's scientific world has many different techniques for brain imaging and investigation, however the measuring of electrical activity in different scales is an essential part to understand the principles of the brain functioning. Also nowadays this field of research undergoes rapid increasing in numbers of channels for recording systems and fast evolution in hardware and software. Systems that enable recordings in freely behaving animals are typically complex and do not have enough flexibility. Even rapid growing low-cost open-source systems do not fully correspond to the needs for experiments, which require animal to be completely freely behaving. Most of such systems work with animals with implanted electrode array and head stages connected with data acquisition modules by cables and tethers. We present here the concept of a low-cost backpack system for multichannel recordings in freely behaving animals.

1. Aim and task of the research

In the current paper, we discussed the design of flexible system for extracellular recordings in rodents from freely accessible parts.

2. Analysis of alternative open-source systems

Fast evolution of microelectronics and increased requirements for flexibility of systems for electrophysiology triggered a series of projects for low-cost open source recording systems in rodents, monkey and humans [10, 13, 15, 17, 18, 25, 29]. The first open-source and low-cost systems for multichannel physiology include A/D system in 1994 created in Bruce McNaughton's lab, which was redesigned as ArtE later (<https://github.com/imalsogreg/arte>

ephys). The next was MEA Bench in 2000 created by Daniel Wagenaar, Tom Demarse, and Steve Potter [25]. Neuro Righter system was developed in 2000th by John Rolston, Riley Zeller-Townson, and Jon Newman [10, 13, 15]. The cost of Neuro Righter had fallen from 60000\$ to 10000\$ compared with the MEA Bench [17] due to recent progress of electronic components.

The next boom started after production of amplifier chips RHD, RHA and RHS series by Intan Technologies, when Jacob Voigts and Josh Siegle found Open Ephys initiative, which included acquisition board and dynamically evolved software for close-looped experiments [18, 29]. It consists of hardware block using FPGA-based acquisition card for recordings and software package for real-time data visualization and analysis. It allows recordings from 128–512 channels simultaneously with real-time spike sorting and detection. However, this system requires commercial Intan technologies head stage. The head stage should be installed on the animal skull and animal is tethered during recordings [3, 18, 28]. Open Ephys system becomes the most wide-used closed-loop system for multichannel electrophysiology in different laboratories all over the world.

Also a lot of small projects were developed in different laboratories including both recording and stimulation options [2, 4, 9, 16, 27].

The last outbreak in the field of multichannel electrophysiology was in 2017, made by collaboration of Howard Hughes Medical Institute, Wellcome Trust, Gatsby Charitable Foundation and Allen Institute for Brain Science. They developed shank probe with amplifiers cascade and ADC located directly on the probe and capable to record from more than 400 sites simultaneously [8, 11, 21, 22]. Neuropixel probe is not completely open-source project, however it can work with different hardware, it is flexible and has the lowest price per channel. These characteristics make Neuropixel the cheapest alternative compared even with open-source platforms. However, animals are tethered in their configuration also [1, 6].

Cost of the recording systems has dropped by near two orders from the A/D system to the lowest level for NeuroPixel today (Fig. 1) [10, 13, 15, 17, 21, 22, 25]. Price per channel for our system is about 22 USD.

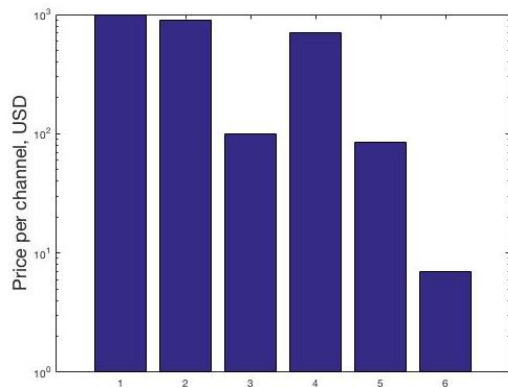


Fig. 1. Cost per channels for different recording systems has decreased by nearly two orders for last decades (1 – A/D (1994), 2 – MEABench (2000), 3 – NeuroWrighter (2008), 4 – ArtE (2011), OpenEphys 5 – (2012), 6 – NeuroPixel (2017))

As was mentioned above, development of low-cost, compact and flexible system from freely accessible parts allowing recordings from untethered animals is still actual. Realizations of such recordings in completely freely behaving animals are possible in two general concepts. The first one uses wireless signal transmission gathered from the implanted electrode array mounted on the skull of animal or on the animal itself as a backpack. Then with a receiver, analogous or already digitalized signal is transmitted recorded on PC [5]. In the second concept all cycle of data collection can be realized on the animal and data can be recorded on the memory card [20, 24]. The main problems of such systems are high power consumption, limitation for numbers of channels and operational time. The second concept is autonomous system, which can give to researchers an option to make recordings in untethered animals.

The aim of the study: Development and validation of low-cost system for multichannel electrophysiological recordings in anesthetized and freely behaving animals in the framework of second concept.

3. Material and methods

The system was developed for unit activity and LFP recordings in anesthetized and freely behaving animals. DAQ-module powered with mini-battery was designed to be mounted as a back-pack in animal and should be connected with electrode array by use of a flat flex cable (Fig. 2).

DAQ card for multichannel electrophysiology based on core Intan RHD2132 chip. This chip includes fully integrated low-noise amplifier array, adjustable analogue filters and 16-bits ADC. ADC operation is 1.05 MSamples per second and supports sampling 32 amplifier channels at 30 kSamples/s sampling rate for each channel (Fig. 3). Also the chip includes optional on-chip DSP high-pass filters for amplifier offset removal and auxiliary ADC inputs for interfacing additional sensors [29]. Parameters of the system are shown in Table 1.

Microcontroller STM32L12KB is operated with the core chip through SPI or low-voltage digital signal interface (LVDS). Data transfer occurs using additional FRAM memory to compensate small buffer size allocated in the microcontroller memory. Data are recorded in the microSD card as binary file and can be processed offline after finish the recordings (Fig. 4). Filter's parameters, list of active channels and sampling rate can be programmed through custom-written software (C++) before start of experiment. Recordings can be initiated and finished with pressing of button on the board. LED indicates start and finish of recordings, charge level of battery and presence of microSD card by blinking in specific manner for each case.

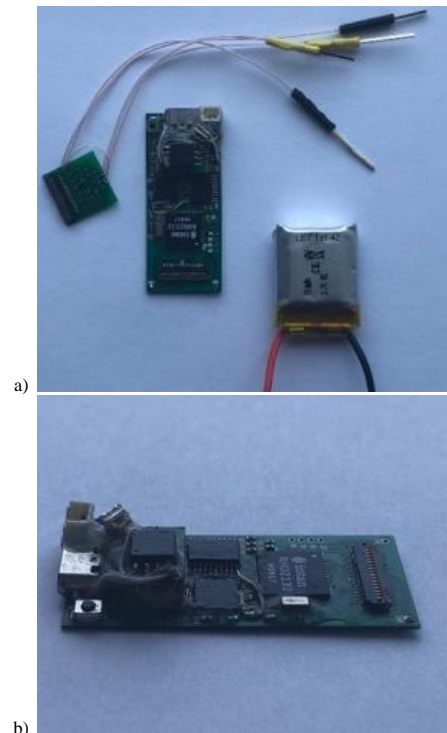


Fig. 2. General (top and side) view of the DAQ card, battery and connectors for signal simulation

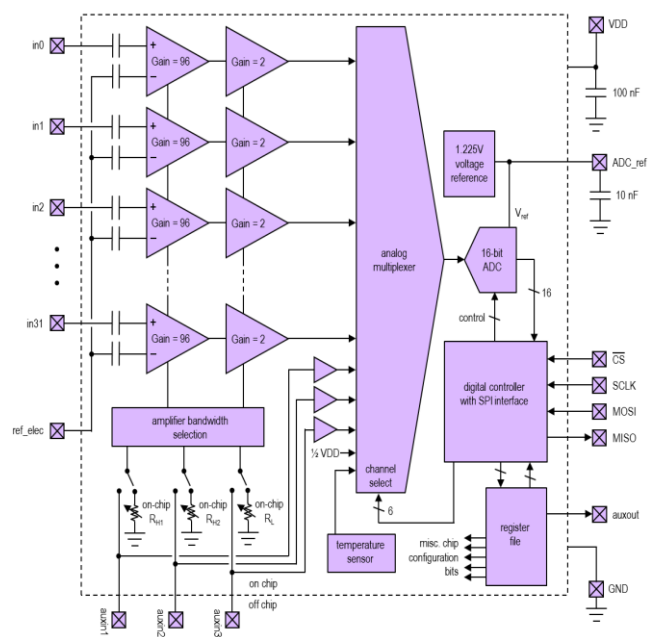


Fig. 3. Simplified core chip diagram from Intan RHD series datasheet [29]

Table 1. Properties of the data acquisition system

Parameter	Value
Dimensions	17×41 mm
Weight without battery	2.95 g
Battery weight	5.05 g
No. of channels (programmable)	up to 32
Gain	192 V/V
Filters range (fLC/fUC) programmable	0.5–500Hz/100–20000Hz
Input referred noise	2.4 μ Vrms

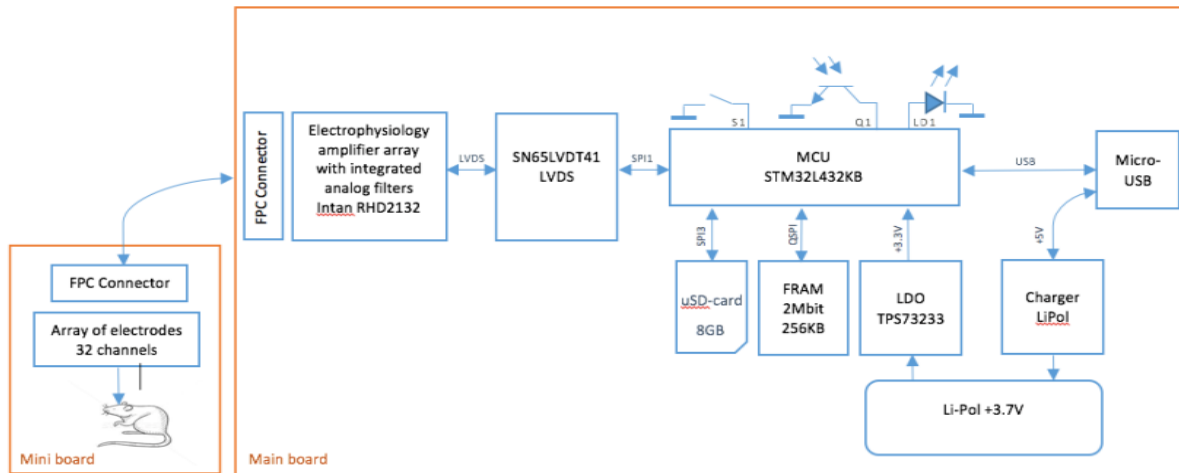


Fig. 4. Block-scheme of data acquisition card: signal from implanted electrode array, connected to DAQ module with FPC cable, collected with Intan RHD2132 core chip (signal is amplified, filtered and digitalized). Core chip is operated by microcontroller (MCU STM32L432KB). MCU using FRAM records data on the microSD card. System is powered with Li-polymer battery (Li-Pol). LVDS Driver – driver of low-voltage differential signaling, S1 – switch, LD1 – signaling LED, Q1 – phototransistor, LDO – low drop out regulator

Custom software was written for our DAQ-card. Data acquisition was organized in the following flow chart:

- Intan RHD2132 chip is connected to μC by SPI3 – μC uses SPI3 to connect to μSD -card;
- 32 kB buffer of command array is transferred to the Intan in cyclic mode through SPI using DMA TX channel;
- 32 kB array with data is received in cyclic mode simultaneously using DMA RX channel;
- Recordings on the μSD -card is made by 16 kB blocks;
- Writing speed should be more than capture of data;
- μSD -card shows 250 ms time gaps during recordings, that is why data is collected in the intermediary buffer in the external FRAM memory by 16 kB blocks.

To test the accuracy of data acquisition we conducted several bench tests. The first stages of system validation were performed with generated signals. The signals were sent and detected with known signals on the different channels of the system. Tests were carried out in different frequency range, sampling rates and connection of electrode array to DAQ card to check the functionality and accuracy of recordings.

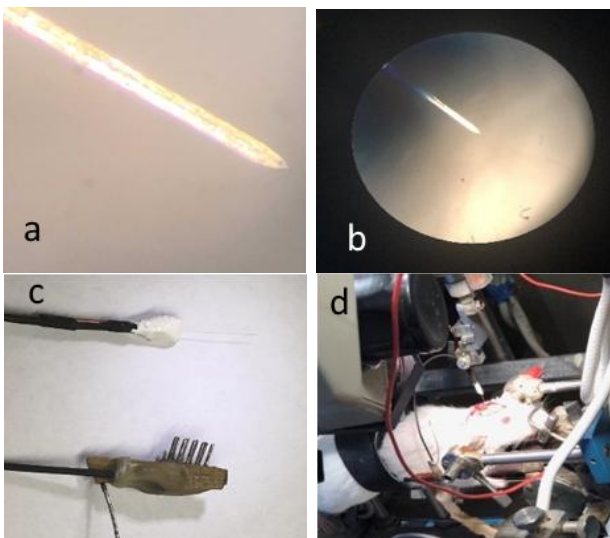


Fig. 5. (a, b) – tip of the 8-channel electrode array; (c) – 8-channel electrode array with connector for signal visualization on oscilloscopes, (d) – animal with implanted electrodes during recordings

At the next stage, the system was validated on the anaesthetized rats. 8-channel microware array was implanted in the hippocampal area of adult Wistar rat. Experiment was carried out in accordance with the National general principles for experiments on animals. The rat was anaesthetized with ketamine (100 mg/kg) – xylazine (10 mg/kg) as intraperitoneal injection and was given subcutaneous injection of lidocaine to minimize pain [19]. Craniotomy was made in the projection of right hippocampus (4.2 mm – P, 3.6 mm – L). Dura was pricked and microelectrode array was implanted. Array consisted of 8 tungsten wire with $d = 12 \mu\text{m}$ /each electrode (Fig. 5).

The electrode array had integrated reference coil and ground wire, which were placed around drilled hole under the skull. Using custom made micro-manipulator, the electrode array was moved into the targeted brain area with the $5 \mu\text{m}$ step, until stable neural signal was recorded. Verification of a single unit activity was proved with wireless 8-channel system for extracellular electrophysiology [12, 14, 23] with simultaneous visualization of signal on oscilloscopes [6, 26].

4. Results and discussion

Fabrication, assembling and programming of the system had taken about 8 months. All parts of DAQ-card are freely accessible. Validation was performed on the generated signals, which were sent directly to the DAQ-card inputs through custom made PCB-board with electrodes and connector on the first stage (Fig. 6a) or through 8-channels microelectrode array through saline on the second stage (Fig. 6b). Tests showed high quality of signal and no cross-talk between the channels (Fig. 6a).

On the second stage the signals with different frequency were sent to DAQ-module from 8-channel microelectrode array through saline. Fourier transform confirmed data acquisition accuracy (Fig. 7).

At the next stage, the neural signal was recorded from hippocampal area of anaesthetized rat. The signal processing and spike detection were done offline. The signal was filtered between 244 Hz and 6 kHz with 4th order Butterworth band pass filter and spikes were extracted (Fig. 8).

In the current version, our system does not include several necessary options, such as synchronization with external devices, visualization of data, spike detection and sorting modules. We plan to expand functionality in the next modifications.

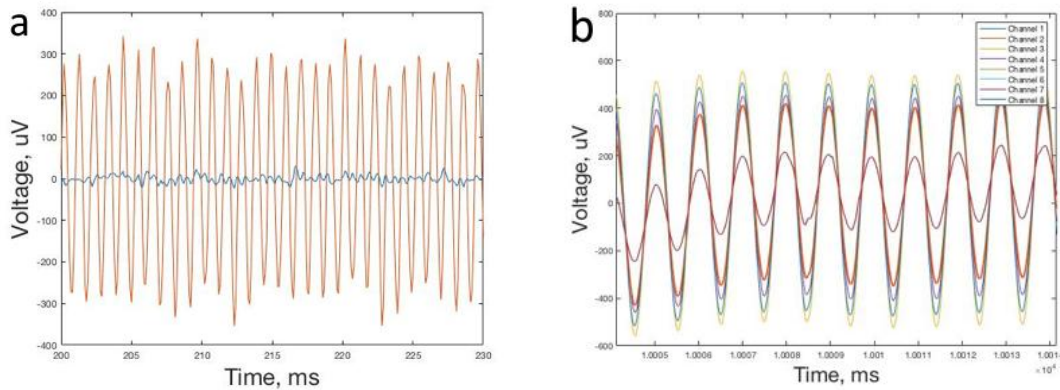


Fig. 6. a) simulated signal was sent to DAQ-card directly. Data from channel 1 and channel 4 are presented, signal parameters: amplitude – $\sim 300\mu V$, frequency – 1000 Hz on channel 1 (red curve), channel 4 was grounded (blue curve), b) simulated signal was sent to DAQ-module directly. 8 channels are shown signal parameters amplitude – $\sim 500\mu V$, frequency – 1000 Hz

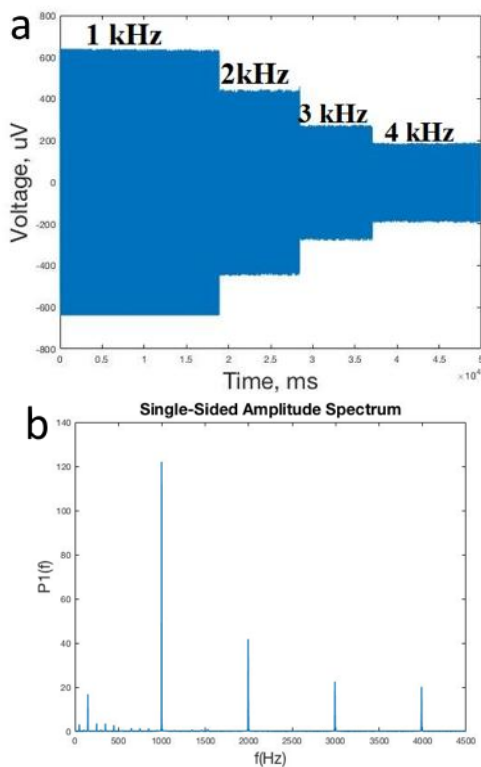


Fig. 7. Generated sine wave recorded with DAQ-card, data from channel 1 are presented. Signal parameters: (a) voltage – $300\mu V$, frequency 1 kHz, 2 kHz, 3 kHz, 4 kHz (b) Fourier transform of recorded signal showed peaks on the testing frequencies

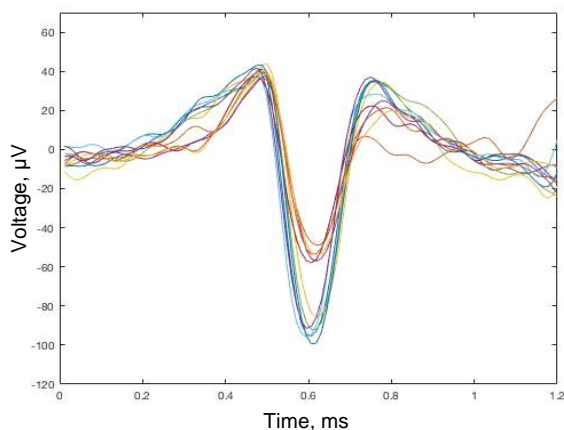


Fig. 8. Superposition of detected and separated spikes after signal processing

5. Conclusions

Designed open source low-cost system for multichannel electrophysiology was built on widely used parts and can record simulated and neural signals with high accuracy. It can be used in different modes for particular experimental requirements. It has several limitations – lack of memory for stable recordings at high sampling rates, does not have option to be precisely synchronized with other devices, absence of real-time data visualization and spike detection and sorting functions. Further optimizations of the system are underway and can overcome most of these limitations to extend the modes of data acquisition and increase experimental flexibility.

References

- [1] Al_Omari A. K., Saied H. F. I., Avrunin O. G.: Analysis of Changes of the Hydraulic Diameter and Determination of the Air Flow Modes in the Nasal Cavity. Image Processing and Communications Challenges 3. Springer, Berlin, Heidelberg 2011, [DOI: 10.1007/978-3-642-23154-4_34].
- [2] Alam M., Chen X., Fernandez E.: A low-cost multichannel wireless neural stimulation system for freely roaming animals. Journal of neural engineering 10(6), 2013, 066010.
- [3] Bennett C. et al.: Higher-order thalamic circuits channel parallel streams of visual information in mice. Neuron 102(2), 2019, 477–492.
- [4] Erickson J. C. et al.: Intsy: a low-cost, open-source, wireless multi-channel bioamplifier system. Physiological measurement 39(3), 2018, 035008.
- [5] Fan D., Rich D., Holtzman T., Ruther P., Dalley J. W., Lopez A., et al.: A wireless multi-channel recording system for freely behaving mice and rats. PLoS ONE 6(7), 2011, e22033, [DOI: 10.1371/journal.pone.0022033].
- [6] Fyrmipas G. et al.: The value of bilateral simultaneous nasal spirometry in the assessment of patients undergoing septoplasty. Rhinology 49(3), 2011, 297–303.
- [7] Ghomashchi A. et al.: A low-cost, open-source, wireless electrophysiology system. 36th Annual International Conference of the IEEE Engineering in Medicine and Biology Society, 2014.
- [8] Juvinett A. L., Bekheet G., Churchland A. K.: Chronically implanted Neuropixels probes enable high-yield recordings in freely moving mice. eLife 8, 2019, e47188.
- [9] Kinney J. P. et al.: A direct-to-drive neural data acquisition system. Frontiers in neural circuits 9, 2015, 46, [DOI: 10.3389/fncir.2015.00046].
- [10] Laxpati N. G. et al.: Real-time in vivo optogenetic neuromodulation and multielectrode electrophysiologic recording with NeuroRighter. Frontiers in neuroengineering 7, 2014, 40.
- [11] Liang B., Ye X.: Towards high-density recording of brain-wide neural activity. Science China Materials 61, 2018, 432–434, [DOI: 10.1007/s40843-017-9175-3].
- [12] Moroz V. M. et al.: Coupled Spike Activity in Micropopulations of Motor Cortex Neurons in Rats. Neurophysiology 42(2), 2010, 110–117.
- [13] Newman J. P. et al.: Closed-loop, multichannel experimentation using the open-source NeuroRighter electrophysiology platform. Frontiers in neural circuits 6, 2013, 98.
- [14] Nosova Ya. V., Faruk K. I., Avrunin O. G.: A tool for researching respiratory and olfaction disorders. Telecommunications and Radio Engineering 77(15), 2018, 1389–1395.
- [15] Rolston J. D., Gross R. E., Potter S. M.: NeuroRighter: closed-loop multielectrode stimulation and recording for freely moving animals and cell cultures. Annual International Conference of the IEEE Engineering in Medicine and Biology Society, 2009.
- [16] Rotermund D. et al.: Open hardware: Towards a fully-wireless sub-cranial neuro-implant for measuring electrocorticography signals. BioRxiv 036855, 2017.

- [17] Slegle J. H. et al.: Neural ensemble communities: open-source approaches to hardware for large-scale electrophysiology. *Current opinion in neurobiology* 32, 2015, 53–59.
- [18] Slegle J. H. et al.: Open Ephys: an open-source, plugin-based platform for multichannel electrophysiology. *Journal of neural engineering* 14(4), 2017, 045003.
- [19] Sikes R. S., Gannon W. L.: Guidelines of the American Society of Mammalogists for the use of wild mammals in research. *Journal of Mammalogy* 92(1), 2011, 235–253.
- [20] Spivey R. J., Bishop Ch. M.: An implantable instrument for studying the long-term flight biology of migratory birds. *Review of Scientific Instruments* 85(1), 2014, 014301.
- [21] Steinmetz N. A. et al.: Challenges and opportunities for large-scale electrophysiology with Neuropixels probes. *Current opinion in neurobiology* 50, 2018, 92–100.
- [22] Steinmetz N. et al.: Dataset: simultaneous recording with two Neuropixels Phase3 electrode arrays. *CortexLab at UCL*, 2016.
- [23] Vlasenko O. et al.: Multichannel system for recording myocardial electrical activity. *Information Technology in Medical Diagnostics II: Proceedings*

- of the International Scientific Internet Conference “Computer Graphics and Image Processing” and the XLVIIIth International Scientific and Practical Conference “Application of Lasers in Medicine and Biology”. CRC Press, 2019.
- [24] Vyssotski A. L. et al.: Miniature neurologgers for flying pigeons: multichannel EEG and action and field potentials in combination with GPS recording. *Journal of neurophysiology* 95(2), 2006, 1263–1273.
- [25] Wagenaar D., DeMarse T. B., Potter S. M.: MeaBench: A toolset for multi-electrode data acquisition and on-line analysis. *Conference Proceedings. 2nd International IEEE EMBS Conference on Neural Engineering*, 2005.
- [26] Wójcik W., Pavlov S., Kalimoldayev M.: *Information Technology in Medical Diagnostics II*. CRC Press, London 2019, [DOI: 10.1201/9780429057618].
- [27] Woods V. et al.: A low-cost, 61-channel μ ECoG array for use in rodents. *7th International IEEE/EMBS Conference on Neural Engineering (NER)*, 2015.
- [28] Yüzgeç Ö. et al.: Pupil size coupling to cortical states protects the stability of deep sleep via parasympathetic modulation. *Current Biology* 28(3), 2018, 392–400.
- [29] RHD2000 Series Digital Electrophysiology Interface Chips RHD2116, RHD2132. *Intan Technologies, LLC*.
http://intantech.com/files/Intan_RHD2000_series_datasheet.pdf

M.Sc. Olga Chaikovska

e-mail: chaikovska.olga@vnm.u.edu.ua

Ph.D. student at the Department of Human Physiology, Vinnytsia.

The field of scientific interest is dopaminergic system pathology, changing in neural dynamics and behavior during neurodegenerative diseases, electrophysiological markers (early stages) for neurodegenerative diseases.



ORCID ID: 0000-0002-6489-6040

Eng. Oleksandr Ponomarenko

e-mail: alux.ponomarenko@gmail.com

Engineer at the Department of Human Physiology.

Scientific interests: hardware development of data acquisition system for biopotentials recordings in small animals.



ORCID ID: 0000-0002-3058-7637

Ph.D. Oleksandr Dovgan

e-mail: alexander.d1980@gmail.com

Docent at the Department of Human Physiology.

Scientific interests is focused on the organization of motor programs in different cortical area and subcortical structures, investigation of neural processes during motor learning, changes in neuronal activity in hypothalamus and amygdala during prolonged starvation and after operant movements learning.



ORCID ID: 0000-0002-8740-0650

Ph.D. Ihor Rokunets

e-mail: rokunets@vnm.u.edu.ua

Docent at the Department of Human Physiology.

Scientific interests: electrical activity of neurons on the group level in the motor cortex and hippocampus; development of neurophysiological equipment (electrophysiology), polycardiography (phonoCG, ECG, ballistocardiography) on the open heart and in freely behaving animals, techniques for dynamic assessment of human pose and algorithm for data analysis.



ORCID ID: 0000-0002-8255-6007

Prof. Sergii Pavlov

e-mail: psv@vntu.edu.ua

Doctor of Technical Sciences, Professor, Academician of the International Academy of Applied Radioelectronics. Vice-rector of for Scientific Work of Vinnytsia National Technical University, professor of biomedical Engineering

Scientific direction – biomedical information optoelectronic and laser technologies for diagnostics and physiotherapy influence. Deals with issues of improving the distribution of optical radiation theory in biological objects, particularly through the use of electro-optical systems, and the development of intelligent biomedical optoelectronic diagnostic systems and standardized methods for reliably determining the main hemodynamic cardiovascular system of comprehensive into account scattering effects.



ORCID ID: 0000-0002-0051-5560

D.Sc. Olena Kryvoviaz

e-mail: 16124sk@gmail.com

Doctor of Sciences, docent.

The head of Department of Pharmacy of National Pirogov Memorial University of Vinnytsia. Scientific direction – pharmacy technology.



ORCID ID: 0000-0001-5441-1903

Prof. Oleg Vlasenko

e-mail: vlasenko@vnm.u.edu.ua

Doctor of Medical Sciences, Professor. Vice-rector of for Scientific Work of National Pirogov Memorial University of Vinnytsia, professor at the Department of Human Physiology.

Scientific direction – neural circuits that are responsible for voluntary control of movements, interaction between autonomic and somatic divisions of CNS during operant movements, detection of stress by dynamical position of body center mass and physiological parameters.



ORCID ID: 0000-0001-8759-630X

otrzymano/received: 01.11.2019

przyjęto do druku/accepted: 06.12.2019

DOI: 10.35784/IAPGOS.116

ATRIAL FIBRILLATION DETECTION ON ELECTROCARDIOGRAMS WITH CONVOLUTIONAL NEURAL NETWORKS

Viktor Kifer¹, Natalia Zagorodna¹, Olena Hevko²¹Ternopil Ivan Puluj National Technical University, Faculty of Computer Information Systems and Software Engineering, Ternopil, Ukraine²Ternopil Ivan Puluj National Technical University, Faculty of Applied Information Technologies and Electrical Engineering, Ternopil, Ukraine

Abstract. In this paper, we present our research which confirms the suitability of the convolutional neural network usage for the classification of single-lead ECG recordings. The proposed method was designed for classifying normal sinus rhythm, atrial fibrillation (AF), non-AF related other abnormal heart rhythms and noisy signals. The method combines manually selected features with the features learned by the deep neural network. The Physionet Challenge 2017 dataset of over 8500 ECG recordings was used for the model training and validation. The trained model reaches an average F1-score 0.71 in classifying normal sinus rhythm, AF and other rhythms respectively.

Keywords: electrocardiography, machine learning, neural networks

DETEKCJA MIGOTANIA PRZEDSIONKÓW NA ELEKTROKARDIOGRAMACH Z WYKORZYSTANIEM KONWOLUCYJNEJ SIECI NEURONOWEJ

Streszczenie. W tej pracy, przedstawiamy nasze badania, które potwierdzają przydatność zastosowania konwulucyjnej sieci neuronowej dla klasyfikacji zapisów jedno-odprowadzeniowego EKG. (tak brzmi ta nazwa). Proponowana metoda została zaprojektowana dla klasyfikowania prawidłowego rytmu zatokowego, migotania przedsionków (AF), poza-AF powiązanych z innymi nieprawidłowymi rytмами serca i zaszumionymi (głośnymi?) sygnałami. Ta metoda łączy cechy wyselekcjonowane ręcznie z cechami wyuczonymi przez głębokie sieci neuronowe. Zbiór danych Physionet Challenge 2017 zawierający ponad 8500 zapisów EKG został zastosowany dla modelu szkolenia oraz walidacji. Model nauczony (wyszkolony?) osiąga odpowiednio średni F1-wynik 0.71 w klasyfikowaniu prawidłowego rytmu zatokowego, rytmu AF oraz innych rytmów.

Słowa kluczowe: elektrokardiografia, nauczanie maszynowe, sieci neuronowe

Introduction

Heart diseases are the leading cause of death in the EU and the US for both men and women. The fact that around 47% of sudden cardiac deaths occur outside a hospital suggests that many people with heart disease do not react on early warning signs.

An electrocardiogram (ECG) can be used for diagnostics of many heart malfunctions like the presence of any damage to the heart's muscle cells or conduction system. Many handheld ECG recorders were developed to produce a single-lead ECG. WIWE [23], AliveCor [1], OMRON HCG801 HeartScan [22] are the examples.

Automated ECG analysis is a complex problem, which includes a number of basic tasks such as noise reduction, QRS complex detection, P and T wave detection, analysis of the shapes of the waves and their positions and lengths. Each of those tasks is a separate topic of scientific research. For example, noise reduction is a well-explored task with a lot of developed techniques and methods, including band-pass filters [5], spectrograms [6], Fourier [15] and wavelet [8] transformations. QRS detection is also represented with a large list of methods reaching sensitivities and specificities of about 99.5. The detailed comparison of the QRS detection methods is done in [3].

Atrial Fibrillation (AF) is a common type of heart disease that leads to stroke, heart failure or other complications. Every year millions of people get affected by AF, and this number tends to increase. The percentage of people with AF also increases with age: from 0.14% under 50 years old to over 14% for those over 80 years old. And AF is often an episodic event, which makes early diagnostics even more complicated.

AF detection methods can belong to one of two categories: atrial activity analysis-based methods, which search for the absence of P waves or the presence of F-waves in the TQ interval; and ventricular response analysis based on the predictability of the inter-beat timing ('RR intervals').

Park *et al* [9] analyzed heartbeat variability from inter-beat intervals obtained by a wavelet-detector. The features are extracted from the Poincare plot of the intervals. The method performs a binary classification of the signal into AF/non-AF.

Rodenas-Garcia *et al* [11] incorporated wavelet entropy in ECG analysis. The signal is analyzed in chunks of 10 consequent

noise-free heartbeats, for which a median of TQ segment is extracted and the wavelet entropy is computed. The method can be used to detect common cardiac arrhythmias and atrial fibrillation.

Petrenas *et al* [10] proposed a simple method for long-term AF monitoring. The signal is processing with the 8-beat sliding window in order to reduce computational power. The building blocks of the algorithm are the estimation of RR trend and irregularity, ectopic beats filtering, bigeminy suppression and fusion of the signals. The model uses binary AF vs non-AF classification.

Tziakouri *et al* [13] built a 3-stage model for multi-label ECG classification. The first stage analyzes the quality of the signal and rejects noisy signals. In the second stage, the signal is classified into normal sinus rhythm and abnormality. And on the third stage, atrial fibrillation is separated from the other abnormal rhythms.

The previously developed methods are usually limited in applicability due to following reasons: 1) only normal and AF recording were considered, while all the other diseases were discarded; 2) good performance was shown of carefully-selected often clean data; 3) test dataset was not used or was too small for making a conclusion; 4) a small number of patients was used.

The aim of this research is to develop an atrial fibrillation detection model, which would not require complex and long-running computations for feature extraction. The input of our model is a raw ECG signal. The developed algorithm runs initially basic signal filtering and splits the signal into separate heartbeats. Then the sequence of heartbeats is used for heart disease prediction. Our model is also applicable for noisy signals with significant signal-to-noise ratio, because it involves filtering preprocessing algorithms. The model can also distinguish between atrial fibrillation and other abnormal rhythms.

1. Methodology

Our method is based on the usage of state-of-the-art ECG processing techniques in noise reduction and R-peaks combined with deep neural networks. Convolutional neural network layers are used as feature extractors over a 2D matrix of the signal heartbeats. The classification decision is done using fully connected network layers.

1.1. Dataset overview and preprocessing

The dataset used for this project was taken from PhysioNet/Computing in Cardiology Challenge 2017 [2]. It contains 8528 single-lead ECG recordings, sampled at 300Hz and varying lengths from 2700 to 18300 points. The records are labeled with 4 classes: normal sinus rhythm (N, 5154 records), atrial fibrillation (A, 771 records), other abnormal rhythms (O, 2557 records) and noise (originally marked with tilde in the dataset, replaced with P, 46 records).

The first and the most important step of the analysis is the visualization of the data. We plotted some samples from each class and analyze them visually. This helps to identify potential problems with the dataset as well as gives insights on how to create a set of relevant features to represent the data.

We paid more attention to the analysis of the class “Other” as it includes a wide range of heart diseases. We tried to identify those diseases and find out the most common ones. Some of them are 1) atrial flutter; 2) ventricular fibrillation; 3) tachycardia (more than 100 bpm); 4) bradycardia (less than 60 bpm); 5) wide QRS complex (more than 0.1 s – prolonged, more than 0.12 s – abnormal); 6) presence of extrasystole; 7) long PR interval (more than 0.2 s).

The review of the dataset revealed underlying problems, including the following: 1) some of the records were inverted, probably due to electrode misplacement; 2) values of the records are absolute and not restricted to any range; 3) imbalanced representation of the classes.

Our preprocessing steps include:

Noise reduction

The ECG signals are recorded using single-lead, non-medical equipment and usually by patients themselves. It means they are often noisy. The most common sources of noise are:

- electrode contact noise (frequency is about 1 Hz) caused by improper contact between the body and electrodes;
- motion artifacts produced by patient’s movements which affect electrode-skin impedance, resulting in usually short-term distortions;
- muscle contractions - noise with 10% of regular peak-to-peak ECG amplitude and frequency up to 10 kHz;
- baseline wander caused by a respiratory activity with a 0–0.5 Hz frequency.

The goal of this process is to remove noises while keeping as much of the signal as possible.

The most important cardiac information in ECG is stored within a frequency range of 0–20 Hz [14]. We apply both high pass (HPF) and low pass (LPF) FIR filters with the order of 100 (1/3 of the sampling frequency). For HPF cut-off frequency of 0.5 Hz was used to remove the baseline movement of the signal. And LPF was set with a cut-off frequency of 40 Hz to reduce the impact of other noise sources on the ECG.

Signal normalization

The ECG recorder might generate a wide range of values depending on different conditions when the recording was performed (Fig. 1). Also, manufacturers might provide their own value ranges for different recorders.

Neural networks can be considered as a function (usually non-linear) of input values multiplied by weights and combined with a bias. The weights and the bias are estimated during the model training. So, if the range of the input values changes, then the output of the function might also change. To avoid such cases, we applied a standard data normalization technique in the field of neural networks: to scale signal values to a specific range. The values of every record were converted to the range of [-1;1] by dividing original values by the absolute value of the signal.

Lead inversion detection

Inverted ECG signals happen in around 4% of the recordings even during a professional medical examination. Inverted records (for example, A06667, A08477) are more likely to be classified as abnormal rhythm due to changes in morphologies of the QRS and P and T waves.

We used a simple principle of comparing the absolute values of the minimum (abs_min) and the maximum (abs_max) in the QRS complex of the filtered signal.

We applied the lead inversion detection after running low pass and high pass filter. It is important as it removes most of the noise in the ECG signal and reduces misleading high peaks in the data, leaving primarily clear QRS complexes. For those cases, when the abs_max is at least less than 0.6 of abs_min, we considered such a record as inverted and performed the sign change for the values of the record. The algorithm detected and worked out the 734 inverted records in our dataset.

Handling of the imbalanced dataset problem

The dataset is highly unbalanced, which is common for natural signals, but it complicates the training process. While the model should learn the natural distribution of the classes (eg, most people would have normal sinus rhythm, and less would have some disease), the actual goal of the model is disease detection.

Normal sinus rhythm is more than 100 times more represented in the dataset, than noise and about 18 times more – than AF. The model might easily overfit and predict the most represented class. Severe overfitting was observed in early experiments.

There are several known approaches to handle the problem, including the usage of abnormalities detection algorithms. These algorithms apply class weights (penalties) on classifiers and perform data balancing. Another approach is to use the models which are better at handling unbalanced data. The experiments with class weights did not show any significant improvement in classification results. Therefore, data balancing techniques were applied to the dataset, including oversampling and undersampling [4].

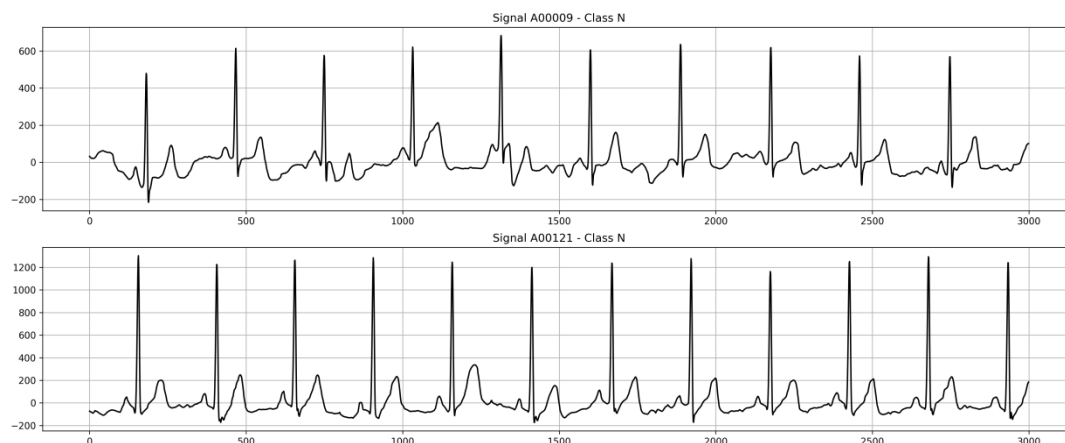


Fig. 1. The difference in value ranges for normal ECG signals (records A00009 and A00121, only 10 seconds of each record)

Data oversampling is used when the amount of collected data is insufficient. The technique is applied to the underrepresented minority classes in the dataset. The main idea is to create synthetic samples of the data based on the characteristics of existing samples. The signals were interpolated in time (either making them shorter or longer) by 10 to 25% (chosen randomly). The generated signals might have a very low or very high heart rate, as we do not take into account the heart rate of the original signal.

If a class of data is the overrepresented majority class, undersampling may be used to balance it with the minority class. This operation took the instances of the majority class and compared the time-shifted filtered signals by the square root of differences in the developed method. About 10% of the records with the lowest differences were removed from the training samples.

1.2. Heartbeat detection

The detection of the heartbeat starts with the search of R-picks, the highest and the most resistant to the noise component of a single heartbeat. This is a well-known problem, and one of the most commonly used methods is the Pan-Tompkins algorithm [7]. The original paper states the detection rate of 99.3%. Our algorithm is a modification of the original one. It runs the Pan-Tompkins algorithm. Then it runs backward and looks for intervals where the RR interval length is larger than 1.5 of the mean RR interval length and reruns R-peak detection with the lower threshold.

After R-picks detection, we started the lookup of the Q and S positions, which are the local minimums on both sides of the R pick. After that, the algorithm also looks for the local maximums

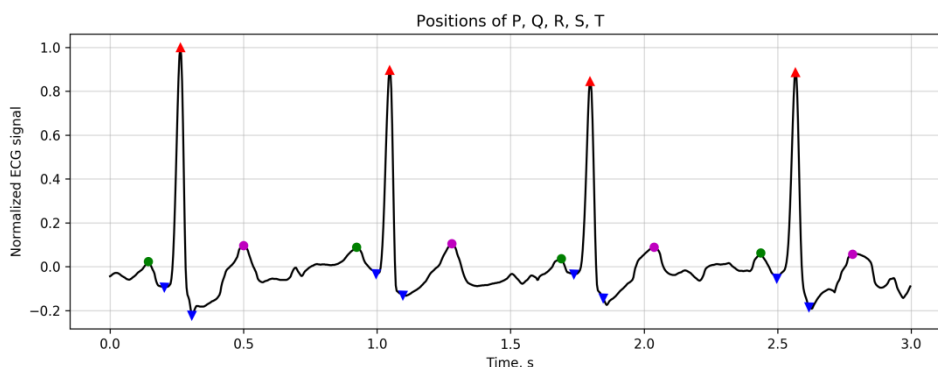


Fig. 2. Detection of heartbeat components: QRS points marked with triangles, maximums of P and T waves with circles

2. Neural network topology

We propose to use a convolutional neural network for ECG classification. Our model was particularly inspired by the VGG-16 neural network [12], which is commonly used for image recognition problems. We reduced the number of layers to 6, which includes two groups of 2 convolutional layers and a group of dense layers.

The input dimension for the neural network was set to 160 by 180, where 160 represents the heartbeats, and 180 is the number of data points per each heartbeat (0.6 s).

The input is supplied into a convolutional layer with 32 filters and a convolution window length 3. It is followed by the rectified linear unit activation (ReLU), a simple non-linear function that replaces all negative values in the activation map by zero. Then it goes the same convolutional layer followed by a max-pooling layer with pool size set to 2 and the downscaling factor of 2. Pooling helps resolve multiple problems related to neural networks: makes input representations smaller, reduces the number of parameters (which makes computations faster and controls overfitting), makes network resistant to small transformations of the input, helps to detect features in data no matter where they are located. Then another ReLU layer follows.

in the interval of 0.2 s before R pick and 0.4s after R pick. Those points are assumed to be positions of the maximum of P and T waves respectively. These important points are marked in Fig. 2.

Based on the positions of R-peaks, we extracted the heartbeats from the filtered signal, using the static window of 0.6 s (Fig. 3). We ignored the heartbeats, where the window cannot be applied (heartbeats on start or end of the signal).

The extracted heartbeat had 180 points. We constructed a matrix filled with all detected heartbeats. Input for the neural network should have the same number of templates for every record, therefore an upper limit of 160 heartbeats was set. In case, there were no enough heartbeats, we added empty heartbeats (zero-values) to the end of the matrix.

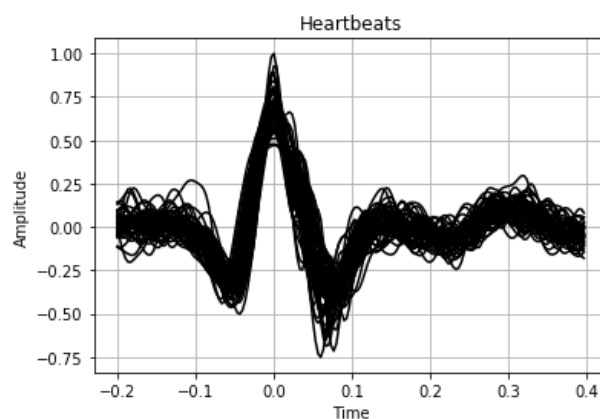


Fig. 3. Extracted normalized heartbeats from the ECG signal

MaxPooling was performed before ReLU activation to reduce the number of operations and fasten the training process. These layers create the first block of our neural network. It is finalized with the drop out layer with a drop rate of 0.25, which has a slight regularization effect and reduces overfitting. The second block is built using the same layers structure as the previous one, but we increased the number of filters in convolutional layers to 64. The architecture of the proposed neural network is given in Fig.4.

We transform the 2D output of the second block into 1D and supply it into a fully connected neural network (third block). This block contains a fully connected layer of 512 units and ReLU activation. It is followed by the drop out layer with a rate of 0.5.

The last layer of the neural network produces the model output. It should have the same number of neurons as the number of possible output labels. Therefore, the neural network ends with a fully connected layer of 4 units. The layer uses softmax activation, which normalizes the layer outputs sum to 1 (eg, each value is a probability of the input to be an instance of a given class).

The network was optimized using Stochastic Gradient Descent with Nesterov momentum of 0.9 and the initial learning rate set to 0.01.

We used categorical cross-entropy as a loss function for the neural network.

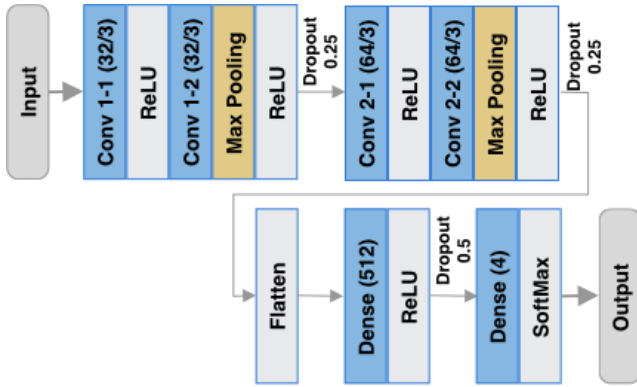


Fig. 4. The architecture of the neural network for ECG classification

1.3. Implementation notes and training procedure

We used Python [19] with Numpy [17] and SciPy [20] for signal processing, Scikit-Learn [18] and Keras [16] with Tensorflow CPU [21] backend for neural network construction and training.

We split the original dataset into training and validation sets, 2/3 and 1/3 respectively. Then we applied over- and undersampling on the training dataset. We used SciPy to resample the signals.

The network was implemented using Keras functional API. Convolutional layers were implemented using *Conv1D* and max-pooling was implemented using *MaxPooling1D* layers.

For neural networks, the categorical value of the output should be encoded with the one-hot encoding. This means that class 0 becomes a vector [1 0 0 0], class 1 becomes [0 1 0 0] and so on. We did that using Keras *to_categorical* utility function.

The neural network was trained in batches with 32 batch size. The training process was initialized with 30 training epochs and a controlling algorithm to stop training after reaching a minimum of the validation loss function. The training stop function was implemented using Keras *EarlyStopping* callback, with the patience parameter set to 7.

We also run a dynamic learning rate algorithm, which reduced the initial learning rate by a factor of 10, when the validation loss function did not improve during the last 3 epochs. The improvement delta was set to 10^{-4} , and the learning rate can be reduced from the initial value of 0.01 to 10^{-6} . It was implemented using *ReduceLROnPlateau* Keras callback.

3. Evaluation

Evaluation of the model is performed using F1 score which is a combination of precision (PPV) and recall (TPR).

$$F1_{class} = \frac{2 * PPV_{class} * TPR_{class}}{PPV_{class} + TPR_{class}} \quad (1)$$

The class detection accuracy of the model is a proportion of the number of true positive (TP) cases to the sum of true positive and false positive (FP) cases.

$$PPV_{class} = \frac{TP}{TP + FP} \quad (2)$$

The class recall of the model is a ratio of the number of true positive to the sum of true positive and false negative.

$$TPR_{class} = \frac{TP}{TP + FN} \quad (3)$$

For multi-class classification, we compute the F1 score for each class and the final score of the model is an average of all scores. But the distribution of normal, atrial fibrillation, other rhythms, and noisy data is highly imbalanced, and the amount of noisy data is significantly less compared to other classes, so the noise class evaluation was excluded from the final score. The F1 score of the model is an average of the scores for AF, N and O classes.

$$F1 = \frac{F1_{AF} + F1_N + F1_O}{3} \quad (4)$$

F1 score helps us to prevent an accuracy paradox, which is very common for the imbalanced datasets.

We also incorporated cross-validation technique, which helps to estimate how accurately a predictive model will perform in practice. It runs in rounds and each round involves partitioning of a dataset into training and test sets, fitting the training data into the model, and validating the classifier on the test data. 5-fold cross-validation was used for this project. This method splits the dataset into 5 subsets, then one subset is used for testing and 4 subsets for training. The parameter 5 not only defines the number of subsets, but also the number of rounds. A new subset is used for testing in each round. This means that during 5 rounds each of the generated subsets was used only once as a testing dataset.

4. Results

The model was validated both locally on the piece of the original dataset and remotely on the PhysioNet challenge hidden dataset.

Table 1 shows the detailed model performance report we generated based on the local test dataset (33% of the original dataset).

Table 1. Results of ECG classification using Convolutional Neural Network

Class	Precision	Recall	F1	Support
AF	0.62	0.64	0.63	183
Normal	0.78	0.92	0.84	1273
Other rhythm	0.70	0.45	0.55	608
Noise	0.61	0.59	0.60	68
Total	0.68	0.65	0.66	2132

As it was mentioned earlier, we also validated the model using 5-fold cross-validation. The model got an average mean F1 score of 0.68 and a standard deviation of 0.016.

Next, we sent the model for evaluation on the hidden dataset. PhysioNet runs the model in the virtual environment and computes the F1 score of the model for classes Normal, AF and Other. The results of the model on the hidden dataset are shown in Table 2.

The final score of the model on the hidden dataset is 0.71.

Table 2. PhysioNet report on the model performance

Class	Normal	AF	Other	Overall
F1	0.88	0.69	0.56	0.71

5. Conclusions

In this paper, we proposed an approach for the automatic detection of atrial fibrillation in single-lead ECGs using a convolutional neural network. Our model is designed to handle noisy signals and distinguish atrial fibrillation from other abnormal heart rhythms. The computational efficiency of the model is reached by using only basic signal preprocessing techniques like filtering and heartbeats detection.

The performance of the model was validated using 5-fold cross-validation, which showed an average F1 score on the test dataset equals 0.68 with a little variance of 0.016. The model accuracy was additionally confirmed by running it on a closed dataset of ECG signals from the PhysioNet website, where the model showed the overall result of 0.71.

Our result is lower compared to the results of the models which include manual feature extraction or a combination of multiple estimators. However, our model uses less computational power and it can be used on devices with limited resources.

There are several directions for future research. In particular, the signal resampling algorithm, used during model training, can be improved by taking the actual heart rate into account.

We also plan to improve the model performance (without reducing efficiency) by adding some of the computationally lightweight expert features like heart rate variability.

References

- [1] AliveCor ECG recording device. <https://www.alivecor.com>
- [2] Clifford G, Liu C, Moody B, Silva I, Li Q, Johnson A, Mark R.: AF classification from a short single lead ECG recording: the PhysioNet Computing in Cardiology challenge 2017. *Computing in Cardiology* 44, 2017, [DOI: 10.22489/CinC.2017.065-469].
- [3] Dilaveris P. E., Kennedy H. L.: Silent atrial fibrillation: epidemiology, diagnosis, and clinical impact. *Clinical Cardiology* 40(6), 413–418, 2017.
- [4] Hernandez J., Carrasco-Ochoa J. A., Martínez-Trinidad J. F.: An Empirical Study of Oversampling and Undersampling for Instance Selection Methods on Imbalance Datasets. In: Ruiz-Shulcloper J., Sanniti di Baja G. (eds): *Progress in Pattern Recognition, Image Analysis, Computer Vision, and Applications. CIARP 2013. Lecture Notes in Computer Science*, vol 8258. Springer, Berlin, Heidelberg 2013, [DOI: 10.1007/978-3-642-41822-8_33]
- [5] Himanshu S., Kumar J. S. J, Ashok V., Juliet A. V.: Advanced ECG Signal Processing using Virtual Instrument. *International Journal on Recent Trends in Engineering & Technology* 3(2), 2010, 111-114.
- [6] Huang J., Chen B., Yao B., He W. ECG Arrhythmia Classification Using STFT-based Spectrogram and Convolutional Neural Network. *EEE Access* 7, 2019, 92871-92880.
- [7] Kohler B.-U., Hennig C., Orglmeister R.: The principles of software QRS Detection. *IEEE Engineering in Medicine and Biology Magazine* 21(1), 2002, 42-57, [DOI: 10.1109/51.993193].
- [8] Mikhled A., Daqrouq K.: ECG Signal Denoising by Wavelet Transform Thresholding. *American Journal of Applied Sciences* 5(3), 2008, 276-281.
- [9] Park J., Lee S., Jeon M.: Atrial fibrillation detection by heart rate variability in Poincare plot. *Biomed engineering online* 8/38, 2009, 1-12.
- [10] Petrenas A., Marozas V.: Low-complexity detection of atrial fibrillation in continuous long-term monitoring. *Comput in Biology and Medicine* 65, 2015, 184-191.
- [11] Rodenas-Garcia J., Garica M., Alcaraz R., Rieta J.: Wavelet Entropy Automatically Detects Episodes of Atrial Fibrillation from Single-Lead Electrocardiograms. *Entropy* 17, 2015, 6179-6199, [DOI: 10.3390/e17096179].
- [12] Simonyan K., Zisserman A.: Very Deep Convolutional Networks for Large-Scale Image Recognition. *Inter Conf on Learning Representations (ICLR)*, 2015. [arXiv preprint arXiv:1409.1556].
- [13] Tziakouri M., Pitris C., Orphanidou C.: Classification of AF and Other Arrhythmias from a Short Segment of ECG Using Dynamic Time Warping. *Comp in Cardio*, 2017, 1-4.
- [14] Velayudhan A., Peter S.: Noise Analysis and Different Denoising Techniques of ECG Signal – A Survey. *IOSR Journal of Electronics and Communication Engineering*, 2016, 40-44
- [15] Wang Z., Wan F., Wong C.M., Zhang L.: Adaptive Fourier decomposition based ECG denoising. *Computers in Biology and Medicine* 77, 2016, 195–205. <https://keras.io> Keras documentation (available: 19.07.2019).
- [16] <https://numpy.org> NumPy official documentation (available 01.07.2019).
- [17] <https://scikit-learn.org> Scikit-Learn official website (available: 01.07.2019).
- [18] <https://www.python.org> Python programming language (available 30.06.2019).
- [19] <https://www.scipy.org> SciPy official documentation (available 01.07.2019).
- [20] <https://www.tensorflow.org> Tensorflow official page (available: 19.07.2019).
- [21] OMRON HCG801 HearnScan ECG recorder. <https://www.omron-healthcare.com/en/products/electrocardiograph>
- [22] WIWE ECG recording device. <https://shop.mywiwe.com/en/ecg-recording-105>

M.Sc. Viktor Kifer

e-mail: kifervictor@gmail.com

Received a master's degree in Software Engineering from Ternopil Ivan Puluj National Technical University in 2018. Currently, he is a Ph.D. student working on biomedical signal processing.



ORCID ID: 0000-0002-0621-9121

Ph.D. Natalia Zagrodna

e-mail: zagrodna.n@gmail.com

In 2003, graduated in Information Control Systems from Ternopil Ivan Puluj State Technical University. From 2007, PhD in Technical Sciences. The Ph.D. thesis was dealt with mathematic modelling, analysis and prognosis of gas consumption. Current position – Head of Cybersecurity Department.



ORCID ID: 0000-0002-1808-835X

Ph.D. Olena Hevko

e-mail: gevkojenka@gmail.com

In 1995, graduated in medicine from Ivano-Frankivsk State Medical Academy. Obtained a Ph.D. in Internal medicine in 2003. In 2008, received an academic title of assistant professor of the Department of Biotechnical Systems.



ORCID ID: 0000-0003-1427-1699

otrzymano/received: 09.09.2019

przyjęto do druku/accepted: 06.12.2019

THE CONCEPT OF A FLYING ELECTROMAGNETIC FIELD MEASURING PLATFORM

Sławomir Szymaniec, Sławomir Szymocha, Łukasz Miszuda

Opole University of Technology, Faculty of Electrical Engineering, Automatic Control and Informatics Institute of Computer Science, Opole, Poland

Abstract. Nowadays, humans are surrounded by more and more devices that artificially generate an electromagnetic field. According to law, supervision of the level of the electromagnetic field requires specific measurements. Measurement performed by traditional methods have several limitations, which come from the infrastructure and time taken to perform the measurement. New methods of measurement are being developed in order to execute the research relatively quickly and repeatedly without any limitations. One of the methods is to use a flying mobile measurement platform.

Keywords: electromagnetic field, flying platform, measuring

KONCEPCJA LATAJĄCEJ PLATFORMY POMIAROWEJ POLA ELEKTROMAGNETYCZNEGO

Streszczenie. Człowieka obecnie otacza coraz więcej urządzeń, które sztucznie generują pole elektromagnetyczne. Zgodnie z prawem nadzór nad poziomem natężenia pola elektromagnetycznego wymaga pomiarów. Pomiar wykonywany metodami tradycyjnymi ma kilka ograniczeń dotyczących infrastruktury i czasu wykonywania pomiaru. Opracowuje się coraz to nowe metody pomiaru aby można było go wykonać w miarę szybko i powtarzalnie bez ograniczeń infrastrukturą. Jedną z metod jest wykorzystanie do pomiarów platform latających.

Słowa kluczowe: pole elektromagnetyczne, platforma latająca, pomiar

Introduction

Direct influence of the electromagnetic field on a human being may cause numerous threats to health or safety. A person within the electromagnetic field is exposed to the presence of a magnetic field and induced electric fields caused by electrical currents flowing through the body.

Human beings are not usually able to feel the direct effect of the electromagnetic field on their organisms. According to studies [6–8, 11], the effects of the electromagnetic field may have other consequences that can be revealed with a time delay, especially during strong exposures, and they include:

- nervous system disorders,
- cardiovascular disorders,
- disorders of the immune system,
- neoplastic processes,
- subjective complaints, such as: headaches, fatigue, memory problems.

The influence of the electromagnetic field can also have an indirect impact on people, interpreted as contact currents that flow through the human body touching a metal object that has a different electrical potential due to the electromagnetic field impact on it [7].

The effects of the indirect impact of the electromagnetic field can also include:

- interference with electronic devices, including medical equipment, electronic implants (such as cardiac pacemakers) and medical devices worn permanently on the body (such as infusion pumps)
- a threat to the functioning of passive metal implants
- damage to magnetic storage media [6].

In our environment, the problem of measuring the electromagnetic field without restrictions coming from the infrastructure and various external conditions has not yet been solved. The generality of infrastructure is now a very big problem when performing an electromagnetic field measurement, because it is not possible to take measurements very close to the source of the electromagnetic field. The main sources of the electromagnetic fields include, for instance: high voltage lines, which during transmission create around themselves an artificial EM field, transformer stations, mobile phone stations, RTV transmitters [6].

1. Measurement of the electromagnetic field

Nowadays, it is difficult to imagine life without electricity anymore. In the early years no one was thinking about the influence of the electromagnetic field and radio waves on living organisms. With time, however, an increasing number of people began to pay attention to the levels of electromagnetic radiation produced by human beings, which surrounds our communities to an ever growing extent [2]. According to the national Act of 27 April 2001 – Environmental Protection Law (unified text Journal of Laws 2013, 1232 with subsequent amendments), electromagnetic fields are defined as electric, magnetic and electromagnetic fields with frequencies ranging from 0 Hz up to 300 GHz. The evaluation of electromagnetic field levels in the environment is carried out as part of the State Environmental Monitoring. The Voivodship Inspector for Environmental Protection conducts periodic studies of the levels of electromagnetic fields in the environment. The number of measuring stations, the type of areas on which measurements are carried out and their frequency in Poland is specified in the Regulation of the Minister of Environment of November 12, 2007 on the range and manner of conducting periodic tests of electromagnetic fields in the environment (Journal of Laws No. 221, item 1645).

As of 1st July 2016, all members of the European Union are bound by the Directive 2013/35/EU of the European Parliament and of the Council dated 26 June 2013 on the minimum health and safety requirements regarding the exposure of workers to the risks arising from physical agents (electromagnetic fields) (20th individual Directive within the meaning of Article 16(1) of Directive 89/391/EEC) and repealing Directive 2004/40/EC [12].

The above Directive was followed by the national Regulation of the Minister of Family, Labour and Social Policy dated 29th June 2016 on the occupational health and safety of workers likely to be exposed to electromagnetic fields.

The Regulation defines the electromagnetic threats as harmful for health and describes hazardous and severe effects of direct or indirect impact of electromagnetic fields (EM fields) in the work space due to, inter alia, direct biophysical effects of EM fields upon the human organism, including:

- thermal effects – heating of the tissue through the EM energy absorbed,
- non-thermal effects, that is: agitation of muscles, nerves or sense organs which are likely to exert deleterious effect upon

the mental and physical health; agitation of sense organs may lead to transient symptoms, such as vertigo or phosphenes that provoke transient afflictions or affect cognitive functions or other brain or muscle functions and as a consequence, are likely to influence the capability to safely perform one's work.

2. Regulations regulating electromagnetic measurement

The regulation defines three basic categories of sites on which EMF monitoring should be carried out:

- 1) Central districts of settlements or cities with a population of over 50,000.
- 2) Other (smaller) cities.
- 3) Rural areas.

For each of the above mentioned area categories there are selected 45 measuring points – a total of 135 points. Measurements at the selected points are repeated after each full, 3-year measurement cycle. Within one year, measurements are made in 45 points (15 per area category). The range of conducted tests of electromagnetic field levels in the environment will include measurement of the intensity of the electrical component of the electromagnetic field in the frequency range of at least 3 MHz up to 3000 MHz. Measurements at each point are performed once a year.

The norm defines the principles of selecting the measurement area. The measurements are conducted with the aid of the so called measurement points: the basic measurement points (corresponding to the actual location of the workers) and the auxiliary measurement points (whose purpose is to obtain the information on the spatial distribution of the fields). The measurements are conducted to the maximum height of 2 m from the ground on which the worker is located. The working conditions of field sources should be selected in a manner allowing for the designation of the maximum value of field intensity in areas where workers are currently stationed or consider the possibility of greater field intensity, compared with the measurements, when assessing the exposure level [10].

Detailed values of permissible intensity of radiation fields have been specified in the ordinance of the Minister of the Environment dated October 30, 2003 on the permissible levels of electromagnetic fields in the environment and ways to check compliance with these levels (Journal of Laws No. 192, item 1883). According to that Regulation, acceptable levels of electromagnetic fields have been designated for "sites dedicated for development" and "places accessible to the public" and refer to different ranges of field frequencies from 0 Hz up to 300 GHz.

From the point of view of environmental monitoring the most important aspect is the frequency range, which might be from 3MHz to 3000MHz. The permissible electromagnetic field intensity for a given range is $E = 7 \text{ V/m}$ for the electrical component and $S = 0.1 \text{ W/m}^2$ for the power density. They are many times more stringent than the WHO recommendations and ICNIRP limits adopted by the EU (from 28 V/m to 61 V/m, depending on the frequency) [14].

The magnitude of measured values of electromagnetic field (EMF) intensities is the resultant of the number of sources and their power.

The norms for maximum levels of electromagnetic fields in most countries around the world are in order with the recommendations of the International Commission on Non-Ionizing Radiation Protection (ICNIRP). The level indicated in the ICNIRP recommendation results from the assessment of a possible thermal effect, the value being several times smaller (by applying an additional margin of safety) in relation to the level of the field considered safe.

Based on the data gathered from five largest operators of overhead high voltage lines, the high voltage network is 32859 km of the HV line. There are 1437 WN/SN stations operating in this network, in which 2630 transformers are installed. In addition, the Polish Office of Electronic Communications has prepared a list of permits for the construction

of base stations of mobile network operators. Their total number was 45456 at the beginning of this year. The list includes GSM network stations operating in the 900 and 1800 MHz as well as WCDMA 2100 MHz. Taking the above data into account and the aforementioned number of measurements carried out by the voivodship environmental inspectorate, it can be concluded that this is a relatively small number. Performed measurements are carried out on the basis of legal regulations [12].

3. Mobile measurement of electromagnetic field

Currently, in times of rapid development of automation and its interference in various areas of our lives, also measurements of the electromagnetic field are carried out using it to a greater or lesser extent. The use of sensors placed on cars affects the availability of measurements. The sensor placed on the roof of a car is limited by environmental and technical conditions where the car can reach. Measurement can be performed relatively quickly and systematically, moving a given vehicle according to predetermined roads. The data transmitted by the sensor also have such parameters as the GPS network data so that the measurement results can be placed on the map and compared with measurements made at another time, in the same place. The levels of measured signals can be shown on the map in different colors.

The next step towards a greater automation of the measurements of the electromagnetic field is the use of a flying platform, under which the sensor were mounted. Currently manufactured sensors, from a technical point of view, can be placed on flying platforms. Performing measurements using a flying platform is the solution to one of the currently unresolved problems, which is the lack of barriers related to the availability of the area. The flying platform has unquestionable freedom of movement in the field. Unpaved roads or places which cannot be reached by a car are no longer a problem. The flight route can be planned in advance and performed without the direct presence of the person supervising the flight. As a result, the "pilot" is not exposed to the fields being measurement. Measurements can theoretically be performed without time limits 24 h/365 days. The flights will be carried out using a previously saved trajectory in autopilot mode with operator supervision. The only limitation are the weather conditions. The sensor moving on the platform has one more advantage, it has the ability to catalog a large area within a relatively short time. Due to this, the measurement performed in a dozen of defined points for each area can be extended to a much larger number of measuring points, thus increasing the quality of the measurement.

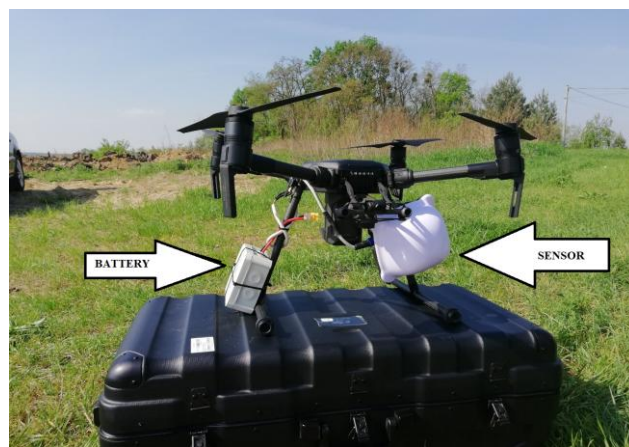


Fig. 1. Mobile platform with sensor and battery

The platform presented in figure 1 has been used to conduct test measurements in order to verify the measurement correctness as well as to control the influence of the mobile platform itself upon the measurement conducted.

The platform is it Quadcopter equipped with TB50 LiPo battery, 4280 mAh, 22.8V LiPo 6S. Can fly 27 minutes. Control: 2.4 GHz: 4.3 miles (7 km, FCC); 2.2 miles (3.5 km, CE); 2.5

miles (4 km, SRRC) 5.8 GHz: 4.3 miles (7 km, FCC); 1.2 miles (2 km, CE); 3.1 miles (5 km, SRRC). Equipped with on-board systems: TimeSync system, accelerometers, gyroscopes, compasses, barometers, ultrasonic sensors, cameras and satellite positioning systems, gyroscopic flight stabilization systems. The measuring sensor used is cMonitEM from Wavecontrol [21] the measurement is isotropic.

The measurements of the intensity of the electromagnetic field plays an important role in relation to the conducted research on the implantation of the electromagnetic network and phone transmitters in close proximity to residential buildings and the influence of the intensity of the electromagnetic field on living organisms.

According to the concept of mobile network systems, the entire field handled by a given network is divided into areas ("cells") presented on propagation maps with the use of hexagons including base transceiver stations (BTS) located in the center. The communication between a moving cell phone user in the most popular GSM 900 network and the base station takes place in the 890–915 MHz bandwidth and between the base station and phone – in the 935–960 MHz bandwidth. Individual "cells" may possess a diameter from a few hundred meters in office centers up to more than a dozen kilometers in areas of a low population density. This means that in large urban agglomerations in order for a network to work properly it requires the functioning of 30–50 base stations which, taking into consideration the presence of three providers on the market (plusGSM, EraGSM, and Idea Centertel), results in a quite vast number of radiation sources.

The configuration of a base station depends on its purpose and location. In cities, sector antennas are usually installed in such a manner so that the main radiation beams are directed in three or four directions, thus ensuring an almost even cover of the entire cell in terms of the radio signal. In terms of base stations located in rural areas as well as near the main road and railroad trails, sector antennas are installed on lattice or concrete-steel towers, and directed at one or two azimuths. It also sometimes happens that some stations include omni-directional radiation antennas.

The radio frequency power (microwave range) provided for each antenna depends on the station's function within the network, and the receivers installed in base stations are selected from a type series offered by a given producer (Nokia, Siemens, Ericsson). For base stations located in cities the typical power provided for each sending-receiving antenna is: 25 W for single system stations and 50 W for dual system stations (GSM/DCS). In stations located outside of cities the power provided for each antenna is slightly lower.

Apart from sector antennas ensuring communication with cell phones, base stations include also radio lines necessary to execute direct communication between individual base stations. Depending on the function within the system, radio line systems include installed parabolic antennas with different diameters (from 0.3 m to 3.0 m) working in the following frequency bandwidths: 7, 15, 23, 38 GHz. Apart from the so called Radio Line Stations which include only radio line antennas (sometimes more than 15) this type of antenna is present in almost all base stations, although the number of radio line antennas usually does not exceed 10. The power provided for radio line antennas is very low and usually does not exceed 1 W.

The power of a base station is oscillatory and this is connected to the fact that the power of the transmitter adjusts to the number of users logged to the station and the technology in which the units operate. This concerns digital systems such as UMTS and LTE meaning that it changes in time [16].

In order to conduct tests, a mobile telephony mast (height 50 m), located in an area characterized by a small density of buildings and other objects, has been selected. The choice was due to the fact that the probability of disrupting the work of the platform in case it flew in excessive proximity to the mast, was too high (likely to provoke the disruption of the signal controlling the platform and, in the worst case, the disintegration of the platform upon the fall from a great height). In order to eliminate the disruptions to the platform, one may replace the radio control

with the laser control, whereas the disruptions in the transmission of data from the sensor might be eliminated by way of transmitting the data through the optical fiber [5]. In many countries and army, wired drones are used [17, 20]. The platform's flight has been supervised by a person with proper qualifications. The measurements have been recorded on a memory card placed in the sensor. The frequency of recording equaled every 1 second. The sensor's producer has also enabled its users to transmit the measurements directly upon the dedicated server. The test results are currently being developed. Performing the measurements concerning the influence of the mobile platform upon the proper measurement of the electromagnetic field is yet another vital test to be considered.



Fig. 2. Flying platform during test testing

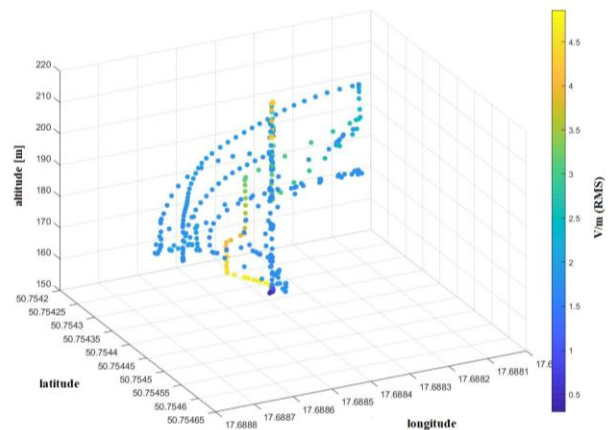


Fig. 3. Developed results of test measurements

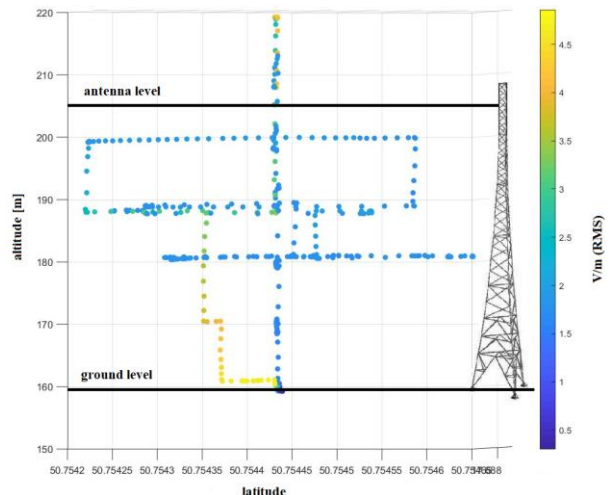


Fig. 4. Developed results of test measurements in relation to the mast height

Figures 3 and 4 present the developed results of test measurements conducted in close proximity to the mobile telephony mast. The levels of electromagnetic fields (based on the electrical component) recorded by the sensors have been presented on the basis of the GPS points assigned to a given field being measured. The flight route of the platform has been selected by way of experiment since it constituted a test measurement. Figure 3 depicts the measurement results in relation to length, latitude and height, whereas figure 4 depicts the same measurement results in relation to latitude and height. The levels of electromagnetic fields measured were assigned to appropriate colors.

A comparative analysis with a meter placed on the ground and an analysis of disturbances in the impact of electronics will take place in the next experiment and its results will be presented in the magazine.

4. Summary

The use of flying platforms to perform measurements of the electromagnetic field is a very good alternative to traditional methods. Thanks to UAV (unmanned aerial vehicle), it is possible to carry out measurements on a larger area in a much shorter period of time. The measurement is not limited by infrastructural barriers, therefore the measurement can be made close to the source of the electromagnetic field. The measurement route, once planned, can be repeated several times in different periods to make the analysis more transparent. This function depends on the software. DJI provides a tool to download aircraft data. Machining is done manually. Then the whole is applied to the IGIS map or connected to the 2D map by means of GPS trajectory.

The first test measurements of electromagnetic field generated by the mobile telephony station, are being followed by preparations to perform other measurements of electromagnetic field generated by radio-tv masts and high voltage lines. Taking the measurements can be accompanied by transmitting them in a real-time to the server where they are displayed after being properly processed. The only hazard observed was the disruption of the mobile platform by the strong sources of electromagnetic field.

By applying colors to the measurement results you can quickly determine how the intensity of the electromagnetic field changes at a given point. The basic advantage of the measurement based on the autonomous unit is the ability to perform measurement of the fields distribution for the magnetic and electrical components. Thanks to the point measurement of the area, it is possible to generate a spatial grid of the fields distribution, which has been difficult so far.

The flying unit is able to study points that were previously unattainable. It would be advisable to use many UAV units controlled by the "Boids" algorithm, which would allow to make measurements with a high density of measurement points [1;2].

At present, quick and efficient measurement of electromagnetic field becomes a necessity in a world where technological development affects every possible field, in particular the field of wireless technologies. Unmanned aerial vehicles might turn out of considerable importance in this respect.

References

- [1] Beni G., Wang J.: Swarm Intelligence. Proceedings of the Seventh Annual Meeting of the Robotic Society of Japan, 425–428, 1989.
- [2] Butlewski R., Kasprzyk R.: Pole elektromagnetyczne jako czynnik szkodliwy w przemyśle elektroenergetycznym. Zeszyty Naukowe Politechniki Poznańskiej. Organizacja i Zarządzanie 59, 19–23, 2013.
- [3] Dyrektywa Parlamentu Europejskiego i Rady Europy 2013/35/UE z dnia 26 czerwca 2013 r. (available: 20.06.2019).
- [4] Eberhart R., Kennedy J.: Particle swarm optimization. Proceedings of the International Conference on Neural Network, 1942–1948, 1995.
- [5] Fritzel T., Strauß R., Steiner H., Eisner C., Eibert T.: Introduction into an UAV-based near-field system for in-situ and large-scale antenna measurements. 2016 IEEE Conference on Antenna Measurements & Applications (CAMA), 2016, 1–3, [DOI: 10.1109/CAMA.2016.7815762].

- [6] Gruber J., Józwiak I., Kowalczyk D.: Metody odzyskiwania i kasowania danych z nośników magnetycznych i nośników pamięci flash. Zeszyty Naukowe Politechniki Śląskiej. Organizacja i Zarządzanie 74, 2014, 35–44.
- [7] Gryz K., Karpowicz J.: Zasady oceny zagrożeń elektromagnetycznych związanych z występowaniem prądów indukowanych i kontaktowych. Podstawy i Metody Oceny Środowiska Pracy 4(58), 2008, 137–171.
- [8] Lewicka M., Dziedziczak-Buczynska M., Buczyński A.: Electromagnetic radiation influence on living organisms. Polish Hyperbaric Research 4(25), 2008, 33–41.
- [9] Tomczykowski J.: Sieci energetyczne pięciu największych operatorów. Energia Elektryczna 5/2015, 23–25.
- [10] Norma Ochrona pracy w polach i promieniowaniu elektromagnetycznym o częstotliwości od 0 Hz do 300 GHz: PN-T-06580:2002
- [11] <http://archiwum.ciop.pl/26003.html> (available: 3.03.2018).
- [12] http://www.opole.pios.gov.pl/wms/Pliki/2017/Ocena_wynikow_pomiarow_monitoringowych_PEM_za_rok_2016.pdf (available: 21.02.2018).
- [13] <http://www.wavecontrol.com/rfsafety/en/> (available: 16.05.2018).
- [14] <http://www.who.int/mediacentre/factsheets/fs193/en/> (available: 10.04.2018).
- [15] http://www.wios.lodz.pl/Monitoring_promieniowania_elektromagnetycznego_PEM_38 (available: 20.04.2018).
- [16] <https://pem.itl.waw.pl/artyku%C5%82y/pomiary-pem-w-otoczeniu-stacji-bazowych-telefonii-kom%C3%B3rkowej-sbt-k-oraz-punkt%C3%B3w-dost%C4%99pu-lokalnych-sieci-dost%C4%99pu-bezprzewodowego-rlan/> (available: 1.07.2018).
- [17] https://tech.nikkeibp.co.jp/dm/atclen/news_en/15mk/010401054/?ST=msbe&P=3 (available: 20.06.2019).
- [18] <https://www.aspen-electronics.com/wcrange.html> (available: 10.04.2018).
- [19] <https://www.piit.org.pl/wazne/pem> (available: 10.05.2018).
- [20] <https://www.riseabove.com.au/powerline-power-tether-system-for-drones> (available: 20.06.2019).
- [21] https://www.wavecontrol.com/rfsafety/images/datasheets/en/cMonitEM_Datasheet_EN.pdf (available: 20.06.2019).

Prof. Sławomir Szymaniec
e-mail: s.szymaniec@po.opole.pl

Prof. dr. Eng. (born 1949, Opole) A: electronics engineer, expert diagnostician, appraiser electric machines; Head of the Department, author of 2 monographs; co-author 2 monograph; author of 236 articles; co-author of 6 patents, 2010 winner of the 15th edition of the competition for the research prize Siemens company for outstanding achievements in technology and research, 1st place winner; he is the creator of the Opole School known in Poland and abroad Diagnostics of Electrical Machines and Drives, organized a research team academy industrial dealing in the operation and diagnostics of machines electric and manages His work; at department in the implementation of 42 scientific works research implemented in industry; author or co-author of 41 expert opinions for industry; managed 2 research projects implemented in industry; co-author of about 1,400 technical works for industry.

ORCID ID: 0000-0002-7642-1456

M.Sc. Sławomir Szymocha
e-mail: slawomir.szymocha@doktorant.po.edu.pl

Born 1989, Lubliniec – M.Sc., Opole University of Technology, two-time winner of the second place in the diploma dissertation competition organized at the Faculty of Electrical Engineering of Automatics and Informatics: Ing 2014, Master. 2015, co-author of two European utility models, Ph.D. student at the Opole University of Technology from 2016, involved in the implementation of projects related to renewable energy and implementation of innovation. Currently employed as a designer of control cabinets.

ORCID ID:0000-0001-6548-9896

M.Sc. Łukasz Miszuda
e-mail: lukaszmiszuda@wp.pl

Born 1991, Prudnik – M.Sc., Opole University of Technology, Ph.D. student at the Opole University of Technology from 2017. He carries out international projects related to control. Currently employed as an industrial automation programmer.

ORCID ID:0000-0003-0289-053X

otrzymano/received: 02.08.2019

przyjęto do druku/accepted: 06.12.2019



LOW COST SOLAR THERMOELECTRIC WATER FLOATING DEVICE TO SUPPLY MEASUREMENT PLATFORM

Andrzej Nowrot¹, Monika Mikołajczyk², Anna Manowska¹, Joachim Pielot¹, Antoni Wojacek¹

¹Silesian University of Technology, Department of Electrical Engineering and Automation in Industry, Gliwice, Poland, ²Famur Institute Ltd, Katowice, Poland

Abstract. This work presents the prototype of the solar – thermoelectric device, which can float on water surface. It produces electrical energy as a result of the Seebeck effect in a commercial, low-cost Peltier module. The main application of the device will be an autonomous and a floating measurement platform. An important advantage of the presented solution is the possibility to work alike at day, when a solar light heats the surface of the absorber, and at night, when the different of temperatures between air and water causes the heat flux and in an effect the electricity. The device is capable of working for many cloudy days and also in winter on very short days. The presented device is based on low-cost and widely available components.

Keywords: thermoelectric devices, solar power generation, energy conversion

TERMOELEKTRYCZNE URZĄDZENIE SOLARNE DO ZASILANIA PLATFORMY POMIAROWEJ

Streszczenie. W pracy zaprezentowano prototypowe solarne urządzenie termoelektryczne pływające po powierzchni wody. Wytwarza ono w niedrogim, komercyjnym module Peltiera energię elektryczną w wyniku zachodzącego w nim zjawiska Seebecka. Docelowo głównym obszarem aplikacyjnym urządzenia będzie zasilanie autonomicznej, pływającej platformy pomiarowa do monitorowania parametrów środowiskowych. Istotną zaletą przedstawionego rozwiązania jest możliwość pracy zarówno w dzień, gdy światło słoneczne ogrzewa powierzchnię absorbera, jak również w nocy, gdy różnica temperatur między powietrzem a wodą powoduje powstawanie strumienia ciepła w module Peltiera. Urządzenie może pracować przez wiele pochmurnych lub krótkich dni, także w zimie. Do konstrukcji układu zastosowano relatywnie tanie i łatwo dostępne w handlu komponenty.

Słowa kluczowe: urządzenie termoelektryczne, solarny generator energii, konwersja energii

Introduction

The most popular power sources for any mobile measurement platforms and low power consumption portable devices is a photovoltaic cell (PVC). An electrical energy produced in that cell is partially used to supply electronics units and is partially stored in batteries or in supercapacitors (SuperCap). A typical energy efficiency of the photovoltaic cell is about over a dozen percent. A significant constraint of commercial photovoltaic cells is a adaptation to work in the visible region only – it is a consequence that the solar cells are made out of n-type and p-type semiconductor materials. It should be note, in this context, the radiant energy emitted from the Sun, approximately 50% lies in the infrared region, about 40% in the visible region and about 10% in the UV region [7]. Moreover, when the sky is cloudy, the generated electrical power by PVCs decreases a few times to even several dozen times. Exemplary, the typical commercial silicon PVC panel (MN Green Power MWG-10, dimensions of cells area 0.30×0.25 m) generates electrical power about 10 W at completely clear skies and at sun rays reaching perpendicular to panel's surface. Whereas, exactly the same cell generates power barely about 0.3 W to 0.6 W on a cloudy day and less than 0.1 W on a cloudy and rainy day. All above values of the power were measured at optimal operating point – it means for the load resistor collecting the maximum generated output power. This result may seem surprising, but that is because the human eye has got approximately a logarithmic characteristic of sensitivity and the changes of light intensity seem deceptively small. Moreover, the output voltage of the non loaded photovoltaic panel (open circuit voltage) depends to small extent on a weather. This voltage for the above exemplary photovoltaic panel is equal up to 21.7 V on a sunny day and about 16 V on a cloudy day. However, if the panel would be loaded by the resistor (several dozen Ohms), the output voltage will decrease at most down to half on a sunny day and it will drastic decrease (ten or more times) on a cloudy day. So, the output voltage of the non loaded PVC panel is very confusing indicator of its electrical power. Much more practical information of electrical properties of photovoltaic cells are given in the work [8].

Another technical possibility to obtain the electricity from solar energy is an application of a thermoelectric generator (TEG) integrated with a solar absorber and a cooler. In 2003, authors in the paper [13] show a low cost stove-top thermoelectric generator for regions with unreliable electricity supply, which is based on a redesigned commercial Peltier module (TEC – Thermoelectric

Cooler). While a wood is burned in the cooker in order to heat the building or cooking, additional the electricity is produced. Nowadays, important application potential of TEGs is in a field of military [16] and space technology [14]. In the paper [14] authors discuss radioisotope thermoelectric generators (RTGs). They have a very long operating time and have been used in many space missions. Another thermoelements – the TECs are generally used inter alia in portable coolers (in cars) or small fridges, but they may work also in reversible mode – as the thermoelectric generator. Principle of operation of TEC working as TEG and the thermocouple are based on the Seebeck effect and consequently many of their features are very similar. The fundamental difference between them is maximal operating temperature and maximal generated electrical power. Due to TEC contains the p-type and the n-type semiconductors, it can work typically in temperature range up to 130–150°C only, but it can produce useful amounts of electrical energy. The thermocouple contains dissimilar electrical conductors (metals) and can work even in temperature of the order of 1000–2000°C, but unfortunately it produces electrical power of order of microwatts. The thermoelectric generator based on Peltier module could be very useful to small-scale an electrical energy produce. The paper [4] includes a review of development of stove-powered TEGs in the last two decades. In recent years, there are new designs and trends of solar thermoelectric generators in the word-wide literature. Generally, in the solar TEGs, the upper surface of the device is heated by the solar radiation and it makes the heat flux which drifts down through the thermoelectric element to the cooler (e.g. dived in water). A typical efficiency of the conversion the heat energy into the electrical energy (while the Seebeck effect) is equal up to a few percents only, but in contrast to photovoltaic cells, a solar absorber (upper surface of the device) is able to absorb light in wide spectra cover the visible and the most of the infrared region – it depends on the spectral properties of the absorber. In this research paper, we propose the new approach in the solar supply the measurement platforms. It is based on solar – thermoelectric unit within a low – cost and commonly used Peltier module associated with the dedicated electronics circuit providing the automatic settings the optimal operation point of the system (maximal generated electrical power). A very important advantage of the presented in this paper device is the possibility of operating without the solar light (e.g. at night) or at the very cloudy day. In this "dark mode", the heat flux in the thermoelectric module is caused by difference of temperature between air and water, but it does not matter if the air is warmer than the water or vice versa. It is a matter of an existence of different temperatures between

them only. The device produces electricity also while a hard winter, when the air temperature is down to -30°C and the temperature of salt water or untreated water covers the range of -2°C to 0°C . We think, it is also possible to work the device, when the cooler radiators are immersed in ice (e.g. in a frozen lake), but we have never tested this case. In the work [9] authors propose an interesting construction of the solar annular thermoelectric generator (SATEG). It provides significantly higher efficiency in compare to so far used flat thermoelectric modules but it simultaneously increases the price of the device and it complicates fabrication process. Authors in the paper [17] show the electric power generation from solar pond using combined thermosyphon and thermoelectric modules. Unfortunately, it is a stationary system and unsuitable for any moveable platform. In conclude, the features of that generator are significantly different in compare to photovoltaic cells. The measurement platform and the proposed for it the low-cost solar thermoelectric water floating device will operate autonomously for a long period of time in the varied weather conditions and seasons, while natural disasters, flood etc. Therefore, the platform needs a reliable power supply based on the shockproof TEG or the hybrid power source based on TEG with the photovoltaic cell. The application the photovoltaic cell only is definitely insufficient to meet the assumed requirements. It is very important, e.g. in the Central Europe, where in the winter the day lasts only a few hours.

1. Proposed device

The illustration in Fig. 1 shows schematic of the mechanical construction of the proposed thermoelectric device. The sunlight passes through the glass cover and next is absorbed in the absorber plane. A commonly use a heat-proof clear glass dish was applied as the cover glass. This 2.5 mm thickness glass very good transmits a solar radiation in the visible and the infrared range. It stops the heated air and prevents heat exchange to outside as a result of gas convection. The absorber has got a shape of a flat plate with dimensions of total diameter 256 mm, useful diameter 244 mm (covered by the glass cover) and thickness 4 mm. It is made of aluminum. The upper absorber surface was treated to one of the galvanization methods – anodizing with blackening. In result, this surface is matt dark and very good absorbs light. The anodized coating is resistant to high temperature and temperature changes in the wide range. That is impossible to obtain using a paint dedicated to aluminum – guaranteed maximum exploitation temperature for popular black paints is up to 50°C . The glass cover is mounted in a shallow hollow ring in the absorber's surface (located close to the outside edge of the absorber plane). The air under the glass cover is dehumidified before its closing.

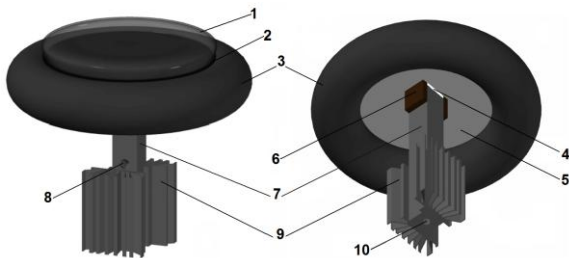


Fig. 1. Schematic of the mechanical construction of the proposed thermoelectric device. 1 – glass cover, 2 – circular absorber plane situated under the glass cover, 3 – buoyancy tube, 4 – Peltier module, 5 – absorber plate bottom covered with the styrofoam isolation layer, 6 – one of the two bakelite connector blocks, 7 – aluminum flat square bar profile, 8 – one of the two side holes to the upper end of the inside channel, 9 – cooler radiators, 10 – bottom hole to inside channel

Directly under the bottom of the absorber plane is centrally situated the Peltier module. We applied a popular and general use Peltier module TEC1-12706 Hebei I.T. Shanghai Co., Ltd. It has got dimensions of $40 \times 40 \times 3.9$ mm and maximal operating current of 6.4 A. The module can work in the range of temperature up to 138°C only, but this value is absolutely enough to operate in the presented device. The carried out measurement showed the

absorber plane surface heats maximally up to about 88°C (conditions: cover glass put on, completely clear sky, the absorber sets perpendicularly to the sun ray, air temperature 33°C). Output wires of the TEC are connect to dedicated electronics unit (it is not shown in Fig. 1). The rest part of the bottom surface of the absorber plane is covered with 2 mm styrofoam layer. Next, under the TEC is mounted to the aluminum flat square bar profile – rectangular block (marked as 7 in Fig. 1). The profile has got dimensions of $40 \times 40 \times 300$ mm and transfers the heat flux from TEC to radiators. There was hollowed out the round channel along the length of the profile. The channel is located between the half of the profile length (marked as 8 in Fig. 1) and the profile bottom (marked as 10 in Fig. 1). It improves water circulation and the cooling process. The absorber plane was mounted to the bar profile through the two flat bakelite blocks (marked as 6 in Fig. 1). The Peltier module is pressed against between them. Due to a bakelite is electrical non conductivity, heat-resistant and non fragile in wide temperature range it was elected to connect of them. Its thermal conductivity is only about $0.2 \text{ W}/(\text{m}\cdot\text{K})$ [9]. The bakelite blocks were threaded and the assembly elements were connected with each other by steel screw. Additional, to reduce the heat resistance in joints absorber plane surface – Peltier module – flat aluminum profile – radiators, the silicone thermal paste was used. A buoyancy tube was applied under the styrofoam layer and the absorber plain. The images in Fig. 2 show the thermoelectric device prototype while "dry testes" – at the beginning experiments without the cover glass and the buoyancy tube.



Fig. 2. Thermoelectric device prototype without the cover glass and the buoyancy tube. 1 – circular absorber plane, 2 – styrofoam layer (thermal isolation), 3 – bakelite connectors, 4 – flat aluminum profile and the upper hole of the internal channel, 5 – radiators

Despite the glass cover and a tank with water to cooling the radiators are not applied in the simplest configuration (Fig. 2), the dark absorber surface is quickly heated in a sunshine and an electrical energy is produced. After 3 minutes exposition for sunrays (the case seen in Fig. 2), the different of temperatures between central point on absorber surface and the aluminum flat profile (measured 5 cm below the TEC) increases to about 16°C . The Peltier module were connected to the external dedicated electronics unit. The unit contains the switching voltage regulators and it is controlled by the main platform's computer. We assume that it will be closed in the waterproof IP68 housing. At the moment, the first version of the electronics unit's prototype has been constructed. One of the most important function of the unit is providing the optimal operating point in the thermoelectric generator. It is needed, because for each temperature different it is possible to determine the electric power vs. load resistance characteristic. Voltage converting and impedance matching are not a simple issue as it might seem. A single Peltier module, while working as a thermoelectric generator, generally provides voltage in range of 0.3 V to 1 V. That is too low to correct operating of any standard and commercial known voltage converter. For example the MCP1623 compact DC-DC converter (Microchip Technology Inc.) has got start-up voltage of 0.65 V for output voltage of 3.3 V and after start, it can operate with minimal input

voltage of 0.35 V. Unfortunately these low voltages are allow for output current of 1 mA only – it is absolutely not enough current to supply the measurement platform. To obtain higher output current it is necessary significantly higher input voltage – 1.2 V for current 50 mA. The application of the MCP1623 requires only five small external electronics components and it probably operates at the lowest input voltage among all boost integrated converters. In conclude, commercial DC-DC converters are not appropriate to work with single module Peltier module working as TEG. Furthermore, above converters do not adapt their input resistance to obtain the maximal electrical power in TEG. In the paper [15] authors discuss a dedicated voltage converter – maximum power point tracker for thermoelectric generators. That boost converter is much more advanced. It contains a discrete MOSFET power transistor, which is driven by PWM and PI controller and the applied algorithm allows to keep maximum generated power for different temperature differences. Whereas our device is even more demanding. If the absorber plane temperature is less than temperature of the flat bar profile and radiators – sometimes that is possible in the winter, then output voltage polarity of the Peltier module is inverted. Moreover, TEGs exhibit dynamic properties related to the intensity of temperature changes, what is often ignored in many considers, and these properties influence to maximum generated power. Dynamic characteristics of TEGs are thoroughly showed in the paper [10]. In view of the above factors, works on constructing the final version of the electronics unit are ongoing and will be considered apart in another paper. An important advantage of the device is low total cost of its constructing. Final cost of the device prototype consists of the cost of materials and labor. Price of aluminum components (a profile bar, a think block and radiators) in Poland is equal about 30 euros. The applied TEC module costs about 8 euros. Price of other components (screws, a buoyancy tube, silicone thermal paste) is up to 10 euros. All above prices include taxes. The cost of machining aluminum components on a lathe and assembling the device is equal up to 8 man-hours. Of course the above estimates do not take into account the long time devoted to the design of the device, its examination and improvement.

2. Results and discussion

The proposed thermoelectric device was tested in various conditions. The image in Fig. 3 shows thermoelectric device prototype while floating on pond water surface on sunny September day in south west Poland. Its total mass is about equal to 3.9 kg. The volume of submerged elements (part of the buoyancy tube, radiators and part of the aluminum flat bar profile) is about equal to $5 \cdot 10^{-3} \text{ m}^3$ and that gives buoyancy force about 50 N. Thereby the proposed device is able to float on water surface. As a buoyancy tube we tested a moped inner tube and a lifebuoy ring.



Fig. 3. Thermoelectric device prototype at the beginning testes while floating on water surface

The temperature difference between the central point on the absorber surface and the aluminum flat bar was measured (3 cm below the Peltier module on flat bar surface). Two temperature measurement methods were used. The first one was a contact method with two DS18B20 programmable resolution digital

thermometer – small integral circuits (products of Dallas Semiconductor). In that application, a digital signal from the thermometer to Arduino UNO microcontroller board was transmitted, and next via USB to a laptop. The second method was a non-contact with the Flir i7 infrared camera. Unfortunately, the last method is more complicated, because needs to multiple and quick taking off the glass cover to correct measure the temperature of the absorber surface. However, after calibrating the IR camera, both above methods have given similar results. For each temperature difference, the current – voltage characteristics were investigated and then, on their basis, the maximum electrical power was determined. Fig. 4 shows an exemplary characteristic for temperature deference of 17°C.

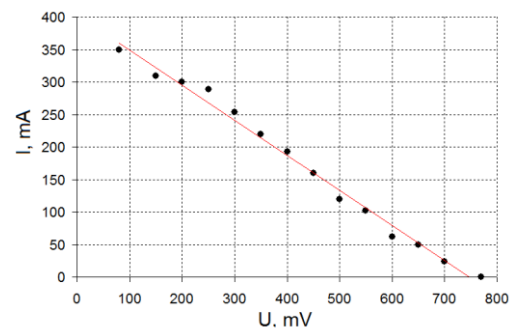


Fig. 4. Exemplary current – voltage characteristic of the Peltier module in the proposed device for temperature deference of 17°C (between the absorber surface and the aluminum bar profile)

To obtain the characteristics, TEC's terminals are connected directly to a voltmeter (input resistance 10 MΩ), which is parallel connected to the circuit consisting of an ammeter in a serial connection with a slide variable resistor – load resistor. The above meters configuration makes that the internal ammeter resistance does not influence to the voltage indication. If the measuring points are arranged approximately along a straight line just like in Fig. 4, then the Peltier module (which working as a thermoelectric generator) could be considered as the Thevenin equivalent circuit connected to a load resistor – Fig. 5. An idea of the Thevenin equivalent circuit have been clearly explained in the book [1]. The voltage U_{TEG} is the thermoelectric force of that TEG and it is the voltage of non loaded TEC (when $R_{LOAD} \rightarrow \infty$). The resistance R_{INT} is mainly related to the p-type and n-type semiconductors resistance inside the structure of the module. For commercially available TEG devices, the value of R_{INT} changes by approximately 0.3–0.75% per 1°C increase of the average temperature between the hot and cold sides [15]. The linear fit in Fig. 4 is given by the Eq. (1). The absolute value of the "a" – directional coefficient represents inverse of an internal resistance R_{INT} in the Thevenin model (Eq. (2)) and the coefficient "b" represent a short circuit current. The same structure of TEG as in Fig. 5 was proposed by the authors in the works [2, 3, 15].

$$I = aU + b \quad (1)$$

where: U – voltage, I – current, coefficients determined for the fit in Fig. 4 ($T = \Delta 17^\circ\text{C}$) $a = -0.54(2) \Omega^{-1}$, $b = 0.403(7) \text{ A}$

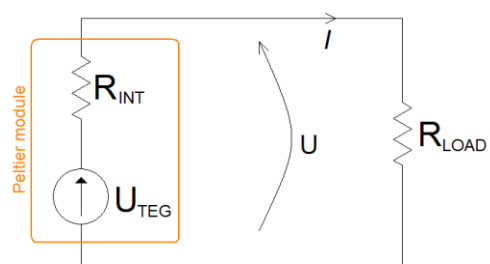


Fig. 5. Peltier module (working as a TEG) represented by the Thevenin equivalent circuit is connected to load resistance U_{TEG} – thermoelectric force – voltage of the non loaded Peltier module, R_{INT} – internal resistance of the Peltier module

$$R_{INT} = \frac{1}{|a|} \quad (2)$$

Typical value of the R_{INT} resistance is of the order of several Ohms. Therefore, an electrical power is the product of voltage and current, having Eq. (1), the generated power can be written by Eqs. (3) – (4). The maximal power can be calculated by equating the derivative of the expression to zero – Eq. (5). In effect the maximal power is given by Eq. (6) – it corresponds to the situation in the schematic in Fig. 5 when the load resistance R_{LOAD} is the same as the internal resistance R_{INT} .

$$P = UI \quad (3)$$

$$P = U(aU + b) \quad (4)$$

$$\frac{\partial P}{\partial U} = 2aU + b = 0 \quad (5)$$

$$P_{max} = -\frac{b^2}{4a} \quad (6)$$

where: P – electrical power, P_{max} – maximal electrical power, the factor "a" is always negative (see Fig. 4 and Eq. (1)).

The plot in Fig. 6 shows maximal electrical power generated by the thermoelectric device as a function of temperature difference. The experimental points are well approximated by mathematical model presented in Eq. (7).

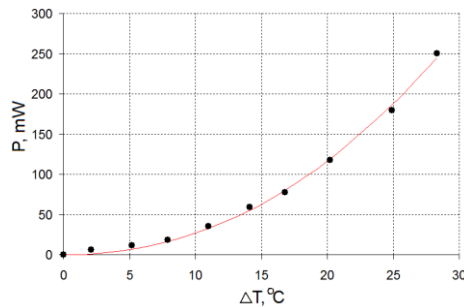


Fig. 6. Electrical power generated by the thermoelectric device vs. temperature difference between the central point on the absorber surface and the aluminum flat bar. As a temperature sensors were applied two DS18B20 digital thermometers

$$P = k \cdot (\Delta T)^n \quad (7)$$

where: P – electrical power in mW, ΔT – temperature difference in °C, k and n – equation coefficients: $k = 0.19(4)$; $n = 2.14(7)$.

The value of the factor "n" in the Eq. (7) indicates that generated electrical power is approximately proportional to the square of the temperature difference. The authors in the paper [5] a very similar experimental results have obtained. In the works [3, 15] have been theoretically demonstrated for the simplified TEG model, that the generated power depends on the square of the temperature difference. A precision theoretical determination of the power – temperature difference characteristic does not make sense in this case, because in practice an electrical power depends on many factors. In materials for TECs, the Fermi level dependence on temperature, electrons and holes diffusion and effects of electron-phonon interaction on transport are observed. They give a complicated mathematical model and moreover many parameters of general use TECs are unknown. Above processes in TEG have been thoroughly discussed in the book [11]. An experimentally determination of the power – temperature difference characteristic (just like in Fig. 6) is more beneficial in practice. The device generates electrical power according to Eq. (7) regardless of how the temperature difference is obtained – by heating the absorber surface with sun rays or by the heat exchange between an air and the absorber profile. It is it's a very important feature. The investigations conducted on January evening (during winter in Poland) showed that, if the air temperature is -3.1°C and temperature of water in the pond is 5.5°C , then the device produced electrical power of about 15.5 mW, while for exactly the same conditions the photovoltaic cell (surface dimensions 0.30×0.25 m) generated power less than 1.9 mW. Whereas, if the

absorber plane is heated by sunrays, its temperature is not the same in any its point. Therefore the Peltier module (situated under the central area of absorber plane) causes heat transfer down to flat bar profile and radiators, measurements with infrared camera were done. An exemplary surface temperature distribution of the absorber upper plane (while the maximum electrical power is generated) is shown in thermograph in Fig. 7. That photo was taken immediately after take off the glass cover (a glass layer misrepresents a true temperature of the covered surface in thermovision). Its central area is clearly cooler (53°C) in compare to other area – up to 58°C near to edge of the absorber plane. The thermograph below (Fig. 7) lets to determine the surface temperature distribution as a function of distance from its center point – Fig. 8.

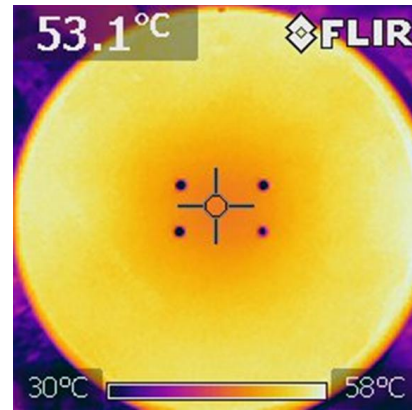


Fig. 7. Exemplary thermograph of the absorber plane surface (surface temperature distribution)

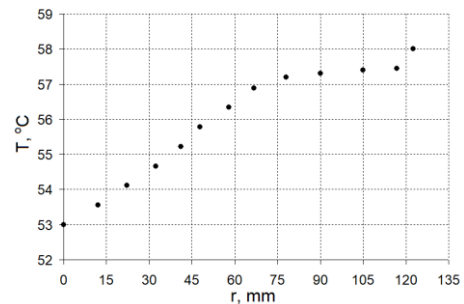


Fig. 8. Surface temperature distribution for the thermograph in Fig. 7 as a function of distance from the absorber center point

Analysis of the results in Fig. 7 and Fig. 8 leads to the conclusion that the main area of heat collection by the Peltier module is located for range $0 < r < 65$ mm – it accounts for about 28% of the total surface. The hottest place for radius $122 \text{ mm} < r < 126$ mm corresponds to the shallow hollow ring in the absorber surface (is dedicated to glass cover). Ignoring that ring, in the range $65 \text{ mm} < r < 122$ mm the temperature changes are less than 1.2°C .

3. Conclusions

This paper presents the prototype of the floating solar – thermoelectric device dedicated to an autonomous measurements platform. In the final construction, the device and the platform will become integrated and will be able to float on water surface. This device generates electrical energy regardless of how the temperature difference is obtained, for example on winter evening while the cooler is warmer than the absorber profile and the heat between air (the environment) and the absorber profile is exchanged. In conclusion, the presented device can work at day, when a solar light heats the surface of the absorber, and at night, when the difference of temperatures arises as a result of the air – absorber heat exchange. It should be noted that, the investigation of single Peltier module is not the same that the investigation of thermoelectric generator based on this module. The conducted

researches have shown that the electrical power could be greater more over three times for the same absorber surface in the device. While the Peltier module generates electric current and heat is collected from the absorber profile to the cooler, the module influences noticeably only for about 28% of the total absorber surface. In the next step, we are going to improve our prototype device and to increase the numbers of TECs to three and thereby the all absorber surface will be efficiently used. In that case, the maximum generated power will be increased to 750 mW. To provide maximum power for each temperature difference, it is needed to adjust and to keep the optimal operating point in the current – voltage characteristic. It will realize in the dedicated voltage converter which will automatically adjust its input impedance. The proposed floating solar thermoelectric device is not very complicated to construct and because it is based on commercial TEC, it is inexpensive – this is an important advantage. Authors in the work [12] clearly, experimentally demonstrated in the temperature range from 0°C to 100°C, that the efficiency of TEC (working as a thermoelectric generator) is very similar to much more expensive (about 15 or more times) commercial thermoelectric power generators. Moreover, in this comparison, for temperatures between 20°C and 40°C, the Peltier module is even a little bit more efficient. The main inconvenience of TEC is not high maximum operating temperature (about 140°C only), but this is absolutely not a problem, because the presented device always works for temperatures below 100°C. Finally, the optimal solution seems to be the simultaneous use of the presented device and a photovoltaic cell. When photovoltaic cells are unable to operate (e.g. on very cloudy days or on short days), the proposed device will provide electrical power to the autonomous measurement platform for many hours or days. On sunny days, the surplus of produced energy can be stored in batteries.

References

- [1] Agarwal A., Lang J. H.: Foundations of Analog and Digital Electronic Circuits. Morgan Kaufmann Publishers (Elsevier), San Francisco 2005.
- [2] Cao Z., Koukharenko E., Tudor M. J., Torah R. N., Beeby S. P.: Flexible screen printed thermoelectric generator with enhanced processes and materials. *Sensors and Actuators A: Physical* 238/2016, 196–206, [DOI: 10.1016/j.sna.2015.12.016].
- [3] Dunham M. T., Barako M. T., LeBlanc S., Asheghi M., Chen B., Goodson K. E.: Power density optimization for micro thermoelectric generators. *Energy* 93/2015, 2006–2017, [DOI: 10.1016/j.energy.2015.10.032].
- [4] Gao H. B., Huang G. H., Li H. J., Qu Z. G., Zhang Y. J.: Development of stove-powered thermoelectric generators: A review. *Applied Thermal Engineering* 96/2016, 297–310, [DOI: 10.1016/j.applthermaleng.2015.11.032].
- [5] Hasani M., Rahbar N.: Application of thermoelectric cooler as a power generator in waste heat recovery from a PEM fuel cell – An experimental study. *International Journal of Hydrogen Energy* 40/2015, 15040–15051, [DOI: 10.1016/j.ijhydene.2015.09.023].
- [6] Laughton M. A., Say M. G.: *Electrical Engineer's Reference Book – Fourteenth edition*. Butterworth International Edition 1990.
- [7] Liou K. N. (Ed.): *An Introduction to Atmospheric Radiation*. *International Geophysics – Chapter 2: Solar Radiation at the Top of the Atmosphere*. *International Geophysics* 84/2002, 37–64, [DOI: 10.1016/S0074-6142(02)80017-1].
- [8] Luque A., Hegedus S.: *Handbook of Photovoltaic Science and Engineering* (2nd edition), Wiley & Sons, 2010.
- [9] Manikandan S., Kaushik S.C.: Energy and exergy analysis of solar heat pipe based annular thermoelectric generator system. *Solar Energy* 135/2016, 569–557, [DOI: 10.1016/j.solener.2016.06.031].
- [10] Merienne R., Lynn J., McSweeney E., O'Shaughnessy S. M.: Thermal cycling of thermoelectric generators: The effect of heating rate. *Applied Energy* 237/2019, 671–681, [DOI: 10.1016/j.apenergy.2019.01.041].
- [11] Morelli D. T.: Thermoelectric Materials. In: Kasap S., Capper P. (eds) *Springer Handbook of Electronic and Photonic Materials*. Springer Handbooks. Springer, Cham.
- [12] Nesarajah M., Frey G.: Thermoelectric Power Generation: Peltier Element versus Thermoelectric Generator (TEC vs. TEG). *Proceedings of the 42nd Annual Conference of IEEE Industrial Electronics Society (IECON2016) 2016*, 4252–4257, [DOI: 10.1109/IECON.2016.7793029].
- [13] Nuwayhid R. Y., Rowe D. M., Min G.: Low cost stove-top thermoelectric generator for regions with unreliable electricity supply. *Renewable Energy* 28/2003, 205–222, [DOI: 10.1016/S0960-1481(02)00024-1].
- [14] O'Brien R. C., Ambrosi R. M., Bannister N. P., Howe S. D., Atkinson H. V.: Safe radioisotope thermoelectric generators and heat sources for space applications. *Journal of Nuclear Materials* 377/2008, 506–521, [DOI: 10.1016/j.jnucmat.2008.04.009].
- [15] Paraskevas A., Koutroulis E.: A simple maximum power point tracker for thermoelectric generators. *Energy Conversion and Management* 108/2016, 355–365, [DOI: 10.1016/j.enconman.2015.11.027].
- [16] Saqr K. M., Musa M. N.: Critical review of thermoelectrics in modern power generation applications. *Thermal Science* 13(3), 2009, 165–174, [DOI: 10.2298/TSCI0903165S].
- [17] Singh R., Tundee S., Akbarzadeh A.: Electric power generation from solar pond using combined thermosyphon and thermoelectric modules. *Solar Energy* 85/2011, 371–378, [DOI: 10.1016/j.solener.2010.11.012].

Ph.D. Eng. Andrzej Nowrot
e-mail: andrzej.nowrot@polsl.pl



Andrzej Nowrot received M.Sc. in Automatic Control and Robotics at the Faculty of Automatic Control, Electronics and Computer Science at the Silesian University of Technology (SUT), Poland, in 2003, and the Ph.D. in Physics from the University of Silesia, Poland, in 2010. Since 2004 he has cooperated with the Institute of Physics SUT. Since 2015 he has been employed at the Department of Electrical Engineering and Automation in Industry SUT. His research interests are sensors and non-electrical quantity measurements, nanomaterials applications in detectors and a renewable energy

ORCID ID: 0000-0001-8977-0316

M.Sc. Eng. Monika Mikolajczyk
e-mail: mmikolajczyk@famur.com.pl



Monika Mikolajczyk received M.Sc. in the Faculty of Mining, Safety Engineering and Industrial Automation at the Silesian University of Technology in the field of Electrical Engineering and Automation in Mining. Currently, he is involved in the design and programming of embedded and prototype systems at Famur Institute Ltd. in Katowice. The area of scientific interest includes conversion of thermal and solar energy into electricity and guaranteed power supply systems.

ORCID ID: 0000-0002-2843-5570

Ph.D. Eng. Anna Manowska
e-mail: anna.manowska@polsl.pl



Anna Manowska is an adjunct at the Department of Electrical Engineering and Industrial Automation at the Silesian University of Technology and a member of the Mining Economics Section of the Polish Academy of Sciences. She is the author of about 80 scientific articles. The area of scientific interest concerns the energy market analysis using advanced IT tools with particular emphasis on the role of hard coal and renewable energy.

ORCID ID: 0000-0001-9300-215X

Prof. Joachim Pielot
e-mail: joachim.pielot@polsl.pl



Joachim Pielot is the head of the Department of Electrical Engineering and Industrial Automation of the Silesian University of Technology and a member of the Association of Polish Electrical Engineers. He is the author of about 130 scientific articles. The area of scientific interest concerns the control of production processes, in particular the optimization of production in technological systems for mineral processing, metrology of electrical and non-electrical quantities, as well as analog and digital signal processing

ORCID ID: 0000-0001-7679-2049

Prof. Antoni Wojaczek
e-mail: antoni.wojaczek@polsl.pl



Antoni Wojaczek is a professor at the Department of Electrical Engineering and Industrial Automation of the Silesian University of Technology and an expert in telecommunications specialization covering design and execution without restrictions in the field of telecommunications. He is the author of about 180 scientific articles. The area of scientific interest concerns telecommunications, especially for mining and electromagnetic compatibility in mining.

ORCID ID: 0000-0002-2256-0661

otrzymano/received: 01.11.2019

przyjęto do druku/accepted: 06.12.2019

DOI: 10.35784/IAPGOS.24

IMPROVING THE DYNAMICS OF AN INVERTER-BASED PV GENERATOR DURING LOAD DUMPS

Łukasz Kwaśny

Lublin University of Technology, Faculty of Electrical Engineering and Computer Science, Department of Electrical Drives and Machines, Lublin, Poland

Abstract. In distribution power grids supplied by dispersed power sources, for example RES (Renewable Energy Sources), in the event of a load dump, unexpected transient states may appear. These states involve a dangerous increase in voltage or current. This situation may lead to the disconnection of these sources. To prevent this phenomenon, a non-linear anti-windup regulator with a conditional integrator has been proposed. This solution allows a significant improvement of the generator's dynamic properties both at load dump and on return to full load.

Keywords: load dump, dynamic states, anti-windup regulator, conditional integrator

POPRAWA DYNAMIKI PRZEKSZTAŁNIKOWEGO GENERATORA PV PODCZAS ZRZUTU MOCY

Streszczenie. W sieciach dystrybucyjnych o rozproszonym charakterze zasilania, np. OZE (Odnawialne Źródła Energii), w przypadku wystąpienia zrzutów mocy mogą pojawić się nieoczekiwane stany nieustalone. Polegają one na niebezpiecznym wzroście napięcia lub prądu. Taka sytuacja może doprowadzić do wyłączenia tych źródeł energii. Aby temu zapobiec, zaproponowano nieliniowy regulator anti-windup z warunkowym integratorem. Rozwiązanie to pozwoliło zdecydowanie poprawić własności dynamiczne zarówno przy zrzucie mocy jak i powrocie do pełnego obciążenia.

Słowa kluczowe: zrzut mocy, stan nieustalony, regulator anti-windup, całkowanie warunkowe

Introduction

Affordable prices, availability and relatively low installation costs of renewable energy sources contribute towards increase of distributed generation share in the energy market. Unfortunately, this trend can cause issues with keeping electrical energy quality within approved boundaries both during static and dynamic states.

The cause of dynamic states are either changes in reference values, or any kind of disturbances affecting control or measurement signals. This paper presents dynamic states caused by load dumps. It shows the characteristics of this kind of disturbance and the consequences that follow. It is proven that the key role in reducing voltage increase during load dumps is played by the power regulator. Thus, selection of this regulator is the research goal of this paper.

A load dump is always accompanied by a change of load parameters. Such a state of systems supplied by renewable generation requires a nonlinear regulator in the power control circuit. The idea of controller proposed by the author implements a logical condition which allows the regulator to avoid saturation of an integral path. This paper presents mathematical models of regulators, research methodology, and finally – laboratory results.

1. Load changes

The increasing number of PV inverters in the electrical grid has highlighted the problem of keeping energy parameters within boundaries set by normative acts. Disturbances, known in the literature as transient or temporary over-voltage (TOV) are especially visible during PV inverter operation [7]. They are especially dangerous for the electrical equipment operating in the grid with the high density of PV generators. There are two main causes of voltage increase:

- Load rejection overvoltage (LRO) [7] (Fig.1),
- Ground fault overvoltage (GFO) [1, 4].

Negative effects can be partially solved by installing a DC/DC converter in the intermediate circuit [2] or adding an active load output [9]. However, these solutions give only partial effects, since a rapid full load return will cause even more problems. These would include short voltage drops or rapid current increase on inverter output. These phenomena often cause the action of overcurrent protection, and as a result – a shutdown of the entire generator [5].

Disturbances caused by load dump can be eliminated by means of nonlinear regulators with conditional operating functions, so called “PI conditional integrators”, which are described in further chapter.

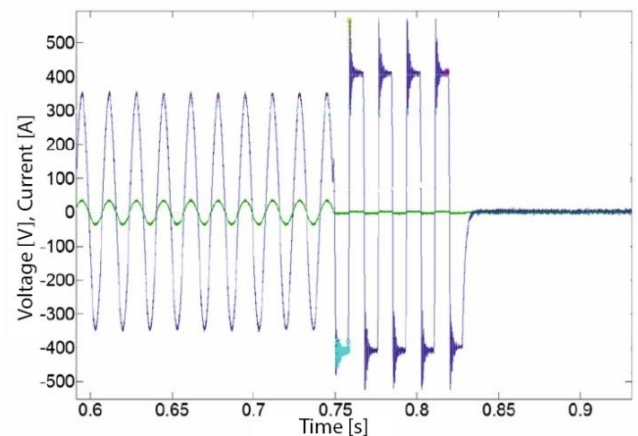


Fig. 1. Exemplary results of current and voltage measurements during load dump in $t = 0.075$ s. Overvoltage level $V_{max}/V_{amp} = 1.75$ achieved for 10% load dump

2. Vector control with decoupling

During the research an inverter with voltage oriented control (VOC) (Fig. 2) was used [7, 8].

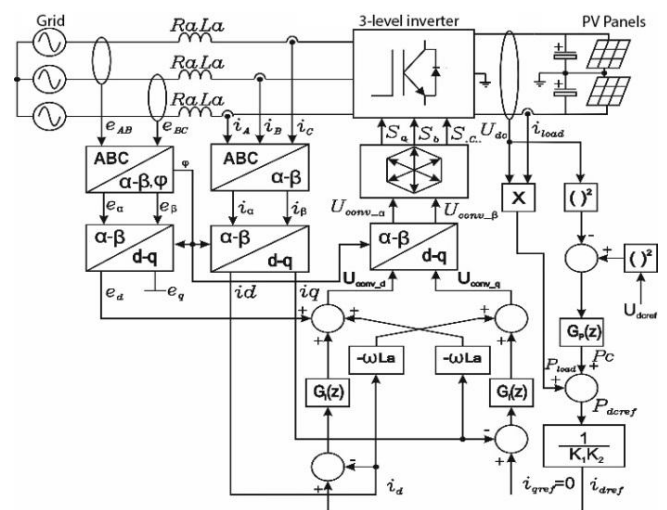


Fig. 2. Vector oriented control with decoupling in current paths i_d , i_q in rotating reference frame d_q

In this system input voltages for the d-q \rightarrow α - β transform are described in equations (1) and (2), which also explain the decoupling method.

$$U_{conv,d} = (i_{dref} - i_d) \cdot G(z) + e_d + -\omega L_g i_d U_{conv,d} = (i_{dref} - i_d) \cdot G(z) + e_d + -\omega L_g i_d \quad (1)$$

$$U_{conv,q} = [(i_{qref} - i_q) \cdot G(z)] - \omega L_g i_q \quad (2)$$

where: i_{dref} , i_{qref} – reference currents, i_d , i_q – measured currents, $G(z)$ – discrete controller transfer function, $\omega L_g i_d$, $\omega L_g i_q$ – voltage drops across inductor.

In the d-q input paths there are $G_1(z)$ controllers, which allow independent control over instantaneous powers p and q . Selection of control algorithm influences the characteristics of dynamic states. This is shown in experimental results, during which three different PI algorithms were used:

- Standard, parallel PI regulator,
- Nonlinear, variable-structure regulator:
 - Regulator with “anti-windup” algorithm,
 - Regulator with conditional integrator.

These regulators are tasked with minimising error in the i_d and i_q current paths. This is achieved by tuning both proportional and integral gains of the regulators, and placing them in current paths, as shown in Fig. 2.

3. PI controller tuning method

In order to achieve the dynamics requirements of the inverter, as well as provide an appropriate phase margin, PI controller tuning was performed. This stage was based on literature [6]. The tuning is presented on the current feedback loop i_{sq} and shown in Fig. 3.

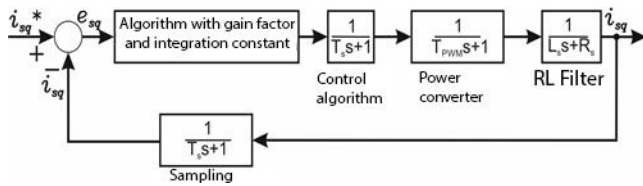


Fig. 3. Model of current control loop in q axis with simulated object and measurement characteristics

In this case, the delay caused by digital conversion was described as a first order transfer function with time coefficient $T_s = 0.1$ ms, for sampling frequency $f_s = 10$ kHz. To keep the power losses in IGBT switches at a minimum level, the time delay of $T_{PWM} = 0.1$ ms was selected. Voltage and current measurements are slaved of PWM modules, which also causes the delay of analogue-digital conversion to be at $T_s = 0.1$ ms. The transfer function of the PI regulator is described in equation (3) [6].

$$PI_{iq} = k_{piq} \left(1 + \frac{1}{T_{iq}s} \right) = k_{piq} \frac{1 + T_{iq}s}{T_{iq}s} \quad (3)$$

where: k_{piq} – proportional gain of current path i_q , T_{iq} – time coefficient of the integration path of current i_q

$$\frac{i_{sq}}{v_{sq}} = \frac{1}{R_s + sL_s} = \frac{1}{R_s} \frac{1}{1 + s \frac{L_q}{R_s}} = \frac{K}{1 + s \tau_q} \quad (4)$$

where:

$$K = \frac{1}{R_s} \quad (5)$$

$$\tau_q = \frac{L_q}{R_s} = 0,025 [s] \quad (6)$$

The transfer function in a closed feedback loop was converted into feedforward. The transformed current loop is shown in Figure 4.

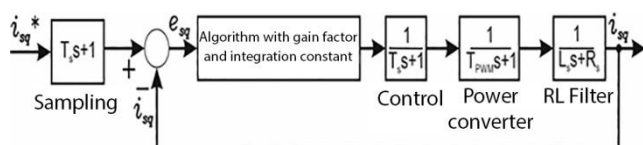


Fig. 4. Model of i_q current control loop with feedforward

The transfer function of the object in open loop is described in equation (7).

$$G_{iq}(s) = k_{piq} \frac{1 + T_{iq}s}{T_{iq}s} K \frac{1}{\tau_q s + 1} \frac{1}{T_s s + 1} \frac{1}{T_{PWM} s + 1} \quad (7)$$

The time coefficient of the PI regulator is selected to compensate the slowest pole of the objects' transfer function, which is approximately defined by the L/R filter coefficient.

$$T_{si} = 2T_s + T_{PWM} = 0.2 + 0.1 = 0.3 [ms] \quad (8)$$

From here, the transfer function of the entire object:

$$G_{iq}(s) = k_{piq} \frac{1}{T_{iq}s} K \frac{1}{T_{si}s + 1} \quad (9)$$

The k_{piq} gain of the PI regulator was calculated on the basis of the modulus optimum (KM). The damping coefficient was selected on the basis of [6] and its value is $\zeta = \frac{\sqrt{2}}{2}$. The transfer function of the second object is described in equation (10).

$$G_{KM} = \frac{1}{2\tau_s(\tau_s + 1)} \quad (10)$$

Converting equations (9) and (10):

$$\frac{k_{piq}K}{T_{iq}} = \frac{1}{2T_{is}} \quad (11)$$

$$k_{piq} = \frac{T_{iq}R_s}{2T_{si}} = 47,87 \quad (12)$$

The regulators tuned in the way described were transformed into discrete functions using Matlab software. Compilation results were implemented in the tested regulators. The results are presented in Figure 8.

4. Nonlinear PI regulators with variable internal structure

During rapid load changes, overshoot of the converter can be limited by means of modified, nonlinear PI regulator.

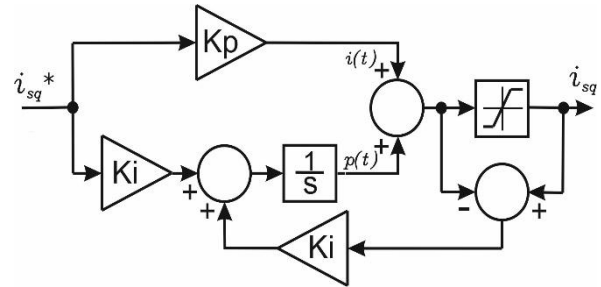


Fig. 5. Nonlinear PI regulator, with “anti-windup” function. K_p , K_i regulator gains, K_s – feedback gain, i_{sq}^* – reference current

The algorithm that deals with overshoot and saturation is shown in Figure 5. When the regulator output becomes saturated, the difference between saturation block input and output occurs. This difference is then amplified in the K_i block, and then subtracted in the sum block of the integration path.

Unfortunately, the dynamics of such a regulator is still insufficient in the case of rapid load changes (Fig. 9). Because of this, a nonlinear algorithm with logical condition and feedback loop was proposed (Fig. 6)

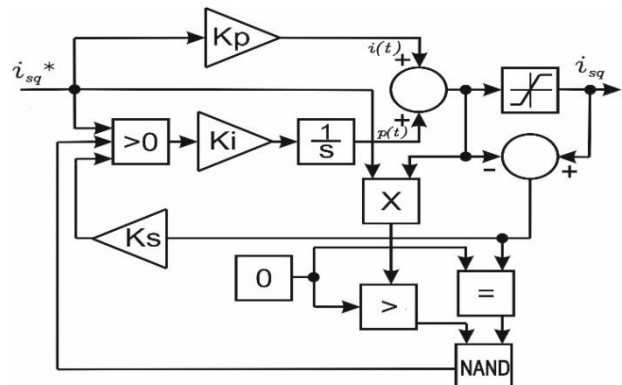


Fig. 6. Nonlinear PI algorithm, with logically controlled strong feedback loop

This implemented feedback loop causes almost immediate return from the saturated state of the algorithm (Fig. 10). The NAND logic gate based system controls the output and checks it for saturation.

5. Experimental results

During experimental research, a VOC controlled inverter was loaded by an electrical grid emulator [3, 10]. The influence of a load dump on converter output voltage at grid connection point was tested on the basis of previously derived control algorithms.

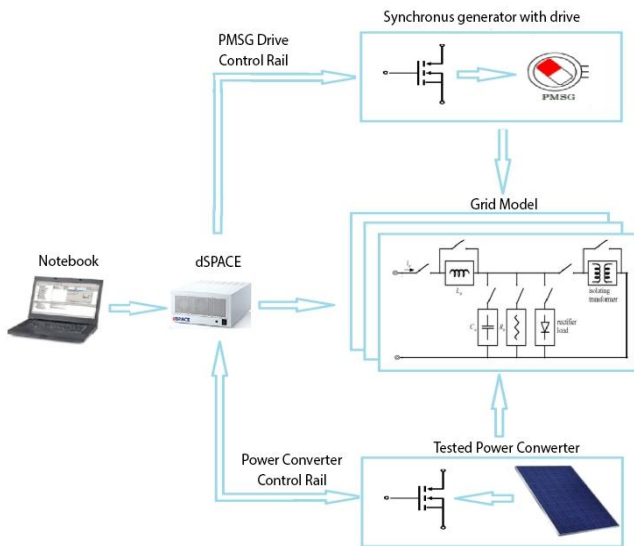


Fig. 7. Simplified diagram of electric grid emulator

The emulator used consists of a synchronous generator PMSG with output power of 5.5 kW, which is driven by a squirrel cage motor and vector oriented inverter. This machine system produces three-phase voltage similar in parameters to the one provided by the grid. A load dump is created by means of changing impedance in the intermediate circuit between the PMSG generator and tested inverter. These changes are performed by a relay matrix. Selected RL elements allow for step increases or decreases of the intermediate circuit impedance. In this way, a load dump was created, reaching 20% of generator nominal power.

Experimental tests were performed for the three aforementioned PI regulators. Activation levels of logical conditions were experimentally selected to achieve the best possible time responses of algorithms. A typical PI algorithm is a sufficient solution when the output power is controlled only by the user. However, in the case of a load dump, and then a return to nominal load, it causes an inverter output power overshoot (Fig. 8).

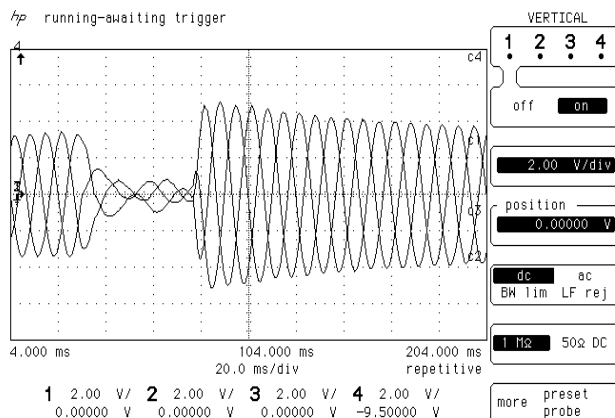


Fig. 8. Current waveforms during load dump with standard PI algorithm. Current scale: 5 A/V

The inverter produces power, which can be a multiple of reference power at the moment of load return. In the model tested, doubling of output power was achieved for a load dump lasting 0.1 s. The time required for the output power to stabilize at reference level was 0.4 s.

In the case of a PI algorithm with “anti-windup” function, results presented in Figure 10 were obtained. Response for a load dump had increased time to return to nominal value.

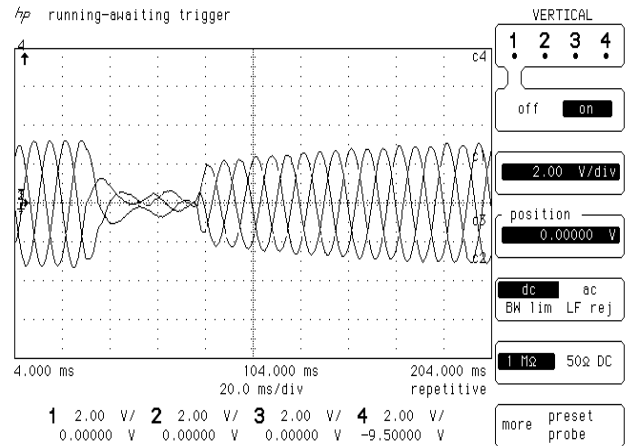


Fig. 9. Current waveforms during load dump with PI algorithm with “anti-windup” function. Current scale: 5 A/V

A slow return to reference output power does not cause short term overloads, but it constitutes too large a delay in return to nominal load. This delay can cause an impermissible voltage drop at the local grid, which can in turn result in a shutdown of certain loads or even of PV generation inverters.

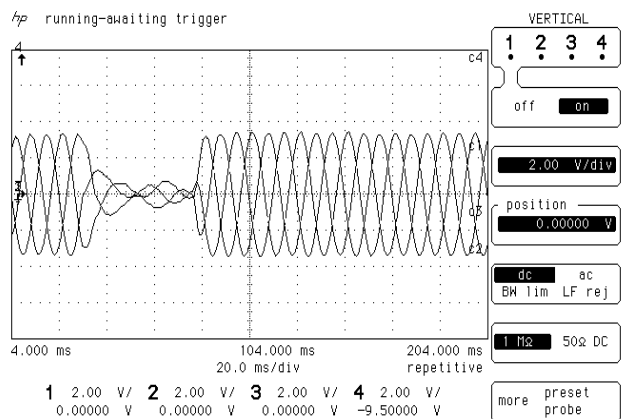


Fig. 10. Current waveforms during load dump with PI algorithms with strong feedback loop. Current scale: 5 A/V

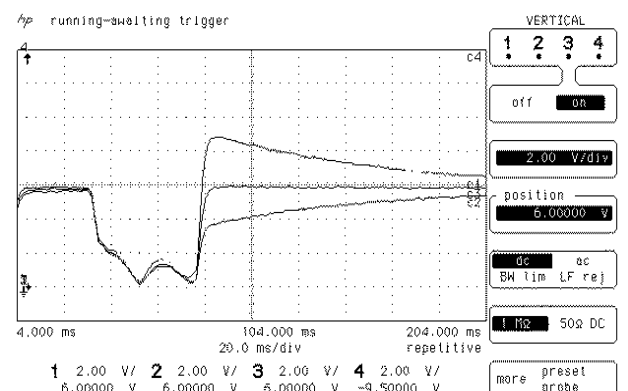


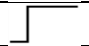


Fig. 11. Output current modulus from inverter to emulated grid for three different PI algorithms. Current scale: 5 A/V

The best results were achieved in the case of a PI algorithm with conditional integration. The response of this algorithm was almost instantaneous (Fig. 10). Multiple tests with different load changes proved that for this type of disturbances this algorithm is the most efficient. Overshoot never crossed 5% of output current reference value. This is due to the fact that as soon as regulator output becomes saturated, the entire integration path is reset to zero. This situation lasts as long as the controller output stays saturated. Because of this, the algorithm is not pushed into further saturation, and can recover its dynamics very fast.

A comparison of all three results is presented on a single graph in Figure 11. This figure proves that the best result was achieved using the third algorithm – a PI algorithm with conditional integration loop.

Table 1. *W Experimental results and reset quality coefficients for three PI algorithms*

Algorithm	Control precision	Overshoot	Error integral I_d	Error integral I_q	Response curve
PI (1)	Very good	>100%	58%	2.5	
PI_N (2)	Very good	no overshoot	41.3%	1,8	
PI_N (3)	Very good	<5%	37.2%	1.49	

6. Conclusions

The load dump problem in an electrical grid becomes more relevant with the increasing number of renewable energy sources in households. The author proposed a solution to this problem by using a nonlinear control algorithm in the current control circuits of renewable generation inverters. The proposed algorithm eliminates such unwanted effects as wind-up saturation. Also, it does not affect generation capability during return to nominal load. Through this, the article's goal was achieved, and the current ripple was reduced to below 5%. The dynamic state duration was also reduced.

References

- [1] Barker P.: Overvoltage considerations in applying distributed resources on power systems. IEEE Power Engineering Society Summer Meeting 1/2002, 109–114.
- [2] Huang S., Wu J.: A control algorithm for three-phase three-wired active power filters under nonideal mains voltages. IEEE Transactions on Power Electronics 14(4)/1999, 753–760.
- [3] Jarzyna W., Lipnicki P., Zieliński D.: Synchronisation of voltage frequency converters with the grid in the presence of notching. COMPEL – The International Journal for Computation and Mathematics in Electrical and Electronic Engineering 34(3)/2015, 657–673, [DOI: 10.1108/COMPEL-10-2014-0266].
- [4] Jarzyna W., Lipnicki P.: The Comparison of Polish Grid Codes to Certain European Standards and resultant Differences for WPP Requirements. 15th European Conference on Power Electronics and Applications (EPE), 1–6, [DOI: 10.1109/EPE.2013.6634748].
- [5] Jarzyna W., Zieliński D., Zielińska K., Fatyga K.: Reduction of voltage and power oscillation in the two-phase shorting of a grid inverter. 19th European Conference on Power Electronics and Applications (EPE'17 ECCE Europe) 2017.
- [6] Kaźmierkowski M. P., Tunia H.: Automatic Control of Converter-Fed Drives. Elsevier, 1995.
- [7] Ropp M.: Inverter grounding and overvoltages. IEEE PES General Meeting, 2014.
- [8] Sedlak M., Styński S., Kaźmierkowski M. P., Malinowski M.: Operation of a four-leg three-level flying capacitor grid-connected converter for RES. IECON 2013 – 39th Annual Conference of the IEEE Industrial Electronics Society, 2013, 1100–1105, [DOI: 10.1109/IECON.2013.6699286].
- [9] Teodorescu R., Lissere M., Rodriguez P.: Grid Converter for Photovoltaic and Wind Power Systems. IEEE-Wiley, New York 2011.
- [10] Zieliński D.: A laboratory system for analysing power inverters during voltage sags. Informatyka, Automatyka, Pomiary w Gospodarce i Ochronie Środowiska 4(2)/2014, 77–80, [DOI: 10.5604/20830157.1109384].

M.Sc. Eng. Łukasz Kwaśny
e-mail: l.kwasny@pollub.pl

Graduated from the Faculty of Electrical Engineering and Computer Science. Since 2016 employed at the Department of Electrical Drives and Machines of the Lublin University of Technology. His interests include power electronics, especially design and modelling of converters for grid-tied applications and renewable energy generation interfaces.



ORCID ID: 0000-0001-7454-9862

otrzymano/received: 01.08.2019

przyjęto do druku/accepted: 06.12.2019

DOI: 10.35784/IAPGOS.221

MEASUREMENT SYSTEMS FOR THE ENERGY PRODUCED BY A PHOTOVOLTAIC SYSTEM AND CONSUMED BY A BUILDING IN THE LUBLIN SCIENCE AND TECHNOLOGY PARK

Arkadiusz Malek

University of Economics and Innovation in Lublin, Faculty of Transport and Computer Science, Lublin, Poland

Abstract. The article contains a description of systems for measuring the energy produced by the photovoltaic system and its consumption by a building. The photovoltaic system consists of two micro-installations supplying two parts of the Lublin Science and Technology Park. An internet platform for monitoring photovoltaic plant operation is presented. The power generated and the amount of electricity produced are assessed. Also, an innovative system for monitoring and analysing the consumption and production as well as the efficient use of electricity in individual parts of the building is described. Based on the measurements carried out, the production of energy exceeded its consumption in one part of the building.

Keywords: photovoltaic systems, energy measurement, energy management, smart devices

SYSTEMY POMIARU ENERGII PRODUKOWANEJ PRZEZ SYSTEM FOTOWOLTAICZNY I POBIERANEJ PRZEZ BUDYNEK LUBELSKIEGO PARKU NAUKOWO-TECHNOLOGICZNEGO

Streszczenie. W artykule zawarto opis innowacyjnych systemów do pomiaru energii produkowanej przez system fotowoltaiczny oraz pobieranej przez budynek. System fotowoltaiczny składa się z dwóch mikroinstalacji zasilających dwa segmenty Lubelskiego Parku Naukowo-Technologicznego. Przedstawiono platformę internetową do monitoringu pracy systemu fotowoltaicznego. Dokonano oceny generowanej mocy oraz ilości produkowanej energii elektrycznej. Następnie opisano innowacyjny system do monitoringu, analizy zużycia i produkcji oraz efektywnego wykorzystywania energii elektrycznej w poszczególnych segmentach budynku.

Słowa kluczowe: system fotowoltaiczny, pomiar energii, zarządzanie energią, inteligentne urządzenia

Introduction

Subjects related to the design, construction and control of energy produced by photovoltaic systems are eagerly taken up by scientists from various scientific disciplines. This is due to the mechatronic nature of photovoltaic farms. They contain mechanical components and electronic control based on measured and processed signals. Photovoltaic systems are devices of the Internet of Things capable of communicating with each other and with the building they supply.

Photovoltaics is one of the main global trends related to obtaining energy from renewable energy sources (RES) [25]. It is an estimated billion dollar market as an alternative to obtaining energy from fossil sources [6]. It turns out that this trend can be combined with other trends, such as Electro mobility. Electric cars, charged with electricity produced by photovoltaic systems [27], become completely zero-emission vehicles [17]. In addition, the increasing number of electric vehicles in Poland [32] and in the world will need large amounts of electricity to charge them [19].

Photovoltaic systems may be divided into stationary and mobile ones. Stationary ones are usually mounted on the roofs of buildings or on the ground [21]. Special ground structures are often created for the production of electricity and shadow generation for parked vehicles – so-called carports [27]. Having a source of electricity next to a parked vehicle, means that it may be used to charge parked electric vehicles [26]. Photovoltaic systems are mounted on various types of vehicles. First, public transport buses began to be used because of the availability of a large area for the installation of photovoltaic panels [30]. Researchers studied the subject of the safety of mobile photovoltaic systems [28] and their productivity [13]. Flexible photovoltaic panels can also be mounted on various body parts of passenger vehicles [14].

A very important area of research and development of photovoltaic system components is material engineering, providing innovative materials for the construction of photovoltaic system and energy inverters. Currently, composite materials [15], metal nanofibers [23], polymers [29] and perovskites [22] are used for the construction of panels. Modern materials are characterized by increasing efficiency, lower price and greater durability to weather conditions which may lead to degradation in photovoltaic system performance [18]. Therefore, these mechanisms should be thoroughly understood in order to effectively counteract them [3].

One of the very popular and useful areas for researching photovoltaic systems is their diagnostics. Intelligent algorithms allow quick and precise detection of irregularities in the operation of a photovoltaic system [10, 24].

In order to effectively control the photovoltaic system itself and the use of produced energy, it is necessary to make precise measurements with a high degree of accuracy. Scientists are still working on the evaluation of mathematical methods characterizing the electrical parameters of photovoltaic panels [2]. The relationships between electrical parameters characterizing the photovoltaic system are very important [7]. Measurements are also very important in managing the energy produced and its use for charging energy storage batteries [1]. The measured parameters are processed and used to optimize the system operation. Developed control algorithms should thoroughly be validated in real conditions [31]. Modern photovoltaic inverters and energy management systems are increasingly advanced and have innovative functions related to the detection of the amount of dirt on panels and the generation of messages about the need to clean them [20]. Short circuits in the installation are also automatically detected and precisely located [5]. Many systems have the ability to monitor the parameters of each panel using individual optimizers [9, 11, 27].

The construction of a photovoltaic installation is widely recognized as a way of becoming independent of the energy produced by Energetic Groups. Every investor, be it an individual or an institution, is looking for the possibility of obtaining a return on the funds invested in the photovoltaic systems in the shortest possible time. By definition, this approach must involve the total or maximum use of energy produced for own needs. Any other eventuality associated with the sale of surplus energy extends the return on investment time. This is due to the manner in which electricity distributors and sellers account for electricity which is unfavourable for renewable energy producers [12]. Intelligent measuring systems are used to accurately measure the electricity produced by the photovoltaic system and the energy consumed by the building.

The Lubelskie Voivodship is located in one of the regions of Poland, considered to be optimal for the use of photovoltaic energy. The insolation is of course different in individual regions of the country and it ranges from 900 kWh/m² to 1200 kWh/m², which can be seen on the map prepared on the basis of the data of the Institute of Meteorology and Water Management (Figure 1).

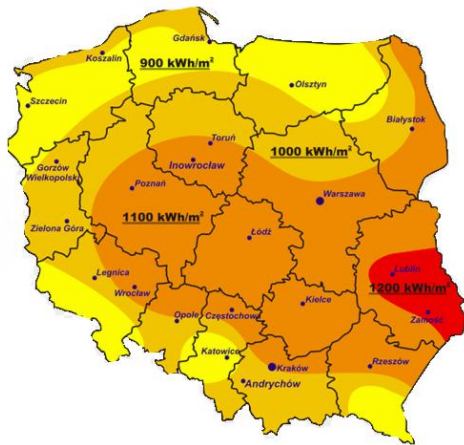


Fig. 1. Insolation in Poland [36]

Significant nationwide photovoltaic energy resources in the region are potentially an opportunity for the region to achieve the position of the national leader in the use of photovoltaic energy used both for heat production and electricity generation.

1. Research object

There is a ground photovoltaic system in front of the building of the Lublin Science and Technology Park (LSTP). These are 2 micro installations with a peak power output of up to 40 kWp each using polycrystalline photovoltaic panels. The system was launched at the end of November 2018 and its appearance is shown in Figure 2. LSTP received funding from the Lublin Agency for Enterprise Support for the construction of the system. LSTP implemented the "Photovoltaic installation project on the ground next to the building of the Lublin Science and Technology Park" co-financed by the European Regional Development Fund under the Regional Operational Program of the Lublin Voivodship for 2014–2020, Priority Axis 4 "Environmentally friendly energy", Measure 4.2 "Energy production from renewable energy in enterprises." The goal of the project is to increase the energy efficiency of the company by building a photovoltaic system in Lublin, next to the LSTP building as part of the project, 2 photovoltaic micro installations with a capacity of up to 40 kWp were built. The project value is PLN 373,920.00, and the grant is PLN 135,324.99, which accounted for 45% of the eligible costs of PLN 300,500.00.

Both micro-installations were connected to two parts of the building and power various types of electric devices. The first micro-installation powers Section 4 of the building, in which most of the electricity supplies the servers of the Centre for Supervision over Eastern Poland Broadband Network. The second micro-installation supplies Section 5 of the building where the offices of the LSTP Board as well as offices and laboratories of tenants are located. The main consumers of electricity in this part are: lighting, air conditioning, office equipment and equipment of low-power research laboratories.

General scheme of the electrical connection of the photovoltaic plant to the building of the Lublin Science and Technology Park is presented in Figure 3.



Fig. 2. Photovoltaic plant in front of the building of the Lublin Science and Technology Park [33]

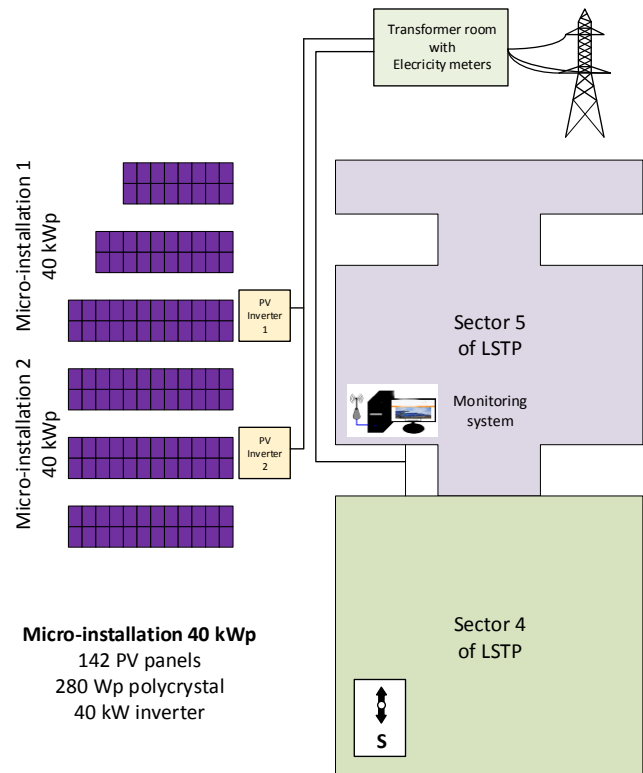


Fig. 3. Scheme of the electrical connection of the photovoltaic plant to the building of the Lublin Science and Technology Park

The aim of the research is to use systems for measuring energy produced by the photovoltaic system and consumed by the LSTP building in order to energy management. In turn, the goal of energy management is the maximum use of electricity produced by the photovoltaic plant for own needs. This approach will allow for the fastest return on investment in the photovoltaic system.

2. Measurement of energy produced by the photovoltaic system

Almost all currently offered photovoltaic inverters have the function of measuring instantaneous power and the amount of produced energy. This measurement data can be transferred by wired or wireless transmission techniques to the server of the inverter manufacturer. After setting up the account and configuring it, the photovoltaic system administrator has access to the most important data related to the system operation [34]. Depending on the type of inverter, the volume of the data is extremely variable. They include a regular measurement of the system power (in kW) or individual strings or even individual panels, which usually takes place every 15 or 20 minutes. In addition, the system records the amount of energy produced (in kWh). Producer of the inverter wrote in User manual: "The display values may deviate from the actual values and must not be used for billing purposes. The inverter's measurement values are required for the operational control and to control the current to be fed into the electricity grid. The inverter does not have a calibrated meter".

Figure 4 presents the course of continuous power generated in total by 2 micro-installations 2x40 kWp on a sunny June day of 2019. It could be observed a very smooth increase in the generated power depending on the height of the sun above the horizon. The lack of large decreases and increases in the generated power means that the measurement concerned a completely cloudless day. The photovoltaic system with a total power output of 80 kWp generated a maximum power of 68769.7 W, which is 85.96% of peak power, which is measured in properly defined conditions.

Photovoltaic energy production on individual days of the month is shown in Figure 5.

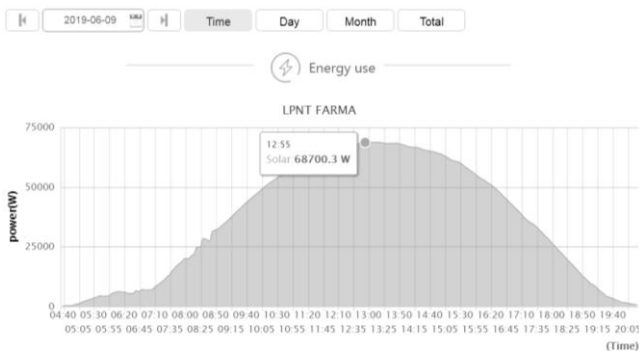


Fig. 4. Power generated by 2 micro-installations 2x40 kWp (total) on June 9, 2019

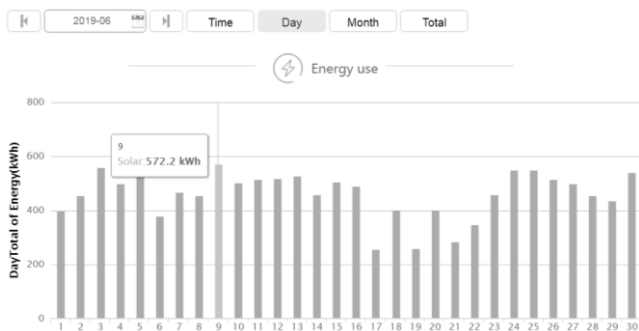


Fig. 5. Energy generated by 2 micro-installations 2x40 kWp on individual days of the month of June 2019

2x40 kWp micro-installations have very similar instantaneous power generated, which provide into very similar amounts of energy produced. Data from the system can be considered separately for each of the micro-installations or for their sum (as in Figure 6). Measurement data can be exported at any time using the Export button visible in the diagram.

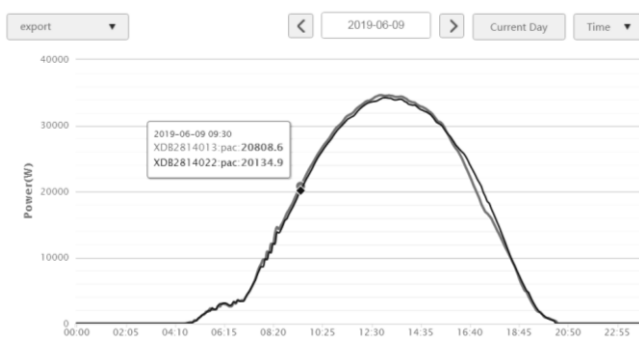


Fig. 6. Energy generated by 2 micro-installations 2x40 kWp on June 9, 2019

3. The requirement of the LSTP building for electricity

The amount of energy drawn from the power grid and the surplus fed into it can be measured using a two-way electricity meter. Innovative measuring system was used to automatically obtain data from electricity meters installed in LSTP Sectors 4 and 5. The device is confirmation that innovative products have their origin and practical application in LSTP.

Used measuring system is an innovative system for monitoring, analysing consumption and production as well as the efficient use of electricity [4, 16, 35]. Its appearance is shown in Figure 7.

It consists of:

- A hardware – a small, battery-powered device that reads measured data from an energy meter.

- An application – an application for Android smartphones, used when synchronizing data from a device (via Bluetooth Low Energy) and as an online gateway.
- A Cloud – an internet platform on which readings preview, profiles, charts, reports, data export and API access are available.

The main advantages of measuring system are simplicity (installation takes place within a few minutes) and versatility. The system may be used by both home users as well as enterprises and companies seeking to optimize energy costs.

The device works with meters in both one- and three-phase electricity grid installations.

It is mounted on the optical port of the energy meter and obtains measurement data through the IEC 62056-21 protocol, making it compatible with many meter models of the largest manufacturers (Apator, Landis + Gyr, Iskra, Pozyton et al). The team has recently implemented the SML (Smart Meter Language) protocol used in meters in Germany and is working on adding meter support via the DLMS protocol. In this case the accuracy of measurement depends on other device – electricity meter. Metering accuracy of active/reactive energy is Class B (1.0)/2.0 respectively.

The measuring system Home version retrieves active energy consumption data and allows users to track costs, while the Business version also provides reactive energy data and allows users to adjust the ordered power. If measuring system is mounted on a bidirectional energy meter, the user also receives information about the energy fed into the energy grid, which is important for owners of photovoltaic systems.

The measuring system team is currently developing the second generation of the product called IoT based on LoRA, LTE-M and NB-IoT communication. The works are carried out with the technological support of Nordic Semiconductor. The project received a grant from the National Centre for Research and Development, which also includes intelligent algorithms and additional energy management tools.



Fig. 7. Appearance of the measuring device

Two measuring system Business devices were purchased and installed. The measuring device, in the form of a beacon, works with bidirectional electricity meters on the LSTP Sectors 4 and 5. Then, via Bluetooth transmission, it transmits the measurement data obtained from the energy meter to the cloud. Data collected in the cloud can be displayed in the form of readable charts both on a PC and on a mobile device [3]. In June 2019, LSTP photovoltaic plant produced 13.8 MWh of electricity (data from Figure 8) and production from both installations was very close to the 50:50 ratio (according to Figure 6).

From the Sector 4 measurement data, it appears that almost all the energy produced by 1 micro-installation is used for the LSTP building's own requirements. The surplus produced and sold to the power grid was only 616 kWh compared to consumption of almost 12 MWh. Almost total use of energy produced for own needs is a method for quick return of money invested in the photovoltaic system.

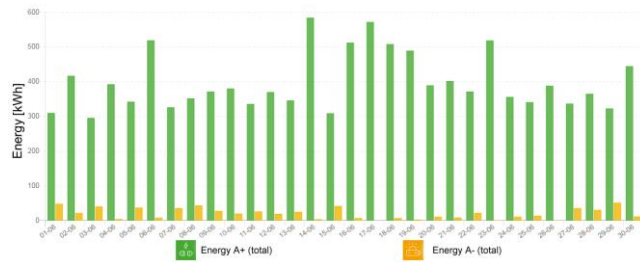


Fig. 8. Graph of energy consumed (A+) and donated (A-) in Sector 4 LSTP in the month of June 2019

The situation in the Sector 5 of LSTP looks worse as shown in Figure 9. Compared to Segment 4, there is much lower daily energy consumption and a much larger surplus of energy produced. Predictions regarding the increase in energy consumption in Sector 5 during the summer did not come true. In the spring months from March to May, the building's management observed sporadic use of air conditioning by both LSTP administrative staff and tenants. A very warm June completely changed the situation and very frequent or continuous use of all available air conditioning during work was noted. This resulted in an increase in energy consumed by Sector 5. But the increase was more than offset and the surplus of energy production in June increased compared to April and May.

The surplus of energy produced by enterprises is resold to an energy seller at a very unfavourable price constituting less than 25% of the total purchase price (including distribution and sale). This means a 4-fold increase in the payback time in the case of a large ratio of surplus energy sold to the distributor. To counteract this situation, the option of connecting other Sectors to Sector 5 should be considered. However, the situation is complicated by the ownership structure and the current design of the electrical network throughout the building.

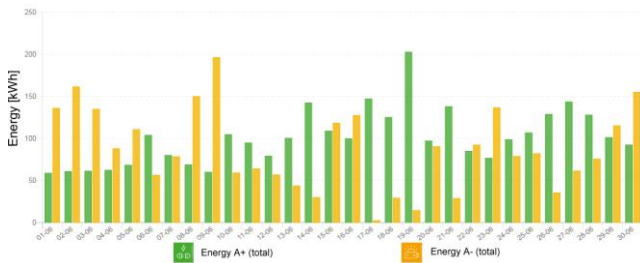


Fig. 9. Graph of energy consumed (A+) and donated (A-) in Sector 5 LSTP in the month of June 2019



Fig. 10. Graph of energy consumed (A+) and donated (A-) in Sector 5 LSTP on a weekday – June 13, 2019

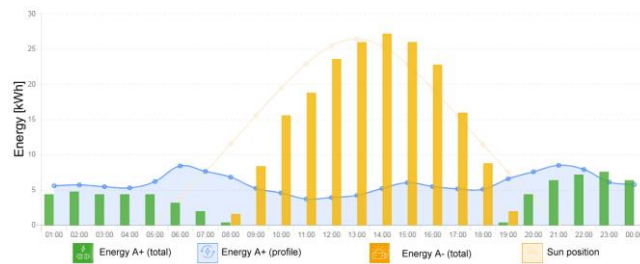


Fig. 11. Graph of energy consumed (A+) and donated (A-) in Sector 5 LSTP on a weekend day – June 9, 2019

The overview of consumption on weekdays (Figure 10) and on weekends (Figure 11) showed that the surplus of energy produced is much higher on non-working days.

The Cloud internet platform allows users to generate graphs of selected parameters, view meter readings and generate graphical reports from a selected period of time [4].

Standard charts allow users to track during the year, month, week, day (hour) and day (quarter hour):

- Active energy consumed (Energy A+),
- Energy given away (Energy A-),
- Reactive energy.

These data are raw data and carry a lot of useful information. They can clearly show when the preordered power is exceeded in a selected period. However, much more information can be obtained from reports that the online platform offers to generate automatically. Such an energy consumption report is divided into 3 parts, which correspond to the tabs on the platform:

- 1) Energy costs,
- 2) Energy consumption,
- 3) Power consumption.

The graphs of consumption profiles in the Power consumption tab seem to be very interesting [1]. The graph in Figure 12 shows the profile of active power consumed during the day. The minimum, maximum and average values are presented in 15-minute intervals. The profile clearly shows the night consumption values when the photovoltaic system is not working. During the day, the impact of energy produced by the micro-installation is visible, which during photovoltaic hours reduces the power consumed by Sector 5 to values close to zero. Maximum values occur on days of very low sunlight, when the power generated by the photovoltaic system is not able to cover the needs of Sector 4. Therefore, the maximum values inform users about the potential power consumption of the building without a photovoltaic system.

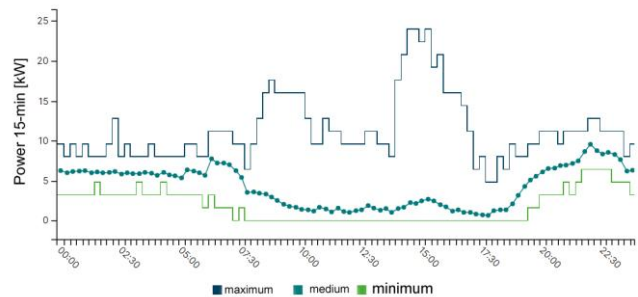


Fig. 12. 15-minute profile of active power consumed in Sector 5 LSTP in the month of June 2019

The average value is calculated from data from all days in the selected period of time, as shown in Figure 13. The graph shows a comparison of daily profiles of the active power consumed from the selected period. Users can learn from it how much the active power profiles tested differ for each day and detect anomalies. Importantly, users can take into account the average profile run on selected days of the week for the calculation.

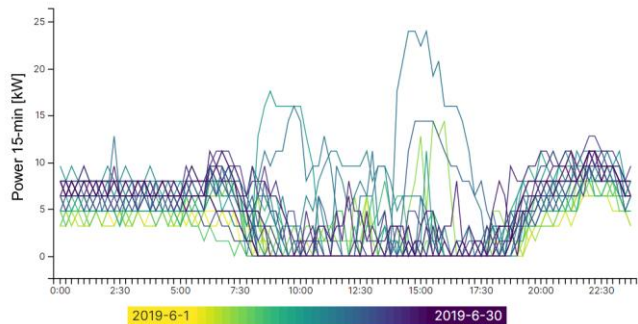


Fig. 13. Comparison of 15-minute profiles of active power consumed in Sector 5 LSTP in the month of June 2019

This is the output of the producers of the measuring system to electricity consumers characterized by differentiated power consumption over various periods of time. Such extensive analysis capabilities allow users to detect certain relationships and use them in effective management of energy produced and consumed.

The graph in Figure 14 shows the trend of active power consumption in the selected range as in the example of a box graph. Using a given graph, it is possible to identify whether the active power consumption trend is symmetrical, how much data is grouped, and whether and how the power consumption trend is distorted.

Of course, the producers of the platform provide a detailed description of all values displayed in the form of a box chart for all interested parties – see Figure 15.

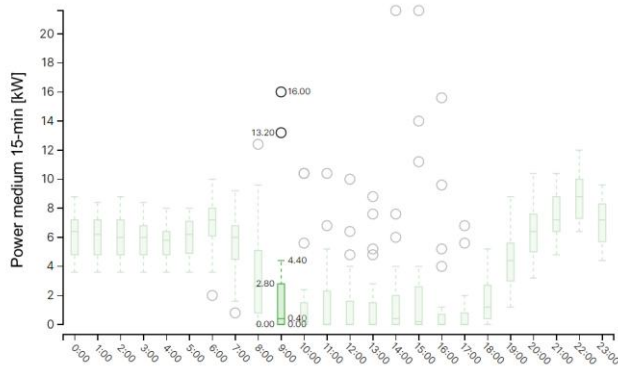


Fig. 14. 15-minute medium power – box chart in Sector 5 LSTP in the month of June 2019

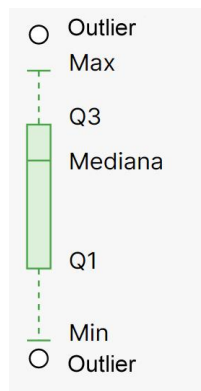


Fig. 15. Description of the values displayed on the box chart

The load duration curve, shown in Figure 16, describes the power consumption over the selected period. For example, a value of 1 kW for 10% means that for 10% of the period the power consumption was greater than or equal to 1 kW. It can also be read for how long was exceeded the preorder power.



Fig. 16. Load duration curve for active power in Sector 5 LSTP in the month of June 2019

Table 1 presents the values of energy consumed and given away to the power grid in various months of 2019. Sector 4 LSTP is characterized by high monthly electricity consumption. The amount of energy returned to the external grid is very small. This means that almost all the energy produced by the photovoltaic micro-installation is used for own needs. Sector 5 LSTP has a much lower monthly energy consumption than Sector 4. In addition, Sector 5 is not able to use all the energy produced by the photovoltaic system. In individual months, the surplus of electricity produced was found to range from 964.4 to 2622.4 kWh.

Table 1. Active energy consumed and energy given away in various months of 2019 year in Sector 4 and 5 LSTP

Month of 2019	Sector 4		Sector 5	
	Energy consumed [kWh]	Energy given away [kWh]	Energy consumed [kWh]	Energy given away [kWh]
April	12 123.0	568.0	4 043.0	1 898.0
May	12 696.5	594.0	3 305.6	2 162.8
June	11 973.5	616.0	3 038.4	2 622.4
July	12 740.0	527.5	3 682.4	1 928.4
August	14 735.0	317.5	4 848.8	1 728.8
September	13 560.0	376.5	3 680.8	1 511.2
October	15 009.5	109.5	4 330.4	964.4

These are significant amounts of energy given away in Sector 5 that can significantly affect the payback time of an investment in a photovoltaic micro-installation. The author propose to use the excess energy produced to charge electric cars.

4. Summary and conclusions

A photovoltaic system consisting of two micro-installations with a power output of up to 40 kWp each was built to supply electricity to two sectors of the Lublin Science and Technology Park. The manager of the photovoltaic system has set himself the goal of returning the money invested in its construction in the shortest period of the time. The way to achieve it is total or maximum use of energy produced for own needs. Any other eventuality associated with the sale of surplus energy extends the return on investment time. This is due to the method of business practices electricity distributors and sellers which are unfavourable for the RES energy producers. The presented online platform for monitoring photovoltaic system operation is a very useful tool for monitoring performance and diagnosing photovoltaic system operation. It was used to assess the power generated and the amount of electricity produced by the photovoltaic system. An innovative system for monitoring, analysing consumption and production as well as efficient use of electricity in individual building sectors produces very wide possibilities. With its help, a surplus of produced energy was found in one of the sectors.

Sector 4 LSTP is characterized by high monthly electricity consumption. The amount of energy returned to the external grid is very small. This means that almost all the energy produced by the photovoltaic micro-installation is used for own needs. Sector 5 LSTP has a much lower monthly energy consumption than Sector 4. In addition, Sector 5 is not able to use all the energy produced by the photovoltaic system. It was proposed that it should be used to charge electric vehicles.

Bibliography

- [1] Al Essa M. J. M.: Home energy management of thermostatically controlled loads and photovoltaic-battery systems. Energy 176/2019, 742–752
- [2] Aoun N., Bailek N.: Evaluation of mathematical methods to characterize the electrical parameters of photovoltaic modules. Energy Conversion and Management 193/2019, 25–38.

- [3] Azizi A., Logerais P. O., Omeiri A.: Impact of the aging of a photovoltaic module on the performance of a grid-connected system. *Photovoltaic Energy* 174/2018, 445–454.
- [4] Bień A., Janicki A.: Simple and efficient profiling of electricity consumer. *Wiadomości Elektrotechniczne* 3/2019, 42–45 [DOI: 10.15199/74.2019.3.8].
- [5] Bliss M., Betts T., Gottschalg R.: Interlaboratory comparison of short-circuit current versus irradiance linearity measurements of photovoltaic devices. *Photovoltaic Energy* 82/2019, 256–263.
- [6] Choudhary P., Srivastava R. K.: Sustainability perspectives- a review for photovoltaic trends and growth opportunities. *Journal of Cleaner Production* 227/2019, 589–612.
- [7] Cibira G.: Relations among photovoltaic cell electrical parameters. *Applied Surface Science* 461/2018, 102–107.
- [8] Coria G., Penizzotto F., Pringles R.: Economic analysis of photovoltaic projects: The Argentinian renewable generation policy for residential sectors. *Renewable Energy* 133/2019, 1167–1177.
- [9] Dubard J., Filtz J. R., Cassagne V., Legrain P.: Photovoltaic module performance measurements traceability: Uncertainties survey. *Measurement* 51/2014, 451–456.
- [10] Gallardo-Saavedra S., Hernández-Callejo L., Duque-Pérez O.: Quantitative failure rates and modes analysis in photovoltaic plants. *Energy* 183/2019, 825–836.
- [11] Gao Q., Zhang Y., Yu Y., Liu Z.: A direct current-voltage measurement method for smart photovoltaic modules with submodule level power optimizers. *Photovoltaic Energy* 167/2018, 52–60.
- [12] Gluchy D.: The comparative analysis of the profitability of investments in the renewable energy source. *Informatyka, Automatyka, Pomiary w Gospodarce i Ochronie Środowiska* 4b/2012, 28–31.
- [13] Grabowski, L.: The productivity of photovoltaic structures mounted on the roof of city bus. *Logistyka* 3/2014, 2114–2120.
- [14] Hai Vu N., Pham T.-T., Shin S.: Flat concentrator photovoltaic system for automotive applications. *Photovoltaic Energy* 190/2019, 246–254.
- [15] Imbuluzqueta G., Yurrita N., Aizpurua J., Cano F. J., Zubillaga O.: Composite material with enhanced ultraviolet performance stability for photovoltaic modules. *Photovoltaic Energy Materials and Photovoltaic Cells* 200/2019, 109947.
- [16] Janicki A.: Enhancing Electricity Meters with Smart Functionality Using Metering System with Optical Sensors. *ALLSENSORS* 2019.
- [17] Judzińska-Kłodawska A.: Energy consumption in electric cars and environment impact. *Autobusy: technika, eksploatacja, systemy transportowe* 6/2014, 149–151.
- [18] Katayama N., Osawa S., Matsumoto S., Nakano T., Sugiyama M.: Degradation and fault diagnosis of photovoltaic cells using impedance spectroscopy. *Photovoltaic Energy Materials and Photovoltaic Cells* 194/2019, 130–136.
- [19] Krupa K., Kamiński J.: Impact analysis of electromobility development on Poland's electricity consumption. *Rynek Energii* 6/2017, 8–13.
- [20] Lay-Ekuakille A., Ciaccioli A., Griffo G.: Effects of dust on photovoltaic measurements: A comparative study. *Measurement* 113/2018, 181–188.
- [21] Lis P., Pieszyk J.: Energy consumption and energy efficiency of buildings. *Fizyka Budowli w Teorii i Praktyce* 3/2016, 21–28.
- [22] Liu G., Kong L., Yang W., Mao H.: Pressure engineering of photovoltaic perovskites. *Materials Today* 27/2019, 91–106.
- [23] Liu J., Jia D., Gardner J. M., Johansson E. M. J., Zhang X.: Metal nanowire networks: Recent advances and challenges for new generation photovoltaics. *Materials Today Energy* 13/2019, 152–185.
- [24] Lu X., Lin P., Cheng S.: Fault diagnosis for photovoltaic array based on convolutional neural network and electrical time series graph. *Energy Conversion and Management* 196/2019, 950–965.
- [25] Łukaszewski, J.: Trzy trendy na 2019 rok, które zmieniają filozofię produkcji, zarządzania i zużycia energii. *Napędy i Sterowanie* 2/2019, 46–47.
- [26] Małek A., Filipowicz I.: Charging the electric vehicle from the photovoltaic minicarport. *AUTOBUSY–Technika, Eksploatacja, Systemy Transportowe* 11/2018, 37–40 [DOI: 10.24136/atest.2018.343].
- [27] Małek A., Kowalczyk D.: Photovoltaic carport for electric vehicle charging. *Autobusy: technika, eksploatacja, systemy transportowe* 11/2016, 93–97.
- [28] Siadkowska K., Grabowski L.: Safety of using mobile photovoltaic installations. *Logistyka* 6/2014, 9476–9485.
- [29] Tasi E., Griffini G.: Polymeric materials for photon management in photovoltaics. *Photovoltaic Energy Materials and Photovoltaic Cells* 196/2019, 43–56.
- [30] Wielgus J., Kasperek D., Małek A., Lusiak T.: Developed generations of electric buses produced by Ursus. *Autobusy: technika, eksploatacja, systemy transportowe* 11/2017, 20–25.
- [31] Yin E., Li Q., Xuan Y.: Experimental optimization of operating conditions for concentrating photovoltaic-thermoelectric hybrid system. *Journal of Power Sources* 422/2019, 25–32.
- [32] Zarajczyk K., Małek A., Koško M.: Constructional and functional assumptions of a Ursus Elvi vehicle with an electric drive. *Autobusy: technika, eksploatacja, systemy transportowe* 6/2018, 309–313 [DOI: 10.24136/atest.2018.082].
- [33] <http://lpnt.pl/> (access 2019.07.09).
- [34] <http://server.growatt.com/login.do> (access 2019.07.09).
- [35] <https://onemeter.com/pl/> [access 2019.07.09].
- [36] <http://renovi.pl/naslonecznienie-w-polsce/> (access 2019.10.02).

Ph.D. Eng. Arkadiusz Małeke-mail: arkadiusz.malek@wsei.lublin.pl

Assistant professor at the Faculty of Transport and Computer Science at the University of Economics and Innovation in Lublin. Machine, tooling and vehicle designer. In his scientific work, he deals with the use of alternative fuels for vehicle propulsion (LPG, CNG, E85, H2). Designer of photovoltaic systems for charging electric vehicles. Coordinator of many research and development projects. He actively cooperates with companies to apply to national and EU projects for research and development in enterprises. A long-time employee of the Lublin Science and Technology Park.



ORCID ID: 0000-0001-7772-2755

*otrzymano/received: 20.08.2019**przyjęto do druku/accepted: 06.12.2019*

DOI: 10.35784/IAPGOS.728

DESIGN, CONSTRUCTION AND AUTOMATIC CONTROL SYSTEM OF SINGLE-STAGE SIX-BED ADSORPTION HEAT PUMP

Katarzyna Zwarycz-Makles¹, Sławomir Jaszczak²¹West Pomeranian University of Technology Szczecin, Department of Heating, Ventilation and Heat Engineering, Szczecin, Poland, ²West Pomeranian University of Technology Szczecin, Department of Methods of Artificial Intelligence & Applied Mathematics, Szczecin, Poland

Abstract. The construction and automatic control of single-stage six-bed adsorption heat pump for heating and cooling purposes is discussed. The presented device is design to simulate operating conditions as well as temperature and uptake changes in the adsorbers/desorbers and consequently to describe the performance of the six-bed adsorption heat pump. The authors focus on advanced operation and strategy of multi-bed heat pump adsorber/desorber performance configuration. Through the use of a sequential system of sorption columns operation, the continuous character of the gained power of device in a wide range is obtained. It is possible as a result of using in the device the quantitative control of the pump by switching sequentially columns (sequential control), quality control by changing the temperature of heating/cooling water flowing in series or parallel through sorption columns and by changing the time parameter of sorption process (adsorption/desorption time) of the bed.

Keywords: heat pump, adsorption, automatic control

PROJEKT, BUDOWA I SYSTEM AUTOMATYCZNEJ REGULACJI JEDNOSTOPNIOWEJ SZEŚCIOKOMOROWEJ ADSORPCYJNEJ POMPY CIEPŁA

Streszczenie. W artykule przedstawiono projekt budowy i automatycznej regulacji jednostopniowej sześciokomorowej adsorpcyjnej pompy ciepła zastosowanej do uzyskania ciepła i chłodu. Omawiane urządzenie zaprojektowano w celu oceny parametrów pracy oraz zmian temperatury i stężenia w adsorberze/desorberze a w konsekwencji w celu określenia efektywności sześciokomorowej adsorpcyjnej pompy ciepła. Autorzy skoncentrowali się na możliwości zaawansowanej regulacji pracy i efektywności wielokomorowego urządzenia. Poprzez zastosowanie sekwencyjnego układu komór sorpcyjnych otrzymano ciągly charakter uzyskiwanej mocy w szerokim zakresie. Jest to możliwe w wyniku zastosowania w urządzeniu regulacji ilościowej mocy pompy poprzez załączanie kolejnych segmentów (regulacja sekwencyjne), regulację jakościową poprzez zmianę temperatur wody grzewczej/chłodzącej przepływającej szeregowo/równolegle przez kolumny sorpcyjne oraz przez zmianę parametru czasu pracy (czasu adsorpcji/desorpcji) kolumny.

Słowa kluczowe: pompa ciepła, adsorpcja, automatyczna regulacja

Introduction

Contemporary directions of technical development are inextricably linked to the rational management of natural resources and the protection of the natural environment. In the field of heat pumps, the compressor ones are still the most popular. However, it is not insignificant that electric energy is required for their work, the production of which causes increased emission of greenhouse gases during the conversion of energy accumulated in natural fuels into electricity. For this reason, it is important to limit the consumption of fossil fuels and that is why the sorption technologies (absorption and adsorption), which directly use heat, especially of low temperature sources to drive the heat pumps, are becoming more and more important [8, 9, 13, 15, 20].

The adsorption methods are widely used in chemical industry, environmental protection and other fields, for separation and purification of gases and liquids [2, 6, 10]. During the past two decades, this phenomenon was exploited to produce cooling and heating [11, 17, 19]. With the increasing prices of electricity, the advantage of sorption pumps is the use of thermo-chemical compression, instead of mechanical compression, therefore instead of electricity, the adsorption heat pump drives heat [4, 5, 7, 12]. Recently a large amount of research was done on various types of adsorption heat pumps, as an alternative to vapour compression systems [1, 14, 16].

Adsorption devices can be used in two main ways, giving a wide range of user experience. The first application, becoming more and more important, is the use for cold production, the second – the use of adsorption systems for heat production [3, 18].

In relation to adsorption heat pumps, the requirement of competitiveness in technical and economic terms is faced with the classical technology of heat production in compressor systems. However, the problems of the appropriate construction of adsorbers and desorbers, so that they provide favourable conditions for heat and mass exchange inhibit the development and installation of these units in heating and cooling systems, because they do not achieve satisfactory values of the COP

(Coefficient of Performance) as well as the coefficient SCP (Specific Cooling Power) in relation to the high price of the unit.

In order to increase the efficiency of utilization of low temperature heat source, to increase efficiency of the adsorption heat pump, modification of the basic single-stage two-bed construction of the adsorption heat pump to the multi-bed construction is proposed [21, 22]. In this paper advanced operation and strategy of single-stage six-bed heat pump adsorbers/desorbers performance is presented. The presented device is design to simulate operating conditions as well as temperature and uptake changes in the adsorbers/desorbers and consequently to describe the performance of the six-bed adsorption heat pump.

1. Design and construction of single-stage six-bed adsorption heat pump

Heat pump under consideration is designed as multifunctional device which could be operated in: serial-serial, serial-parallel, parallel-parallel mode of heating/cooling water flow.

Technical project of the six-bed adsorption heat pump with serial-serial flow of heating/cooling medium and its automatic control is presented. The heating and cooling power of device can be controlled: quantitative (control in steps), qualitative and working time of bed.

1.1. Construction and technical parameters

Multi-bed heat pump consists of the same basic elements as the conventional two-bed heat pump (evaporator, adsorber/desorber columns and condenser) but involve the sequential application of the sorption columns therefore is equipped with additional control valve blocks (the so-called multivalve). Adsorption heat pump, presented in the Fig. 1, operates with silica gel as adsorbent and water adsorbate. There are two basic circuits: closed internal circulation – in which the adsorbate (refrigerant vapour – water vapour) circulates, and an open external circuit as the heat transport outside the device (heating/cooling water).

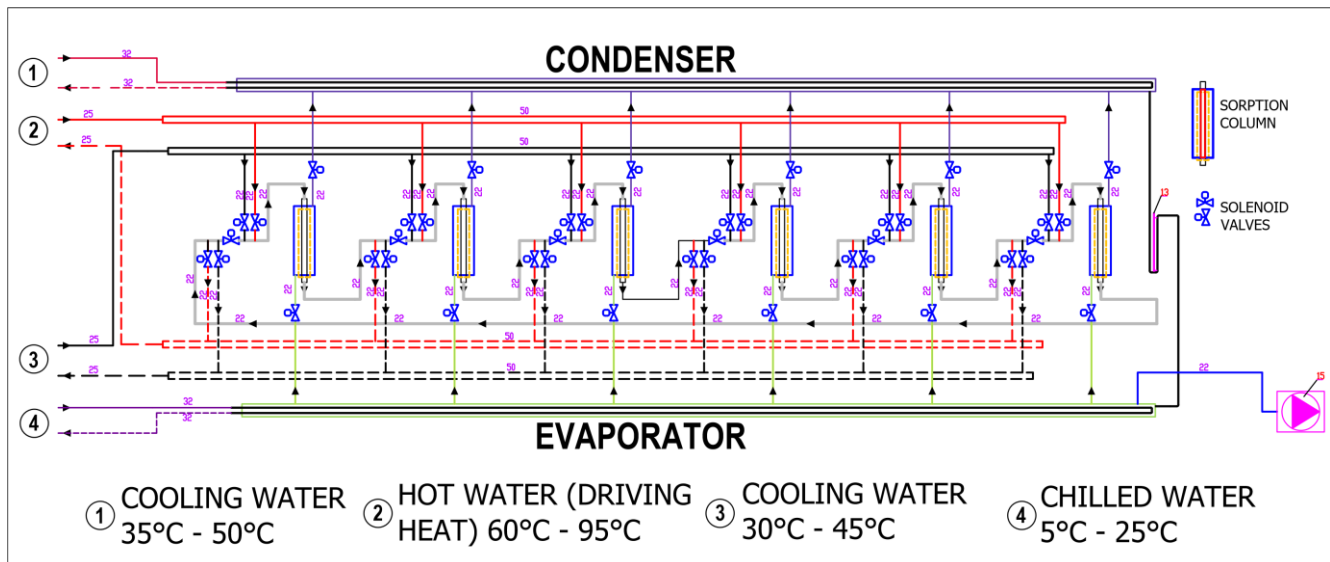


Fig. 1. Scheme of the six-bed adsorption heat pump with serial heating/cooling water flow and sequential application of the sorption columns

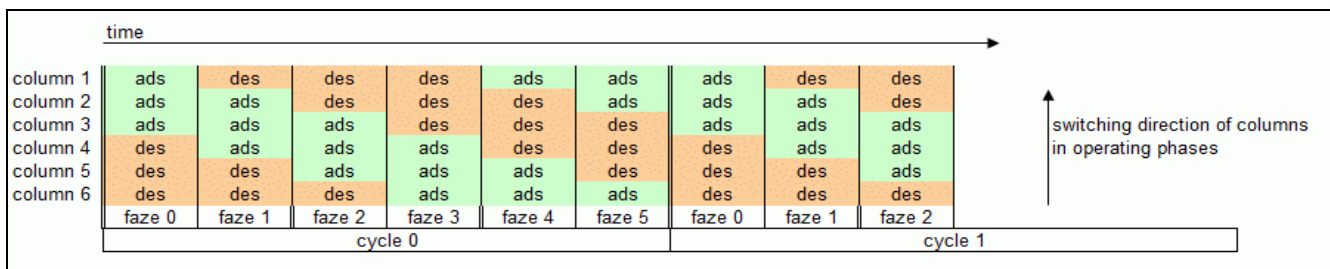


Fig. 2. Operating phases of the sorption beds of the six-bed adsorption heat pump in the serial-serial system (3 columns for adsorption / 3 columns for desorption)

The adsorption heat pump under consideration consists of an evaporator, six adsorber/desorber columns and a condenser. The sorption column contains tube with deposited adsorbent (silica gel).

The sorption column performs dual function: it works as an adsorber when cooled by cooling water and as a desorber when heated by hot driving water from outside. The adsorber/desorber is connected to the evaporator on one side while plugged in to the condenser on the other side with control valves. During the adsorption process, the adsorbate (refrigerant vapour) enters the adsorber after leaving the evaporator. When cooling water is switched to hot water, the adsorbate is directed to the condenser – this is the desorption phase.

The following technical parameters of the device were designed:

- sorption column power: up to 200 W per 1 meter of pipe in the adsorber/desorber,
- length of adsorber/desorber column: 1.0 m,
- diameter of the pipe inside adsorber/desorber: Cu 22x1 mm,
- coating of the pipes inside adsorber: stainless steel 103x1,5 mm,
- silica gel layer thickness: 15 mm,
- mass of the silica gel in the sorption column: 1.05 kg
- max. power of evaporator (3 working sorption columns): 800 W,
- max. power of condenser (3 working sorption columns): 600 W,
- temperature of cooling water in adsorption: 30°C–45°C,
- water mass flow of cooling water in adsorption: 0.06 m³/h–0.23 m³/h,
- pressure drop of cooling water in adsorption: 1.5 kPa–25 kPa
- temperature of heating water in desorption: 60°C–95°C,
- water mass flow of heating water in desorption: 0.06 m³/h–0.23 m³/h,
- pressure drop of heating water in desorption: 1.5 kPa–25 kPa,

- temperature of cooling water in condenser: 35°C–50°C,
- water mass flow of cooling water in condenser: 0.08 m³/h–0.35 m³/h,
- pressure drop of cooling water in adsorption: 2.5 kPa–30 kPa
- temperature of chilled water in evaporator: 5°C–25°C,
- water mass flow of chilled water in evaporator: 0.08 m³/h–0.35 m³/h,
- pressure drop of chilled water in evaporator: 2.5 kPa–30 kPa.

1.2. Design and realization of the adsorption/desorption process

Through the use of a sequential system of sorption columns work, the continuous character of the gained power of the device in a wide range is obtained.

It is assumed that the full cycle of the process is divided into sub-phases, the number of which is equal to the number of operating adsorption columns. After completion of the partial sub-phase in the last column the heat pump begins first partial phase, and thus starts the next full cycle of its operation (Fig. 2). Operating sub-phases of the sorption columns of the six-bed adsorption heat pump in the serial-serial mode, always assuming that three columns participate in the adsorption process and three columns participate in the desorption process (3 columns for adsorption / 3 columns for desorption).

In the Fig. 1, adsorption heat pump during the zero phase of the cycle, regarding the external refrigerant circuit is presented. The cooling water from the supply distributor is directed to the first sorption column carrying out the adsorption process. Then after receiving the heat resulting the adsorption, it leaves it and flows into subsequent adsorption columns in series. Since the cooling water warmed up initially during its passage through the column 1 and 2, therefore, the adsorption process in the 3rd column is slower. Cooling water, after flowing through three columns, supplies flow distributor and is intended for further use. After the adsorption process 1st column is switched to desorption

process and is supplied with heating water (driving heat) during the next phase of the cycle.

Similar to the previous process, the desorption column is supplied with heating water from distributor. The high temperature heating water is directed to column 4 and then flows through column 5 and 6 after which it is directed to the heating water return distributor. As a result of desorption heating water is cooled down. During desorption the refrigerant is desorbed very quickly in the first column, thus this column is assigned to the adsorber process and is supplied with water as the last one in series during the next cycle.

In the next phase of the cycle, columns 2, 3 and 4 participate in the adsorption process, however, it is column number 2 supplied with cooling water from the water distributor as the first in series to obtain the highest possible concentration of vapour (uptake) in the sorption bed. In columns 3 and 4 the adsorption process is being continued. Analogously, columns 5, 6 and 1 participate in the desorption process, however column 5 is supplied with heating water from the distributor as first in order. For the considered adsorption heat pump, regardless of the phase in progress, the assumption that three columns participate in the adsorption process and three columns participate in the desorption process is always accepted.

Conducting subsequent cycles of the heat pump operation allows to obtain the assumed saturation of the bed, required concentration or to obtain the assumed temperature of the utilized water as a medium.

Through the use of a sequential system of sorption columns, a continuous and adjustable character of the heating/cooling power in a wide range is obtained. It is possible as a result of using in the device the quantitative control of the pump by switching sequential columns (step control), quality control by changing the temperature of heating/cooling water flowing in series or parallel through sorption columns and by changing the time parameter of sorption process (adsorption/desorption time) of the bed. The described adjustment possibilities were obtained with the use of a control "multivalve" (Fig. 3). Its task is to perform the set algorithm of sequential operation of the multi-bed adsorption heat pump.

Designed multivalve, in general, is a set of valves with actuators for switching inflow/outflow of water from/to distributors and columns. This ensures the implementation of three major states of the multivalve in the adsorption heat pump:

- water flow between the adsorption/desorption columns,
- supply/return water to/from the column during adsorption,
- supply/return water to/from the column during desorption.

Valves with actuators, controlling the flow of water ensure the supply of the heating/cooling medium at the assumed temperature level and thus allow the control of the sorption process in columns, either as adsorber or desorber. The operation of valves is coordinated with the valves that open access to the evaporator or condenser. Sorption column operating as adsorber is connected to the evaporator and the column operating as desorber is connected to the condenser. The circulation of the working vapour (adsorbate) remains the same as in regular two-bed adsorption heat pump.

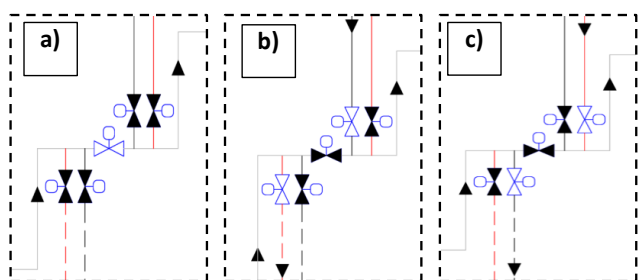


Fig. 3. Major states of the multivalve: a) water flow between the bed, b) supply/return water to/from the bed during adsorption, c) supply/return water to/from the bed during the desorption

2. Automatic control system of single-stage six-bed adsorption heat pump

2.1. Requirements analysis

The selected task of the control system is to automatically control the temperature of the utility medium in the adsorption heat pump by switching on the solenoid valve sections that change the directions of vapour and water flow.

Based on the initial assumptions, the following system functions were determined:

- Checking the pre-conditions necessary for the correct operation of the device;
- measuring the temperature of water and vapour at specific points of the installation;
- measurement of water pressure and vapour at certain points of the installation;
- measurement of water and vapour flow at specific points of the installation.
- controlling the direction of water and vapour;
- communication with the operator – manual or e.g. heating curve setting temperature;
- signalling of process states and alarms.

The diagram illustrating the individual functions of the device is shown in Figure 4.

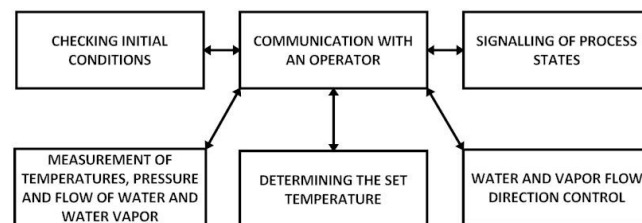


Fig. 4. Functional structure of the adsorption heat pump control system

Detailed functions of the control system:

1. System activation – the conditions for activation are:

- properly functioning control system (presence of power supply, controller in run mode, program in the controller running),
- an emergency switch not active,
- adequate vacuum (vacuum),
- specific water flow through the evaporator and condenser,
- specific vapour flow from the evaporator to the sorption chamber.

2. Temperature, pressure and flow measurement:

- it must be done by a device independent of the controller,
- the device must support signal variability ranges, in accordance with Table 1,
- detailed requirements for measuring devices are set out in Table 1,
- supply voltage for the measuring devices – 24 VDC.

3. Communication with the operator (operator's activities):

- system activation – active system (power supply for actuators, i.e. pump and valves),
- switching on the control – starts controlling the directions of water and vapour flows,
- alarms clearing – a continuation of the control,
- emergency stop – stopping the control by means of the emergency stop switch, which should cut off the power supply to the controller outputs and the power supply to actuators, regardless of the controller.

4. Process status signalling

- system ready – waiting for the control to be turned on,
- system during work – control,
- alarm – control stopped – alarm occurs if:
 - the permissible temperature for silica gel in the sorption chamber will be exceeded,

- there will be no vapour flow – no proper vacuum pressure (vacuum pump not working, leakage, etc.)
 - the maximum heating water temperature is exceeded
 - reporting alarm states of all measured variables, e.g. assumed *VarHiHi* values (maximum critical value of a specific variable), *VarLoLo* (minimum critical value of a specific variable), *VarHi* (max allowable value of a specific variable), *VarLo* (min allowable value of a specific variable).
- 5. Determining the set temperature of the utility medium**
- manual entry of the set temperature value,
 - setting the set temperature based on the heating curve,
- 6. Controlling the direction of flow of water and vapour**
- controlling the number of adsorbers working in series (from 1 to 3) by opening the vapour supply valve of the switched device and opening the bypass valve and closing the valves on the supply and return of the previous adsorber,
 - after reaching the maximum number of adsorbers switched on, reducing the flow of the utility medium.

Table 1. Technical parameters of measuring devices

Parameter	Symbol	Range
Sensors of water parameters at the adsorbers		
Water temperature	TT1–TT12	0–100°C
Water pressure	PT1–PT12	0–40 kPa
Flow	FT1–FT6	0–0.2 l
Sensors of vapour parameters at adsorbers, evaporator and condenser		
Vapour temperature	TT13 – TT20	0–100°C
Vapour pressure	PT13 – PT20	0–40 kPa
Flow	FT7	0–1 m ³ /h
Flow	FT8	0–6 m ³ /h
Sensors of water supplying to adsorbers		
Water temperature	TT21– TT24	0–100°C
Water pressure	PT21 – PT24	0–40 kPa
Water flow	FT9 – FT10	0–0.8 l/s
Sensors for evaporator and condenser feed water parameters		
Water temperature	TT25 – TT28	0–100°C
Water pressure	PT25 – PT28	0–40 kPa
Water flow	FT11 – FT12	0–0.8 l/s
Condensate parameters sensors (returning to the evaporator)		
Flow	FT13	0–2 l/s

2.2. Functional modules of the control system

Based on requirements analysis the control system can be divided into a number of separate, functionally dependent components, shown in Figure 5:

- control system,
- activation system,
- water and vapour temperature measurement systems,
- water and vapour pressure measurement systems,
- water and vapour flow measurement systems,
- solenoid valves sequential activation system,
- operator panel,
- supply system.

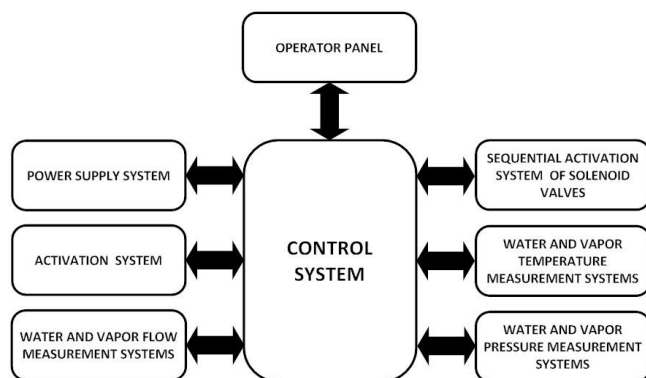


Fig. 5. Functional modules of the adsorption heat pump control system

Control system – the construction is based on the programmable controller, which will be used as an executive platform for control algorithms. After adding up all the inputs and

outputs of individual system components, it turned out that the controller must have at least 10 binary inputs, at least 42 binary outputs and at least 69 analogue inputs. Due to the type of switched signals, the binary outputs are to be of transistor/relay type. Due to the possibility of interference with analogue signals and the length of the cabling, a 4–20 [mA] current standard should be used.

Activation system – turns on the power of actuators only after the full start of the controller and constantly checks whether adequate vacuum is provided, whether there is the required water flow through the evaporator and the condenser, whether there is the required vapour flow from the evaporator to the sorption chamber, disconnects the power supply and sends information about it to the control system. The system consists of: two-state sensors for vacuum, vapour and water flow, emergency stop switch and toggle switch. We describe below specific functions of all inputs and outputs in accordance with the variable type in the control program.

Outputs:

- "Active system" light – 1 bit
- "Controller ready" light – 1 bit

Inputs:

- switch (key) "Activate system" – 1 bit
- "Negative pressure OK" sensor – 1 bit
- "OK vapour flow" sensor – 1 bit
- "Water flow OK" sensor – 1 bit

Solenoid valves sequential activation system its task is to sequentially switch on the appropriate solenoids, providing vapour and water flows in a given direction.

Outputs:

- solenoid valve control – 42 bits
- vacuum pump control – 1 bit

Temperature, pressure and flow measuring systems for water and vapour – are designed to read the current value of a specific parameter and send it to the control system as an electric signal, i.e. current. An arrangement of all analogue measuring devices is shown in Figure 6.

Inputs:

- information from sensors – 69 – 16 bits words

Operator panel – buttons and switches used to control the process and indicator lights informing about the status of the process. The following operations planned from the panel are planned:

- system activation – mode of operation, inputs and outputs, described in the section Activation system.
- switching on and stopping the control

Outputs:

- "Active Control" light – 1 bit

Inputs:

- "Start" button – 1 bit
- "Stop" button – 1 bit
- Alarm clearing – after the alarm signal has been cleared, the control continues.

Outputs:

- "Alarm" light – 1 bit

Inputs:

- "Alarm Reset" button – 1 bit

- Emergency stopping of the device – when any abnormal or dangerous situation occurs, an operator should immediately stop the heat pump.

Outputs:

- "Failure" lamp – 1 bit

Inputs:

- "Emergency Stop" switch – 1 bit

Power supply system – in the heat pump control system two separate supply systems will be used for the control system and external devices. Supply systems should provide standard 24VDC supply voltage for the control system and external devices – sensors, solenoid valves and relays.

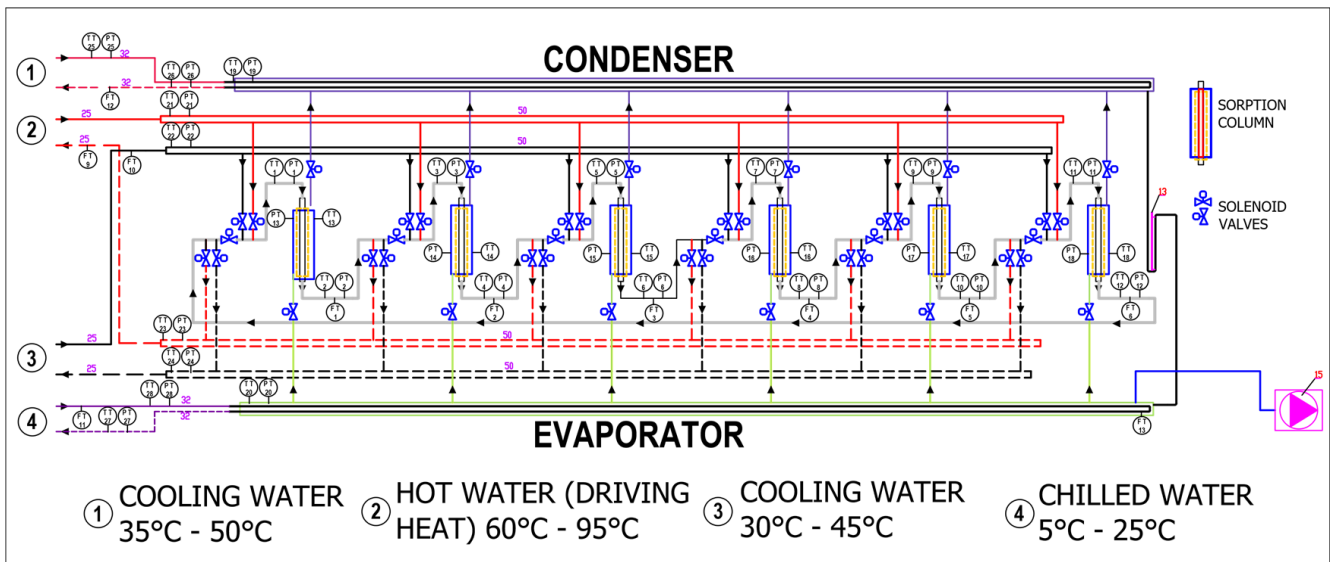


Fig. 6. Arrangement of analogue measuring devices for the six-bed adsorption heat pump

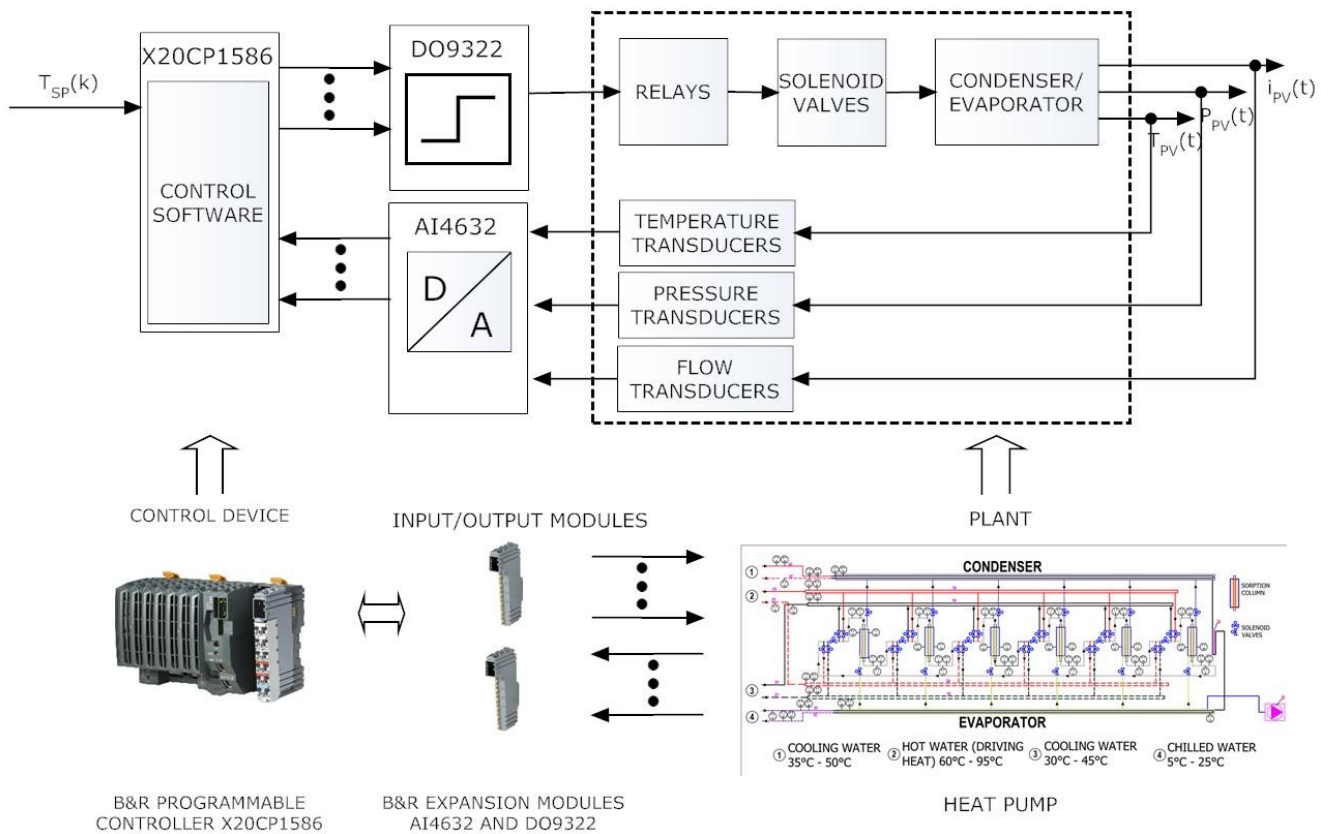


Fig. 7. General diagram of the adsorption heat pump control system

2.3. Hardware configuration of the control system

A general diagram of the heat pump control system is presented in Figure 7. The main part of the control system is the control device (X20CP1586), which is a programmable digital controller, typically used in industrial automation systems. A control device cooperates with the plant by means of input/output devices i.e. analogue/digital inputs and digital inputs/outputs.

The main task of the control system is to make a temperature $T_{PV}(t)$ stable and close as possible to the set temperature $T_{SP}(t)$.

By means of analogue/digital modules (AI4632) are proceeded signals from temperature, pressure and flow transducers. Based on these measurements and sequential procedure, described earlier, the programmable controller X20 CP1586 activates solenoid valves by means of digital output modules (DO9322) to achieve set temperature $T_{SP}(t)$ of the utility medium. A crucial for proper control operations is developed sequential control algorithm.

3. Conclusion

Through the use of a sequential system of sorption columns operation, the continuous character of the gained power of the device in a wide range is obtained. It is possible as a result of using in the device the quantitative control of the pump by switching sequential columns (sequential control), quality control by changing the temperature of heating/cooling water flowing in series or parallel through sorption columns and by changing the time parameter of sorption process (adsorption/desorption time) of the bed. The described control possibilities were obtained by using of a "multivalve" control, which task is to perform a given algorithm for sequential heat pump operation.

The described nature of the operation of a multi-bed heat pump refers to a system in which the heating/cooling water flows through the sorption columns in series mode, and the number of columns assigned for adsorption or desorption is half of the total number of columns in the device. However, the presented method of control enables the device to be launched in accordance with other systems. For example, in one of them, the number of sorption columns assigned to the adsorption/desorption process may be asymmetric (more for adsorption due to the slower course of this process). The next system is one in which the heating/cooling medium flows through the sorption columns in parallel (to each column directly from the distributor). The additional variance is a system in which, through the adsorbent beds the cooling medium flows, for example, in series, and through the desorption column, in parallel.

The heat pump control system presented in the last part of the article enables flexible automatic temperature control. But this requires multi-point measurement of temperature, pressure and flow of both water and vapour. Apart from measurement part, a sequencer control algorithm is needed for the proper solenoid valves manipulations.

References

- [1] Akisawa A., Miyazaki T.: Multi-bed adsorption heat pump cycles and their optimal operation. In: Saha B.B., Ng K. C. (Ed.): *Advances in Adsorption Technology*. Nova Science Publishers, 2010.
- [2] Badura J., Wiśniewski A.: Dociążenie obiegu energetycznego elektrociepłowni z wykorzystaniem urządzeń chłodniczych i pomp ciepła. In: Trela M. (Ed.): *Ciepło skojarzone: komfort zimą i latem – trójgeneracja : materiały z konferencji naukowo-technicznej*, Wydawnictwo Instytutu Maszyn Przepływowych, Gdańsk 2005.
- [3] Chua H. T., Ng K. C., Malek A., Kashiwagi T., Akisawa A., Saha B. B.: Multi-bed regenerative adsorption chiller – improving the utilization of waste heat and reducing the chilled water outlet temperature fluctuation. *International Journal of Refrigeration* 24(2), 2001, 124–136.
- [4] Demira H., Mobedi M., Ülkü S.: A review on adsorption heat pump: Problems and solutions. *Renewable and Sustainable Energy Reviews* 12, 2008, 2381–2403.
- [5] Fan Y., Luo L., Souyri B. B.: Review of solar sorption refrigeration technologies: Development and applications. *Renew. Suist. Energy Rev* 11(8), 2007, 1758–1775.
- [6] Grisel R. J. H., Smeding S. F., De Boer R.: Waste heat driven silica gel/water adsorption cooling in trigeneration. *Applied Thermal Engineering* 30, 2010, 1039–1046.
- [7] Grzebielec A.: Zastosowanie i perspektywy rozwoju adsorpcyjnych urządzeń chłodniczych w chłodnictwie i klimatyzacji. *Chłodnictwo i Klimatyzacja* 4, 2005, 52–57.
- [8] Gwadera, M., Kupiec, K.: Adsorpcyjne układy chłodnicze. *Inż. Ap. Chem.* 50(5), 2011, 38–39.
- [9] Idczak M.: Współczesne technologie wykorzystania ciepła do produkcji chłodu małej wydajności. *Workshop: Wykorzystanie ciepła sieciowego do produkcji*

chłodu, sposobem na zwiększenie efektywności systemów ciepłowniczych, Warszawa 2008.

- [10] Jaskólski M.: Adsorpcyjne układy klimatyzacyjne. In: Trela M. (Ed.): *Ciepło skojarzone: komfort zimą i latem – trójgeneracja : materiały z konferencji naukowo-technicznej*, Wydawnictwo Instytutu Maszyn Przepływowych, Gdańsk 2005.
- [11] Meunier F.: Solid sorption heat powered cycles for cooling and heat pumping applications. *Applied Thermal Engineering* 18, 1998, 715–729.
- [12] Nunez T., Mittelbach W., Henning H. M.: Development of an adsorption chiller and heat pump for domestic heating and air-conditioning applications. *Appl Therm Eng* 27(13), 2007, 2205–12.
- [13] Paderewski M. L.: *Procesy adsorpcyjne w inżynierii chemicznej*. Wydawnictwa Naukowo-Techniczne, Warszawa 1999.
- [14] Park I., Knaebel K. S.: Adsorption breakthrough behavior: unusual effects and possible causes. *AIChE Journal* 38(5), 1992, 660–670.
- [15] Rosiński M.: *Odzyskiwanie ciepła w wybranych technologiach inżynierii środowiska*. Oficyna Wydawnicza Politechniki Warszawskiej, Warszawa 2008.
- [16] San J.-Y., Hsu H.-Ch.: Performance of a multi-bed adsorption heat pump using SWS-1L composite adsorbent and water as the working pair. *Appl Therm Eng.* 29(8–9), 2009, 1606–1613.
- [17] Srivastava N. C., Eames I. W.: A review of developments in solid–vapour adsorption refrigeration and heat pump systems. *Journal of the Institute of Energy* 70, 1997, 116–127.
- [18] Wang A., Chua H. T., Ng K. C.: Experimental investigation of silica gel–water adsorption chillers with and without a passive heat recovery scheme. *International Journal of Refrigeration* 28(5), 2005, 756–765.
- [19] Yildirim Z. E., Mobedi M., Ulku S.: *A Review on proper working pairs for solar adsorptions heat pumps*. Proceedings Book: Solar Future, 2010.
- [20] Zarzycki R.: *Wymiana ciepła i ruch masy w inżynierii środowiska*. Wydawnictwa Naukowo-Techniczne, Warszawa 2010.
- [21] Zwarycz-Makles K., Kuczynski K.: Model and simulation of six-bed silica gel-water adsorption heat pump. In: Stanek W., Gładysz P. et al. (Ed.): *4th International Conference on Contemporary Problems of Thermal Engineering*. The Silesian University of Technology, Institute of Thermal Technology, Gliwice-Katowice 2016, 809–818.
- [22] Zwarycz-Makles K., Szafflik W., Kuczynski K., Nejránowski J.: Projekt sześciokomorowej adsorpcyjnej pompy ciepła i jej automatycznej regulacji. In: Besler M., Fijewski M. (Ed.): *2014 Air & Heat Energy in Buildings*. Oficyna Wydawnicza Politechniki Wrocławskiej, Wrocław 2014, 317–322.

Ph.D. Eng. Katarzyna Zwarycz-Makles

email: Katarzyna.Zwarycz-Makles@zut.edu.pl



M.Sc. Eng. graduate at Technical University of Szczecin in 2000, Faculty of Civil Engineering, field of study: Sanitary Devices. In 2002 UNU scholarship in Reykjavik in geothermal water utilization. Ph.D. defended in 2006 at Faculty of Mechanical Engineering, field of study: modelling of heat exchange in ground heat storage. 3 years of professional experience in designing of building installations and in the selling of ventilation devices. From 2008 assistant professor in Department of Heating, Ventilation and Heat Engineering. Manager of research project in 2011–2014. Research interests include renewable, alternative and conventional heat sources, external heating installations i.e. snow melting, mathematical modelling of heat transfer.

ORCID ID: 0000-0002-3738-9596

Ph.D. Eng. Sławomir Jaszczak

email: sjaszczak@zut.edu.pl



Since 1994 as an assistant at the Department of Maritime Technology of the Technical University of Szczecin was leading research connected with an underwater vehicles control using artificial intelligence methods. Since 2002 as a professor assistant at the Department of Computer Science of the West Pomeranian University of Technology in Szczecin. Current scientific activity is related to the implementation of digital control algorithms based on the PLC platform.

ORCID ID: 0000-0002-5591-2512

otrzymano/received: 11.1.2019

przyjęto do druku/accepted: 06.12.2019

LIST OF REVIEWERS COOPERATING WITH THE JOURNAL IN 2019

LISTA RECENZENTÓW WSPÓŁPRACUJĄCYCH Z CZASOPISMEM W ROKU 2019

Prof.	Andruszkiewicz	Artur	Wroclaw University of Technology (Wroclaw, Poland)
Prof.	Barabahs	Oleg	State University of Telecommunications (Kyiv, Ukraine)
Ph.D.	Bednarz	Jarosław	AGH University of Technology (Cracow, Poland)
Ph.D.	Boyko	Oksana	Danylo Halytsky Lviv National Medical University (Lviv, Ukraine)
Prof.	Cięszczyk	Sławomir	Lublin University of Technology (Lublin, Poland)
Ph.D.	Dorosh	Nataliya	Danylo Halytsky Lviv National Medical University (Lviv, Ukraine)
Prof.	Druzhinin	Volodymyr	National Technical University of Ukraine "Igor Sikorsky Kyiv Polytechnic Institute" (Kyiv, Ukraine)
Prof.	Franiv	Andriy	Ivan Franko National University of Lviv (Lviv, Ukraine)
Ph.D.	Gromaszek	Konrad	Lublin University of Technology (Lublin, Poland)
Ph.D.	Gumeniuk	Larysa	Lutsk National Technical University (Lutsk, Ukraine)
Ph.D.	Haliuk	Serhii	Yuriy Fedkovych Chernivtsi National University (Chernivtsi, Ukraina)
Prof.	Hlaponin	Yurii	Kyiv National University of Construction and Architecture (Kyiv, Ukraine)
Prof.	Hotra	Zenon	Lviv Polytechnic National University (Lviv, Ukraine)
Prof.	Hotra	Oleksandra	Lublin University of Technology (Lublin, Poland)
Ph.D.	Ilarionov	Oleg	Taras Shevchenko National University of Kyiv (Kyiv, Ukraine)
Prof.	Jaglarz	Janusz	Cracow University of Technology (Cracow, Poland)
Prof.	Kaidan	Mykola	Lviv Polytechnic National University (Lviv, Ukraine)
Ph.D.	Kalizhanova	Aliya	Institute of Information and Computational Technologies SR MES RK (Almaty, Kazakhstan), Al-Farabi Kazakh National University (Almaty, Kazakhstan)
Ph.D.	Kłosowski	Grzegorz	Lublin University of Technology (Lublin, Poland)
Prof.	Klymash	Mykhailo	Lviv Polytechnic National University (Lviv, Ukraine)
Prof.	Knyazeva	Nina	Odessa National Academy of Food Technologies (Odessa, Ukraine)
Prof.	Korobchynskiy	Maksym	Military-Diplomatic Academy Named Eugene Bereznyak (Kyiv, Ukraine)
Prof.	Korzeniewska	Ewa	University of Warmia and Mazury in Olsztyn (Olsztyn, Poland)
Prof.	Koshevyi	Vitaliy	National University "Odessa Maritime Academy" (Odessa, Ukraina)
Prof.	Kostruba	Andriy	Stepan Gzhytskyi National University of Veterinary Medicine and Biotechnologies (Lviv, Ukraine)
Prof.	Kotyra	Andrzej	Lublin University of Technology (Lublin, Poland)
Prof.	Kovalyuk	Zakhar	institute For Problems of Material Science I.M. Frantsevich National Academy of Science (Kyiv, Ukraine)
Ph.D.	Krzaczek	Paweł	University of Life Sciences in Lublin (Lublin, Poland)
Prof.	Kudrya	Volodymyr	Odessa National Polytechnic University (Odessa, Ukraine)
Ph.D.	Kurz	Dariusz	Poznan University of Technology (Poznan, Poland)
Prof.	Liubchyyk	Vitalii	Khmelnytskyi National University (Khmelnytskyi, Ukraine)
Prof.	Luján Mora	Sergio	University of Alicante (Alicante, Spain)
Prof.	Lytvyenko	Volodymyr	Kherson National Technical University (Kherson, Ukraine)
Ph.D.	Mastny	Petr	Brno University of Technology (Brno, Czech Republic)
Ph.D.	Mazurek	Paweł	Lublin University of Technology (Lublin, Poland)
Ph.D.	Moravek	Jan	Brno University of Technology (Brno, Czech Republic)
Prof.	Mosorov	Volodymyr	Lodz University of Technology (Lodz, Poland)
Ph.D.	Naumchuk	Oleksandr	National University of Water and Environmental Engineering (Rivne, Ukraine)
Prof.	Olszewski	Serge	Taras Shevchenko National University of Kyiv (Kyiv, Ukraine)
Ph.D.	Omiotek	Zbigniew	Lublin University of Technology (Lublin, Poland)
Ph.D.	Paszkiel	Szczepan	Opole University of Technology (Opole, Poland)
Prof.	Pavlov	Sergey	Vinnitsia National Technical University (Vinnitsia, Ukraine)
Ph.D.	Penkała	Piotr	Lublin University of Technology (Lublin, Poland)
Ph.D.	Plechawska-Wójcik	Małgorzata	Lublin University of Technology (Lublin, Poland)

Ph.D.	Porzuczek	Jan	Cracow University of Technology (Cracow, Poland)
Ph.D.	Rolek	Jarosław	Kielce University of Technology (Kielce, Poland)
Ph.D.	Romanyk	Igor	Quartz Plant LLC (Chernivtsi, Ukraine)
Prof.	Rozorinov	Heorgiy	National Technical University of Ukraine "Igor Sikorsky Kyiv Polytechnic Institute" (Kyiv, Ukraine)
Ph.D.	Rymarczyk	Tomasz	Research & Development Centre Netrix S.A. (Lublin, Poland), University of Economics and Innovation in Lublin (Lublin, Poland)
Prof.	Semenko	Anatoliy	State University of Telecommunications (Kyiv, Ukraine)
Prof.	Semenov	Andriy	Vinnitsia National Technical University (Vinnitsia, Ukraine)
Ph.D.	Smailova	Saule	D. Serikbayev East Kazakhstan State Technical University (Ust-Kamenogorsk, Kazakhstan)
Prof.	Smolik	Waldemar	Warsaw University of Technology (Warsaw, Poland)
Prof.	Sokolovsky	Alexander	Oles Honchar Dnipro National University (Dnipro, Ukraine)
Prof.	Sorokatyi	Ruslan	Khmelnyskyi National University (Khmelnyskyi, Ukraine)
Ph.D.	Stepanchenko	Olga	National University of Water and Environmental Engineering (Rivne, Ukraine)
Prof.	Stepanov	Mykola	National Technical University of Ukraine "Igor Sikorsky Kyiv Polytechnic Institute" (Kyiv, Ukraine)
Prof.	Sulemenov	Batyrbek	Kazakh National Research Technical University After K.I. Satpayev (Almaty, Kazakhstan)
Prof.	Szromba	Andrzej	Cracow University of Technology (Cracow, Poland)
Prof.	Toliupa	Serhii	Taras Shevchenko National University of Kyiv (Kyiv, Ukraine)
Prof.	Vasiuta	Konstantyn	Ivan Kozhedub Kharkiv National Air Force University (Kharkiv, Ukraine)
Ph.D.	Yegoshyna	Hanna	Yuriy Fedkovych Chernivtsi National University (Chernivtsi, Ukraine)
Prof.	Zabolotnii	Serhii	Cherkasy State Technological University (Cherkasy, Ukraine)
Ph.D.	Zabolotnyi	Oleg	Lutsk National Technical University (Lutsk, Ukraine)
Ph.D.	Zagorodna	Natalia	Ternopil Ivan Puluj National Technical University (Ternopil, Ukraine)
Ph.D.	Żelazna	Agnieszka	Lublin University of Technology (Lublin, Poland)
Prof.	Ziółkowski	Marcin	West Pomeranian University of Technology Szczecin (Szczecin, Poland)
Ph.D.	Zyska	Tomasz	Lublin University of Technology (Lublin, Poland)